

Coventry University
Faculty of Engineering, Environment & Computing
Department of Mechanical, Aerospace & Automotive
Engineering



**6051MAA Individual Project
Final Project Report & Logbook**

**Model Based Control Design and Analysis of a
Multi-Axis Solar Tracking Array for Optimal Power
Output Using MATLAB and Simulink.**

Submitted in partial fulfilment of the requirements for the degree of Bachelor
of Engineering

**H. West SID: 11052582
BEng Mechanical Engineering
Supervisor: Dr A. Pike
April, 2025**

Declaration: The work described in this report is the result of my own investigations. All sections of the text and results that have been obtained from other work are fully referenced. I understand that cheating and plagiarism constitute a breach of University Regulations and will be dealt with accordingly.

Signed:
Harrison West

Date: 14-04-2025

Acknowledgements:

This project, and my degree as a whole, would have not been even remotely possible without the help of a few key people:

I wanted to thank my supervisor, Dr Andrew Pike, for supporting my passion for control & instrumentation. I attribute much of the path I have taken forward to the advice given by you and will always remember you as a mentor and a friend.

To my partner, Kayleigh, your patience is unmatched – thank you for your love and the support you give to me. You should be coming on stage with me to collect your degree in engineering, after all the endless nights troubleshooting.

Finally, to my amazing parents. Thank you for your endless support and belief in me. From telescopes on the balcony to solar module controllers. You are my inspiration.

I did it.

Contents

1.0 – Abstract	5
2.0 – Introduction	5
3.0 – Literature Review.....	6
3.1 - Boundary Conditions and Scoping	6
3.2 - Axes Control.....	6
3.3 – PV Modelling.....	7
3.4 - Conclusions.....	7
4.0 – Methodology	8
4.1 – Inputs	8
4.1.1 – Inputs Design	8
4.1.1a – Solar Position.....	8
4.1.1b – Solar Irradiance.....	11
4.1.2 – Inputs Validation	13
4.2 – Photovoltaic Cell Model	14
4.2.1 – Photovoltaic Cell Model Design.....	14
4.2.2 – PV Model Validation.....	18
4.3 – Controllers	21
4.3.1 – MPPT Photovoltaic Controller Design	22
4.3.2 – MPPT Axes Controller Design	28
4.4 - Test Scenario Derivation	37
5.0 – Results, Analysis and Discussion	40
5.1 – Test conditions	40
5.2 – Results	40
6.0 – Conclusion & Future Recommendations	43
6.1 - Conclusions.....	43
6.2 – Further Recommendations.....	45
7.0 – References.....	46
8.0 – Appendix A	47
i – Nomenclature	47
ii – List of Figures.....	48
iii – List of Tables.....	54
8.1 – Test Case Derivation	55
8.1.1 - Test Case Data.....	56
8.2 – Inputs Validation.....	72
8.3 – Solar Inputs (Solar Azimuth, Solar Altitude, Solar Irradiance, ambient temperature) 78	78

8.4 – PV Model	83
8.4.1 – PV Model Simulink	83
8.4.1a – Full PV Simulink Model	87
8.4.2 – Photovoltaic model validation	88
8.5 – Results	99
8.5.1 – Scenario 1	99
8.5.1a – Dual Axis.....	99
8.5.1b – Single Axis	100
8.5.2 – Scenario 2	103
8.5.2a – Dual Axis.....	103
8.5.2b – Single Axis	105
8.5.3 – Scenario 3	108
8.5.3a – Dual Axis.....	108
8.5.3b – Single Axis	109
8.5.4 – Scenario 4	112
8.5.4a – Dual Axis.....	112
8.5.4b – Single Axis	114
8.5.5 – Scenario 5	117
8.5.5a – Dual Axis.....	117
8.5.5b – Single Axis	119
8.5.6 – Scenario 6	122
8.5.6a – Dual Axis.....	122
8.5.6b – Single Axis	124
8.5.7 – MPPT Efficiency as % of Maximum Irradiance Incident on Module	127
8.5.8 – MPPT Efficiency as % of Maximum Power Generated by Module	130
9.5.9 - % Difference Between Incident and Maximum Irradiation on Module	133
8.5.10 – Efficiency of Tracking Strategies in all 6 Scenarios.....	136
8.5.11 – Raw Data Extracted	138
8.5.11a – Double Axes.....	138
8.5.11b – Single Axis.....	140

1.0 – Abstract

This report describes the methodologies and research associated with the simulation of a maximum power point tracking controller for both single and double axis solar modules for the purpose of discussing their viability in different regions. This is undertaken via use of the MathWorks Simulink and MATLAB software and several of their respective toolboxes. This was done in the hopes that in doing so, the gap in global and generalised analyses solar array controller strategies adopted based on regional positions, may be addressed in part. The hypothesis of this study was that for regions beyond $\pm 30^\circ$ latitude, dual axis tracking will produce a significant increase in power generated than that of single axis altitude tracking methods. The result of this discussion appears to partially support this hypothesis, with double axis tracking strategies consistently yielding greater than 40% more of the total power available in regions north of $+30^\circ$ latitude than the single axis counterpart. However, below -30° latitude, the results are inconsistent with this trend, resulting in an anomalous 18% difference in the efficiencies. As a result, further investigation is required to conclude the impact of southern hemisphere latitudes on the solar tracking strategies used.

2.0 – Introduction

The use of solar arrays for power generation is becoming an increasingly viable option. In many first world countries, there is growing support for renewable energies to take the place of their non-renewable counterparts (Wang et al., 2022). In developing countries, the same attitudes are combined with an enthusiasm for simple and effective sources of energy. Solar energy, particularly in recent years with the development of more efficient and productive photovoltaic materials (Pourasl et al., 2023), has become an increasingly viable option for these communities in satisfying their energy demands.

However, with the increasing positivity towards solar energy as a whole, there are some additional limitations on the performance of solar panels in general use which affect their viability. In particular, due to the changing seasons in the year, the solar position and intensity of solar irradiance is vastly variable for many regions (Mendoza, 2005), leading to variable energy yields and ultimately resulting in the inevitable reliance on old technologies which provide on demand and predictable energy yields, i.e. fossil fuels and natural gas (Handayani et al., 2018) (Arora et al., 2023).

Although there is no way to directly control the solar resource itself, there are methods by which the resource can be tapped to a more significant degree of its potential. One example of such a method is through the use of maximum power point tracking (MPPT) algorithms (Verma et al., 2015). These algorithms can be implemented in several ways, and there are many different forms and strategies which can be adopted. In general, the inspiration of these algorithms is to determine an ideal set point by which will allow for the greatest power generation by the solar array.

In the following sections, the MPPT algorithms will be seen in two separate forms: one, in the form of a variable load by which the power generated may be maximized, and two, a modified perturb and observe algorithm which is often seen in industrial applications.

The aim of this report is to address the gap in research of solar tracking uses based on regional variables. This was done through several objectives: The design of input signals, the design and modelling of a photovoltaic model, the design and implementation of a voltage controller and a

positional controller, and finally to make an effective analysis of data gathered through the use of the designed simulation.

The contents of this report will introduce the state of current research then detail the methodology used to achieve results. This methodology first approaches the simulation inputs, then the photovoltaic model used, then the controller strategies utilised, then finally some comments on test scenarios used to gather results. Following this, the results will be discussed in detail, before finally discussing conclusions and future recommendations.

3.0 – Literature Review

Research done was focussed on a single aim and several objectives. The aim of this discussion was to design a maximum power point tracking controller for a simulated solar array for optimal solar power generation. The initial hypothesis attributed to this study is that dual axis solar tracking will significantly increase power generation when compared to fixed axis methods.

3.1 - Boundary Conditions and Scoping

The use of simulation in discussing performance of solar arrays has also been actively pursued. One study approached simulation of a photovoltaic array in order to investigate the impact of the configurations of these solar arrays, i.e. in series, or parallel, using MATLAB and Simulink. In this case, a PV system was developed to discuss performances through the use of standard test conditions. These conditions are an irradiance of $1000Wm^{-2}$ and an ambient temperature of $25^{\circ}C$. This study also discussed the use of these conditions to impart partial shading conditions, where some modules in the array receive lower irradiances and the effects this has on the larger solar farm (Pendem & Mikkili, 2018). Very few simulations discuss real irradiance values taken from existing databases.

Another approaches a unique strategy of solar tracking, integrating weather and solar data in order to find the optimal tracking angles based on several models. Following analysis, the actuation of the solar array occurred only three times in a given day, yielding 91-94% of the potential yield for the chosen location (Batayneh et al., 2018). Again, the discussions made are for local climates and solar behaviours. No attempt at generalisations have been made. The climatological data used in the discussion, however, allowed for some predictive behaviour to be modelled, resulting in experimental results agreeing with the simulated outputs to within 20%. This is an example where climatological data has been used and as a direct result, the simulated outputs are generally relevant.

Although there are numerous studies on specific locations, very few make generalised conclusions based on the location of the solar module on the globe. One study discussed the effectiveness of making use of a calculated solar positioning controllers, based on the local time and date, in Malaysia. This study is extremely limited in location, taking into account a single location, experimentally. Although this study discusses the use of the dual axis tracking system described in multiple conditions, the study does not consider a variation in global position (Ahmad et al, 2013). Other studies similarly calculated the solar position, some as inputs to their simulations but others, like the aforementioned study, use the calculated position to directly control the axes.

3.2 - Axes Control

Concerning double axis tracking systems, many approaches have been discussed in depth. One “smart” automatic approach discussed the use of four light dependant resistors to sense

the intensity of the sun in four locations along the outer border of the array, allowing for the detection of the optimal alignment of the solar array with the position of maximum power. This was done experimentally, making use of an Arduino and servomotors on the two axes, azimuth and altitude. The results of this discussion boasted an increased efficiency of 19.73% when compared to the non-tracking alternative (Das et al., 2015). Another, taking an alternative approach, discussed the use of solar tracking through the use of spherical axial control, in both azimuth and altitude axes. This approach required no additional sensors to be used, only the existing historical solar position and PID based controllers to reduce any errors (Sidek et al., 2014).

Another investigation discusses the use of single axis solar trackers, making use of constraining the altitude angle of the solar array to an optimal tilt and allowing the variation of the azimuth angle (Chang, 2009). Often found is the discussion of the optimal tilt angle and its effects on the overall efficiency of the PV array. Referring again to the study by Batayneh et al. (2018), the tracking strategy discussed here actively approached minimal tracking efforts in order to reduce wasted energy in actuating the array. Rather than chasing the solar position, the strategy developed merely actuated the array to an optimal tilt and varied the arrays azimuth angle thrice per day. This study attempts to bridge the gap between single, double and fixed axial control.

3.3 – PV Modelling

There are many sources of literature which discuss, in depth, the modelling of PV systems. Many take advantage of very similar equations, with minor deviations. Abdin et al. (2018) discussed in detail the simulation of large photovoltaic arrays. The aim of the discussion was to open dialogue concerning power losses in large arrays resultant from inhomogeneity of cell temperatures and variabilities in photovoltaic modules. The resulting discussion determined that the five parameter model described is effective in describing photovoltaic behaviours. Another study previously described, (Pendem & Mikkili, 2018), describes a similar model taking advantage of the same five parameters described previously. This model, in particular, discussed the output of the modelled response when in an array of modules.

3.4 - Conclusions

To summarise, consistently when simulating solar tracking methods, a solar path is calculated. In most cases, the solar irradiance used to simulate the tracking methods are according to standard test conditions of irradiance, $E = 1000Wm^{-2}$, and at a temperature of $T = 25^{\circ}C$. Although several tracking strategies are discussed and simulated, the discussion of their compatibility for several locations is not often seen. Individual case studies are most common, approaching local scenarios with local data which allows for the opportunity to experimentally validate any developed model.

This study aims to address this gap, approaching the use of both single axis and double axis solar tracking methods based on local climatological data and regional positioning. By doing so, an understanding of the ideal solar array tracking configurations can be made possible, based on global positioning for stand-alone photovoltaic systems.

As a result of this review, the hypothesis of the report needs to be reviewed to match the adjustments in aim. The revised hypothesis predicts that for regions beyond $\pm 30^{\circ}$ latitude, dual axis tracking will produce a significant increase in power generated than that of single axis, altitude tracking, methods.

4.0 – Methodology

4.1 – Inputs

4.1.1 – Inputs Design

Defining the inputs of the simulation is a crucial step in ensuring that the simulation is accurate and to what extent. For solar arrays, the primary source of power generation is through the energy from the solar insolation (Fara et al, 2017). This is the core property which allows for power generation to occur in photovoltaics. This quantity is intuitively sourced from the sun, which moves across the sky based on the location and time of observation (Rosa-Clot et al, 2018). All equations and methods described were implemented into a Simulink model which was used to generate an inputs signal as required. This signal contains the aforementioned solar position, local irradiance, and local temperatures.

4.1.1a – Solar Position

To define solar position, spherical coordinates are most often utilized. These coordinates allow for the accurate description of a bodies position based on its location along two axes, rather than 3 as in cartesian coordinates. These coordinates are quantified in degrees and so allow for intuitive implementation into two axes controllers in both the azimuth and altitude axes. This was done utilising a mathematical approach.

To determine the azimuth, γ (Wang, 2019), and altitude, α , (Mghouchi et al., 2015), angles:

$$\alpha = \arcsin(\cos(\varphi) \cos(\omega_h) \cos(\delta) + \sin(\varphi) \sin(\delta))$$
$$\gamma = \begin{cases} \omega_h < 0, & \arccos\left(\frac{(\cos(\varphi) \sin(\delta) - \cos(\delta) \sin(\varphi) \cos(\omega_h))}{\cos(\alpha)}\right) - 180^\circ \\ \omega_h \geq 0, & -1 \cdot \left(\arccos\left(\frac{(\cos(\varphi) \sin(\delta) - \cos(\delta) \sin(\varphi) \cos(\omega_h))}{\cos(\alpha)}\right) - 180^\circ\right) \end{cases}$$

Where φ =positional latitude of the array, ω_h =local hour angle, and δ =solar declination angle (varying from 23.17° to -23.17° seasonally). From these equations, it is clear that there are only a few variables required to calculate the suns position for any given day, time, and location:

- The local latitudinal position of the observer,
- The solar declination angle of the chosen date,
- The local hour angle of the chosen time.

The latitudinal position of the observer is dependant on the vertical location of the observer on the globe taken from the equator. The local hour and solar declination angles, however, are determined as follows (Kalogirou, 2009):

$$\text{Local hour}, \quad \omega_h = 15 \cdot (12 - T_{sv})$$

Where T_{sv} is the true solar time in hours, based on a 24 hour system:

$$T_{sv} = T_l - \Delta T_{l,s} + \frac{(\Delta t + T_E)}{60}$$

where, T_E = equation of time

$$= 9.87 \cdot \sin\left(2 \cdot (N_d - 81) \cdot \frac{360}{364}\right) - 7.53 \cdot \cos\left((N_d - 81) \cdot \frac{360}{364}\right) - 1.5 \cdot \sin\left((N_d - 81) \cdot \frac{360}{364}\right)$$

And,

$$\text{solar declination, } \delta = 23.45 \cdot \sin \left[\frac{2\pi \cdot (284 + N_d)}{365} \right]$$

Where N_d =day number in the year, day 1 = January 1st (Rosa-Clot et al, 2018).

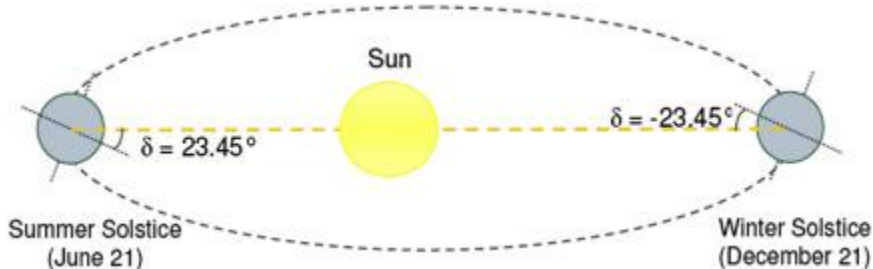


Figure 1: Solar declination angle variation demonstrated (Wang Z., 2019)

Utilising these equations, the solar altitude and azimuth can be calculated for the entire duration of a chosen day in each month, for a chosen location. The Simulink model can be populated utilising these equations as per section [9.3 – Solar Inputs](#). Note that there is no consideration of the local longitudinal position in any of the equations related to the solar position. As such, when considering building of the test cases, the longitudinal position can be safely neglected.

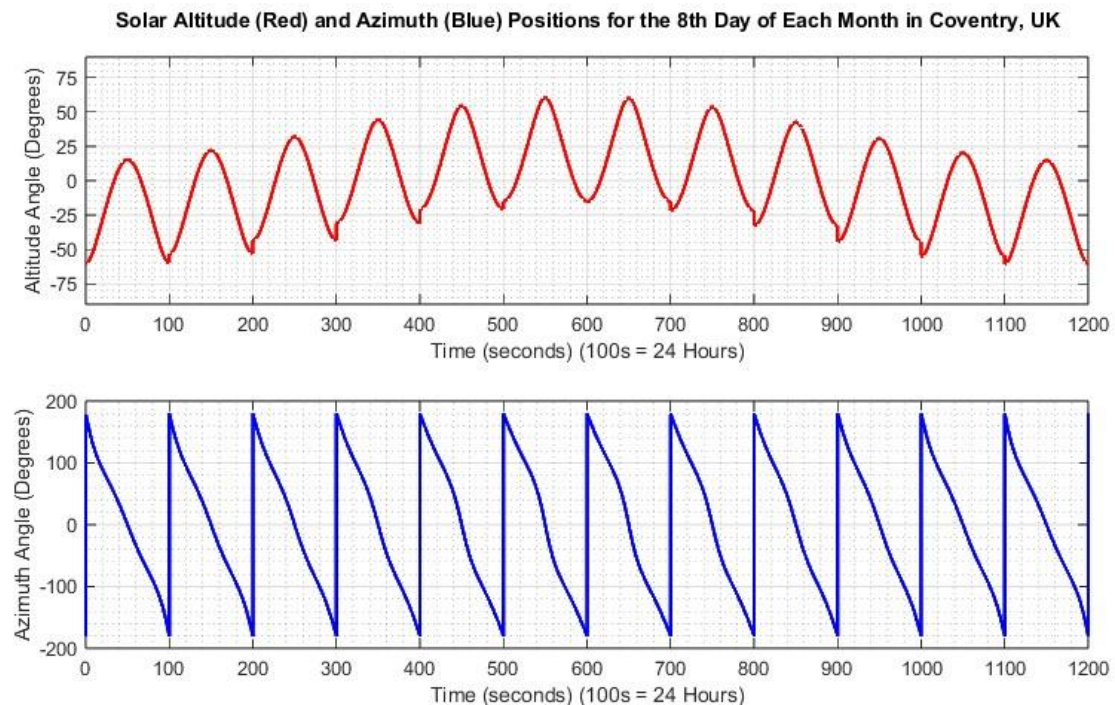


Figure 2: Simulated solar altitude (Top) and solar azimuth positions simulated for the 8th day in each month where 100 seconds in the simulation is equal to 24 hours of real time.

In simulating the solar position, it is important to discuss timescale. In order to entirely observe the effect of changing solar position seasonally, an entire year must be simulated. Doing this in real time would cause issues regarding the completion of this coursework, therefore so adjustments must be made. As such, in the simulation, 100 seconds equates to 24 hours of time in real life. As such, the simulation runs for 1200 simulation seconds to simulate 12 full days.

These scenarios were simulated making use of an application developed, inputting the required variables into the Simulink model, allowing for the timeseries signals to be output and saved separately. This output is used in a later section as an input to the controller Simulink model.

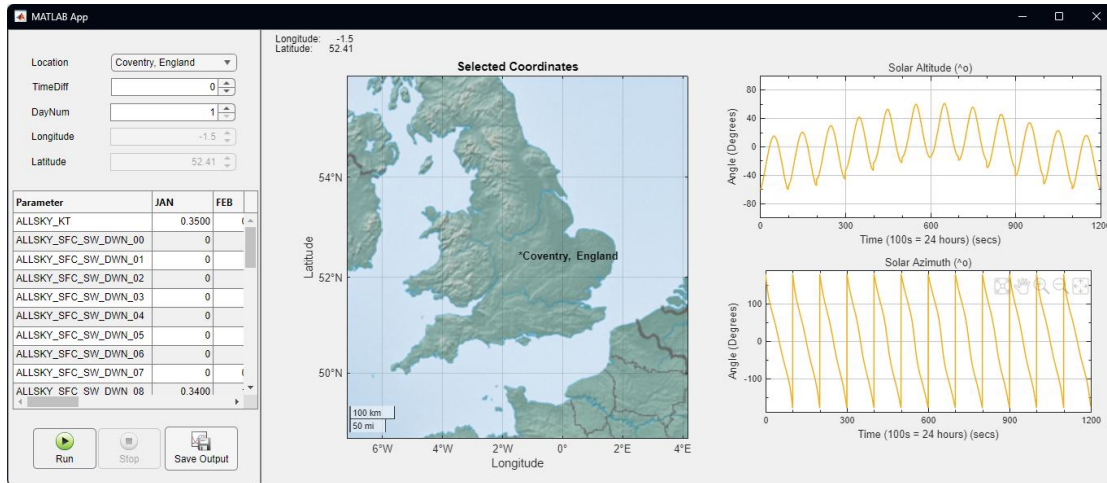


Figure 3: Developed Simulink application, inputting location on the Earth, time difference of the said location, and day number needing simulated (from 1-28). This application also displays and saves key information required later.

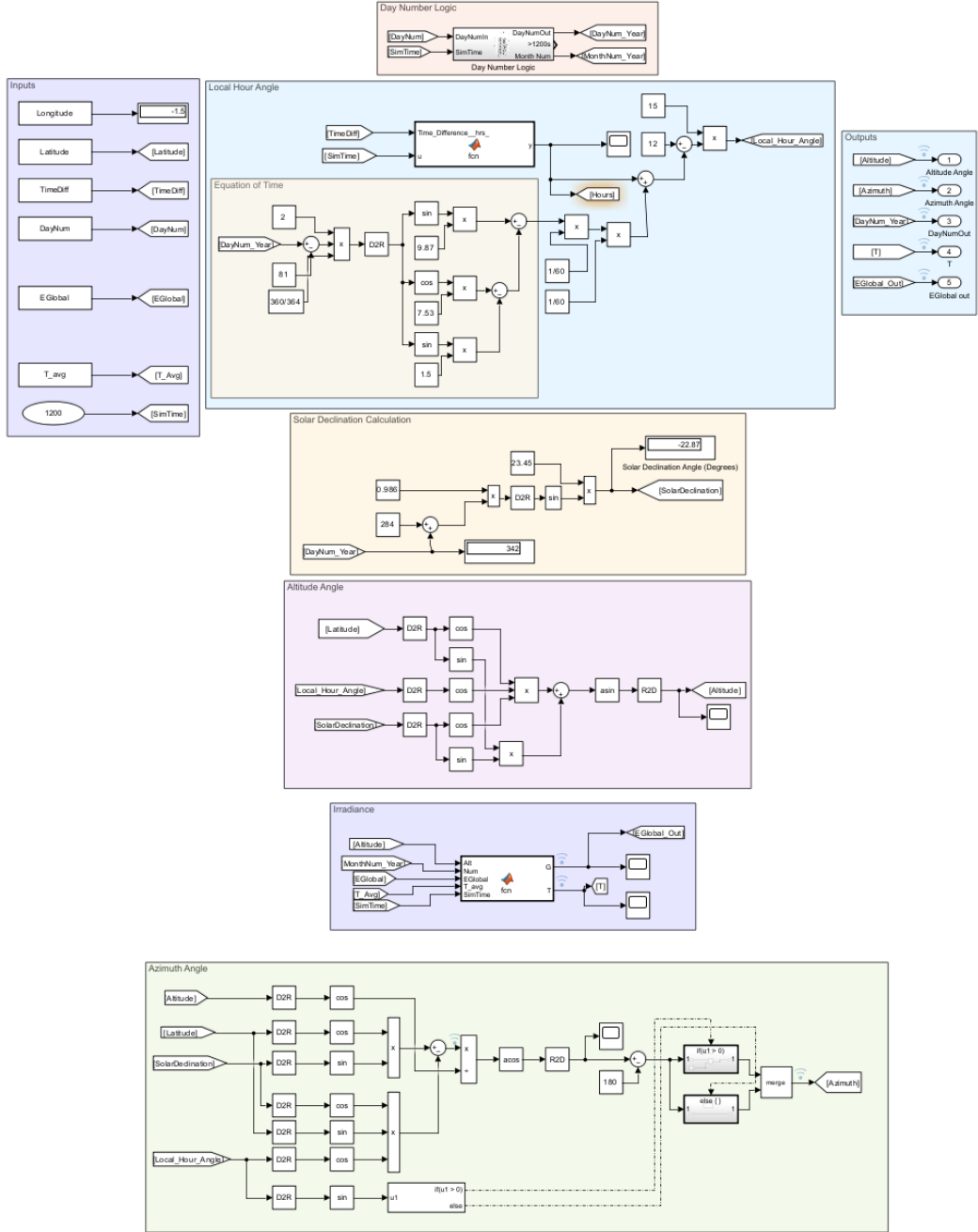


Figure 4: Entire solar positional model. Takes inputs on the left of longitude, latitude, local time difference, day number simulated, array of irradiance data, array of temperature data and finally the simulation time.

The simulation uses these inputs to form output signals of solar azimuth and altitude signals for a given time as well as observed maximum irradiance and temperature, all as timeseries signals.

4.1.1b – Solar Irradiance

The solar irradiance incident on the solar array surface is much more complicated to calculate. There are many variables which impact the solar irradiance (Rosa-Clot et al, 2018) (Randall & Jacot, 2003). Although it is intuitive to calculate the extraterrestrial irradiation incident on the edge of the atmosphere (Camacho et al., 2012), the complexity comes from the effects of the atmosphere from that point onwards. From this point, irradiation is affected by the air mass, the total clearness index of the sky at a given time, as well as several other variables which scatter and absorb the insolation.

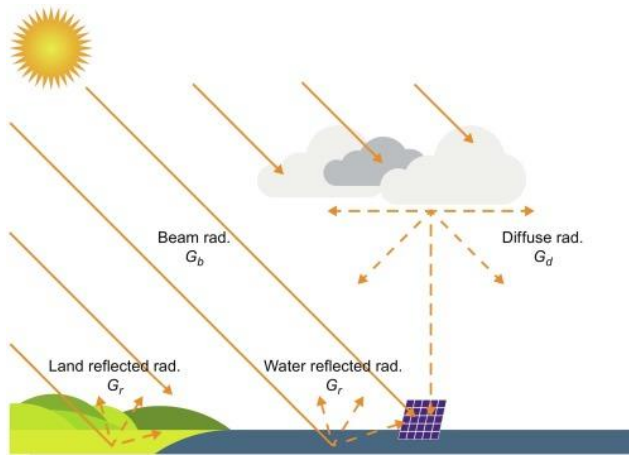


Figure 5: Solar irradiation components and sources (Rosa-Clot et al, 2018)

As such, the irradiance values utilised were acquired through existing data gathered by NASA. The data was obtained from the National Aeronautics and Space Administration (NASA) Langley Research Center (LaRC) Prediction Of Worldwide Energy Resources (POWER) Project funded through the NASA Earth Science/Applied Science Program.

Data was extracted for the following variables:

- Hourly average global clear sky irradiance per month, ALLSKY_SFC_SW_DWN_*00->23* [kWh/d]
- Average clearness local clearness index per month, ALLSKY_KT [No Units]
- Average cloud cover percentage per month, CLOUD_AMT [No Units]
- Average daily ambient temperature per month at 2 meters altitude, T2M [$^{\circ}\text{C}$]

These datapoints allow for the specific behaviours of the locations to be modelled to a certain degree of accuracy. This way, generalised comments can be made using an informed approach. This approach cuts out the requirement for any complex modelling of atmospheric conditions but allows for the consideration of these conditions nonetheless by having these parameters describe the actual behaviour observed in these locations.

As this data is considering local climates, average irradiance and clearness index will vary massively from location to location. This allows for generalised comparisons between a number of different climates throughout the range of longitudinal positions on each latitude will be necessary to come to accurate conclusions about the effectiveness of the methodologies presented in this analysis. This will also confirm the correlation between the solar position and incident irradiance by confirming the relationship between irradiance incident and the latitude of the observer, by showing a lack of variance based on solely longitude.

These locations are grouped by local latitude, and separated by longitude. This allows for a range of different climates to be modelled in order to derive several test cases which demonstrate the average hourly irradiance for each latitude, nullifying the climate differences in part. Doing so, the locations are segregated into 7 groups:

- Group 1 - +70 Latitude
- Group 2 - +60 Latitude
- Group 3 - +30 Latitude
- Group 4 - +0 Latitude
- Group 5 - -30 Latitude
- Group 6 - -60 Latitude
- Group 7 - -70 Latitude

From these groups, 6 test cases were derived with their corresponding groups latitude and the ambient temperature of 25°C .

Details on test case derivations are found in a later section, 4.4 – Test Scenario Derivation.

4.1.2 – Inputs Validation

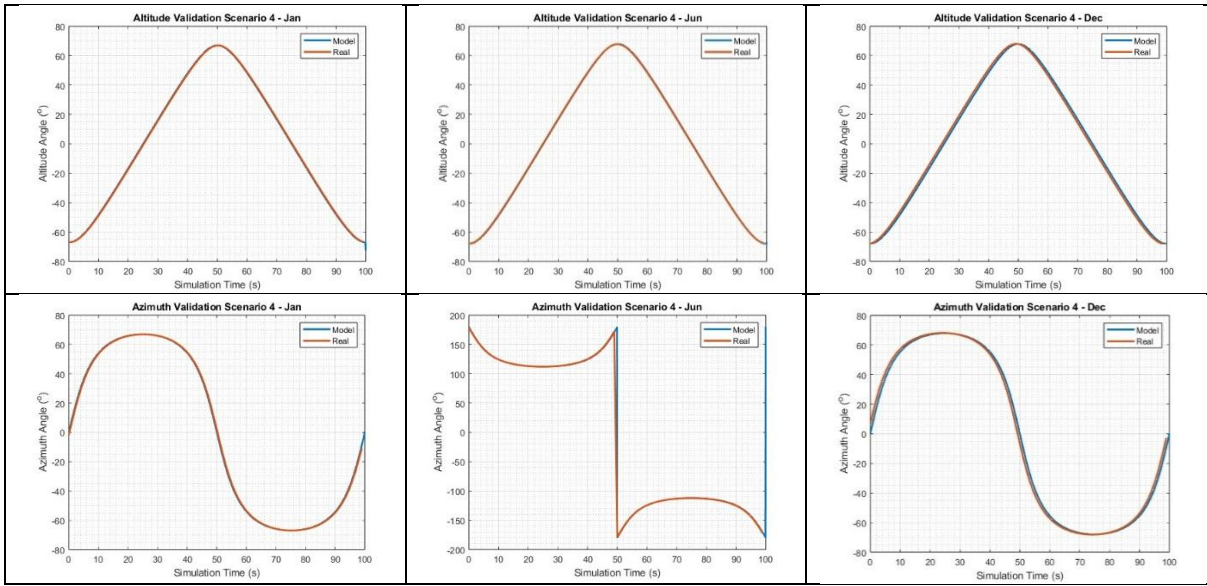
In order to claim that the data simulated for each location is a valid representation of the real alternative, the inputs must be validated. Using the test cases described, and the longitude of 0° , their coordinates can be utilised to simulate a given month, in this case: January, June, and December. The data gathered for each simulated month can then be plotted against the real validated data for the same position over the same time period.

The Data used to validate the model developed was gathered from an in-depth publication with a helpful web application, handily exporting its data in CSV format (Reda & Andreas, 2003). Data exported was about a different orientation, taking azimuth about, $0 < \gamma \leq 360^{\circ}$, and the simulation described here is modelled as per, $-180 < \gamma \leq 180^{\circ}$. This is easily corrected in post-processing.

The months chosen allow for any compounding errors in the developed model to be highlighted in December, due to simulating of a whole year prior. They also allow for proper maximum and minimum solar position in the sky per location, by exposing the uniqueness of each locations seasons to be observed. The results of this comparison determined that the developed model performed within 5% of the real values consistently, with the largest error occurring in December. Again this is likely due to any compounding errors in the developed simulation as a direct result of the limited considerations of several conditions. This will, however, be more than accurate enough for the purpose of this discussion.

Irradiance is taken from a validated source. As such, there is no need to validate the data independently.

Table 1: Example of validation graphs, plotting real and modelled solar positions (labelled) for scenario 4, Lat=0 Long=0.



4.2 – Photovoltaic Cell Model

In this section, a discussion of the photovoltaic cell model will be formed with inclusions of setup and validation included. The result of the process described is a model validated from 250 W to 3000 W of solar irradiance for temperatures from 0 to 50 degrees Celsius. The model derived is validated to within 5% for values of irradiance between 500W and 3000W, and to within 10% for values of irradiance between 250W to 500W. all irradiance below 250W, the correlation between actual maximum power point observed and the model are not significantly correlated. For all values of temperature measured, the model performs within 3% of the standard test conditions.

4.2.1 – Photovoltaic Cell Model Design

Photovoltaic cells take advantage of positive-negative junctions in semiconductor materials. As such, their performance is largely dependent on several independent material properties unique to these materials. In short, the primary function of photovoltaics are the capability of utilising photons which are equal to or greater than in energy content than the energy band gap between the p-type and n-type semiconductors, i.e. the p-n junction. In such a case, photovoltaics utilise these photons energy to allow for photo-generated carriers allowing the flow of electrons. In other words, the photon energy is the driving force of the flow of electrons. This current is proportional to the photon intensity (Lorenzo, E., 1994).

To model the photovoltaic cell, the equivalent circuit of the cell can be found as:

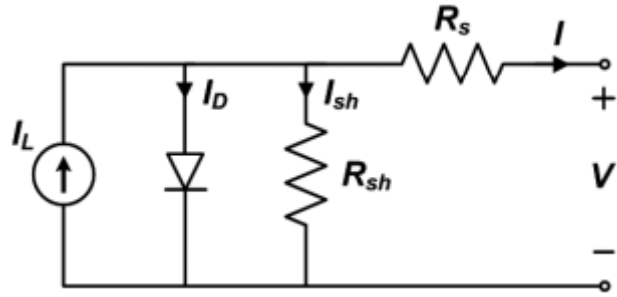


Figure 6: Equivalent circuit of a solar cell (Di Carlo et al., 2020).

As shown above, simplest equivalent circuit of a solar cell is an irradiance dependant current source in parallel with a diode. Shunt and series resistances are included in parallel and series respectively to account for any behaviour which is not ideal.

From literature, the equations which define the performance of the given equivalent circuit can be found as (Lorenzo, E., 1994) (Abdin et al., 2018), specific definitions can be found in the nomenclature found in the appendix:

- (1) Thermal Voltage, $V_t = \frac{kT_{op}}{q}$
- (2) Diode Current, $I_d = I_s \cdot \left[e^{\frac{V+I \cdot R_s}{n \cdot V_t \cdot N_{cells} \cdot N_s}} - 1 \right] \cdot N_p$
- (3) Diode Reversed Saturation Current, $I_s = I_{rs} \cdot \left(\frac{T_{op}}{T_{ref}} \right)^3 \cdot e^{\left[\left(\frac{q \cdot E_g}{n \cdot k} \right) \cdot \left(\frac{1}{T_{op}} - \frac{1}{T_{ref}} \right) \right]}$
- (4) Diode Reversed Saturated Current @ STC, $I_{rs} = \frac{I_{sc}}{\left[e^{\frac{V_{oc} \cdot q}{k \cdot N_{cells} \cdot T_{op} \cdot n}} - 1 \right]}$
- (5) Shunt Current, $I_{sh} = \frac{V + I \cdot R_s}{R_{sh}}$
- (6) Photon Generated Current, $I_{ph} = G_k [I_{sc} + k_I (T_{op} - T_{ref})]$
- (7) Current output, $I = I_{ph} N_p - I_d - I_{sh}$

From these equations, the photovoltaic cell has several dependencies on the output current:

- Temperature of the cell,
- Number of parallel cells,
- Irradiation incident on the cell,
- Leakage current to the ground (shunt),

Note that standard test conditions (STC) of a solar array in industry is at 1000W of irradiance and 25°C as an ambient temperature.

These dependencies, along with the material properties to be defined, allow for the calculation of the output current by the photovoltaic cell. These link back to the input variables discussed in the previous section. Considering this, new definitions need to be made for the remaining variables. To do this, a solar panel is found to be modelled. The modelled solar array is the KYOCERA-KC200GT PV module, with parameters as follows:

Table 2: Unique parameter values for KYOCERA-KC200GT photovoltaic module (Kyocera, 2007).

Symbol	Parameter	Value	Units
--------	-----------	-------	-------

P_{max}	Maximum Power	200.143	W
V_{MP}	Maximum Power Voltage	26.3	V
I_{MP}	Maximum Power Current	7.61	A
V_{OC}	Open Circuit Voltage	32.9	V
I_{SC}	Short Circuit Current	8.21	A
K_v	Temperature Coefficient of Open Circuit Voltage	-0.1230	V/K
K_I	Temperature Coefficient of Short Circuit Current	0.0032	A/K
N_{cells}	Number Of Cells Per Module	54	n/a
R_S	Series Resistance	0.221	Ω
R_{sh}	Shunt Resistance	415.405	Ω
n	Diode Ideality Factor	1.3	n/a

This photovoltaic module was chosen due to several restrictions to values modelled in Simulink Simscape's own "PV Array" block. This block does not allow for temperature coefficients of open circuit voltage to be above -0.1 nor below -1 V/K. Similarly, the temperature coefficient of short circuit current must be between -0.2 and 1 A/K, among other restrictions to be discussed in the validation section. These restrictions, although somewhat broad and understandable in nature, resulted in the current selected photovoltaic model to be selected. These restrictions were obeyed to ease validation later, which would need to be completed using this Simulink Simscape block.

Utilising these parameters and the dependencies highlighted previously, the following Simulink model can be derived:

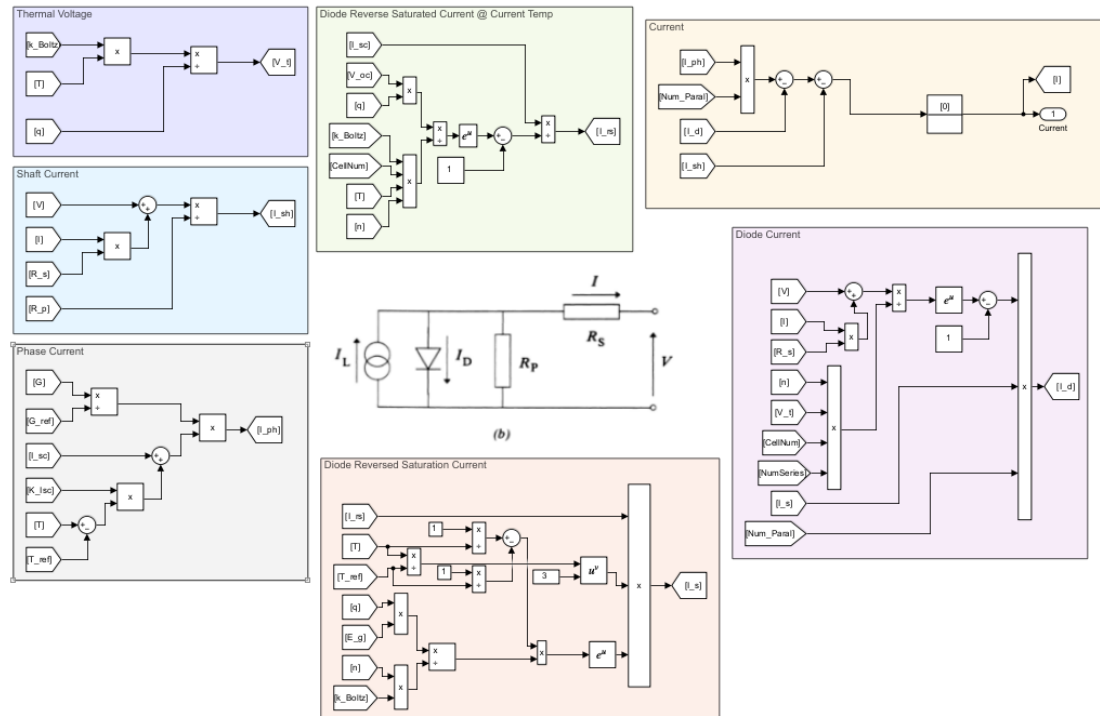


Figure 7: Developed photovoltaic model utilising the system equations previously discussed.

This model allows for the calculation of the output current by the photovoltaic module based on the input variables of current circuit voltage, incident irradiation, and temperature.

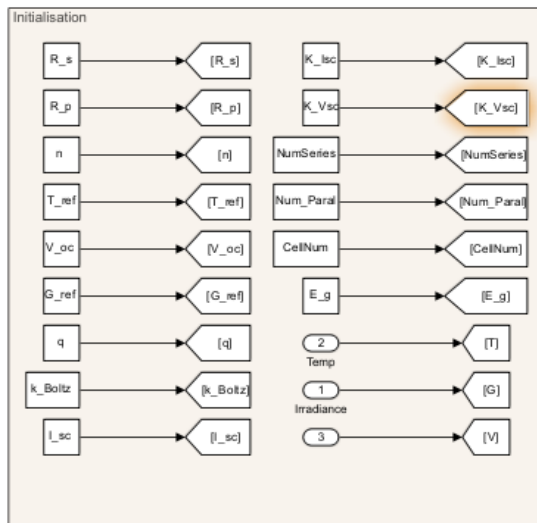


Figure 8: Input variables into the photovoltaic model developed and shown in the previous figure. refer to nomenclature for specific definitions.

4.2.2 – PV Model Validation

To validate the developed model, the values output by the photovoltaic model derived must be compared to that of an already validated data source. In this case, for ease of access and development of test frameworks, the Simulink Simscape “PV Array” block has been used to validate the response of the developed system.

The developed photovoltaic model outputs a generated current for any given irradiance and temperature. This current value was used to drive a current source with a variable load resistance in series. In parallel with the variable load resistance is a voltmeter, reading the voltage across the load for any given current. The load resistance was given a ramp signal input, varying from 0 to $+70\ \Omega$. This variable load allows for a constant irradiance input and a constant temperature input to be inserted into the PV model, and for the power-voltage relationship to be determined for those given inputs.

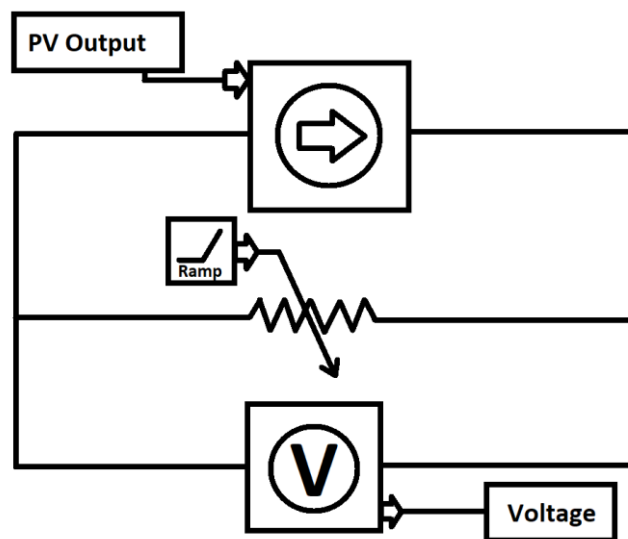


Figure 9: Diagram of load circuit used to validate the Power-Voltage response of the developed photovoltaic model.

This behaviour is crucial to model correctly as this behaviour allows for the correct point of maximum power generated by the PV cell for a given irradiance and temperature to be defined, which is the core target of the voltage controller defined in a later section. Modelling a variable load allows for the demonstration of the impact of a changing voltage input to the PV model. More specifically, it demonstrates how that voltage impacts the function of the model and ultimately the power generated by the array. Plotting the Power-Voltage and the Current-Voltage responses allows for a graphical representation of the relationship between voltage and current to be demonstrated and for the maximum power point to be identified. This is the point of interest of the power point controller discussed in a later section.

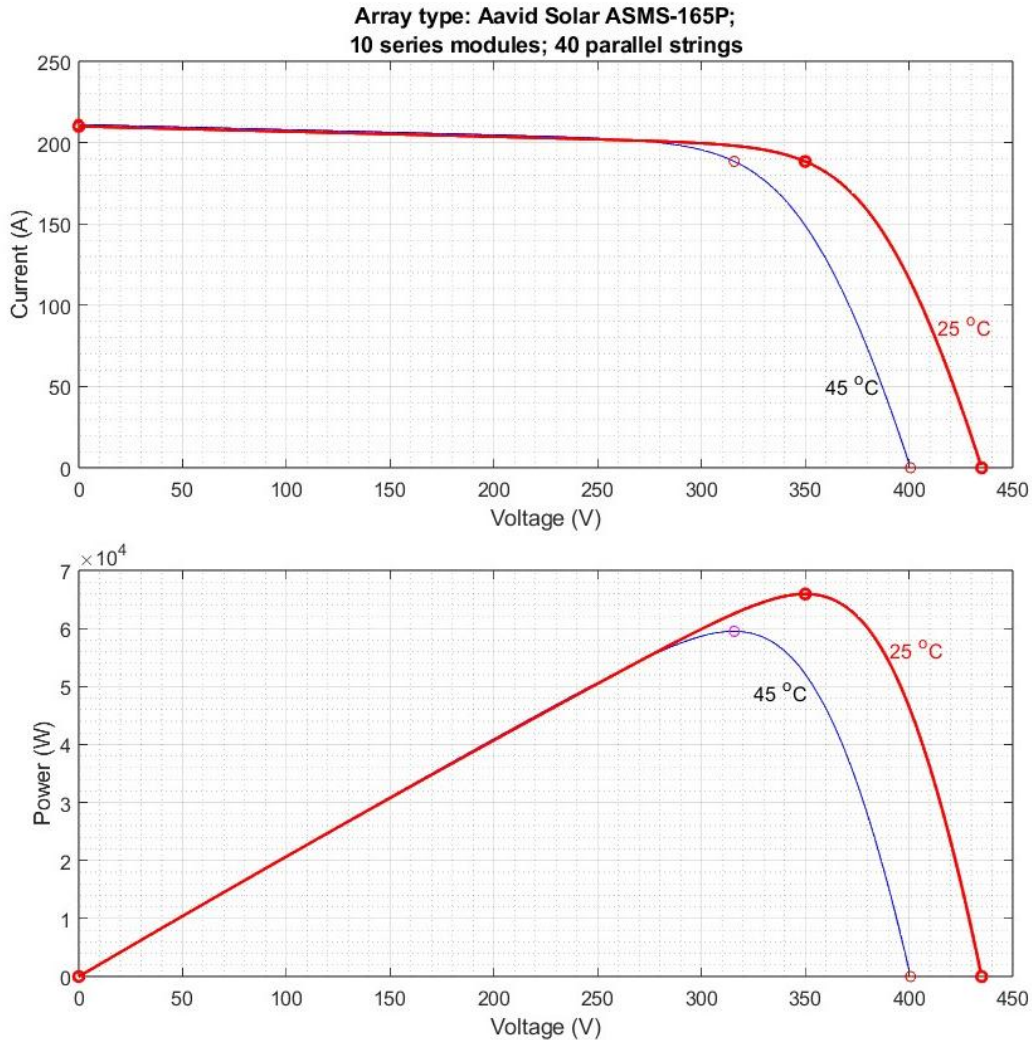


Figure 10: Current-Voltage (Top) and Power-Voltage (Bottom) relationships for STC (Red) and 45 (Blue) with a constant irradiance of 1000W for an Aavid Solar ASMS-165P array. Note the turning point of Power values at a given voltage, this is the maximum power point at which the current-voltage relationship is such to generate the maximum power.

The figures above are based on Simulink Simscape stored values for the selected solar array, containing 10 of the selected modules in series and 40 of the same in parallel.

As such, this was the property which was utilised to validate the model by. The selected assembly was determined to have a single module in series and in parallel. The model was validated based on the response, given a constant temperature and a changing irradiance, then the response of a changing temperature with a constant irradiance. In both cases of constant values used, standard test case conditions were utilised, converting the temperature into kelvin.

Table 3: Validation test cases used to collect data for validation of the photovoltaic module model.

Test Num	Irradiance	Temperature
1	1000	0
2	1000	10
3	1000	15
4	1000	20
5	1000	25
6	1000	30
7	1000	35
8	1000	40
9	1000	45
10	1000	50
11	3000	25
12	2500	25
13	2000	25
14	1500	25
15	1000	25
16	750	25
17	500	25
18	400	25
19	300	25
20	250	25
21	200	25
22	150	25
23	100	25

The results of this validation process concluded that the maximum power point calculated for each test case performed within 5% of the ideal value for irradiances from 3 kW to 700W, and within 10% of the ideal value for irradiances between 700W and 250W. Below 250W of irradiance, the power point accuracy degrades significantly to closer to 50%. The modelled response performed within 5% of maximum power points for the full range of temperatures 0°C to 50°C.

The degradation of the modelled response from the ideal relationship for low irradiances is likely due to the phase current relationship described, since this is the only aspect which considers the irradiation incident on the solar cell. The equation utilised is a ratio between the incident irradiation and that of standard test conditions. This is likely an over-idealised relationship. Other research suggests that the relationship is less linear and more directly related to the photon flux and the actual wavelength of the irradiance incident (“Practical Handbook of Photovoltaics,” 2012). This modelled response will be sufficient for the analysis described in this discussion, however, will need to be noted in future findings.

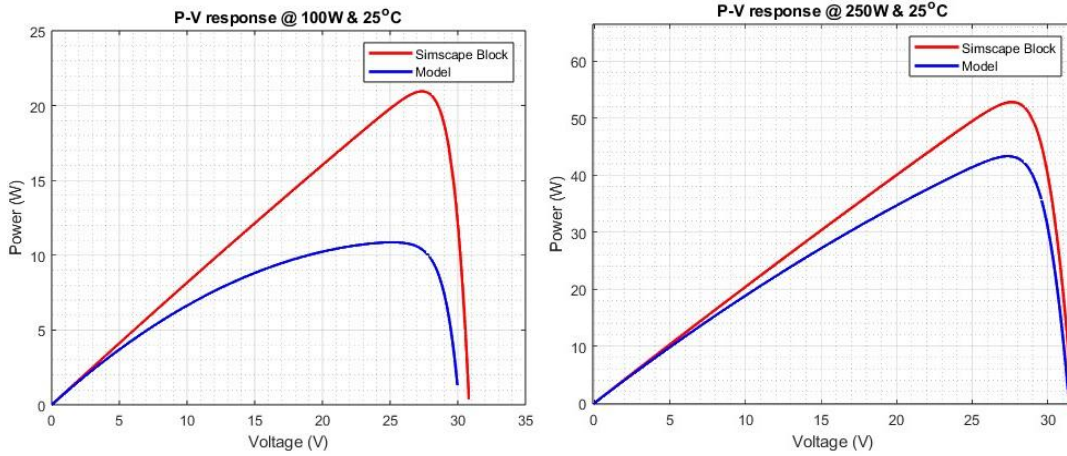


Figure 11: P-V relationships for 100W (Left) and 250W (Right) irradiance at 25°C for both Simulink Simscape (Red) and modelled (Blue) photovoltaic models.

It is also worth noting the validation of irradiances beyond STC. For these irradiances, the power generated is significantly greater than the maximum allowable power rating of the solar array. To begin, note that these values are unrealistic, as the sun emits a relatively consistent irradiance, known as the solar constant, $E_s = 1361 \text{ Wm}^{-2}$, as such any irradiance on the surface observed above this value is highly irregular. Any irradiance observed above this 1000W will be capped at the maximum value of $P_{Max} = 200.143\text{W}$ in the discussion.

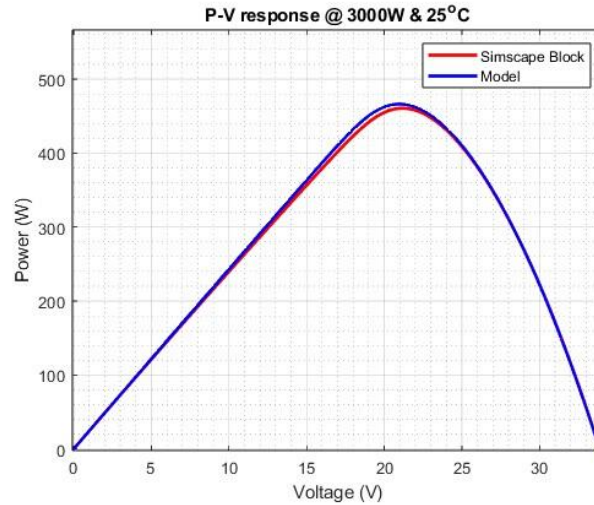


Figure 12: PV response of Simulink Simscape and Modelled photovoltaic arrays for an irradiance of 3 kW.

4.3 – Controllers

This section describes, in detail, the approach taken to develop and implement two separate controller strategies. The first of which is for the tracking of the maximum power point of the photovoltaic array by changing a load voltage in order to generate the greatest power from the environmental conditions of solar irradiance and ambient temperatures. The second, takes the power generated by the photovoltaic cell and compares its value to the previous time step value, moving the axis accordingly. The results of this section describe the appropriate data driven implementation of a lookup table to control a variable load on the photovoltaic cell, and the use of a perturb and observe algorithm in order to actuate the solar array axes. Two

separate approaches were taken for double and single axis controllers, to achieve an optimal path.

4.3.1 – MPPT Photovoltaic Controller Design

Initially, a direct perturb and observe approach was taken in order to achieve the greatest power point for a given current. This was done by boosting the voltage based on a PWM signal, adjusted by the perturb and observe algorithm. This methodology attempted to make use of a buck converter controlled by a PWM signal in order to control the voltage of the system.

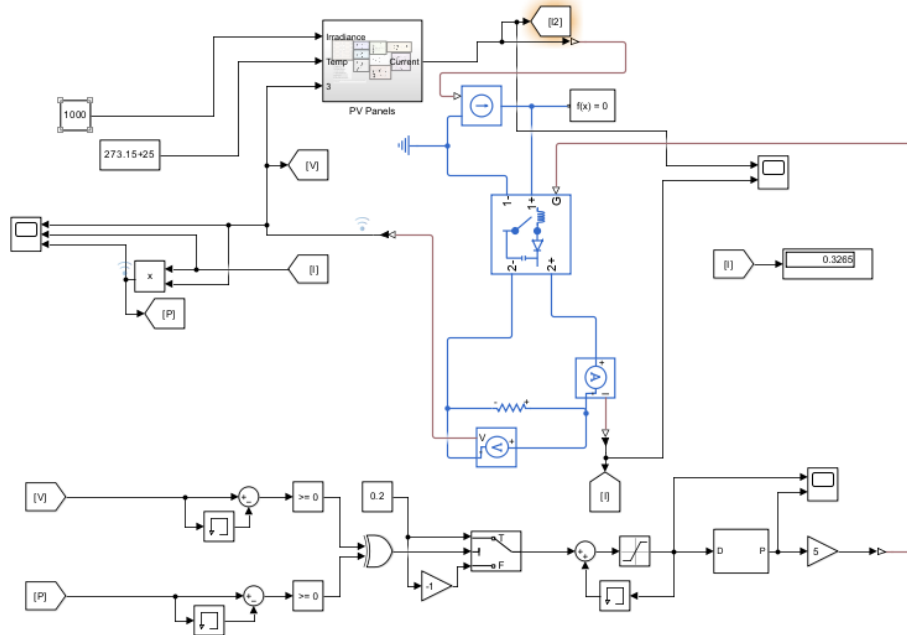


Figure 13: Example attempt at implementing a buck converter in order to boost the voltage of the load circuit with respect to the power generated by the array – this was done utilising a perturb and observe method, adjusting the duty cycle of the PWM gated signal into the buck converter.

The aim of this approach was to generate a varying duty cycle based on whether or not the perturbation of the duty cycle done in the previous step was effective at increasing the power output of the photovoltaic model. If this was implemented effectively, this strategy would allow for the maximum power output to be found and settled at for the given input. This, however, was not the case. Due to the algebraic loop present in the photovoltaic model, and certainly a flaw in the logic developed, the voltage value generated by the buck converter was not coordinated, and rather proceeded to perform wildly. The implementation of this circuit also caused a significant increase in the time required to simulate the experiment, due to the use of physical signals required and the use of PWM (pulse width modulated signal) generators.

An alternative approach was taken to combat these issues. This approach was to vary the load of the photovoltaic circuit, rather than perturbing a duty cycle and changing the voltage as a result of said duty cycle. This, however, faced the same issues as the buck converter method. This method, however, inspired the derivation of a lookup table in order to determine the ideal load of the circuit which may be used to achieve the maximum power point.

A test scenario was derived in order to examine the behaviour of the system for a range of irradiances and temperatures. The fundamental aim of this scenario was to test the full range of loads, as per the ramp signal used to validate the model, for each temperature, from 0°C to 50°C and for each irradiance, from 100W to 3000W. This was to be done in a single simulation,

forming a single database of monitored signals. For each timestep, irradiance, current temperature in kelvin, current temperature in Celsius, current observed power, current observed voltage, and finally current observed current were recorded.

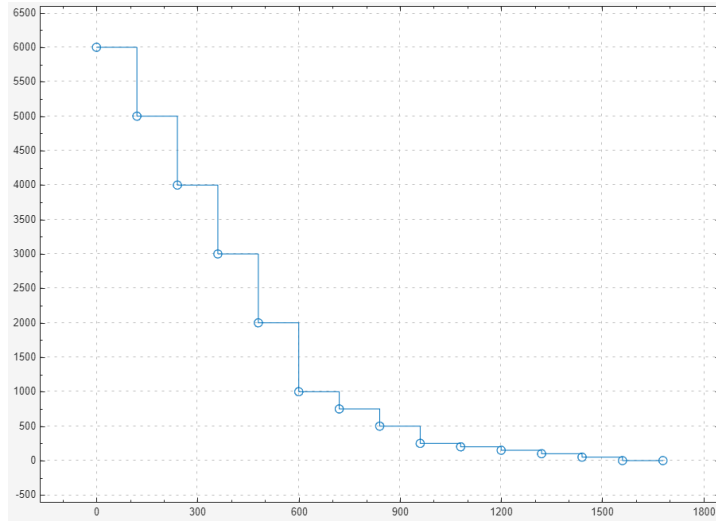


Figure 14: Range of Irradiances input into the photovoltaic model for data gathering purposes. X axis = simulation time (seconds), Y axis = irradiance (W)

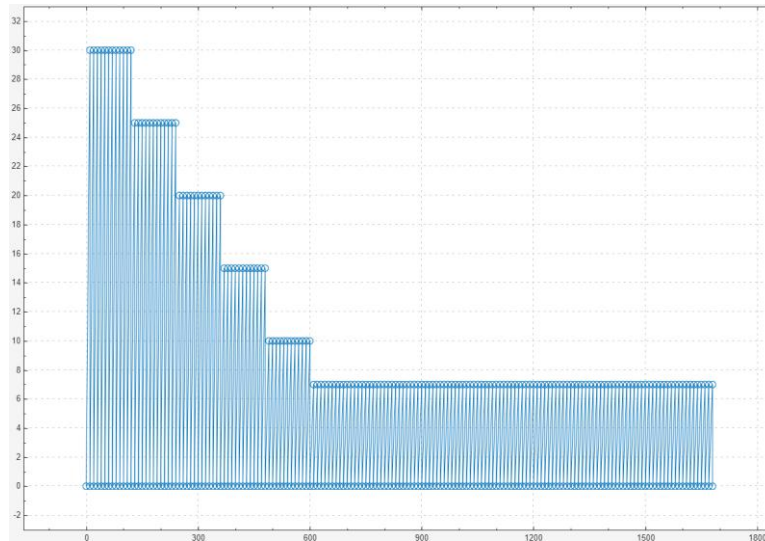


Figure 15: Sawtooth ramped signal used to vary the load over the duration of the scenario, varying with respect to the selected irradiance to allow for the entire behaviour of the system to be identified. X axis = simulation time (seconds) and Y axis = variable load (Ohms).

From this data, for any given irradiance and temperature, the maximum power can be acquired. For this maximum power, the load utilised to achieve said maximum power can be calculated using the voltage and the current. This allows for the behaviour of the model to be defined, allowing for extrapolation of values between each measured datapoint.

Load Required to Achieve MPP for range of Irradiance and Temperature

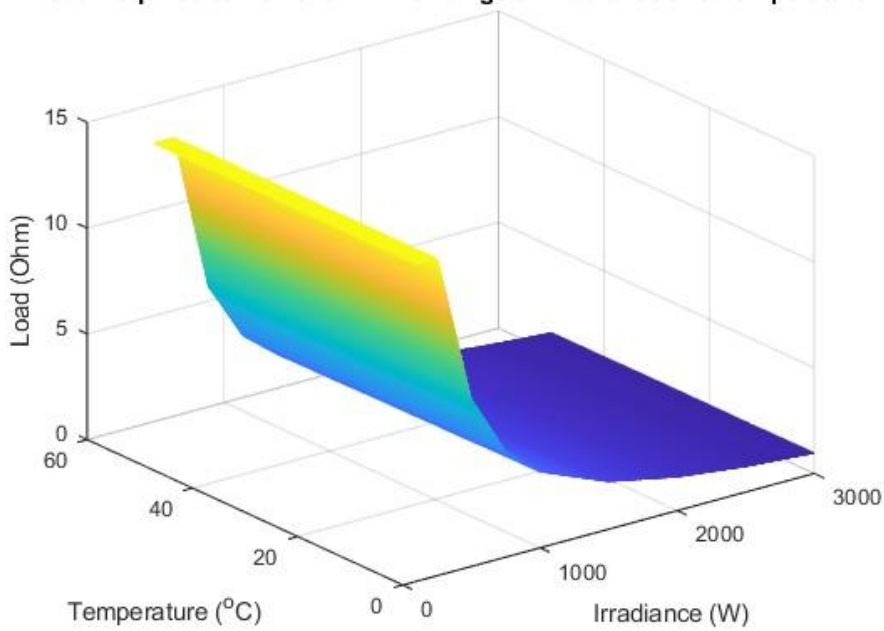


Figure 16: Load required to be in series with the photovoltaic module for a given irradiance and temperature for the KYOCERA-KC200GT PV module.

Load Required to Achieve MPP for range of Irradiance and Temperature

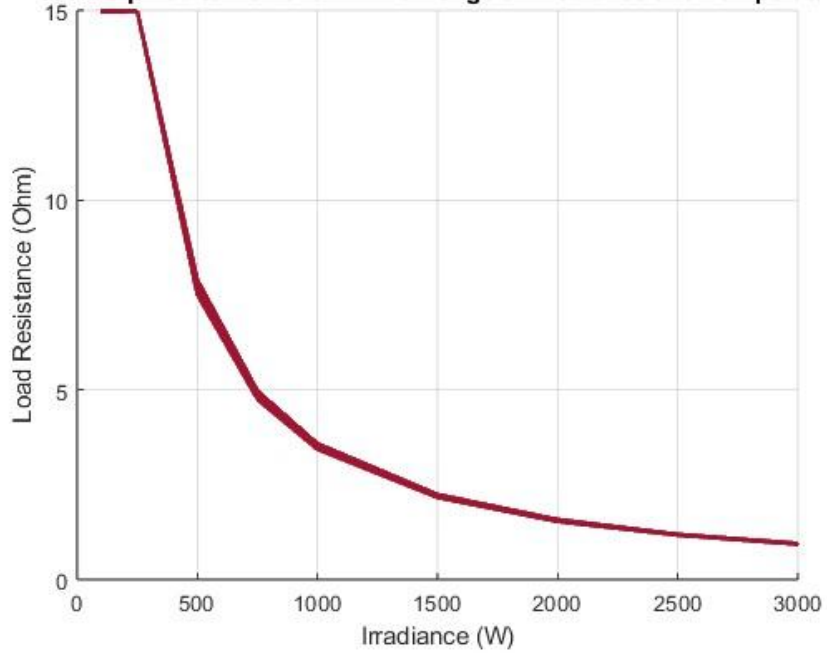


Figure 17: Load required to be in series with the photovoltaic module for a given irradiance for the KYOCERA-KC200GT PV module.

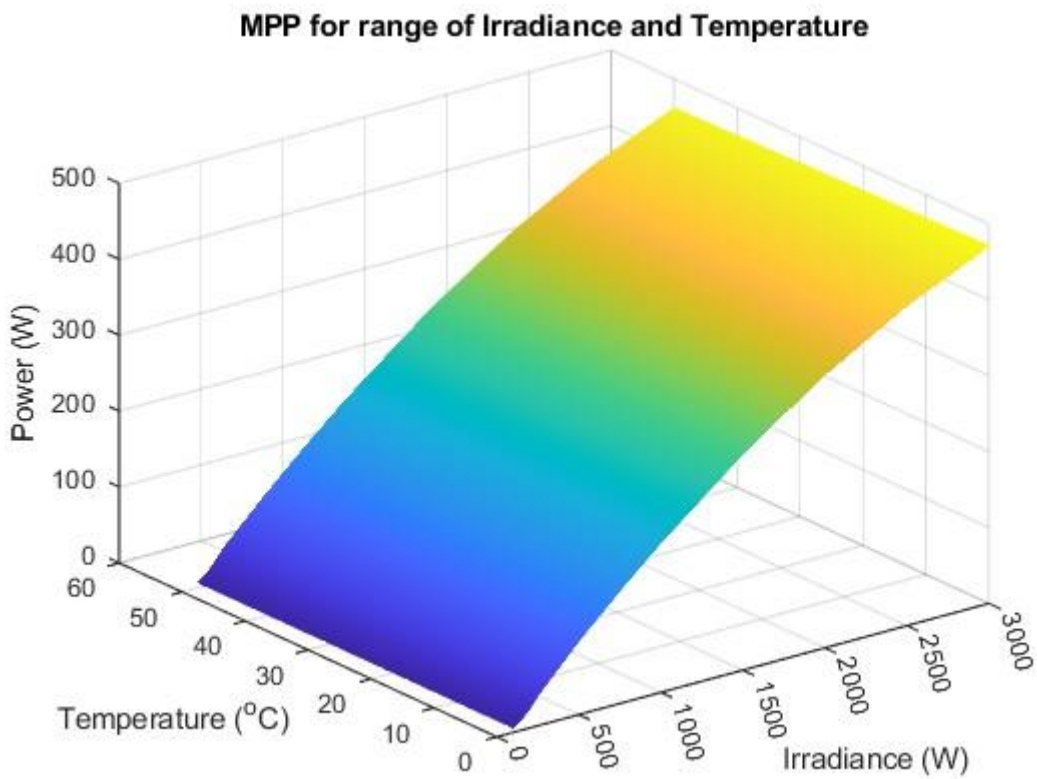


Figure 18:Maximum power output from the photovoltaic module for a given irradiance and temperature for the KYOCERA-KC200GT PV module.

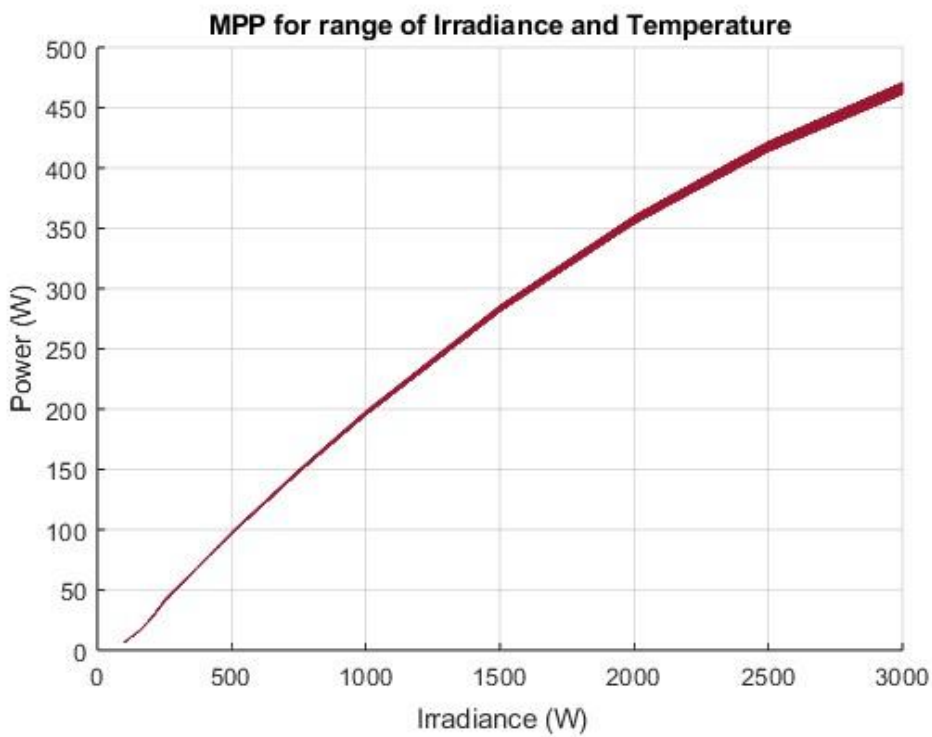


Figure 19:Maximum power output from the photovoltaic module for a given irradiance for the KYOCERA-KC200GT PV module.

As demonstrated by the figures above, although the relationship between irradiance and maximum power, and by extension the load required to achieve maximum power, strongly impact each other, the impact of temperature on this relationship is minimal for normal ranges of irradiance. Referring to the table below, it is seen that a maximum variance in resistance is seen to be 5.88% from 0°C to 50°C. While this is statistically significant, the trend of variance due to temperature decreases as the irradiance increases. At STC, the variance is 4.68% which then becomes statistically insignificant, being below a p value of 0.05. Similarly, the change in maximum power as a result of temperature is consistently below 5%, with all non-anomalous results taking a variance of less than 2.5% due to temperature. The effect of temperature is even less significant, taking the variance from the STC, consistently achieving a variance of less than 1.4% for all non-anomalous results.

Note that for irradiances 100-250W, required resistance to achieve maximum power point was restricted to allow for convergence to occur in the simulation. As such, the values for these loads are capped and not representative of the true values which would produce a maximum power point.

Table 4:Extracted resistance values gathered in derivation of the lookup table required for load control for maximum power point for each irradiance. Data contains minimum, maximum, and STC values gathered for load and power, for a given irradiance due to a change in temperature from 0°C to 50°C.

Irradiance (W)	R @ STC (Ω)	MinR (Ω)	MaxR (Ω)	P @ STC (W)	MinP (W)	MaxP(W)	% Change R (Max Min)	%Change R (STC)	% Change P (Max Min)	%Change P (STC)
100	15.0	15.0	15.0	6.6	6.5	6.8	0.10%	0.00%	4.20%	1.89%
150	15.0	15.0	15.0	14.9	14.6	15.2	0.10%	0.10%	4.19%	1.93%
200	15.0	15.0	15.0	26.4	25.9	27.1	0.10%	0.10%	4.25%	2.00%
250	15.0	15.0	15.0	41.2	40.5	41.9	0.10%	0.10%	3.45%	1.76%
500	7.7	7.4	7.9	97.1	96.2	97.8	5.88%	3.31%	1.61%	0.93%
750	4.9	4.7	5.0	148.3	146.9	149.4	5.06%	2.73%	1.72%	0.99%
1000	3.5	3.4	3.6	196.6	194.5	198.1	4.68%	2.78%	1.78%	1.02%
1500	2.2	2.1	2.2	283.4	280.3	285.7	4.67%	2.72%	1.91%	1.09%
2000	1.6	1.5	1.6	357.1	352.9	360.3	4.40%	2.56%	2.04%	1.17%
2500	1.2	1.2	1.2	417.8	412.6	421.8	3.75%	2.53%	2.18%	1.25%
3000	0.9	0.9	1.0	466.1	460.0	470.9	3.12%	1.59%	2.31%	1.31%

As such, it can be determined that the lookup table can be restricted to a single dimension, change in resistance based on the irradiance. The lookup table is populated with data gathered for standard test conditions, allowing for minimal variance from the ideal values to be achieved, as seen in the table above. As such the lookup table data appears as follows:

Table 5: Lookup table data, one dimensional, with an input irradiance and an output load as a result.

Irradiance (W)	Load (Ω)
100	14.97
150	14.985
200	14.985
250	14.985
500	7.695
750	4.865
1000	3.521
1500	2.205
2000	1.560
2500	1.185
3000	0.945

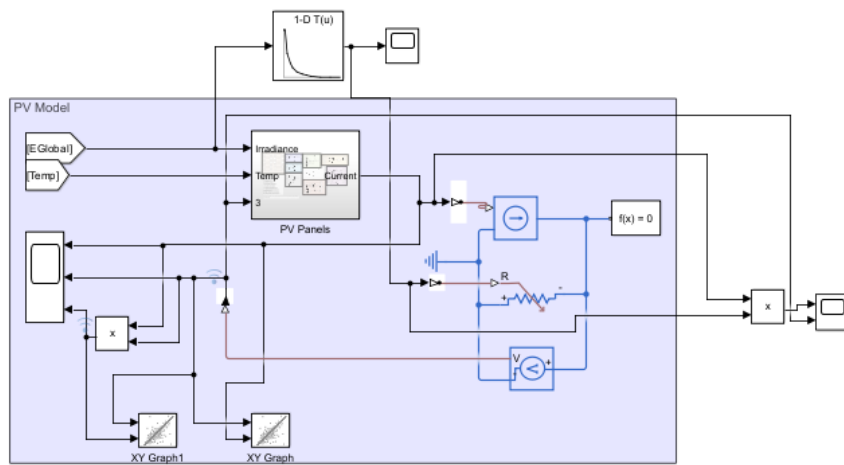


Figure 20: Resultant 1 dimensional lookup table with an input of the tracking surface irradiance and an output of the required load resistance input into the variable resistor to simulate a changing load using Simulink Simscape Electrical physical signals.

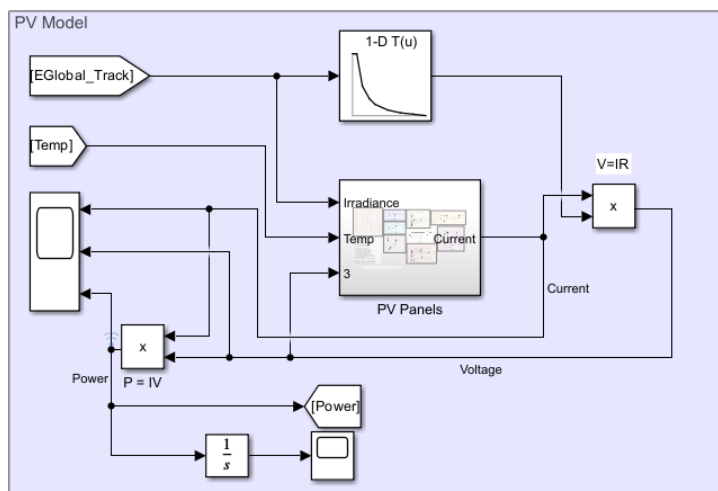


Figure 21: Resultant 1-dimensional lookup table with an input of the tracking surface irradiance, and an output of the required load resistance to achieve maximum power without the Simulink Simscape Electrical physical signals, utilising the product block to simplify the expression and reduce computational load.

The final lookup table data was added to a 1-dimensional lookup table block in Simulink. A mathematical approach was taken to simulate the impact of the load on the voltage, rather than maintaining the “Simscape Electrical Model” approach seen in figure 20. This is primarily due to the increased duration of simulation when physical signals are included in the simulation. The resulting lookup table produces significantly more power than utilising a continuous voltage value.

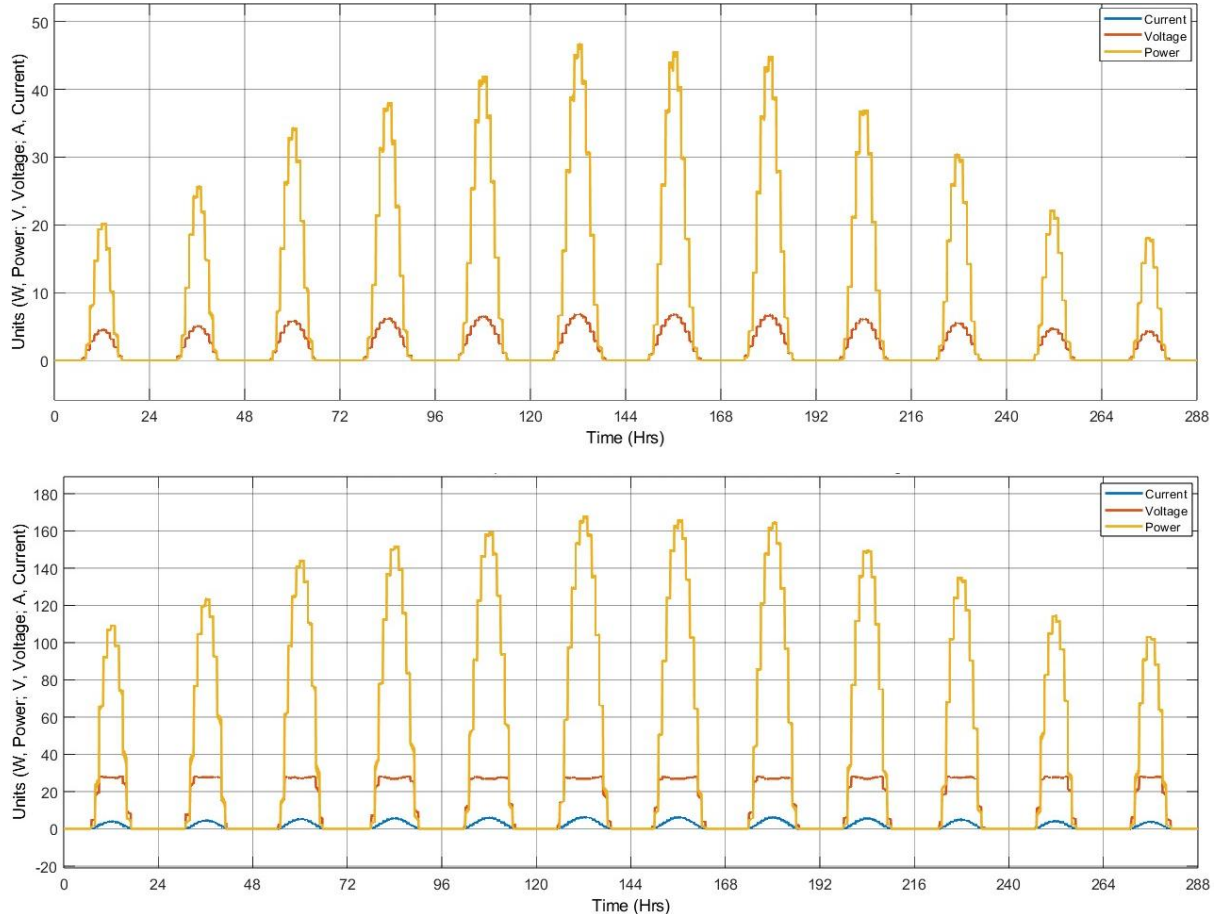


Figure 22:Power yield of solar array with a constant load of 1Ω (Top) and with the lookup table-based load controller (Bottom) for scenario 3 – Latitude=30 Longitude=0.

As demonstrated in the above figures, the maximum power generated by the photovoltaic cell model was massively increased after implementing the variable voltage controller. Power output is at best 5 times the power output utilising a constant load approach, and at worst 3 times as much. As such, the value of this controller is self-explanatory.

4.3.2 – MPPT Axes Controller Design

This section details the effective design and implementation of the orientation controller strategies. The core aspects of the discussion are for the design of the algorithm utilised, but also for the variation of optimal path calculations providing weightings for the tracking surface irradiation. The result of these designs allows for the effective tracking of the maximum power point in the sky, by tracking the optimal path derived. For simulation purposes, the “Using the Worm and Gear Constraint Block – Solar Tracker” Simulink Simscape Multibody example was used to simulate the actuation of the array.

4.3.2a – Double Axes Control

To define the solar position, two axes are utilised in the spherical domain: azimuth, γ , and altitude, α . These axes are described using solely angles. Using this knowledge, it can be determined that the accurate tracking of the sun can similarly be done using the same axes, with the solar array at the point of origin, and the position of the perpendicular normal axes from the arrays surface being the orientation of the array.

Utilising this convention, and the law of cosines, it can be concluded that the irradiance incident on the solar array surface is directly proportional to the magnitude of the maximum irradiance multiplied by the cosine of the angle between the two angular positions. This is the primary principle which influences the calculation of the incident irradiation on the solar array surface and is a mathematically intuitive principle.

$$\cos(\gamma_{Ideal} - \gamma_{Array}) \cdot \cos(\alpha_{Ideal} - \alpha_{Array}) = Scaling\ Coefficient = \phi$$

$$\therefore E_{Array} = E_{Ideal} \cdot \phi$$

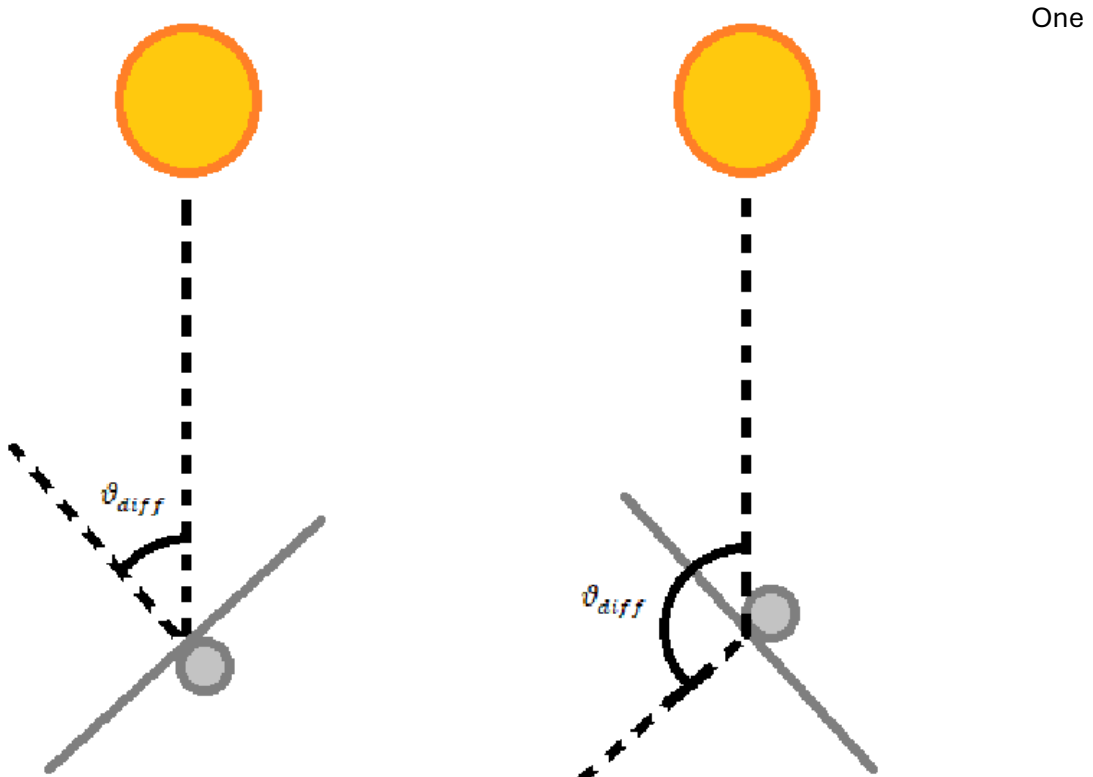


Figure 23: Graphical representation of incident irradiation on the solar array surface, with angular difference in positional vectors labelled.

Figure 24: Graphical representation of "blind condition", with angular difference in positional vectors labelled.

disadvantage of this method is also a simple limitation of cosines: past 90°, the response is mirrored. This causes false positives and ultimately opens the potential to be out of phase with the actual optimal position by up to 90°. To counter this, the angle between the two positional vectors can be saturated, at 90°. This essentially causes any angular difference beyond 90° to be interpreted as a 90° difference, rather than as the true angle, i.e. a scaling coefficient, ϕ , equivalent to 0.

This is the “blind condition” which can be interpreted as the solar array facing away from the sun by 90 degrees or more, causing the array surface to be entirely in shadow.

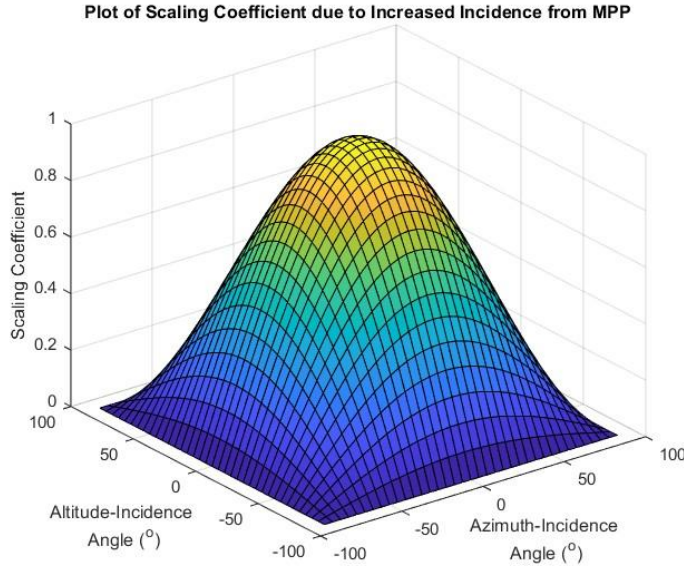


Figure 25: Visual mesh plot representation of the cosine coefficient described above, demonstrating the blind condition for any angle greater than 90°.

Utilising these principles, the axial control can be conducted. Taking the irradiance on the surface of the solar array as defined previously, and inputting that value into the photovoltaic model developed, a relative power output can be determined. Since the irradiance input into the photovoltaic model is relative to the arrays position, as is the power generated by the array. This power output is the primary control variable utilised to control both the azimuth and altitude axes.

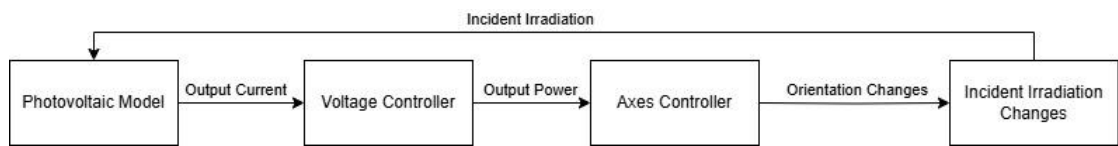


Figure 26: Flow diagram for the system modelled as a whole, demonstrating the relationship between the axes controller and the incident irradiation on the array surface, as well as how the loop encourages convergence on an optimal path.

The maximum power point of the solar array for a given irradiance and temperature is described in 4.3.1. In this section, the maximum power point tracking algorithm derived is a perturb and observe algorithm which directly compares power values generated by the array. In industry, this is an extraordinarily common algorithm used to track the maximum power point (Verma et al., 2015).

This algorithm measures the power output by the photovoltaic module and perturbs the axial position by a step size, holding that position. The power generated is measured again and compared to the previous power value measured. If the power generated in the new position is greater than that of the original position, then the new position is held until the next sample. Otherwise, the position recedes by two steps and the power is measured again. This time, the new power value is measured and compared again to the original power value. If the new power value is greater than the original power value, then the new position is held until the next

sample. Otherwise, the angular position is increased by a single step, returning the angular position of this axis to its original position. This algorithm is used on both axes separately.

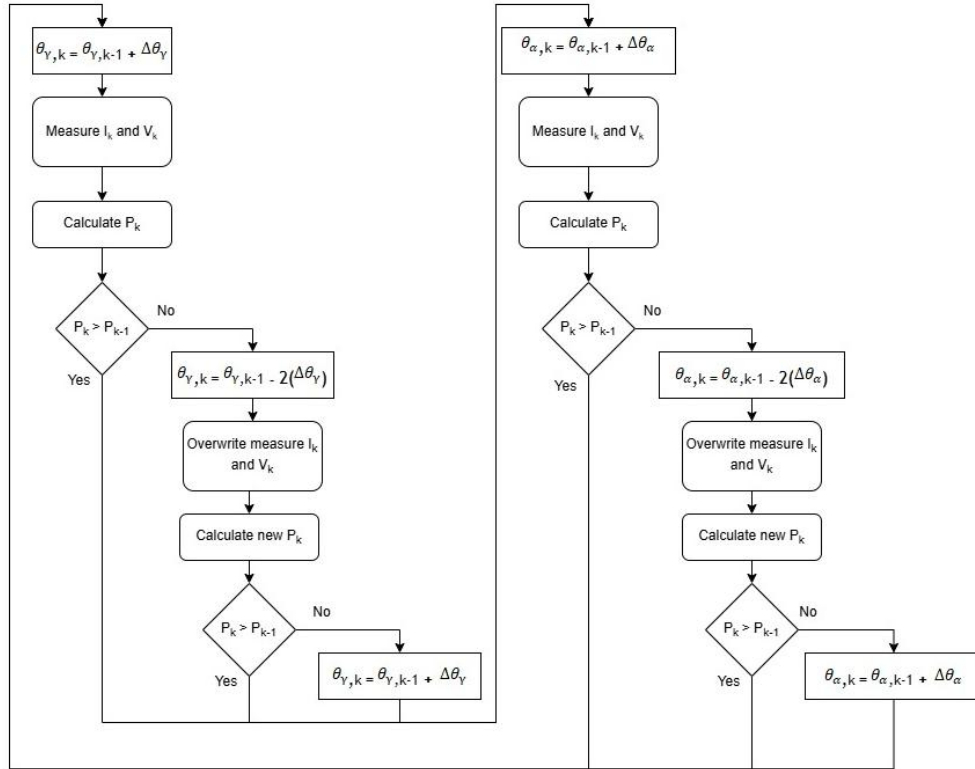


Figure 27:Perturb and Observe algorithm used to determine the position of greatest power yield.

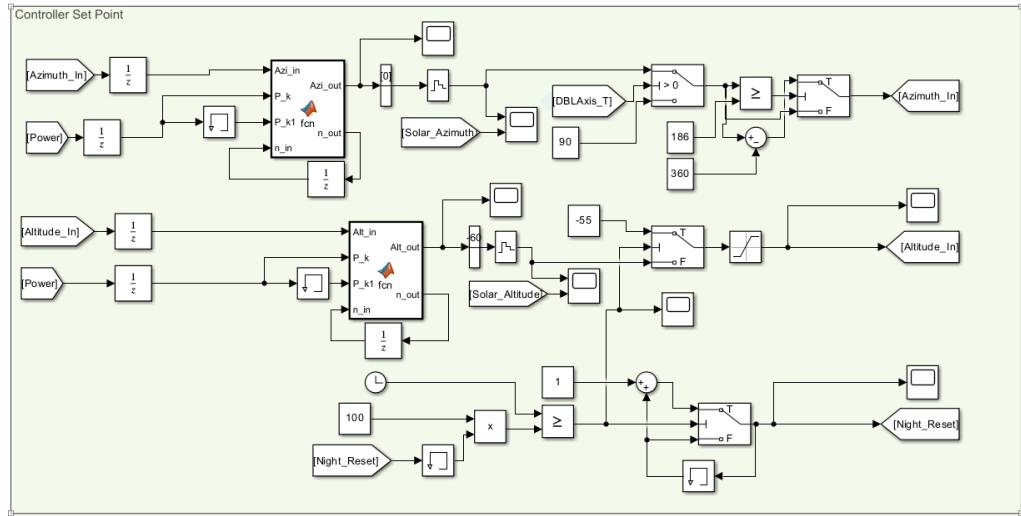


Figure 28:Simulink block diagram representing the implementation of each axial controller.

To ensure that the two controllers do not impact each other, their timings are out of phase with each other. This was done by delaying one controller by a time step, not equal to nor a multiple of the sampling frequency, then providing both controllers with the same sampling frequency. This causes the two controllers to be out of phase by exactly the duration of the initial delay imposed on the system. Without this consideration, the array would not be capable of interpreting which axes cause the change in power output, potentially causing a breakdown in the efficiency of the controllers in tracking the solar position in both of these axes. This is due to

the axes simply moving together, diagonally perturbing in a linear fashion along a combined and angled axis, rather than along the two axes desired.

A nightly reset of the altitude position was also implemented, allowing the position of the altitude controller to reset at the minimal position, set to -55° to conform to mechanical limits. This, when paired with limits imposed on the azimuth position, allows the array to only oscillate between $-55^\circ \leq \alpha \leq +55^\circ$, and for the azimuth position between $-180^\circ \leq \gamma \leq +180^\circ$. Without these limitations, the azimuth position would end up straining the physical connections contained within the array structure. The altitude position would, without said functions, potentially ignore the solar position entirely, given that the final solar position on a given day was more than 90° from the solar array for either altitude or azimuth positions, satisfying the “blind condition”. This is particularly an issue in equatorial regions where the solar position is close to the solar zenith.

In this simulation, the controller sampling rate is 1 sample every 0.01s. This translates to 1 sample every 10 seconds in real life. As such, each axis will be repositioned every 10 seconds from the previous sample. In this simulation, the phase difference of these controllers was taken as 0.005s which translates to approximately 5 seconds phase difference. This means that one axis shall perturb every five seconds, switching between the two axes, one after the other.

Concerning the step size used to actuate each axis, this value was derived from the resultant change in solar irradiance incident on the array representative of 5% change from directly incident. This was calculated as follows:

$$\begin{aligned} 0.05 &= \cos(\Delta\theta) \\ \text{acos}(0.05) &= 87.13^\circ \\ \therefore 2.87^\circ &= 1 \text{ step} \approx 3^\circ \end{aligned}$$

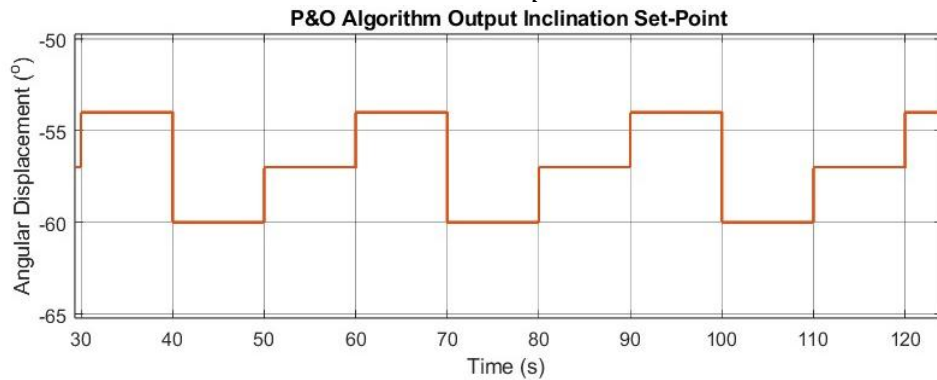


Figure 29: Perturb and Observe algorithm effect on orientation inclination.

For the dual axis portion of this simulation, these controllers allow for effective tracking of the solar position in both axes.

4.3.2b – Single Axis Control

For single axis control, a unique problem arose. In the existing form of this model, there is the capability to actuate both azimuth and altitude axes. In single axis control, by definition only one axis can be controlled. In order to continue using the conventions used throughout the previous discussions, accuracy of both azimuth and altitude positions was required. By restricting any single axis, the tracking position quickly deviates from the actual maximum power point, either chasing an invalid power point or restricting itself from the actual solar position. As such, a new approach is needed.

By locking any single axis, using the approach detailed in the previous section, one axis may continue tracking appropriately as per the same component in the solar position, however the other axis will be locked. For example if the azimuth axis is locked, altitude varies from $+90^\circ$ to -90° without tracking the azimuth. As such, as soon as the solar azimuth is beyond 90° from the locked azimuth position, the incident irradiance is 0 W, but the altitude controller never identifies this issue as, relative to the solar altitude position, the tracker is perfectly on track. This issue is entirely due to the limitations of spherical coordinates due to their lack of linear axes.

In order to correct this issue, these spherical coordinates gathered must be converted into cartesian coordinates. By doing so, position vectors can be derived for the solar position and the position of the perpendicular normal axis of the solar array. These position vectors contain the coordinates of the position of the sun and the solar array normal axis assuming a radius of 1 unit length, normalised. By doing so, the magnitude of the angle between the vectors can be determined. From this, the cosine scaling coefficient can be derived.

Utilising this convention, the irradiance incident on the solar array surface is directly proportional to the magnitude of the maximum irradiance multiplied by the cosine of the angle between the two vectors.

$$\frac{\begin{bmatrix} X_{Array} \\ Y_{Array} \\ Z_{Array} \end{bmatrix} \cdot \begin{bmatrix} X_{Ideal} \\ Y_{Ideal} \\ Z_{Ideal} \end{bmatrix}}{\left[\begin{bmatrix} X_{Array} \\ Y_{Array} \\ Z_{Array} \end{bmatrix} \cdot \begin{bmatrix} X_{Array} \\ Y_{Array} \\ Z_{Array} \end{bmatrix} \right] \cdot \left[\begin{bmatrix} X_{Ideal} \\ Y_{Ideal} \\ Z_{Ideal} \end{bmatrix} \cdot \begin{bmatrix} X_{Ideal} \\ Y_{Ideal} \\ Z_{Ideal} \end{bmatrix} \right]} = \cos(\Delta\theta),$$

where $\Delta\theta = \text{angle between vectors}$

From this, depending on the orientation of the tracker being simulated, a single coordinate may be set to a constant value, for the array. This allows for the relationship between the array position and the solar position to be quantified and for the accurate tracking along any single plane.

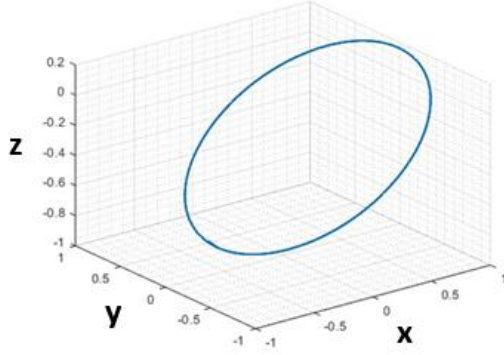


Figure 30: 3D representation of a generic normalised solar path in the cartesian domain, having been transformed from the spherical domain.

Consider the above cartesian solar path. In order to track the position without leaving a given plane, e.g. being restricted to only X-Z plane, a single coordinate must be restricted to that single plane, e.g. $y=0$ in the case of observing X-Z plane. From this perspective, the optimal path is two dimensional, as seen below. This is where spherical coordinates lose their resolution. Spherical coordinates demand three dimensions in order to properly describe any position. By switching domains to the cartesian domain, the solar position can be described in three or two dimensions. This is the driving principle which allows for the optimal tracking of the solar position with any given planar restriction. By using this convention, the existing perturb and observe algorithm can be utilised to track this optimal path.

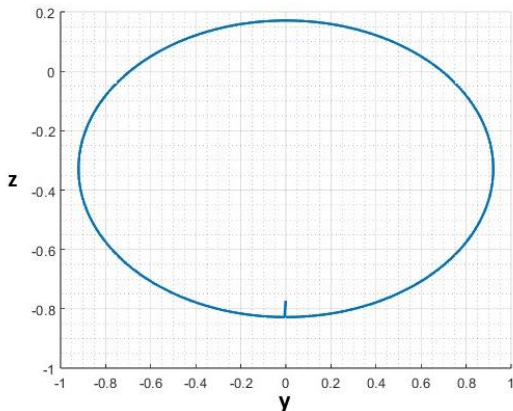


Figure 31: 2D representation of the above figure, representing the path considering a restricted X plane $X=0$, allowing only variance in Y-Z plane.

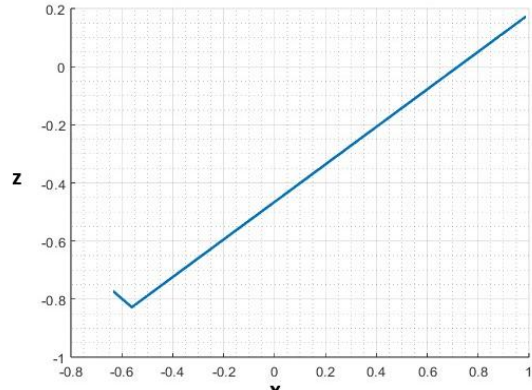


Figure 32: 2D representation of the above figure, representing the path considering a restricted Y plane $Y=0$, allowing only variance in X-Z plane.

In this application, restricting any given coordinate is interpreted as limiting the controller azimuth to a given orientation, i.e. East-West tracking, locked azimuth at $y = -90^\circ$, or in cartesian, $x = 0$. The resultant path shown by the remaining axes is the path which the

altitude controller should follow to track the optimal path. This is what the equation determined earlier in this section describes.

Transforming from spherical to cartesian coordinates is intuitive and textbook knowledge:

$$x = \cos(\alpha) \cos(\gamma)$$

$$y = \cos(\alpha) \sin(\gamma)$$

$$z = \sin(\alpha)$$

Some resolution is lost due to the nature of sinusoids repeating past specific values, requiring some consideration of the quartile of the coordinates.

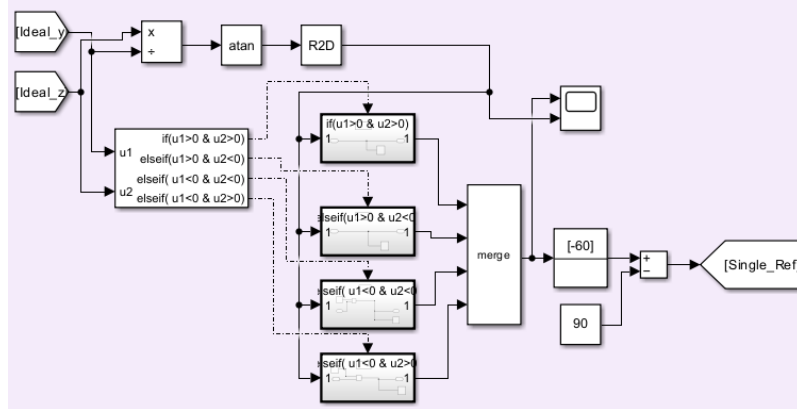


Figure 33:Algorithm utilised in derived Simulink model for East to West tracking of the solar position.

Unfortunately due to time restrictions, this approach was not able to be implemented for both single and double axes tracking methods, but was effectively implemented for east to west tracking methodologies. As such, east to west single axis altitude tracking is the single axis method utilised in the discussion.

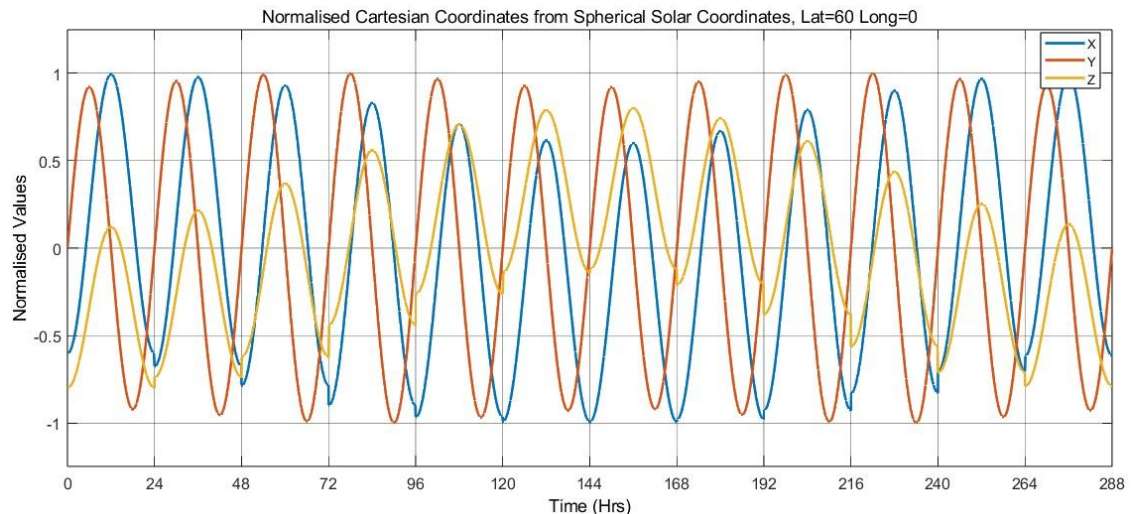


Figure 34:Normalised cartesian coordinates of the solar path derived from the transform of spherical coordinates into cartesian coordinates, for test case 2.

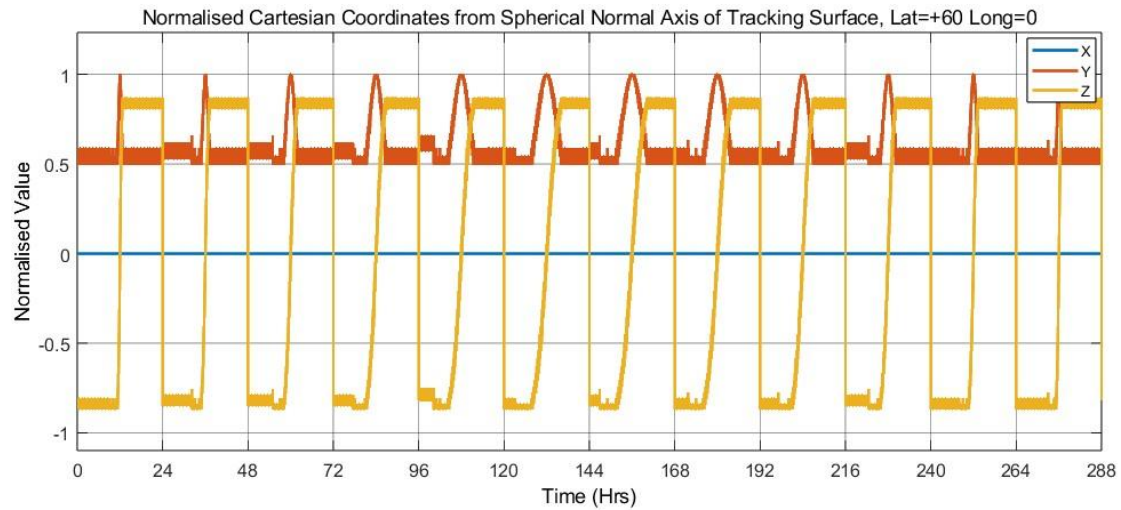


Figure 35: Normalised cartesian coordinates of the controller set point path derived from the transform of spherical coordinates into cartesian coordinates, for test case 2.

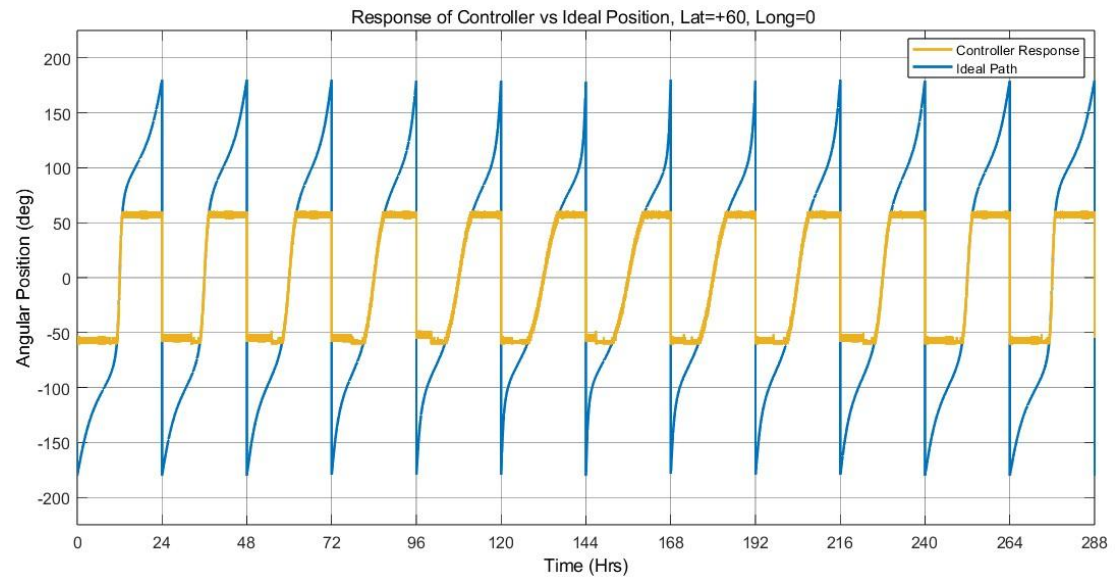


Figure 36: Demonstration of the new controller optimal path, along the East-West plane, with controller response in yellow and ideal path in blue. Note the limitation of the solar actuation beyond the limits $-55^\circ \leq \alpha \leq 55^\circ$.

4.4 - Test Scenario Derivation

33 different locations were acquired across a range of different latitudes and longitudes. These are targeted around population centres due to the greater data consistency in these regions. These locations each had a list of parameters extracted:

- Hourly average global clear sky irradiance per month, ALLSKY_SFC_SW_DWN_*00->23*
- Average clearness local clearness index per month, ALLSKY_KT
- Average cloud cover percentage per month, CLOUD_AMT
- Average daily ambient temperature per month at 2 meters altitude, T2M

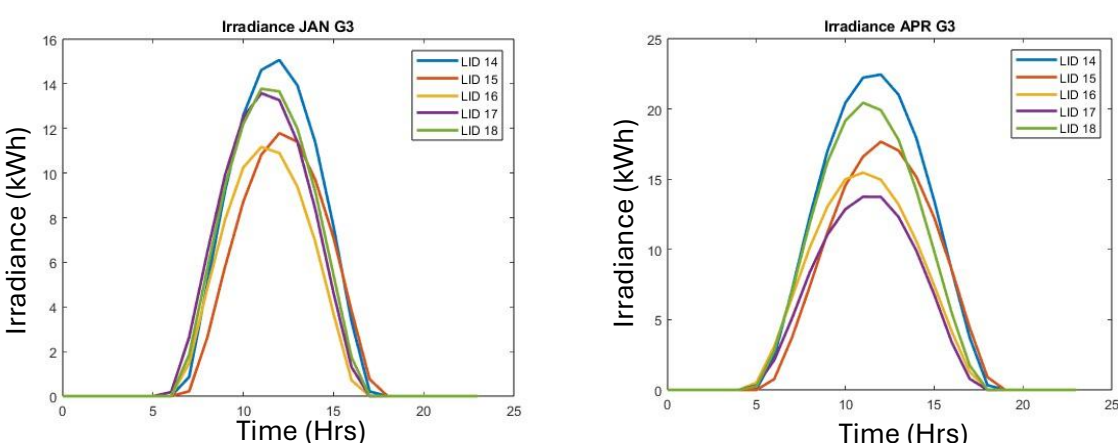
The parameters gathered for each location were grouped based on the latitude of their corresponding locations. The aim of this grouping was to determine whether the conditions observed at each latitude, in terms of irradiation and temperature, could be generalised across all latitudes. To do this, locations were chosen in regular intervals of longitude and latitude.

Data extracted from the database were plotted as follows:

- Average hourly irradiance over the entire corresponding month, plotted over 24 hours in a day.
- Average monthly temperatures, plotted for each month of the year.
- Average monthly cloud cover, plotted for each month of the year.

From the data plotted, there is a clear correlation between latitudinal location and the solar irradiance. Some variances are seen, but generally the trend is clear. For local temperature, it is clear that there is a direct correlation between ambient temperature and the solar position. As local summer comes, temperatures increase – although there is not enough data to determine the exact relationship, and some inconsistencies exist which may be due to climate and atmospheric conditions.

As such, the irradiance values for the test cases are shown in the appendix. In each test case, the ambient temperature will be held at 25 degrees Celsius. By following standard testing conditions for the temperature portion, the unknown effects of the local climate can be neglected, simplifying the discussion in this study. Standard testing conditions were also opted for due to the lack of validation of the photovoltaic model beyond the range of $0^{\circ}\text{C} \leq T \leq 50^{\circ}\text{C}$. Although the global temperature rarely reaches beyond 50°C , several locations are observed to have average temperatures below 0°C . Any results output by the simulation outside of the validated range cannot be relied on and so as such, standard test conditions can be abided by.



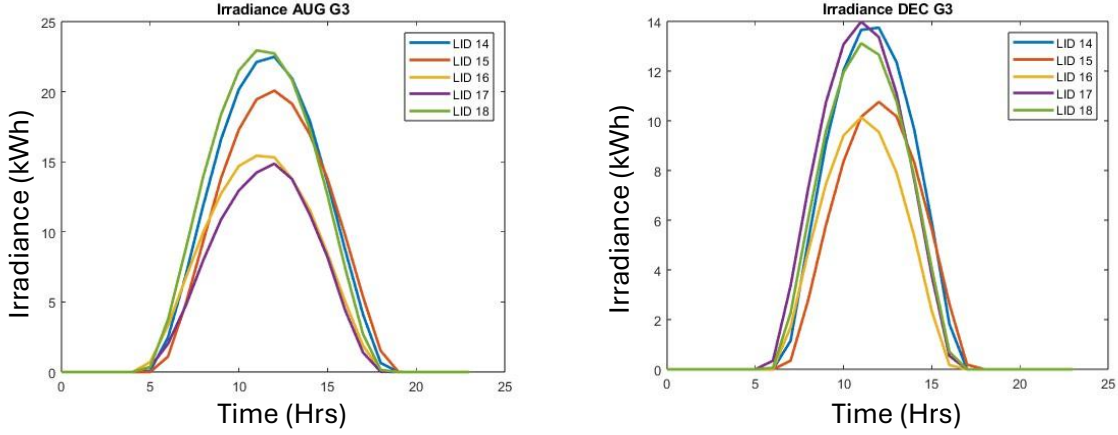


Figure 37: Group 3 average hourly irradiance (kWh) over a 24-hour period for January (Top-Left), April (Top-Right), August (Bottom-Left), and December (Bottom-Right), demonstrating consistency of grouping based on latitude.

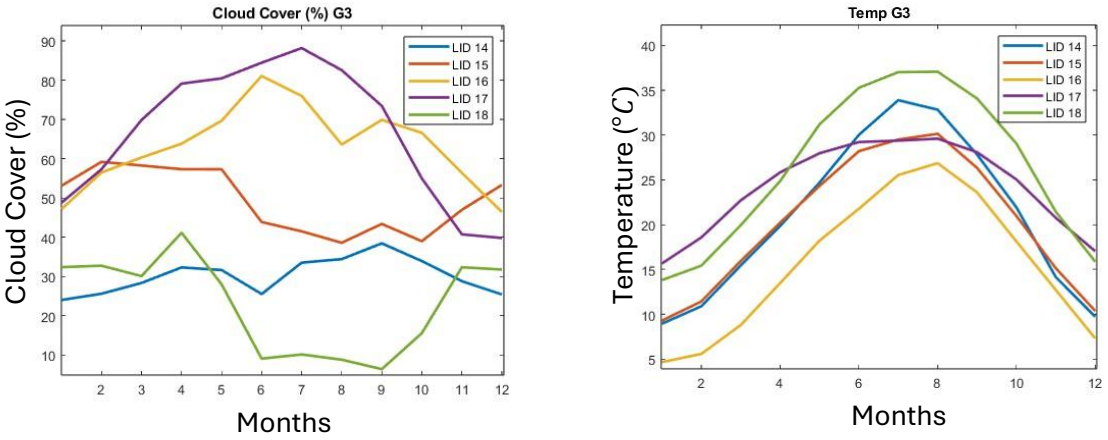


Figure 38: Group 3 average monthly cloud cover (Left) and temperature (Right).

Note: as locations chosen were grouped by latitude, and focussed on settlements or locations of interest, the data gathered for locations in the southern hemisphere were extremely limited. There are few settlements along latitude 60 due to the massive oceans which populate much of the globe at that point on the globe. As such, there is no latitude -60° group, since only a single location of interest could be found on said latitude.

The test cases were finally derived. The locations would take the grouping latitudes and a longitude about 0°. The hourly irradiance values would be taken as the mean value of the hourly irradiances gathered for each group, after filtering any anomalous values. Temperature for each case would be taken as $T = 25^{\circ}\text{C}$.

Table 6: Locations selected with their respective Longitudes and Latitudes, as well as a unique identifier for each location for ease of software identification.

Location_ID	Location_Name	Latitude	Longitude	Comments	Group
1	Nuuk, Greenland	64.17	-51.74	Northernmost settlements I could find of significance	1
2	Qanaaq, Denmark	77.47	-69.23	Northernmost settlements I could find of significance	1
3	Dikson, Russia	73.50	80.50	Northernmost settlements I could find of significance	1
4	Tromso, Norway	69.64	18.93	Northernmost settlements I could find of significance	1
5	Tiksi, Russia	71.64	128.84	Northernmost settlements I could find of significance	1
6	Paulatuk, Canada	69.35	-124.00	Northernmost settlements I could find of significance	1
7	Tilichiki, Russia	60.43	166.07		2
8	Yukta, Russia	63.38	105.67		2
9	Syktyvkar, Russia	61.66	50.82		2
10	Aberdeen, Scotland	57.14	-2.08		2
11	Arsuk, Greenland	61.17	-48.45		2
12	Churchill, Canada	58.77	-94.17		2
13	Anchorage, Alaska	61.18	-149.90		2
14	Bechar, Algeria	31.60	-2.18		3
15	Austin, USA	30.27	-97.74		3
16	Tokyo, Japan	35.68	139.80		3
17	Tinsukia, India	27.49	95.35		3
18	Kuwait City, Kuwait	29.38	47.98		3
19	Libreville, Gabon	0.41	9.45		4
20	Mogadishu, Somalia	2.04	45.34		4
21	Padang, Indonesia	-0.95	100.38		4
22	Jayapura, Indonesia	-2.53	140.72		4
23	Guayaquil, Ecuador	-2.15	-79.95		4
24	Macapa, Brazil	0.02	-51.06		4
25	Cape Town, South Africa	-33.92	18.42		5
26	Manantenina, Madagascar	-25.17	46.70		5
27	Perth, Australia	-31.97	115.84		5
28	Brisbane, Australia	-27.48	152.04		5
29	Auckland, New Zealand	-36.82	174.79		5
30	Puerto Harberton, Chile	-54.87	-67.34		6
31	McMurdo Station, Antarctica	-77.85	166.67	Southernmost settlements I could find of significance	6
32	Aboa Station, Antarctica	-73.04	-13.41	Southernmost settlements I could find of significance	6
33	Davis Station, Antarctica	-68.60	77.21	Southernmost settlements I could find of significance	6

5.0 – Results, Analysis and Discussion

5.1 – Test conditions

The simulation was run for both single and double axis controllers. In this discussion, the single axis tracking strategy simulated was for an east to west tracker, controlling solely the altitude axis of the solar array. For the dual axis controller, both azimuth and altitude controllers were in use. For both cases, altitude was limited to $-55^\circ \leq \alpha \leq +55^\circ$ to simulate mechanical limitations due to contacts with its own assembly.

The test cases utilised were as per the previous section.

- Scenario 1: Latitude= $+70^\circ$ Longitude= 0° T= $25^\circ C$
- Scenario 2: Latitude= $+60^\circ$ Longitude= 0° T= $25^\circ C$
- Scenario 3: Latitude= $+30^\circ$ Longitude= 0° T= $25^\circ C$
- Scenario 4: Latitude= 0° Longitude= 0° T= $25^\circ C$
- Scenario 5: Latitude= -30° Longitude= 0° T= $25^\circ C$
- Scenario 6: Latitude= -70° Longitude= 0° T= $25^\circ C$

For each test case, the average hourly irradiance per month is simulated over a period of 24 hours. This is done for each month in the year, resulting in 12 days being simulated. The date of each simulated day is to be the first day of each month.

5.2 – Results

For double axis trackers, as expected, the difference between maximum daily solar irradiance and the component of that irradiance incident on the solar arrays surface was consistently low. Excluding months where there was no sunlight, the dual axis tracker consistently received up to 80% of the maximum available irradiation. Consistently, greater proportions of the maximum irradiance were received on the arrays surface in summer months. For both northern and southern hemisphere scenarios, the percent difference between maximum and incident irradiation was found to be between 10-20% of the maximum irradiation. This appears to be more impactful for locations of a greater distance from the equator, being seen in scenarios 1, 2, and 6. This is intuitive, since these are the locations which are most impacted by the solar position, resulting in lower solar altitudes in the winter months which are consistently below the minimum limit of the solar array, -55° . As the solar altitude approaches the minimum limit, the component incident on the array becomes greater, explaining the seasonal changes in these regions.

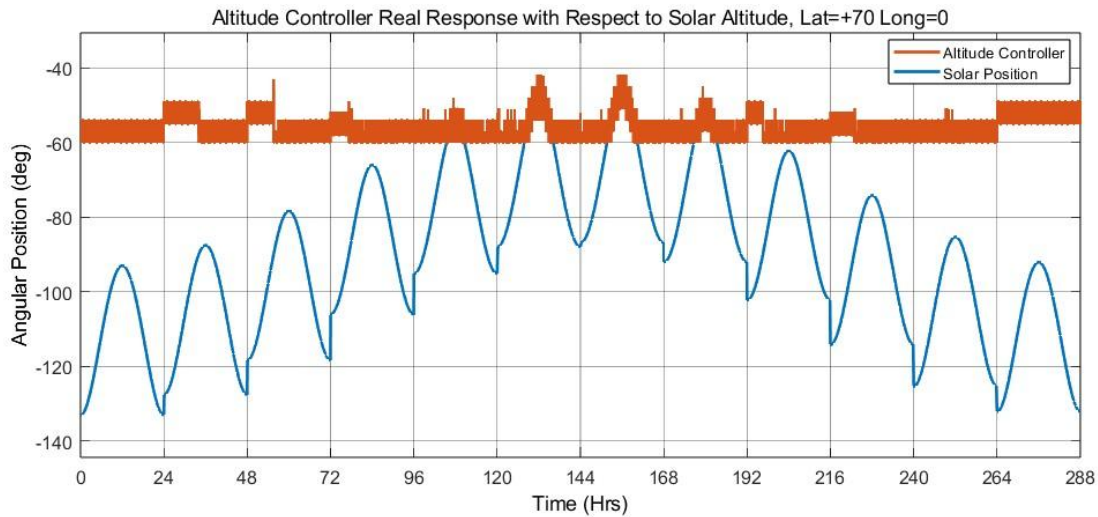


Figure 39: Solar altitude controller response modelled alongside the real solar altitude, where -90° and 90° is the horizon, below which the sun is not visible.

This is further evidenced by the consistent performance of the dual axis performance in regions closer to the equator, where solar altitude angles are consistently above the minimum limit of the solar array. In these regions, solar altitude angles are generally much more consistent. As such, dual axis tracking consistently receives >97% of the maximum irradiation available to the array.

In contrast, the single axis east-west solar tracker performed significantly worse in terms of receiving available incident irradiation. For regions further from the equator, the single axis tracking strategy received high proportions of available irradiation in the regional summer months, but received abysmal proportions in winter months. In scenario 1, 2 and 6, winter months received less than 50% of the available irradiance on the solar arrays surface. In the deep winter months, less than 25% of the available irradiation was incident on the surface of the array.

Although this is the case, the summer months performed to a much better standard. For all tested regions, the portion of available solar irradiance incident on the solar array in the summer months was more than 80%, with performance improving closer to the equator. For scenario 3, the summer months saw up to 98.98% of the available irradiation incident on the single axis array's surface.

To discuss the effectiveness of the solar tracking strategies, the efficiency of each tracking strategy can be calculated by finding the percentage of the maximum power generated which was generated by the solar array. As expected, the dual axis tracking strategy performed significantly better in regions further from the equator, excluding the sixth scenario. In all other scenarios, as seen below, the dual axis tracking strategy performed with an average yearly efficiency of 87.75%, increasing towards the equator to a maximum of 98.98% efficiency.

Alternatively, the single axis tracker performed with a wildly variable efficiency based on the location. For scenarios further from the equator, the solar yield was much lower for a minimum of 39.34% in scenario 6 and a maximum of 95.02% in scenario 4.

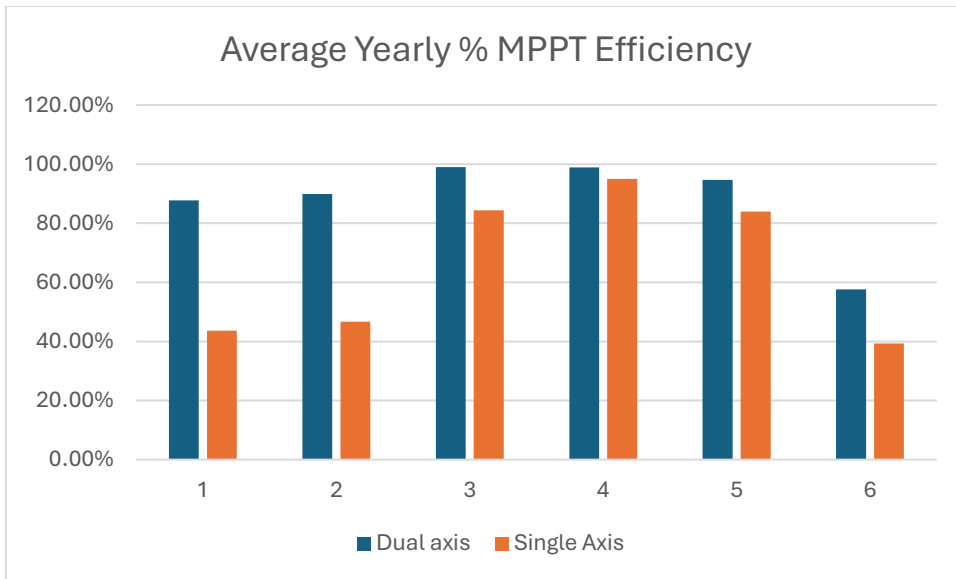


Figure 40: Average yearly efficiency of maximum power point tracking method for axial actuation of the array based on the proportion of total maximum power generated by the photovoltaic model to the actual power generated through incident portion of irradiance.

Notably, the sixth scenario for dual axis tracking performs to a different standard than the first five scenarios. This scenario performs with an efficiency of 57.62% as opposed to the trend shown by the other scenarios at >87.75%. This is likely due to the inconsistency in tracking the azimuth location in this scenario. For some periods, the tracking algorithm appears to follow the solar azimuth position perfectly, however for others, the position is completely compromised. Most notably, there appears to be oscillation at the boundary between +180° and -180°, where the tracker attempts to increase the angle, but the setpoint resets to -180°. This is supposed to consider the mechanical limitations of the array; however it causes blind spots in the incident irradiance and therefore power generated.

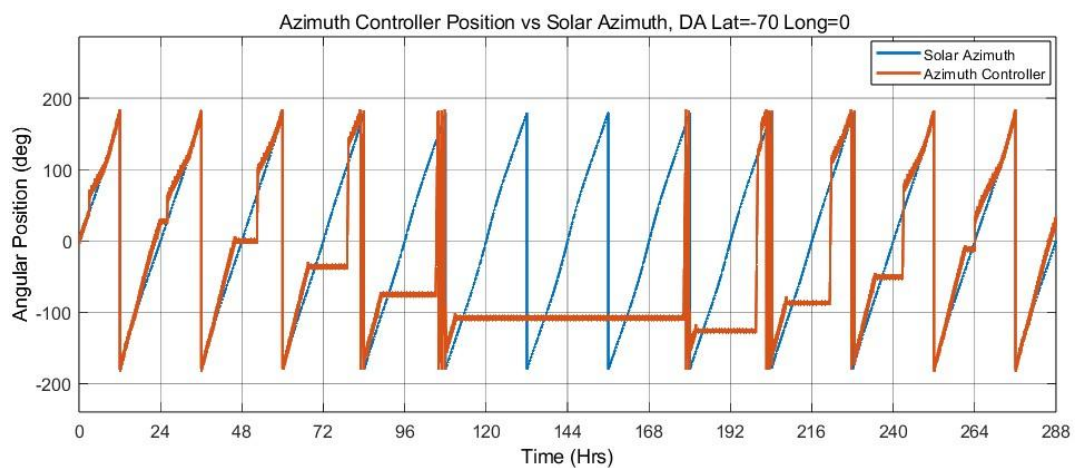


Figure 41: Azimuth position for dual axis tracker for -70° latitude, note the thick sections of the graphed response, demonstrating the oscillation between +180° and -180°.

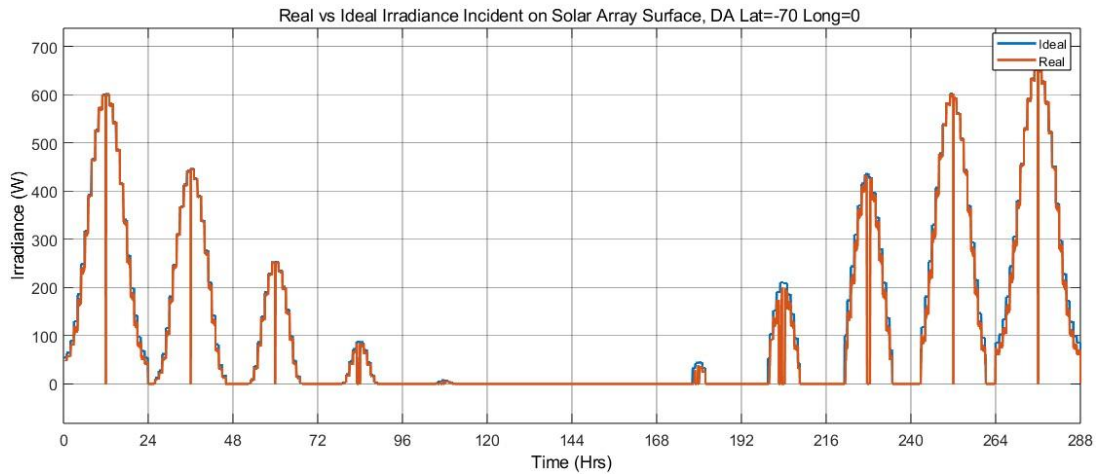


Figure 42: Observed irradiation on the solar array surface, note an incident and sudden drop in incident irradiation, corresponding with the moment between minimum and maximum azimuth orientations.

6.0 – Conclusion & Future Recommendations

6.1 - Conclusions

The hypothesis of this study, as described previously, is that the double axis tracker would significantly outperform the single axis tracker in regions beyond $\pm 30^\circ$ latitude. The data gathered appears to support that hypothesis for regions north of the equator. Comparing year long mean tracking strategy efficiencies, based on the proportion of power generated by the array compared to the maximum potential power generated, for each scenario yields a difference of 44.10% efficiency in scenario 1, 43.20% in scenario 2, 14.63% in scenario 3, 3.85% in scenario 4, 10.69% in scenario 5, and finally 18.29% in scenario 6. Where scenarios 1, 2, and 6 are beyond $\pm 30^\circ$ latitude. Scenario 6 counter-intuitively performs to a lesser quality than the other scenarios, for dual axis tracking. This is likely a result of improper techniques used to manage the offset azimuth location found in these southern regions, resulting in gaps in simulated power generation as the array improperly tracks the solar position.

As shown by the graphs below, dual axis trackers perform generally very consistently well. This is particularly the case in regions closer to the equator, where mechanical limitations are less impactful due to the greater range in solar positions, namely the altitude. Further from the equator, impacts of the lower solar altitude become apparent, reducing incident irradiation on the solar array. Note also the 0% efficiency in winter months, for both northern (scenario 1) and southern (scenario 6) hemispheres, where the sun is consistently below the horizon and no irradiance is visible.

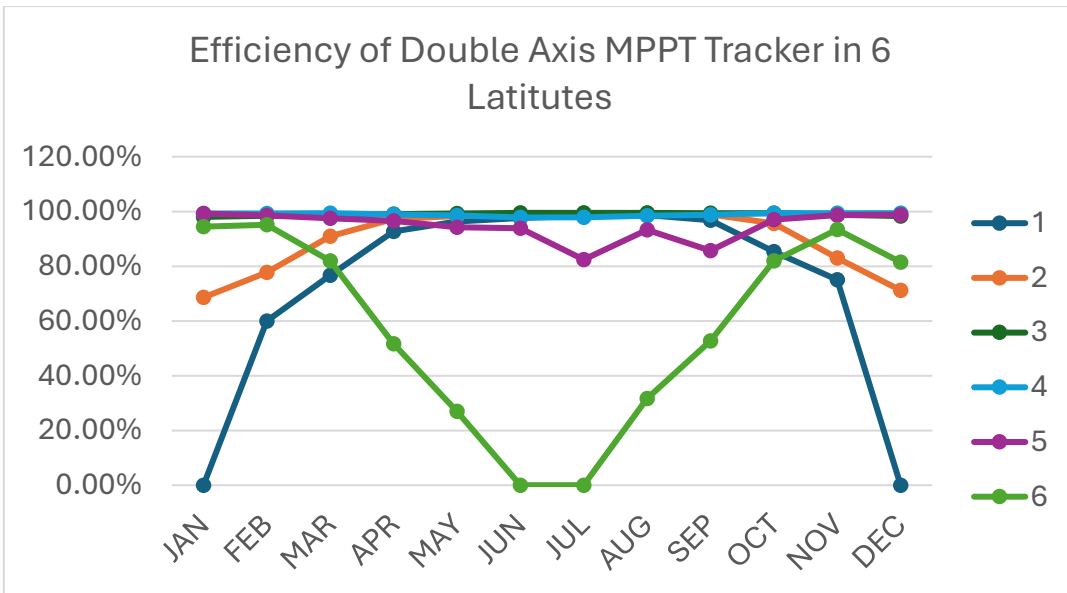


Figure 43: Efficiency of the double axis tracking algorithm in making use of available potential power.

As shown by the graph below, the performance of single axis east to west solar trackers is further impacted by the increased distance from the equator. For regions $\pm 30^\circ$ latitude performance is fairly consistent, with lower variability in the overall efficiency of the tracking method. For regions beyond $\pm 30^\circ$ latitude, performance becomes massively variable, resulting in a much higher performance in summer months than in winter months.

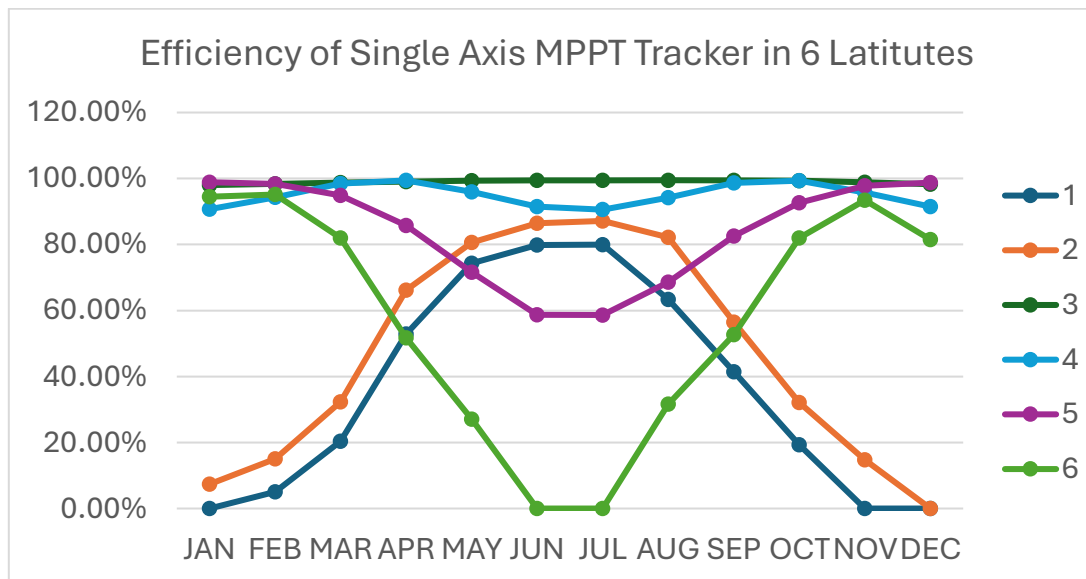


Figure 44: Efficiency of the single axis tracking algorithm in producing the maximum power available to the solar array.

In conclusion, the simulated response appears to support the hypothesis that for regions north of $+30^\circ$ latitude, double axis tracking yields significantly greater efficiencies than the single axis east to west tracking strategy. However, further investigation is required in order to conclude the same correlation for $<-30^\circ$ latitude.

6.2 – Further Recommendations

In future work, implementation of the cartesian optimal path should be utilised for both single and dual axis tracking methods. This would allow for a broader range of tracking strategies to be discussed, rather than the two mentioned here. In future, comparisons of different single axis tracking strategies or even fixed axis tracking strategies should be possible utilising the existing framework and the implementation of this cartesian “optimal path”. In theory, implementing this is simple, however time limitations impacted current implementation.

Furthermore, further improvements should be made to the extra features in the software, namely the mechanical limits considered. In the existing study, the southern most scenario was impacted by the faulty conditions implemented.

In future it would also be beneficial to consider the impact of partial shading conditions, based on climatological data, for solar farms, utilising multiple simulated solar modules in parallel and series as discussed by Pendem & Mikkili (2018). These conditions were considered in this study, but as a gaussian distributed white noise disturbance, this minimally impacted the results generated and so was omitted from the discussion. Investigating this impact on arrays of modules would add further detail to the argument for the strategies uses in specific climates.

7.0 – References

- Wang, X., Wang, G., Chen, T., Zeng, Z., & Heng, C. K. (2022). Low-carbon city and its future research trends: A bibliometric analysis and systematic review. *Sustainable Cities and Society*, 90, 104381. <https://doi.org/10.1016/j.scs.2022.104381>
- Pourasl, H. H., Barenji, R. V., & Khojastehnezhad, V. M. (2023). Solar energy status in the world: A comprehensive review. *Energy Reports*, 10, 3474–3493. <https://doi.org/10.1016/j.egyr.2023.10.022>
- Mendoza, B. (2005). Total solar irradiance and climate. *Advances in Space Research*, 35(5), 882–890. <https://doi.org/10.1016/j.asr.2004.10.011>
- Handayani, K., Krozer, Y., & Filatova, T. (2018). From fossil fuels to renewables: An analysis of long-term scenarios considering technological learning. *Energy Policy*, 127, 134–146. <https://doi.org/10.1016/j.enpol.2018.11.045>
- Arora, I., Sony, N., Joshi, C., Angmo, D., Rajput, P., Biswas, M., & Bhaskarwar, A. N. (2023). Technologies for Hydrogen Production from Fossil Fuels and Hydrocarbons. In *Elsevier eBooks* (pp. 115–124). <https://doi.org/10.1016/b978-0-323-93940-9.00032-3>
- Das, S., Chakraborty, S., Sadhu, P. K., & Sastry, O. S. (2015). Design and experimental execution of a microcontroller (μ C)-based smart dual-axis automatic solar tracking system. *Energy Science & Engineering*, 3(6), 558–564. <https://doi.org/10.1002/ese3.102>
- Sidek, M. H. M., Hasan, W. Z. W., Kadir, M. Z. A. A., Shafie, S., Radzi, M. A. M., Ahmad, S. A., & Marhaban, M. H. (Eds.). (2014). *GPS based portable Dual-Axis solar tracking system using astronomical equation*. IEEE International Conference Power & Energy (PECON). https://www.researchgate.net/profile/W-Wan-Hasan/publication/282271883_GPS_based_portable_dual-axis_solar_tracking_system_using_astronomical_equation/links/56cdacb708aeb52500c33c00/GPS-based-portable-dual-axis-solar-tracking-system-using-astronomical-equation.pdf
- Pendem, S. R., & Mikkili, S. (2018). Modeling, simulation and performance analysis of solar PV array configurations (Series, Series-Parallel and Honey-Comb) to extract maximum power under Partial Shading Conditions. *Energy Reports*, 4, 274–287. <https://doi.org/10.1016/j.egyr.2018.03.003>
- Ahmad, S., Shafie, S., Kadir, M. Z. a. A., & Ahmad, N. S. (2013). On the effectiveness of time and date-based sun positioning solar collector in tropical climate: A case study in Northern Peninsular Malaysia. *Renewable and Sustainable Energy Reviews*, 28, 635–642. <https://doi.org/10.1016/j.rser.2013.07.044>
- Chang, T. P. (2009). Output energy of a photovoltaic module mounted on a single-axis tracking system. *Applied Energy*, 86(10), 2071–2078. <https://doi.org/10.1016/j.apenergy.2009.02.006>
- Fara, L., & Craciunescu, D. (2017). Output analysis of stand-alone PV systems: modeling, simulation and control. *Energy Procedia*, 112, 595–605. <https://doi.org/10.1016/j.egypro.2017.03.1125>
- Batayneh, W., Bataineh, A., Soliman, I., & Hafees, S. A. (2018). Investigation of a single-axis discrete solar tracking system for reduced actuations and maximum energy collection. *Automation in Construction*, 98, 102–109. <https://doi.org/10.1016/j.autcon.2018.11.011>

Randall, J., & Jacot, J. (2003). Is AM1.5 applicable in practice? Modelling eight photovoltaic materials with respect to light intensity and two spectra. *Renewable Energy*, 28(12), 1851–1864. [https://doi.org/10.1016/s0960-1481\(03\)00068-5](https://doi.org/10.1016/s0960-1481(03)00068-5)

Camacho, E. F., Soria, M. B., Rubio, F. R., & Martínez, D. (2012). Control of solar energy systems. Springer Science & Business Media.

Verma, D., Nema, S., Shandilya, A., & Dash, S. K. (2015). Maximum power point tracking (MPPT) techniques: Recapitulation in solar photovoltaic systems. *Renewable and Sustainable Energy Reviews*, 54, 1018–1034. <https://doi.org/10.1016/j.rser.2015.10.068>

Di Carlo, A., Lamanna, E., & Nia, N. Y. (2020). Photovoltaics. *EPJ Web of Conferences*, 246, 00005. <https://doi.org/10.1051/epjconf/202024600005>

Lorenzo, E. (1994). *Solar electricity: Engineering of Photovoltaic Systems*. <https://books.google.co.uk/books?id=lYc53xZyxZQC>

Abdin, Z., Webb, C., & Gray, E. (2018). Simulation of large photovoltaic arrays. *Solar Energy*, 161, 163–179. <https://doi.org/10.1016/j.solener.2017.12.034>

Kyocera. (2007). KC200GT. <https://www.energymatters.com.au/images/kyocera/KC200GT.pdf>

Practical Handbook of Photovoltaics. (2012). In Elsevier eBooks. <https://doi.org/10.1016/c2011-0-05723-x>

Wang, Z. (2019). The solar resource and meteorological parameters. In Elsevier eBooks (pp. 47–115). <https://doi.org/10.1016/b978-0-12-815613-1.00002-x>

Rosa-Clot, M., & Tina, G. M. (2018). Submerged and Floating Photovoltaic Systems. In Elsevier eBooks (pp. 13–32). <https://doi.org/10.1016/b978-0-12-812149-8.00002-8>

8.0 – Appendix A

i – Nomenclature

Table 7:Nomenclature table.

Description	Symbol	Units
Local Hour Angle	ω_h	° or rad
True Solar Time	T_{sv}	Hours
Local Time	T_l	Hours
Local Time Difference	$T_{l,s}$	Hours
Time	t	Seconds
Equation Of Time	T_E	Seconds
Day Number	N_d	Days
Solar Declination	δ	° or rad
Latitude Angle	φ	° or rad
Altitude Angle	α	° or rad
Azimuth Angle	γ	° or rad
Thermal Voltage	V_t	V
Operational Temperature	T_{op}	°C or K
Boltzmann's Constant	k	JK^{-1}
Electron Charge Constant	q	C
Diode Current	I_d	A

Diode Reversed Saturated Current	I_s	A
Photovoltaic Cell Voltage	V	V
Photovoltaic Cell Current	I	A
Series Resistance	R_s	Ω
Parallel (Shunt) Resistance	R_{sh}	Ω
Diode Ideality Factor	n	n/a
Number Of Cells In Module	N_{cells}	n/a
Number Of Modules In Series	N_s	n/a
Number Of Modules In Parallel	N_p	n/a
Diode Reversed Saturated Current At STC	I_{rs}	A
Reference Temperature (Stc)	T_{ref}	$^{\circ}C \text{ or } K$
Band Gap Energy Of The Cell	E_g	eV
Short Circuit Current	I_{sc}	A
Open Circuit Voltage	V_{oc}	V
Solar Irradiance Ratio (To STC)	G_k	n/a
Temperature Coefficient Of Short Circuit Current	k_I	AK^{-1}
Temperature Coefficient Of Open Circuit Voltage	k_v	VK^{-1}
Photon Generated Current	I_{ph}	A
Shunt Current	I_{sh}	A

ii – List of Figures

- Figure 1: Solar declination angle variation demonstrated (Wang Z., 2019) 9
 Figure 2: Simulated solar altitude (Top) and solar azimuth positions simulated for the 8th day in each month where 100 seconds in the simulation is equal to 24 hours of real time. 9
 Figure 3: Developed Simulink application, inputting location on the Earth, time difference of the said location, and day number needing simulated (from 1-28). This application also displays and saves key information required later..... 10
 Figure 4: Entire solar positional model. Takes inputs on the left of longitude, latitude, local time difference, day number simulated, array of irradiance data, array of temperature data and finally the simulation time. The simulation uses these inputs to form output signals of solar azimuth and altitude signals for a given time as well as observed maximum irradiance and temperature, all as timeseries signals..... 11
 Figure 5: Solar irradiation components and sources (Rosa-Clot et al, 2018) 12
 Figure 6: Equivalent circuit of a solar cell (Di Carlo et al., 2020)..... 15
 Figure 7: Developed photovoltaic model utilising the system equations previously discussed. 16
 Figure 8: Input variables into the photovoltaic model developed and shown in the previous figure. refer to nomenclature for specific definitions..... 17
 Figure 9: Diagram of load circuit used to validate the Power-Voltage response of the developed photovoltaic model..... 18
 Figure 10: Current-Voltage (Top) and Power-Voltage (Bottom) relationships for STC (Red) and 45 (Blue) with a constant irradiance of 1000W for an Aavid Solar ASMS-165P array. Note the turning piquing of Power values at a given voltage, this is the maximum power point at which the current-voltage relationship is such to generate the maximum power..... 19
 Figure 11: P-V relationships for 100W (Left) and 250W (Right) irradiance at 25°C for both Simulink Simscape (Red) and modelled (Blue) photovoltaic models. 21

Figure 12: PV response of Simulink Simscape and Modelled photovoltaic arrays for an irradiance of 3 kW	21
Figure 13:Example attempt at implementing a buck converter in order to boost the voltage of the load circuit with respect to the power generated by the array – this was done utilising a perturb and observe method, adjusting the duty cycle of the PWM gated signal into the buck converter.....	22
Figure 14:Range of Irradiances input into the photovoltaic model for data gathering purposes. X axis = simulation time (seconds), Y axis = irradiance (W).....	23
Figure 15:Sawtooth ramped signal used to vary the load over the duration of the scenario, varying with respect to the selected irradiance to allow for the entire behaviour of the system to be identified. X axis = simulation time (seconds) and Y axis = variable load (Ohms).....	23
Figure 16:Load required to be in series with the photovoltaic module for a given irradiance and temperature for the KYOCERA-KC200GT PV module.	24
Figure 17:Load required to be in series with the photovoltaic module for a given irradiance for the KYOCERA-KC200GT PV module.....	24
Figure 18:Maximum power output from the photovoltaic module for a given irradiance and temperature for the KYOCERA-KC200GT PV module.	25
Figure 19:Maximum power output from the photovoltaic module for a given irradiance for the KYOCERA-KC200GT PV module.....	25
Figure 20: Resultant 1 dimensional lookup table with an input of the tracking surface irradiance and an output of the required load resistance input into the variable resistor to simulate a changing load using Simulink Simscape Electrical physical signals.....	27
Figure 21:Resultant 1-dimensional lookup table with an input of the tracking surface irradiance, and an output of the required load resistance to achieve maximum power without the Simulink Simscape Electrical physical signals, utilising the product block to simplify the expression and reduce computational load.	27
Figure 22:Power yield of solar array with a constant load of 1Ω (Top) and with the lookup table-based load controller (Bottom) for scenario 3 – Latitude=30 Longitude=0.....	28
Figure 23:Graphical representation of incident irradiation on the solar array surface, with angular difference in positional vectors labelled.	29
Figure 24:Graphical representation of "blind condition", with angular difference in positional vectors labelled.	29
Figure 25:Visual mesh plot representation of the cosine coefficient described above, demonstrating the blind condition for any angle greater than 90°	30
Figure 26:Flow diagram for the system modelled as a whole, demonstrating the relationship between the axes controller and the incident irradiation on the array surface, as well as how the loop encourages convergence on an optimal path.....	30
Figure 27:Perturb and Observe algorithm used to determine the position of greatest power yield.	31
Figure 28:Simulink block diagram representing the implementation of each axial controller... ..	31
Figure 29:Perturb and Observe algorithm effect on orientation inclination.....	32
Figure 30:3D representation of a generic normalised solar path in the cartesian domain, having been transformed from the spherical domain.	34
Figure 31:2D representation of the above figure, representing the path considering a restricted X plane $X=0$, allowing only variance in Y-Z plane.....	34
Figure 32:2D representation of the above figure, representing the path considering a restricted Y plane $Y=0$, allowing only variance in X-Z plane.....	34

Figure 33:Algorithm utilised in derived Simulink model for East to West tracking of the solar position.....	35
Figure 34:Normalised cartesian coordinates of the solar path derived from the transform of spherical coordinates into cartesian coordinates, for test case 2.....	35
Figure 35:Normalised cartesian coordinates of the controller set point path derived from the transform of spherical coordinates into cartesian coordinates, for test case 2	36
Figure 36:Demonstration of the new controller optimal path, along the East-West plane, with controller response in yellow and ideal path in blue. Note the limitation of the solar actuation beyond the limits $-55^\circ \leq \alpha \leq 55^\circ$	36
Figure 37:Group 3 average hourly irradiance (kWh) over a 24-hour period for January (Top-Left), April (Top-Right), August (Bottom-Left), and December (Bottom-Right), demonstrating consistency of grouping based on latitude.	38
Figure 38:Group 3 average monthly cloud cover (Left) and temperature (Right).....	38
Figure 39: Solar altitude controller response modelled alongside the real solar altitude, where -90° and 90° is the horizon, below which the sun is not visible.....	41
Figure 40:Average yearly efficiency of maximum power point tracking method for axial actuation of the array based on the proportion of total maximum power generated by the photovoltaic model to the actual power generated through incident portion of irradiance.	42
Figure 41:Azimuth position for dual axis tracker for -70° latitude, note the thick sections of the graphed response, demonstrating the oscillation between $+180^\circ$ and -180°	42
Figure 42:Observed irradiation on the solar array surface, note an incident and sudden drop in incident irradiation, corresponding with the moment between minimum and maximum azimuth orientations.	43
Figure 43: Efficiency of the double axis tracking algorithm in making use of available potential power.....	44
Figure 44: Efficiency of the single axis tracking algorithm in producing the maximum power available to the solar array.	44
Figure 48:MATLAB application developed for style and ease of input to simulate various positions yearly solar path.....	78
Figure 49:Simulink Model Inputs.....	79
Figure 50: Day Number Logic - used to iterate the day number based on the chosen input. This is limited between 1-28, to simulate the 1-28 day of each month (i.e. if 3rd is selected, the 3rd of January is simulated, the 3rd of February is simulated and so on.)	79
Figure 51: Calculation of the local hour angle based on the same inputs with a MATLAB function converting between simulation time and real observed time.....	79
Figure 52:Solar declination based on the simulated date in the year, and altitude angle resultant of the previously described models.	80
Figure 53:Solar irradiance, derived from the aforementioned excel document, converting the global irradiance array into a timeseries signal, and the average ambient temperature likewise.	80
Figure 54: Output signals of the simulation.	81
Figure 55: Entire derived Simulink model for solar position and irradiance signal construction.	82
Figure 56:Intialisation of parameters, importing the variables as they were loaded in via MATLAB and sending their values to "GoTo" blocks.....	83
Figure 57:Thermal Voltage calculated as per Eq.1 in 4.2.1 – Photovoltaic Cell Model.	83
Figure 58:Diode current block diagram built in Simulink using Eq.2 in section 4.2.1 - Photovoltaic Cell Model	84

Figure 59:Diode reversed saturation current at STC block diagram built in Simulink using Eq.3 in section 4.2.1 - Photovoltaic Cell Model	84
Figure 60:Diode reverse saturation current at observed temperature block diagram built in Simulink using Eq.4 in section 4.2.1 - Photovoltaic Cell Model	85
Figure 61:Shunt current block diagram built in Simulink using Eq.5 in section 4.2.1 - Photovoltaic Cell Model	85
Figure 62: Photon generated current block diagram built in Simulink using Eq.6 in section 4.2.1 - Photovoltaic Cell Model	85
Figure 63: Total output current by the photovoltaic model.	86
Figure 64: Complete Simulink model of the photovoltaic cell.....	87
Figure 65:Altitude controller real response with respect to solar altitude for scenario 1	99
Figure 66:Azimuth controller real response with respect to solar altitude for scenario 1.....	99
Figure 67:Real vs maximum incident irradiation on dual axis solar array surface for scenario 1	100
Figure 68: Photovoltaic model output for incident irradiation for dual axis tracking of scenario 1.	100
Figure 69: Single axis real vs maximum irradiance incident on the array surface, for scenario 1	100
Figure 70: Normalised cartesian coordinates from spherical solar coordinates for scenario 1,	101
Figure 71: Single axis tracking surface normalised cartesian coordinates from normal of the array surface for scenario 1.	101
Figure 72:Power output by the photovoltaic module utilising the incident irradiation on the single axis tracking solar array surface for scenario 1	101
Figure 73: controller demand (Set point) with respect to the ideal path generated for the single axis tracking solar array in scenario 1.....	102
Figure 74:Real solar altitude angle vs the altitude setpoint demand by the controller, for scenario 1.....	102
Figure 75: Real controller setpoint demand vs solar azimuth position for the single axis tracking of scenario 1.....	103
Figure 76:Altitude controller real response with respect to solar altitude for scenario 2	103
Figure 77:Azimuth controller real response with respect to solar altitude for scenario 2.....	104
Figure 78:Real vs maximum incident irradiation on dual axis solar array surface for scenario 2	104
Figure 79:Photovoltaic model output for incident irradiation for dual axis tracking of scenario 2	104
Figure 80:Single axis real vs maximum irradiance incident on the array surface, for scenario 2	105
Figure 81:Real solar altitude angle vs the altitude setpoint demand by the controller, for scenario 2.....	105
Figure 82:Real controller setpoint demand vs solar azimuth position for the single axis tracking of scenario 2	105
Figure 83:Single axis tracking surface normalised cartesian coordinates from normal of the array surface for scenario 2	106
Figure 84:Power output by the photovoltaic module utilising the incident irradiation on the single axis tracking solar array surface for scenario 2	106
Figure 85:Normalised cartesian coordinates from spherical solar coordinates for scenario 2	106

Figure 86:controller demand (Set point) with respect to the ideal path generated for the single axis tracking solar array in scenario 2.....	107
Figure 87:Altitude controller real response with respect to solar altitude for scenario 3	108
Figure 88:Azimuth controller real response with respect to solar altitude for scenario 3.....	108
Figure 89:Real vs maximum incident irradiation on dual axis solar array surface for scenario 3	109
Figure 90:Photovoltaic model output for incident irradiation for dual axis tracking of scenario 3	109
Figure 91:Single axis real vs maximum irradiance incident on the array surface, for scenario 3	109
Figure 92:Real controller setpoint demand vs solar azimuth position for the single axis tracking of scenario 3	110
Figure 93:Single axis tracking surface normalised cartesian coordinates from normal of the array surface for scenario 3	110
Figure 94:Normalised cartesian coordinates from spherical solar coordinates for scenario 3	110
Figure 95:Power output by the photovoltaic module utilising the incident irradiation on the single axis tracking solar array surface for scenario 3	111
Figure 96:Real solar altitude angle vs the altitude setpoint demand by the controller, for scenario 3.....	111
Figure 97:controller demand (Set point) with respect to the ideal path generated for the single axis tracking solar array in scenario 3.....	112
Figure 98:Altitude controller real response with respect to solar altitude for scenario 4	112
Figure 99:Azimuth controller real response with respect to solar altitude for scenario 4.....	113
Figure 100:Real vs maximum incident irradiation on dual axis solar array surface for scenario 4	113
Figure 101:Photovoltaic model output for incident irradiation for dual axis tracking of scenario 4	113
Figure 102:Single axis real vs maximum irradiance incident on the array surface, for scenario 4	114
Figure 103:Real solar altitude angle vs the altitude setpoint demand by the controller, for scenario 4.....	114
Figure 104:Real controller setpoint demand vs solar azimuth position for the single axis tracking of scenario 4	115
Figure 105:Single axis tracking surface normalised cartesian coordinates from normal of the array surface for scenario 4	115
Figure 106:Power output by the photovoltaic module utilising the incident irradiation on the single axis tracking solar array surface for scenario 4	115
Figure 107:Normalised cartesian coordinates from spherical solar coordinates for scenario 4	116
Figure 108:controller demand (Set point) with respect to the ideal path generated for the single axis tracking solar array in scenario 4.....	117
Figure 109:Altitude controller real response with respect to solar altitude for scenario 5	117
Figure 110:Azimuth controller real response with respect to solar altitude for scenario 5.....	118
Figure 111:Real vs maximum incident irradiation on dual axis solar array surface for scenario 5	118
Figure 112:Photovoltaic model output for incident irradiation for dual axis tracking of scenario 5	118

Figure 113:Single axis real vs maximum irradiance incident on the array surface, for scenario 5	119
Figure 114:Real solar altitude angle vs the altitude setpoint demand by the controller, for scenario 5.....	119
Figure 115:Real controller setpoint demand vs solar azimuth position for the single axis tracking of scenario 5.....	120
Figure 116:Single axis tracking surface normalised cartesian coordinates from normal of the array surface for scenario 5	120
Figure 117:Power output by the photovoltaic module utilising the incident irradiation on the single axis tracking solar array surface for scenario 5	120
Figure 118:Normalised cartesian coordinates from spherical solar coordinates for scenario 5	121
Figure 119:controller demand (Set point) with respect to the ideal path generated for the single axis tracking solar array in scenario 5.....	122
Figure 120:Altitude controller real response with respect to solar altitude for scenario 6	122
Figure 121:Azimuth controller real response with respect to solar altitude for scenario 6.....	123
Figure 122:Real vs maximum incident irradiation on dual axis solar array surface for scenario 6	123
Figure 123:Photovoltaic model output for incident irradiation for dual axis tracking of scenario 6	123
Figure 124:Single axis real vs maximum irradiance incident on the array surface, for scenario 6	124
Figure 125:Real solar altitude angle vs the altitude setpoint demand by the controller, for scenario 6.....	124
Figure 126:Real controller setpoint demand vs solar azimuth position for the single axis tracking of scenario 6.....	125
Figure 127:Single axis tracking surface normalised cartesian coordinates from normal of the array surface for scenario 6	125
Figure 128:Power output by the photovoltaic module utilising the incident irradiation on the single axis tracking solar array surface for scenario 6	125
Figure 129:Normalised cartesian coordinates from spherical solar coordinates for scenario 6	126
Figure 130:controller demand (Set point) with respect to the ideal path generated for the single axis tracking solar array in scenario 6.....	127
Figure 131:MPPT Tracking strategy efficiency as a percentage of maximum irradiation utilised as output power for scenario 1.....	127
Figure 132:MPPT Tracking strategy efficiency as a percentage of maximum irradiation utilised as output power for scenario 2.....	128
Figure 133:MPPT Tracking strategy efficiency as a percentage of maximum irradiation utilised as output power for scenario 3.....	128
Figure 134:MPPT Tracking strategy efficiency as a percentage of maximum irradiation utilised as output power for scenario 4.....	129
Figure 135:MPPT Tracking strategy efficiency as a percentage of maximum irradiation utilised as output power for scenario 5.....	129
Figure 136:MPPT Tracking strategy efficiency as a percentage of maximum irradiation utilised as output power for scenario 6.....	130

Figure 137:MPPT Tracking strategy efficiency as a percentage of maximum power potential to be generated (by direct incidence for all active solar hours) compared to the actual quantity generated for scenario 1.....	130
Figure 138:MPPT Tracking strategy efficiency as a percentage of maximum power potential to be generated (by direct incidence for all active solar hours) compared to the actual quantity generated for scenario 2.....	131
Figure 139:MPPT Tracking strategy efficiency as a percentage of maximum power potential to be generated (by direct incidence for all active solar hours) compared to the actual quantity generated for scenario 3.....	131
Figure 140:MPPT Tracking strategy efficiency as a percentage of maximum power potential to be generated (by direct incidence for all active solar hours) compared to the actual quantity generated for scenario 4.....	132
Figure 141:MPPT Tracking strategy efficiency as a percentage of maximum power potential to be generated (by direct incidence for all active solar hours) compared to the actual quantity generated for scenario 5.....	132
Figure 142:MPPT Tracking strategy efficiency as a percentage of maximum power potential to be generated (by direct incidence for all active solar hours) compared to the actual quantity generated for scenario 6.....	133
Figure 143:Percentage difference between total irradiation and the incident portion on the solar array, for scenario 1	133
Figure 144:Percentage difference between total irradiation and the incident portion on the solar array, for scenario 2	134
Figure 145:Percentage difference between total irradiation and the incident portion on the solar array, for scenario 3	134
Figure 146:Percentage difference between total irradiation and the incident portion on the solar array, for scenario 4	135
Figure 147:Percentage difference between total irradiation and the incident portion on the solar array, for scenario 5	135
Figure 148:Percentage difference between total irradiation and the incident portion on the solar array, for scenario 6	136
Figure 149:Efficiency of double axis tracking strategy for all 6 latitudes, based on the % of maximum power output utilised per month.....	136
Figure 150:Efficiency of single axis tracking strategy for all 6 latitudes, based on the % of maximum power output utilised per month.....	137

iii – List of Tables

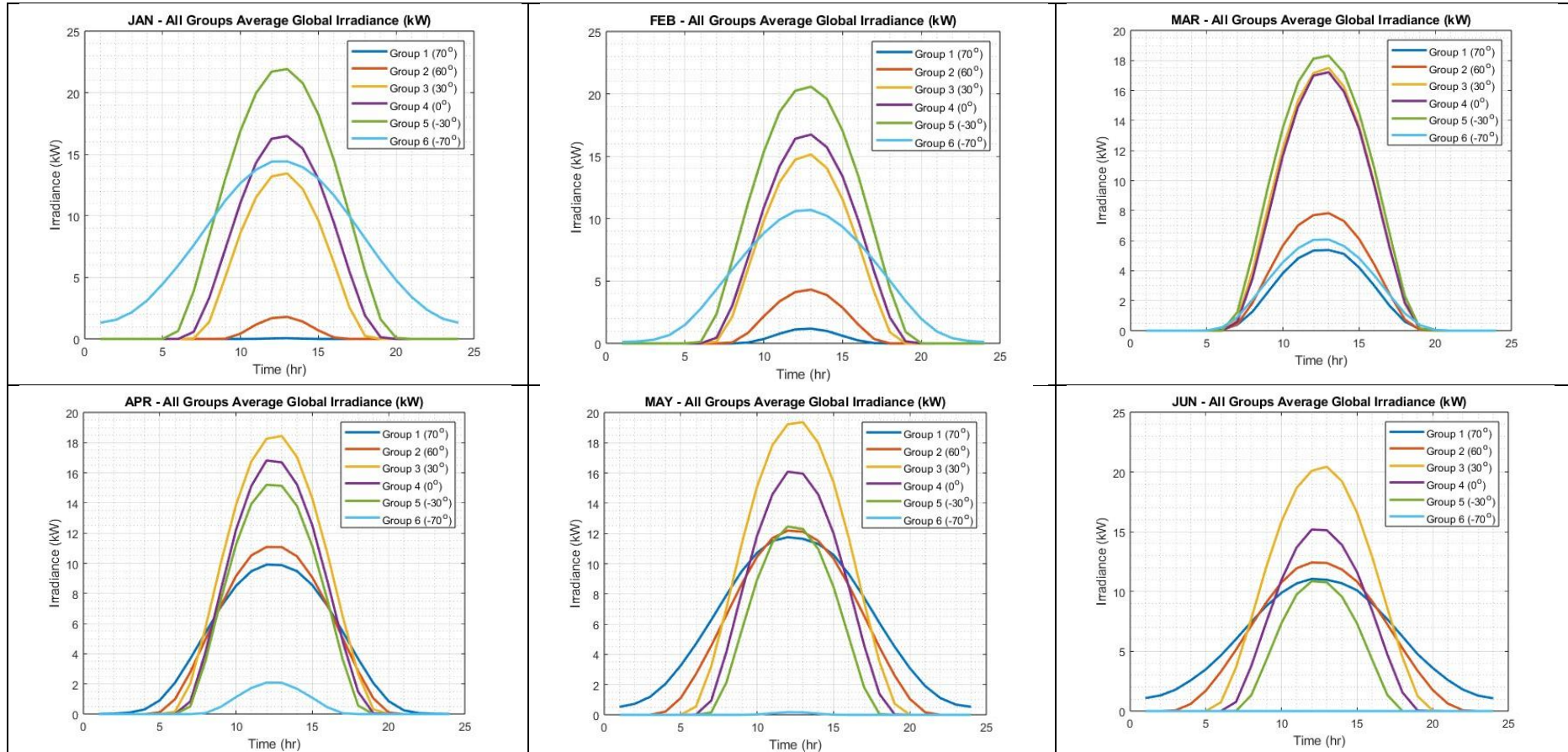
Table 1:Example of validation graphs, plotting real and modelled solar positions (labelled) for scenario 4, Lat=0 Long=0.....	14
Table 2: Unique parameter values for KYOCERA-KC200GT photovoltaic module (Kyocera, 2007).....	15
Table 3:Validation test cases used to collect data for validation of the photovoltaic module model.....	20
Table 4:Extracted resistance values gathered in derivation of the lookup table required for load control for maximum power point for each irradiance. Data contains minimum, maximum, and STC values gathered for load and power, for a given irradiance due to a change in temperature from 0°C to 50°C.....	26

Table 5:Lookup table data, one dimensional, with an input irradiance and an output load as a result.....	27
Table 6:Locations selected with their respective Longitudes and Latitudes, as well as a unique identifier for each location for ease of software identification.	39
Table 8:Nomenclature table.	47
Table 9: Table of graphs containing the average irradiance conditions for each test case in each month of the year.....	56
Table 10: Group 1 average hourly irradiation per day for each month.....	58
Table 11: Group 2 average hourly irradiation per day for each month.....	60
Table 12: Group 3 average hourly irradiation per day for each month.....	62
Table 13: Group 4 average hourly irradiation per day for each month.....	64
Table 14: Group 5 average hourly irradiation per day for each month.....	66
Table 15: Group 6 average hourly irradiation per day for each month.....	68
Table 16: Solar altitude angle validation, real and modelled solar position plotted against simulation time.....	72
Table 17:Solar azimuth angle validation, real and modelled solar position plotted against simulation time.....	75
Table 18:Validation results for the photovoltaic model given a constant irradiance of 1000W and a varying temperature.	88
Table 19:Validation results for varying irradiance for a constant temperature of T=25	93
Table 20:Raw results data gathered by the simulation for double axis controller methods. ...	138
Table 21:Raw results data gathered by the simulation for single axis controller methods.	140

8.1 – Test Case Derivation

8.1.1 - Test Case Data

Table 8: Table of graphs containing the average irradiance conditions for each test case in each month of the year.



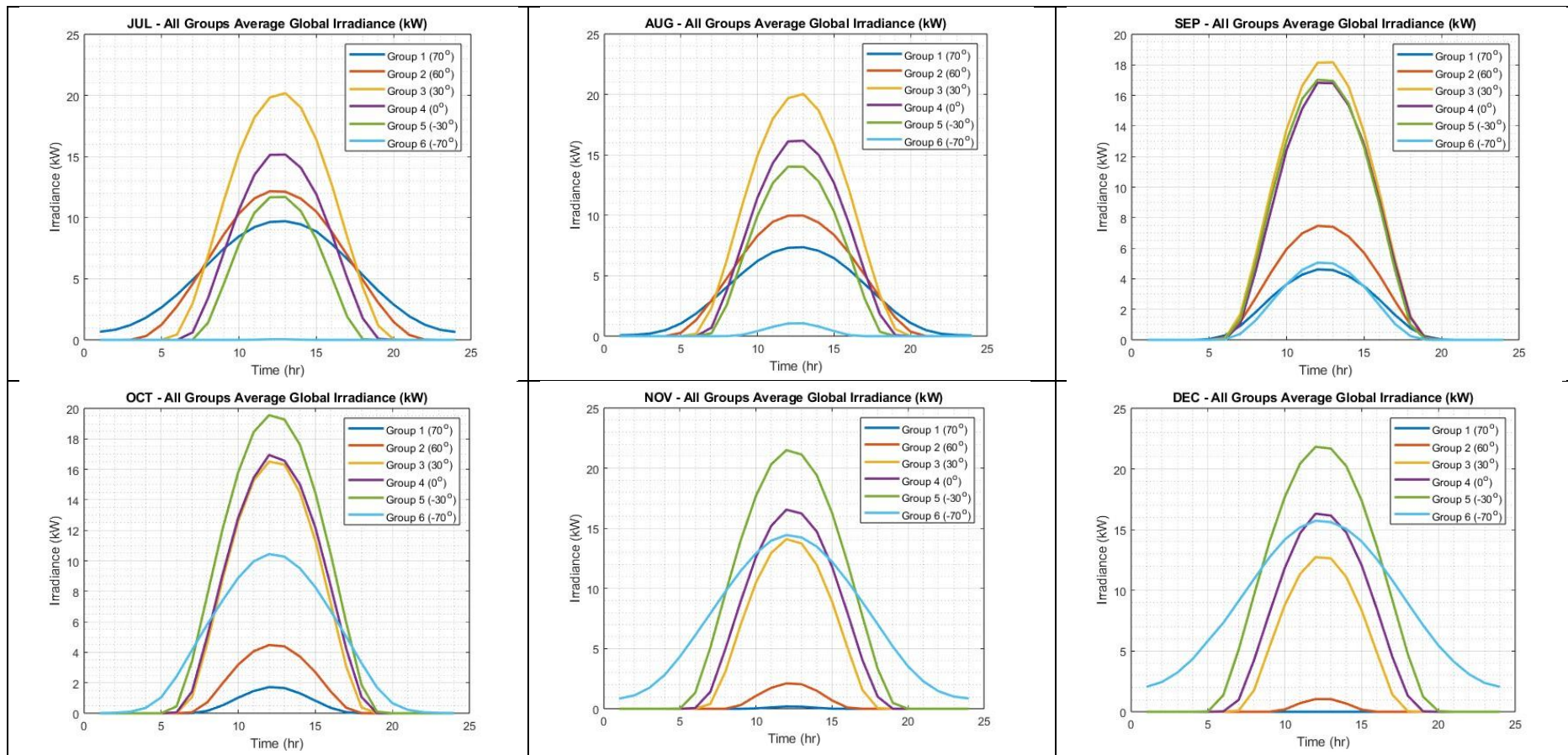
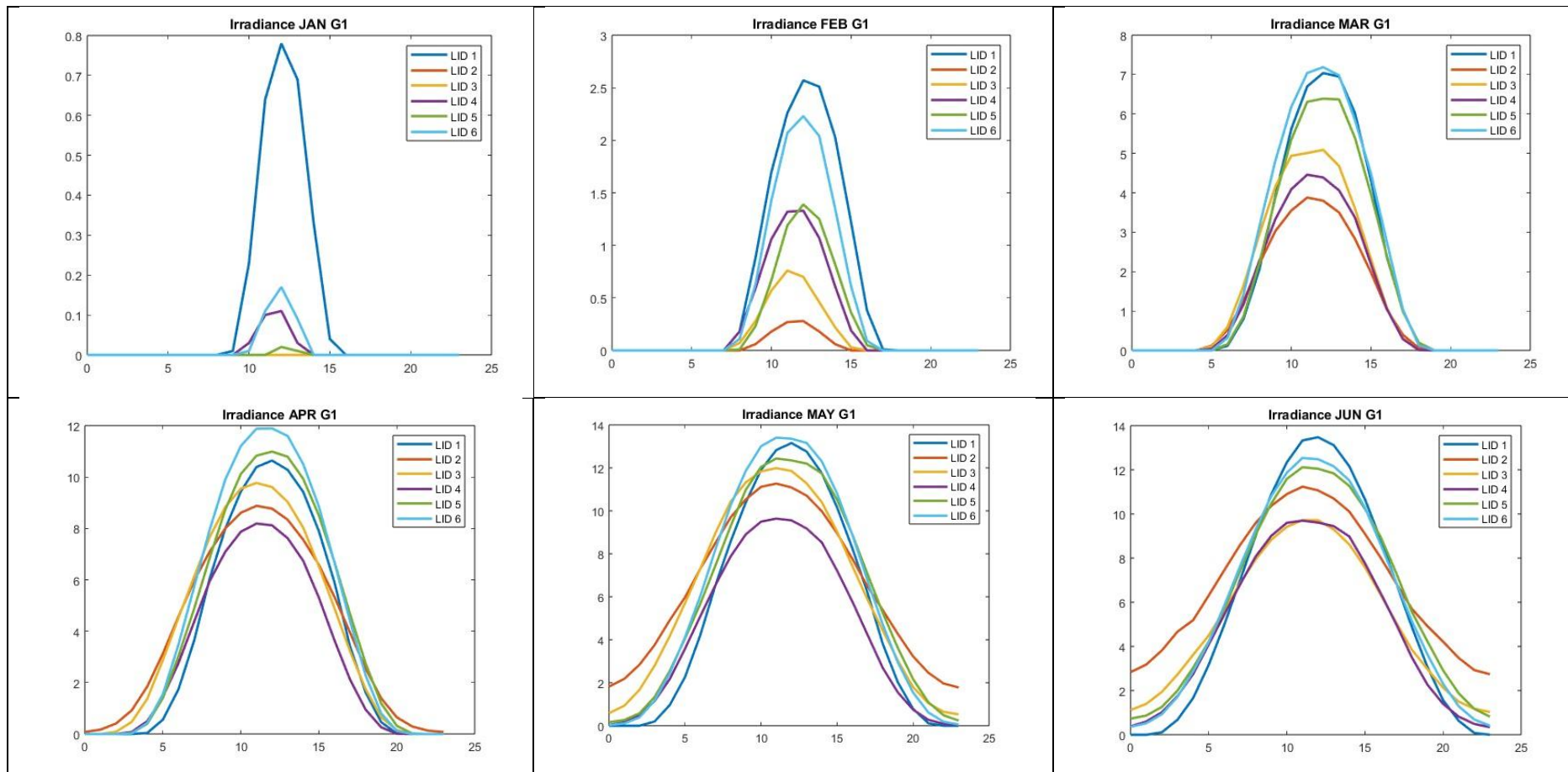


Table 9: Group 1 average hourly irradiation per day for each month.



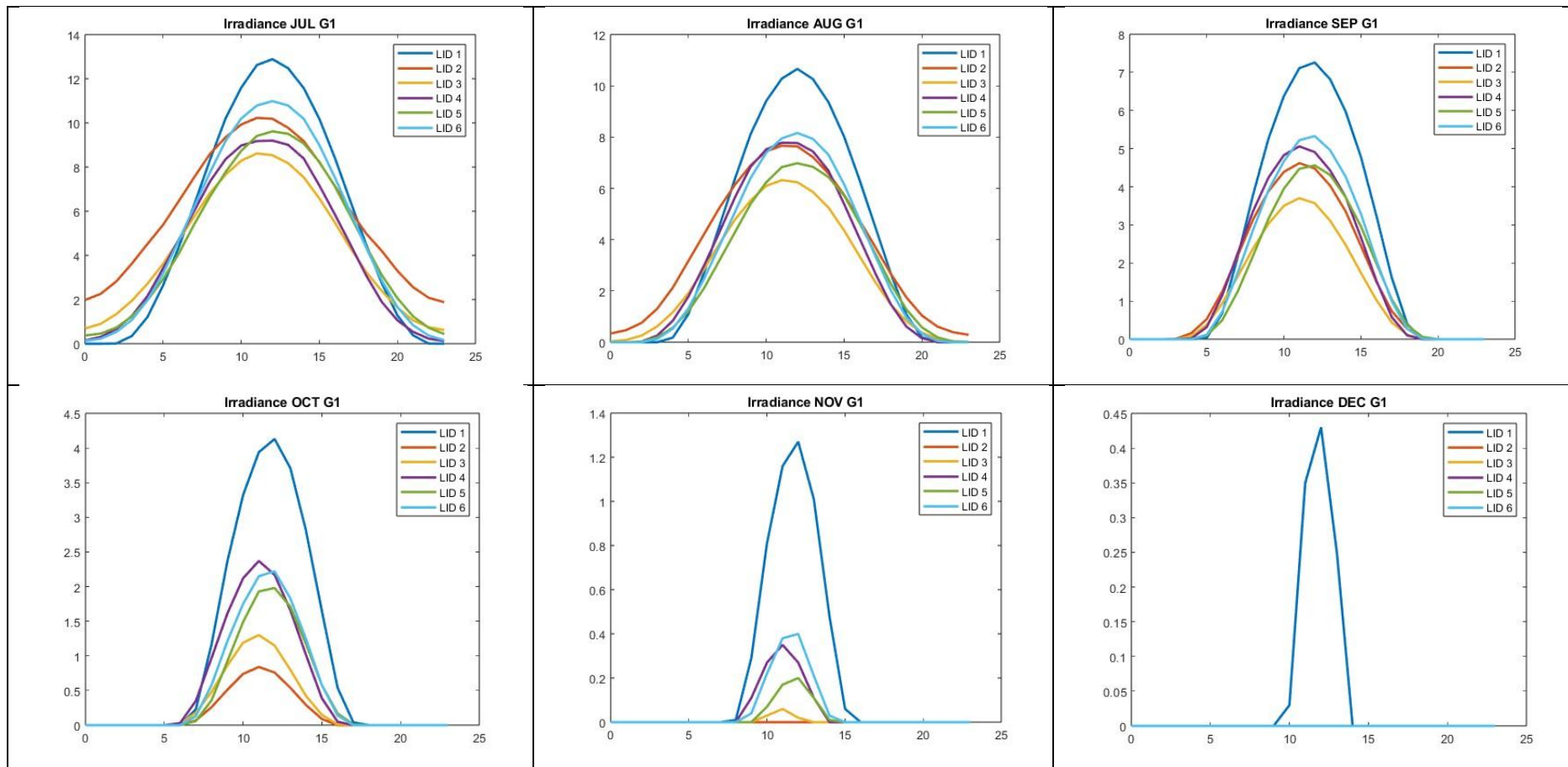
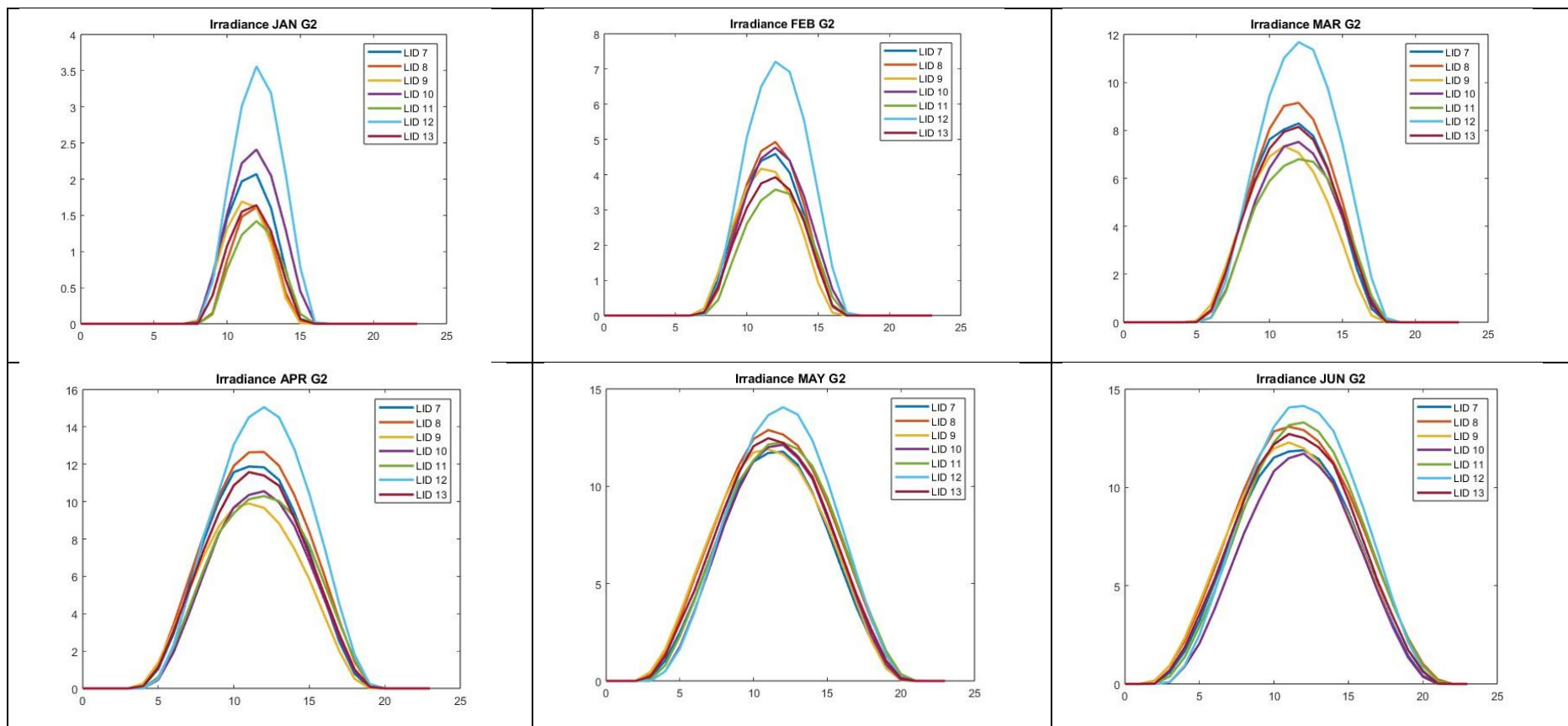


Table 10: Group 2 average hourly irradiation per day for each month



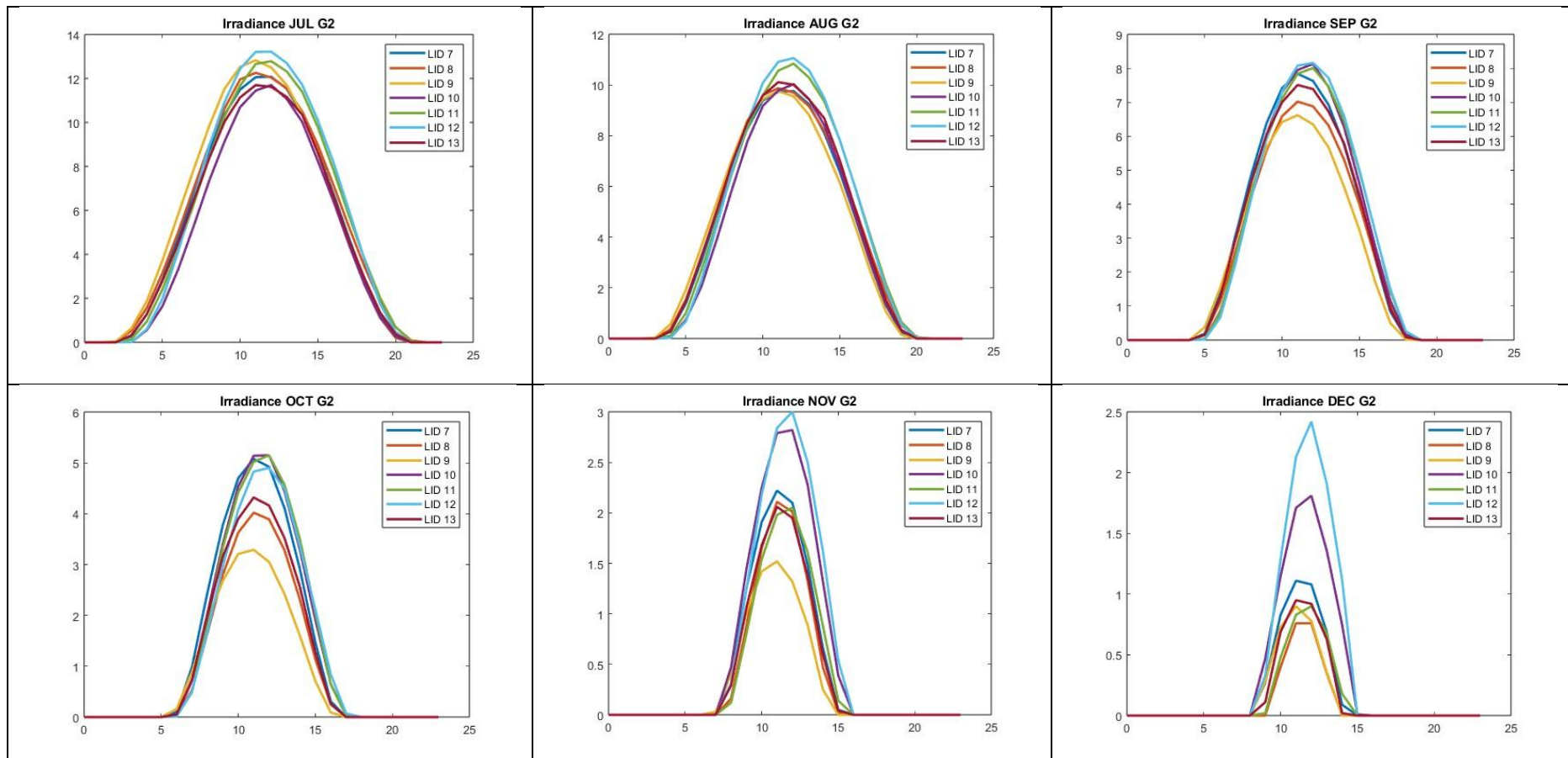
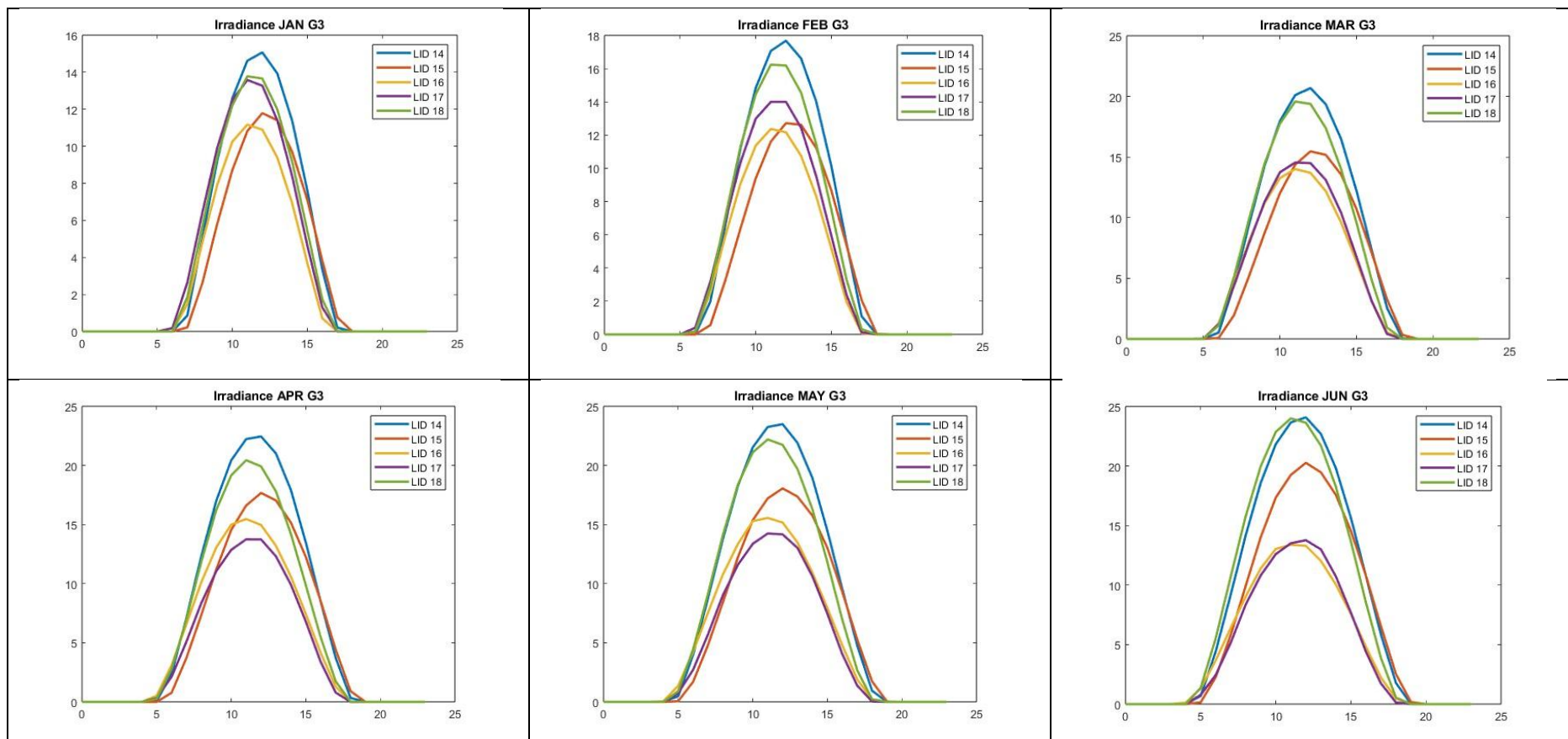


Table 11: Group 3 average hourly irradiation per day for each month



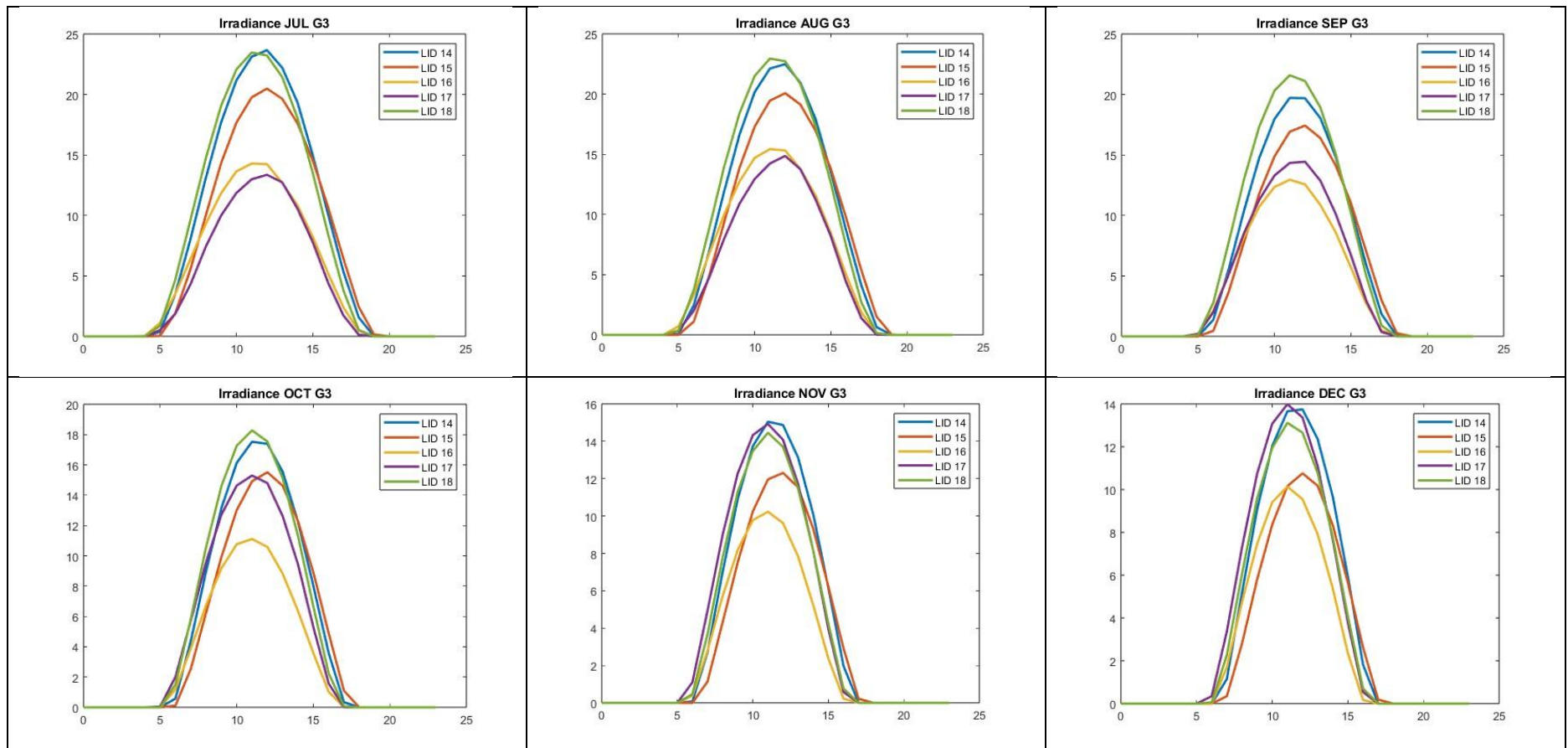
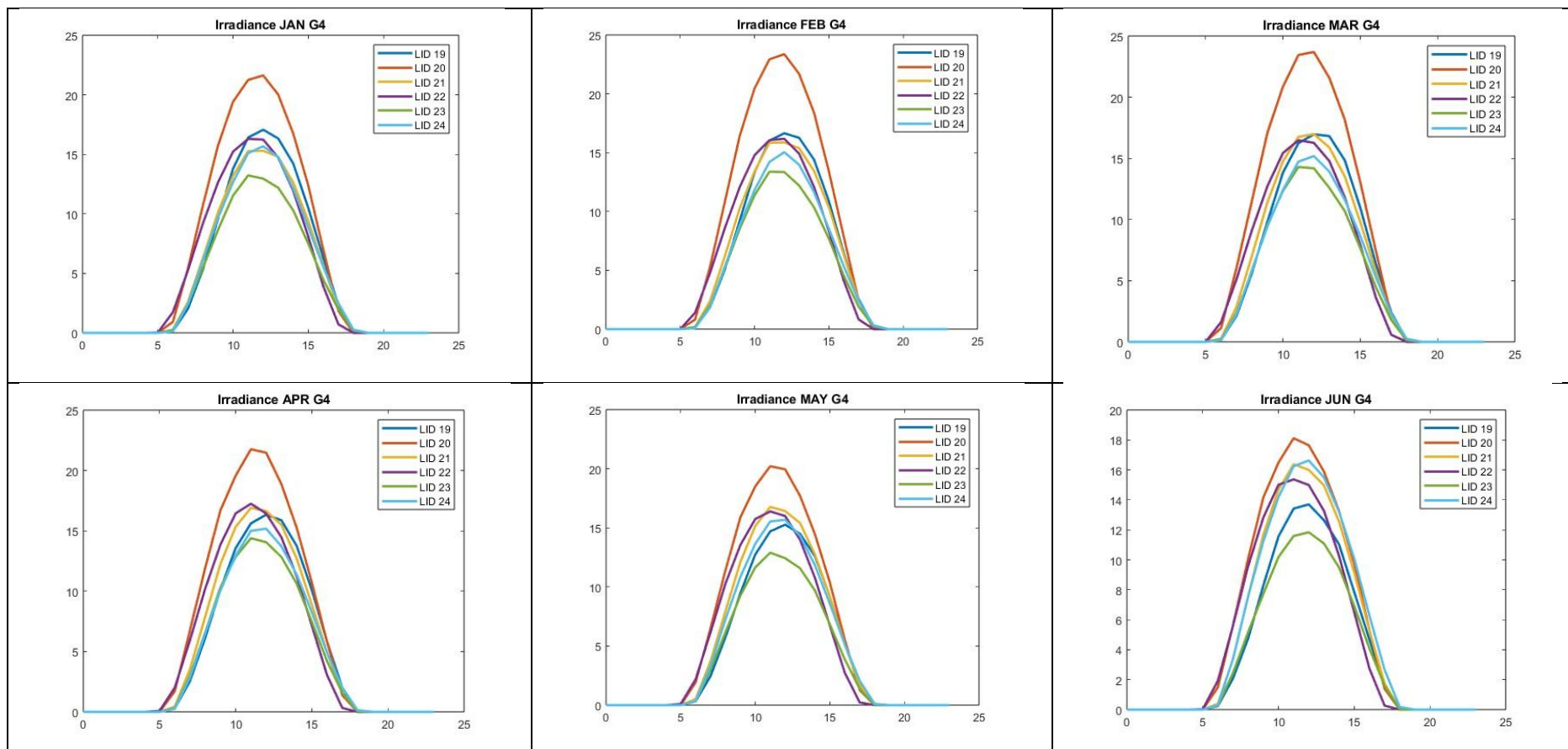


Table 12: Group 4 average hourly irradiation per day for each month



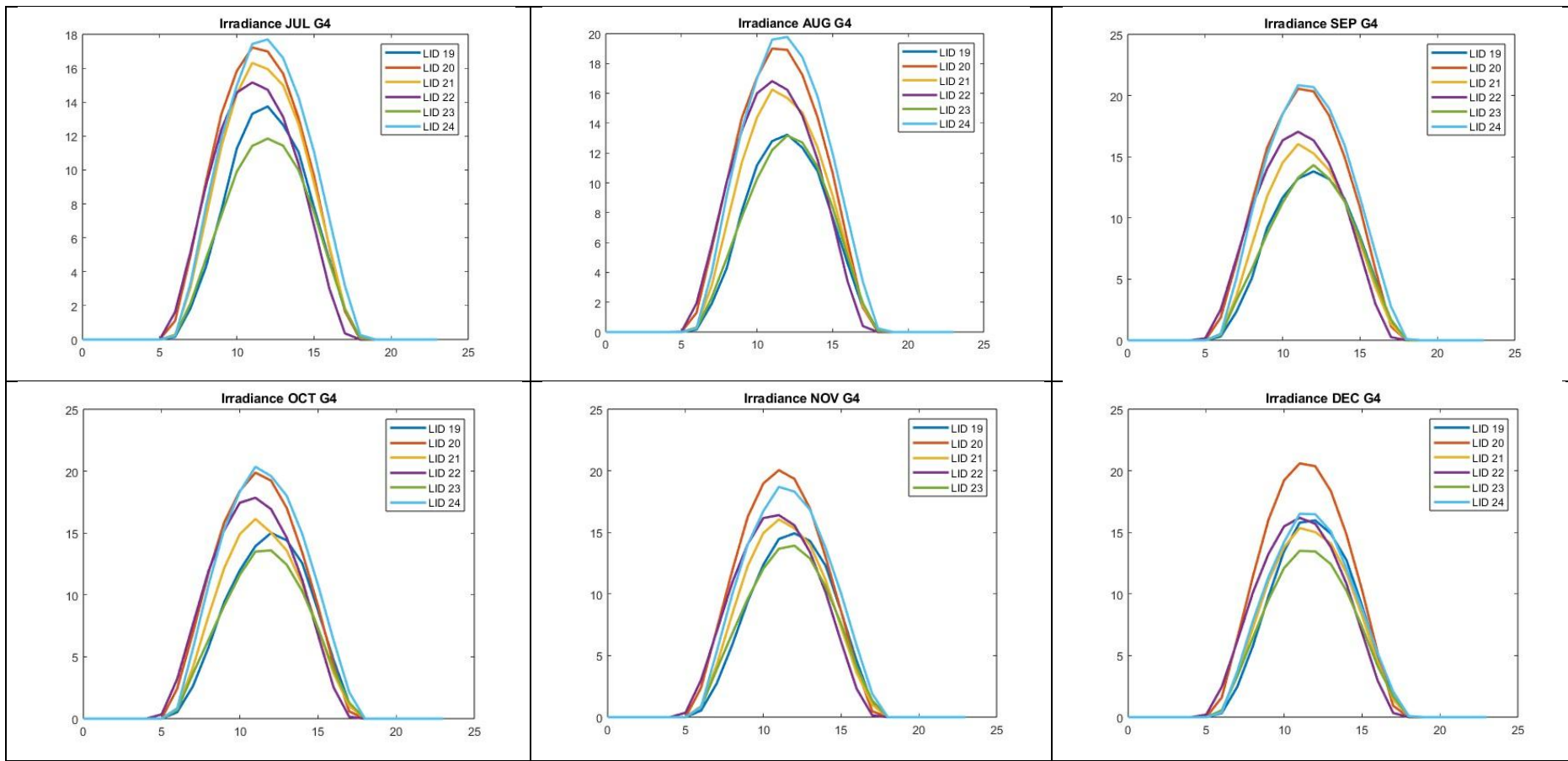
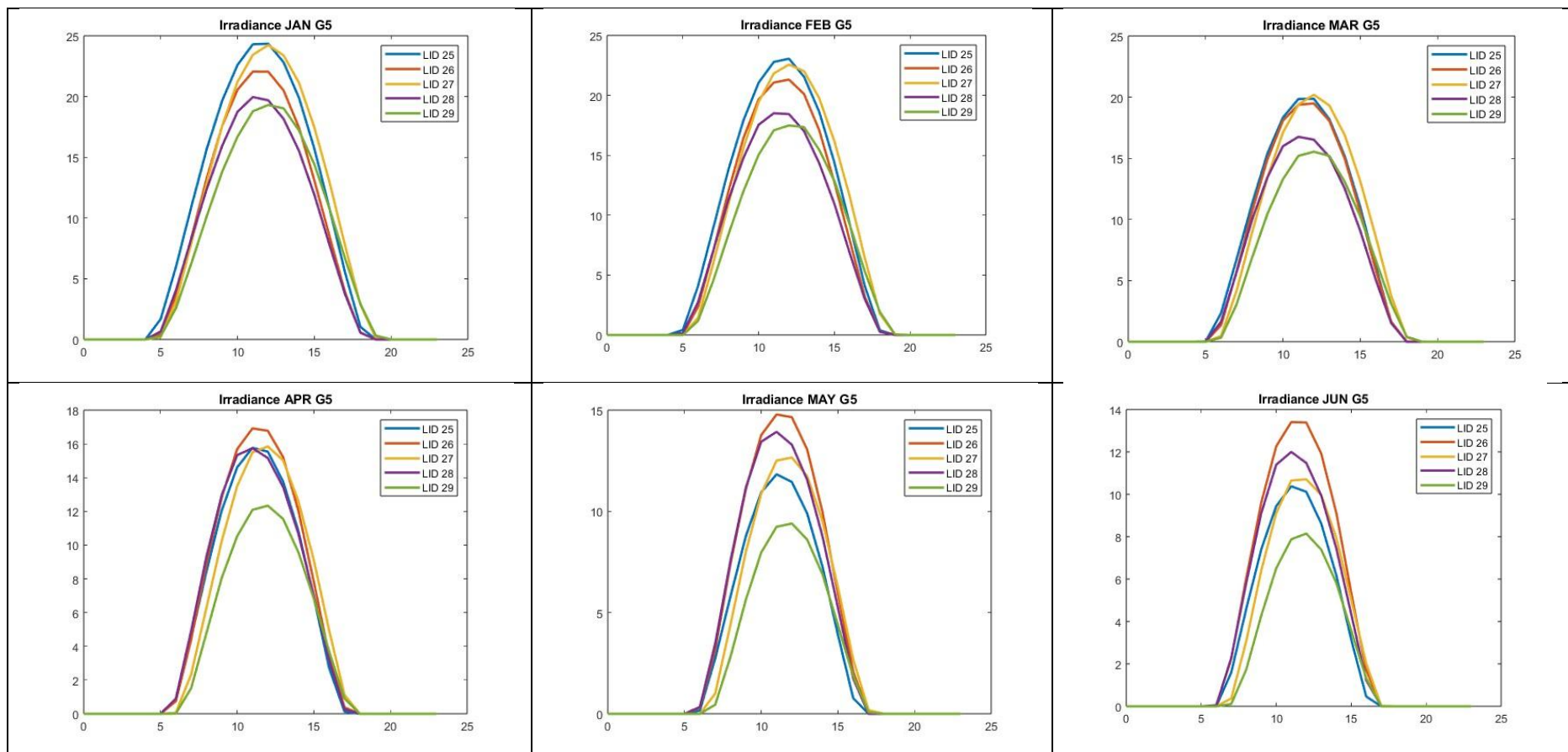


Table 13: Group 5 average hourly irradiation per day for each month



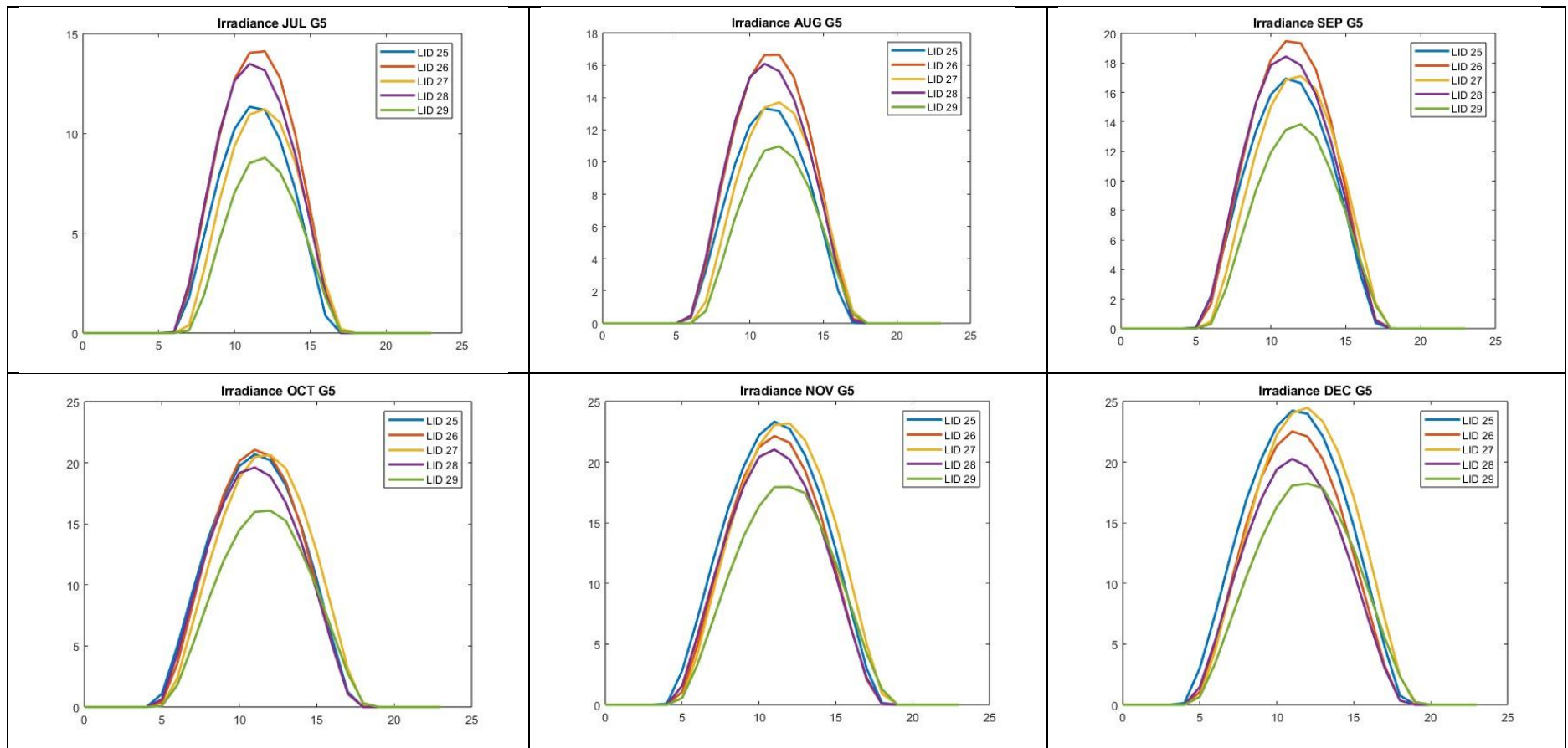
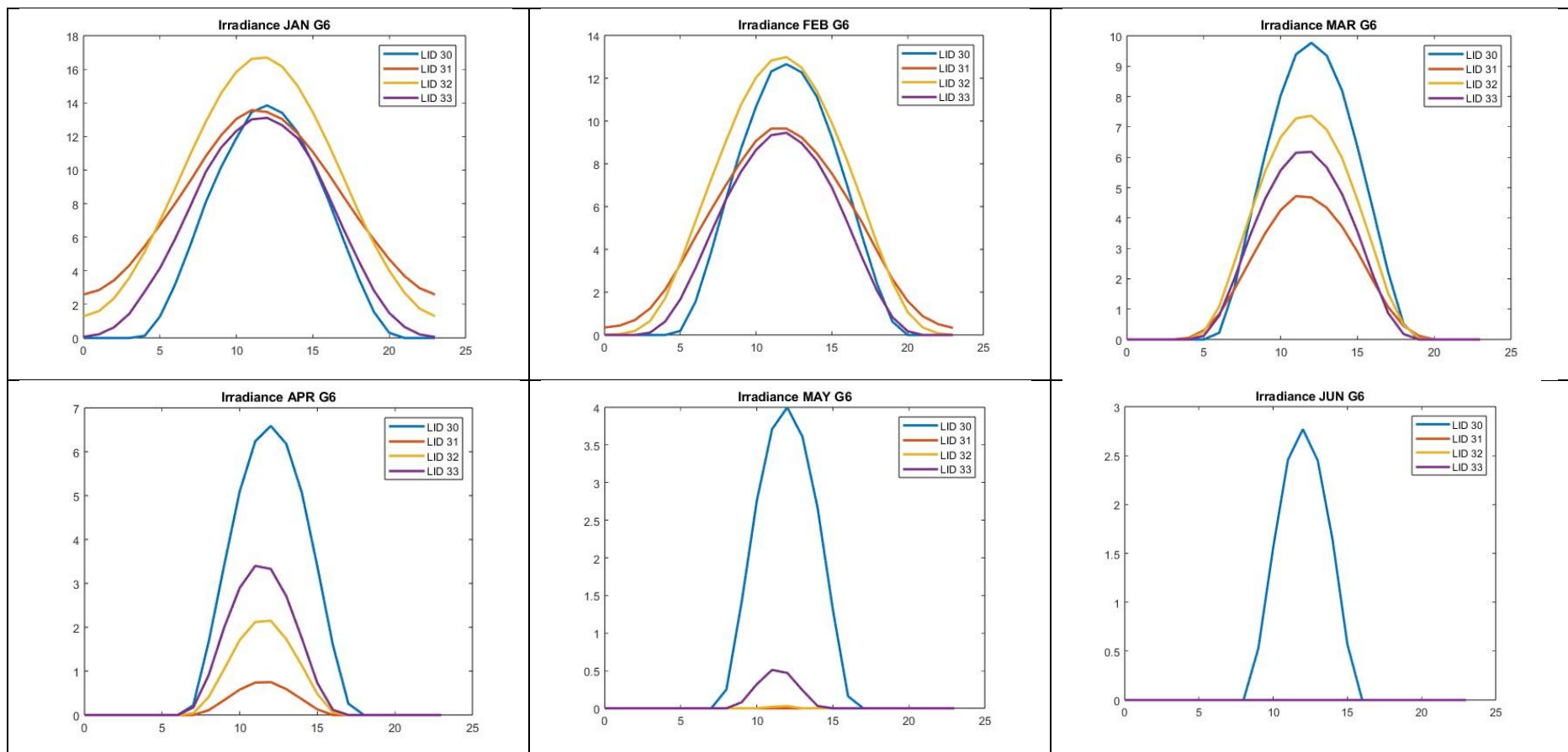
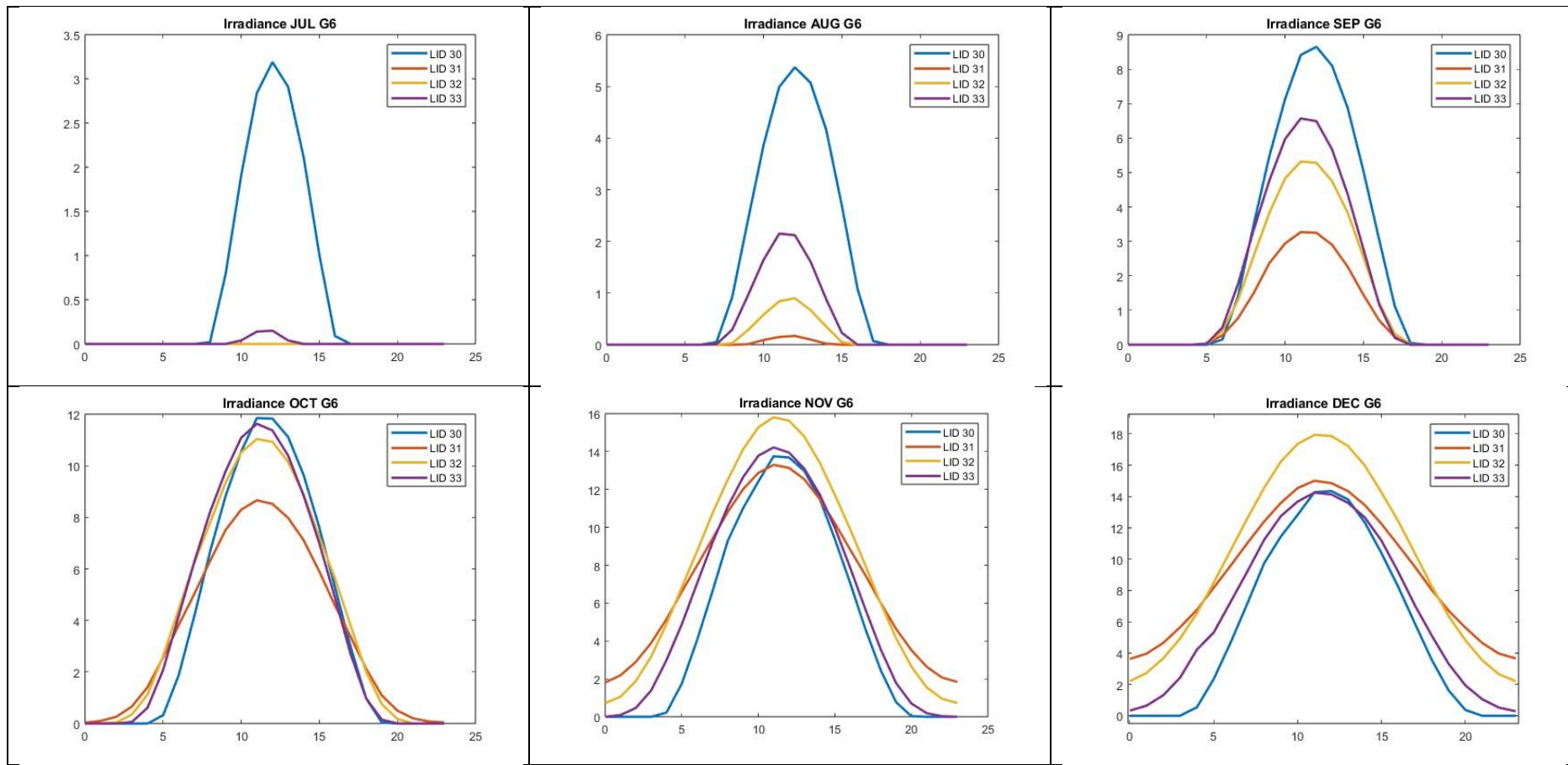
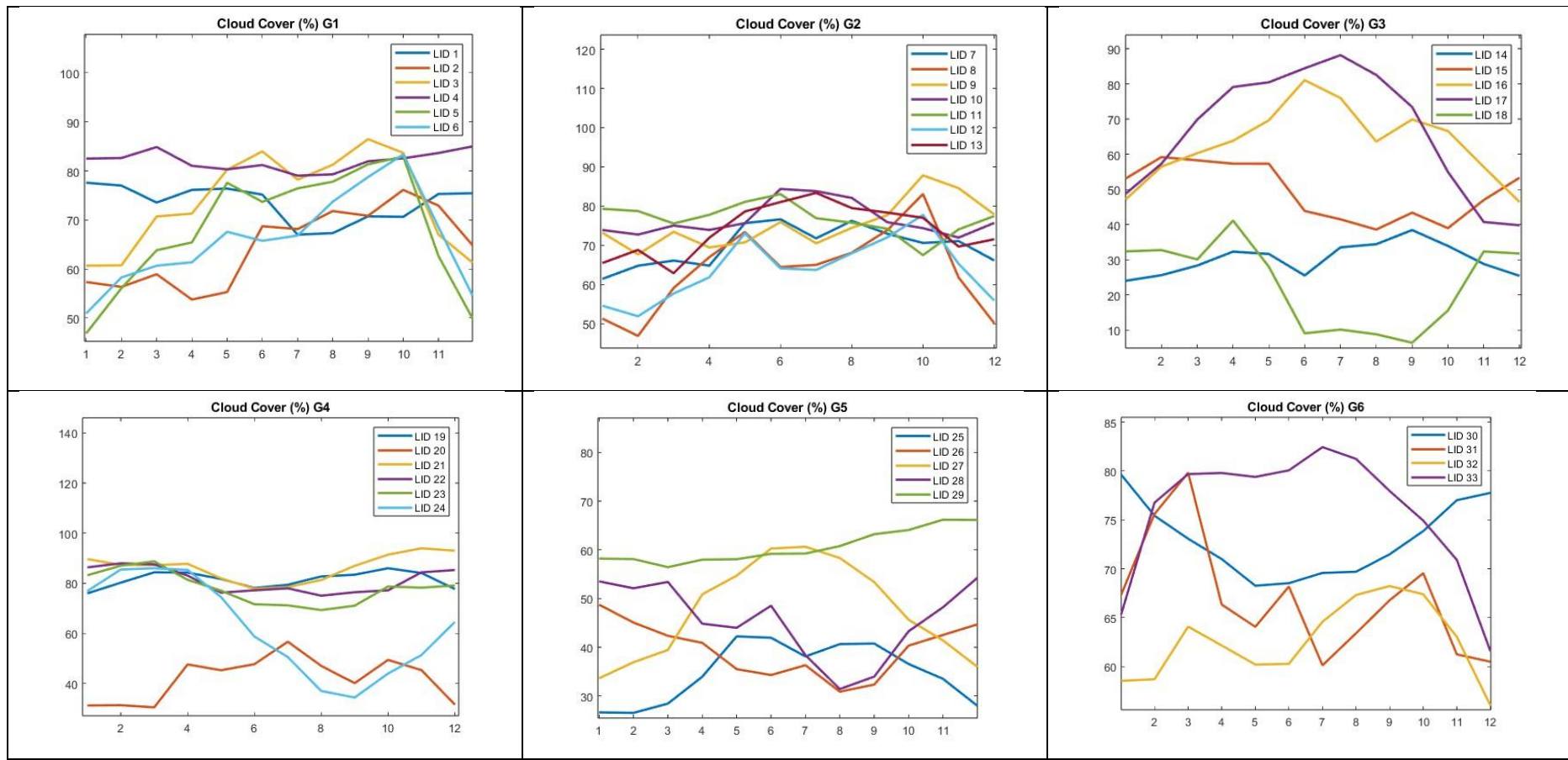
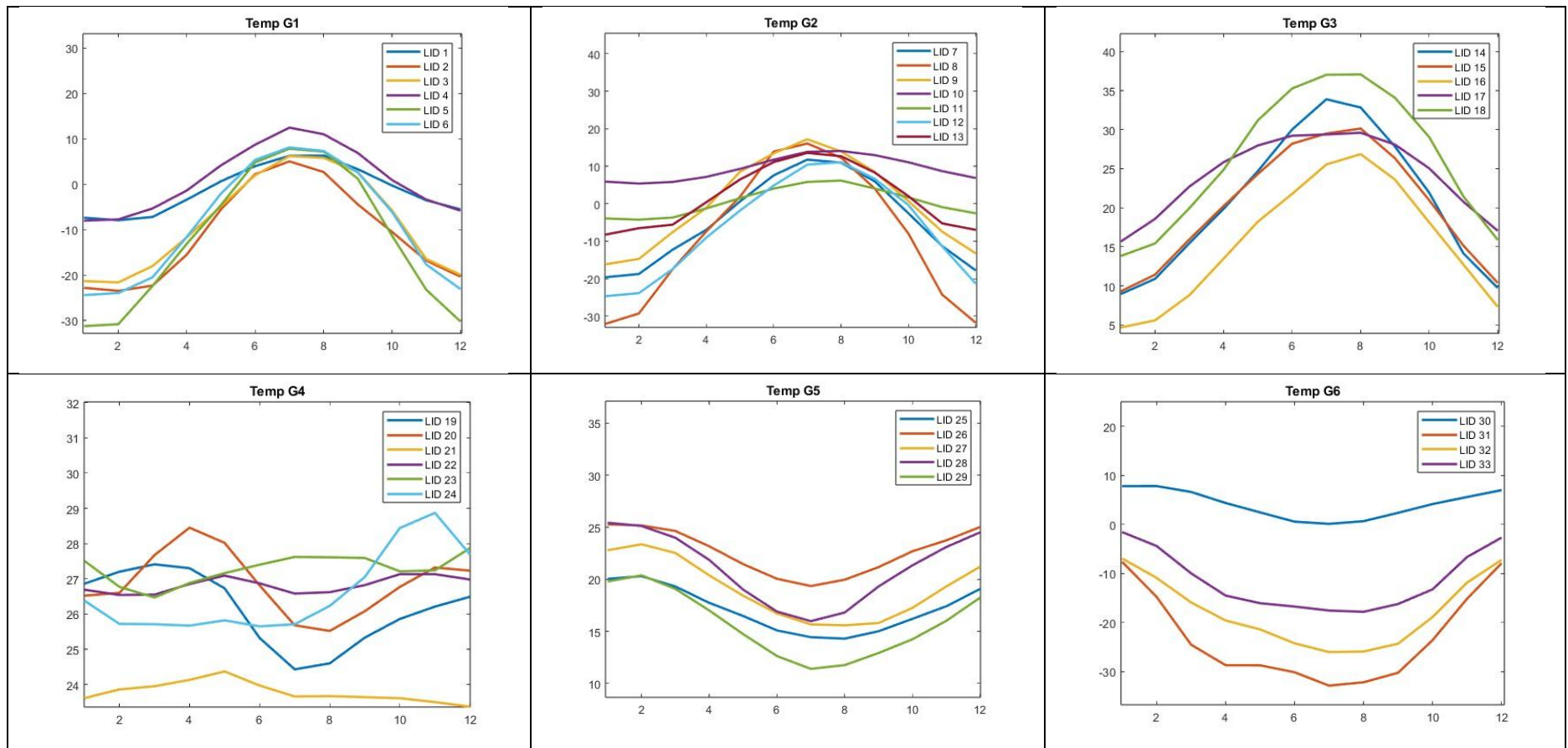


Table 14: Group 6 average hourly irradiation per day for each month



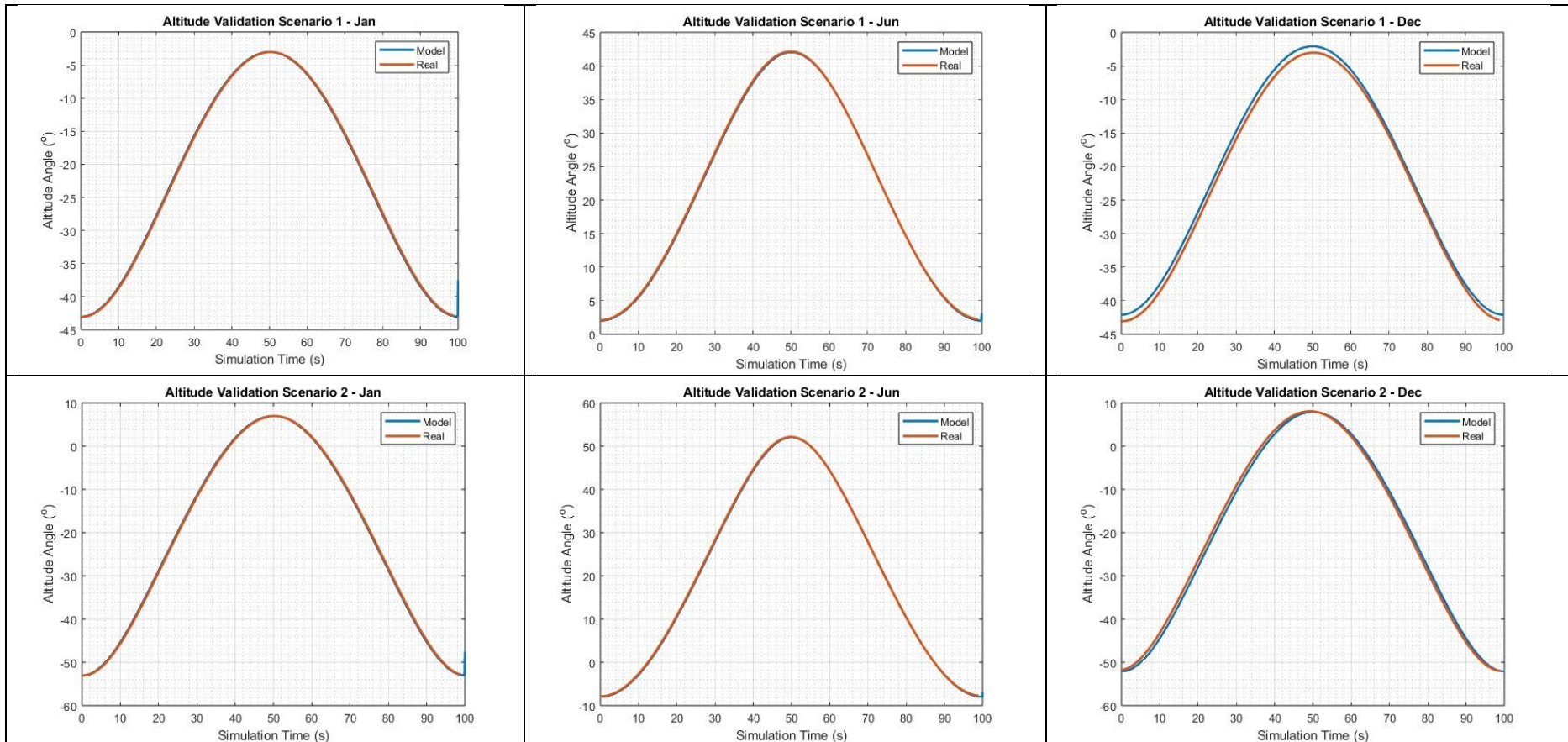


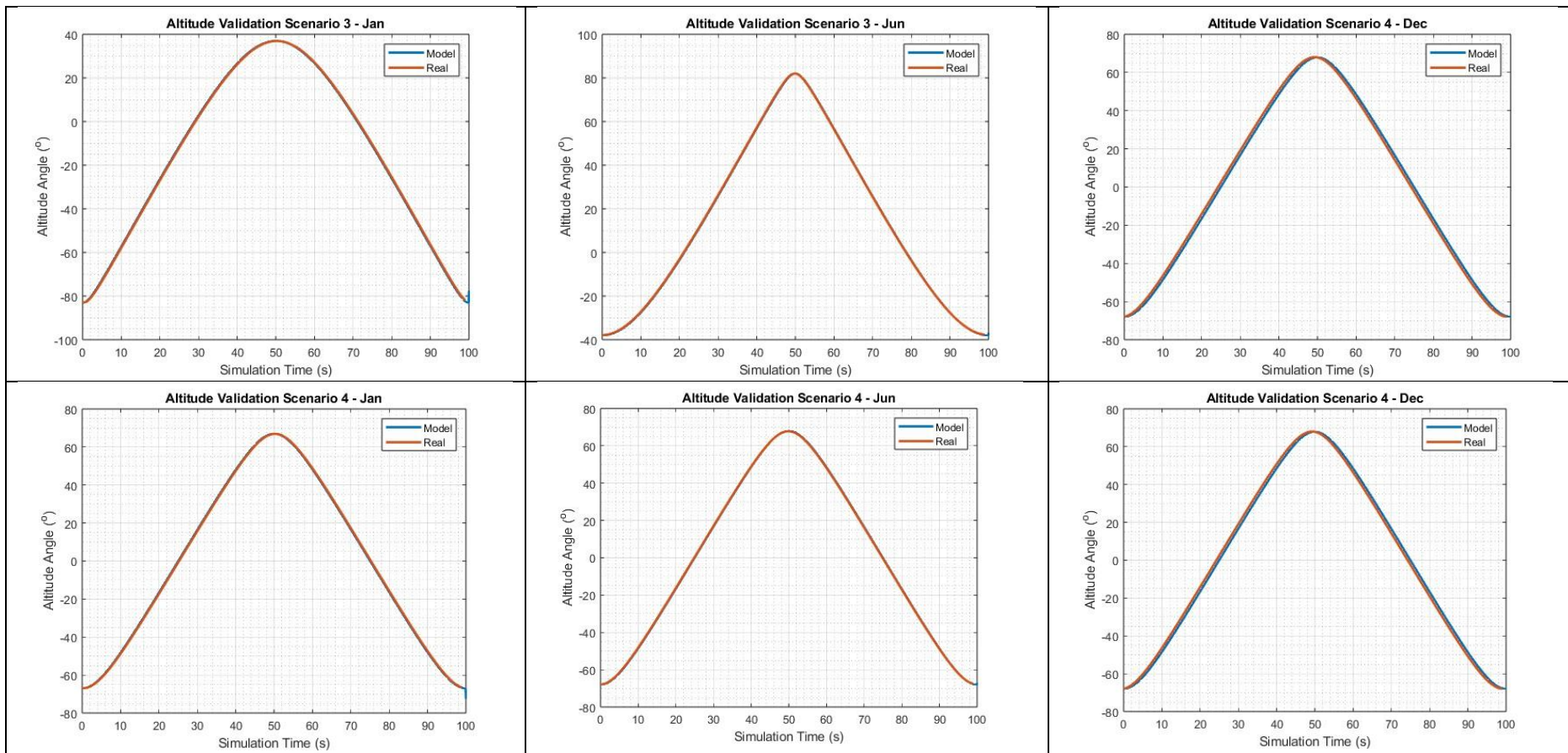




8.2 – Inputs Validation

Table 15: Solar altitude angle validation, real and modelled solar position plotted against simulation time.





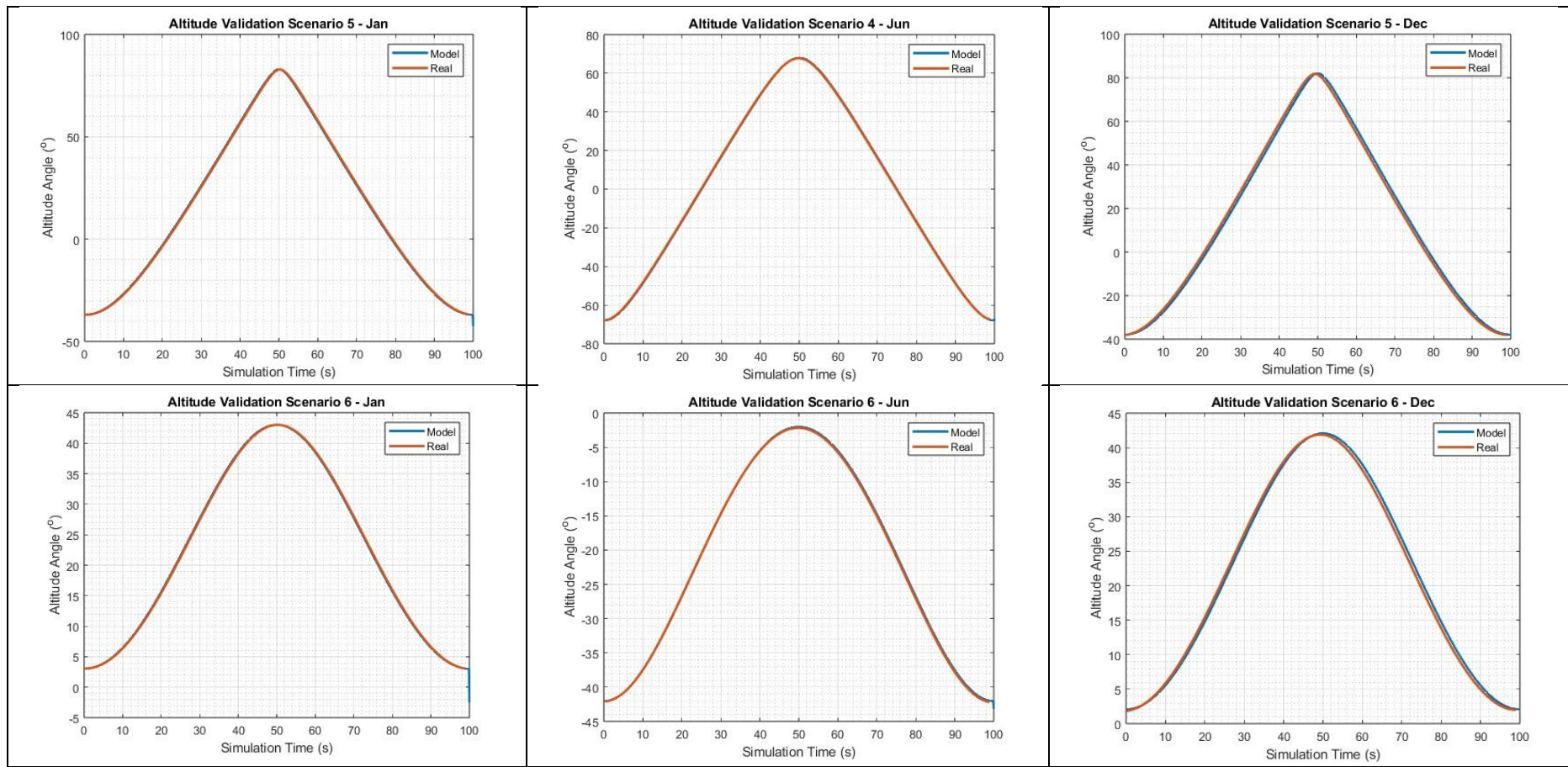
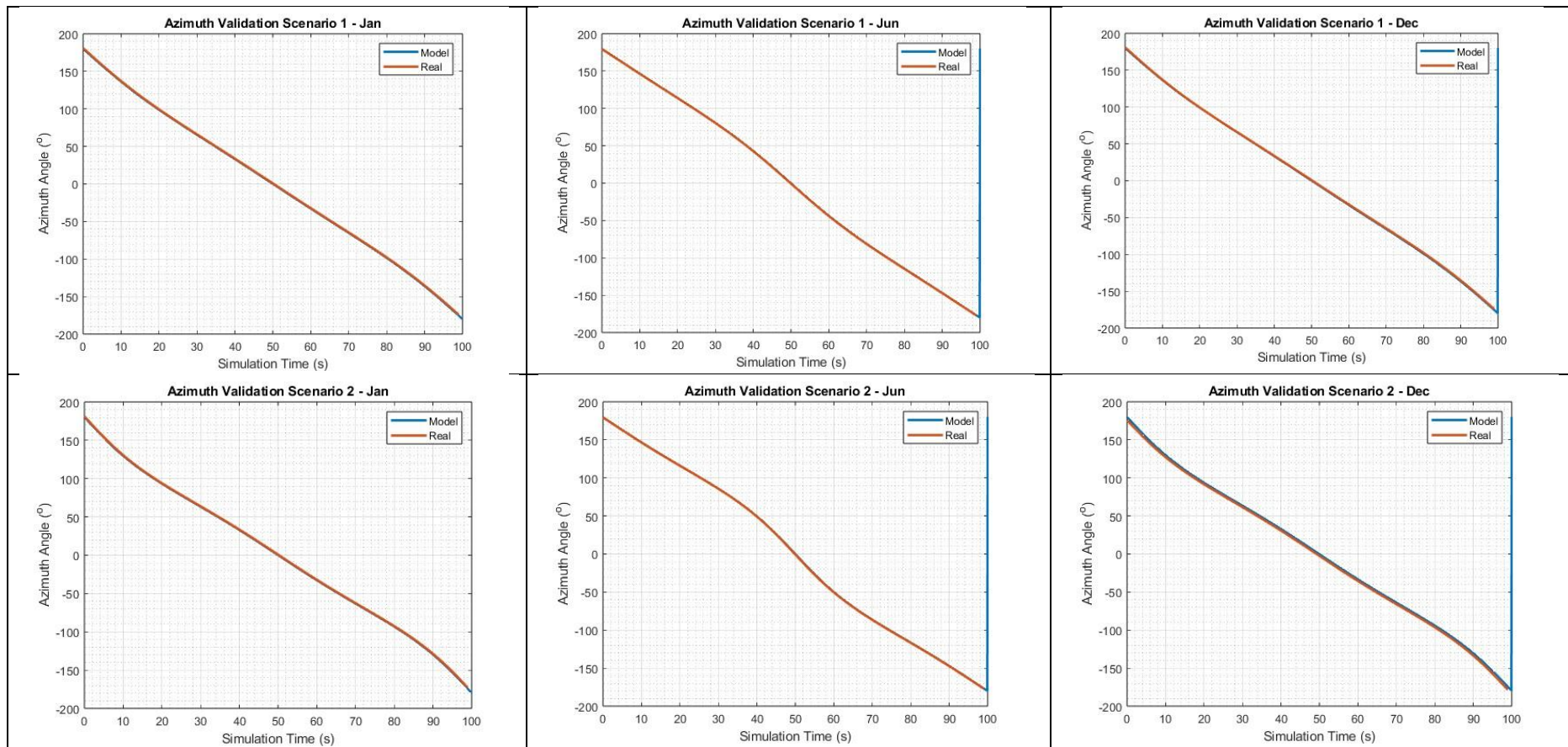
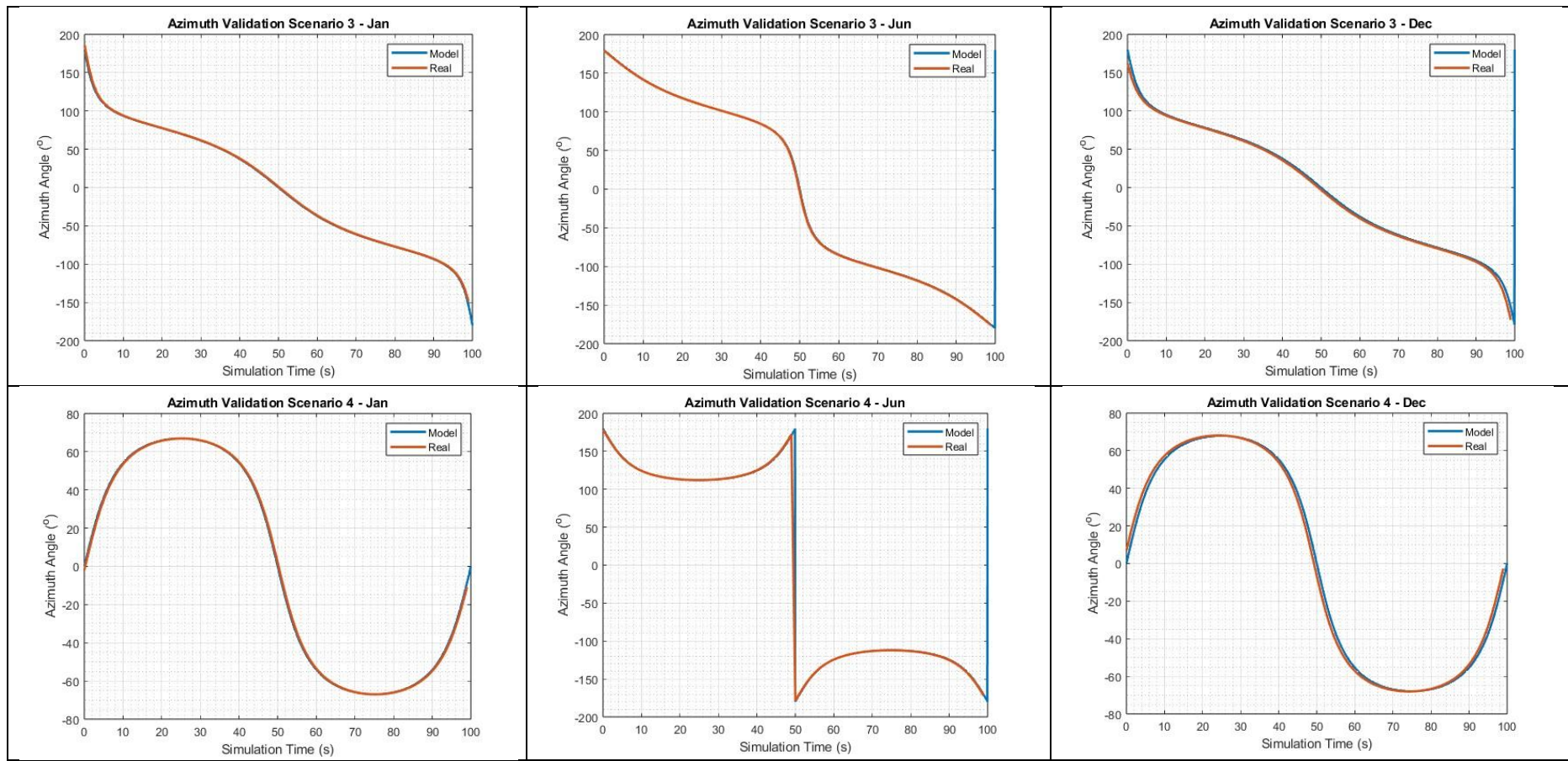
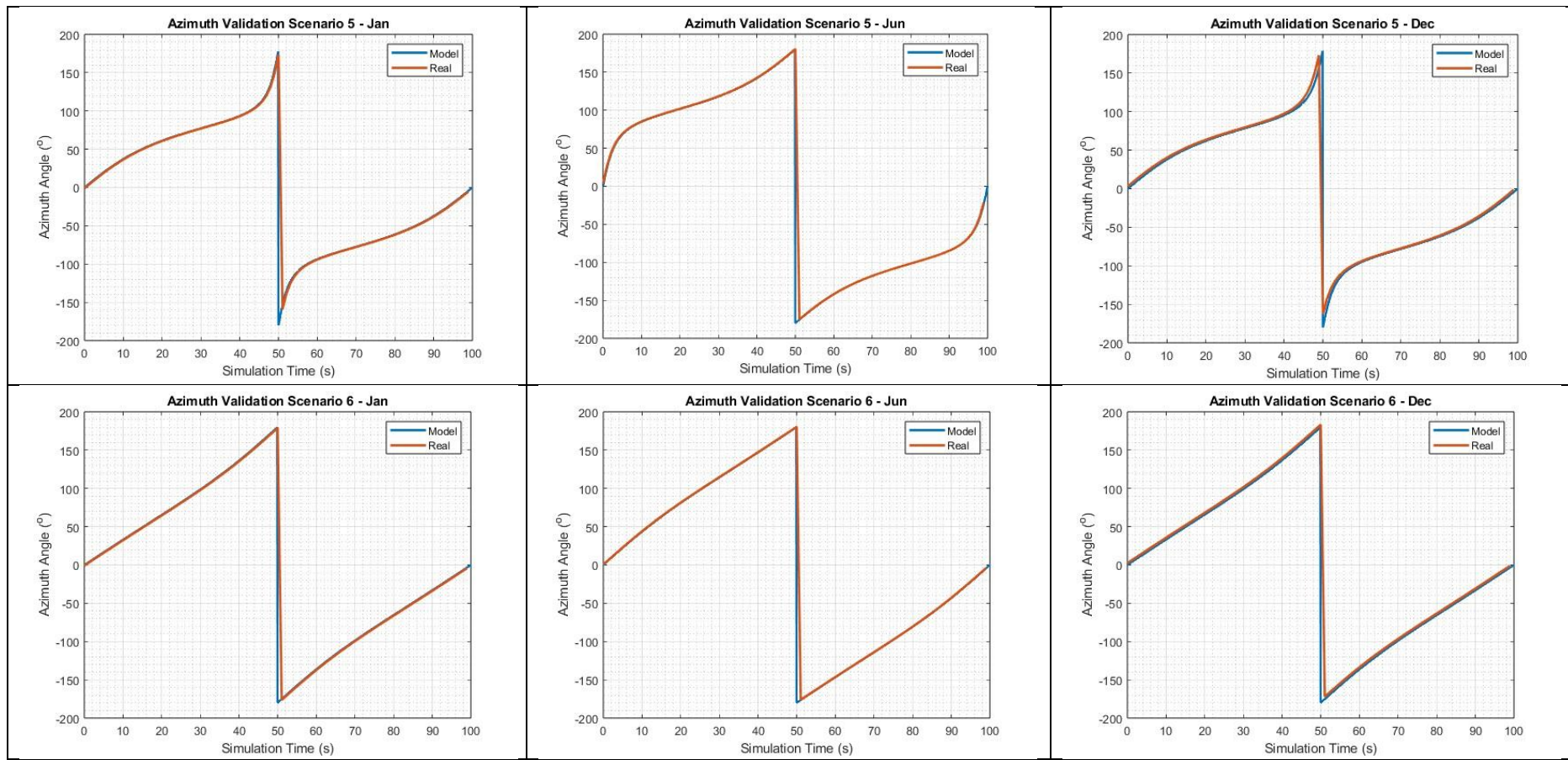


Table 16: Solar azimuth angle validation, real and modelled solar position plotted against simulation time.







8.3 – Solar Inputs (Solar Azimuth, Solar Altitude, Solar Irradiance, ambient temperature)

All inputs are derived from an excel document and an initialisation MATLAB script. The excel document is populated with data extracted from NASA's power DAV data source. Each sheet in the excel document is referenced to the location identified detailed in 10.1. for example, LID 1 (Location Identifier 1) holds data corresponding to Nuuk, Greenland. This pattern is repeated for all LIDs. This allows the MATLAB code to identify the correct sheet of the Excel document to extract the data values from, in order to store their values in MATLAB variables. The Simulink model is also paired to a MATLAB application. This application contains tuneable parameters for location ID and allow the active scoping of the calculated solar azimuth and altitude angles with respect to the location selected. This application was also used to export the gathered variable signals as timeseries objects.

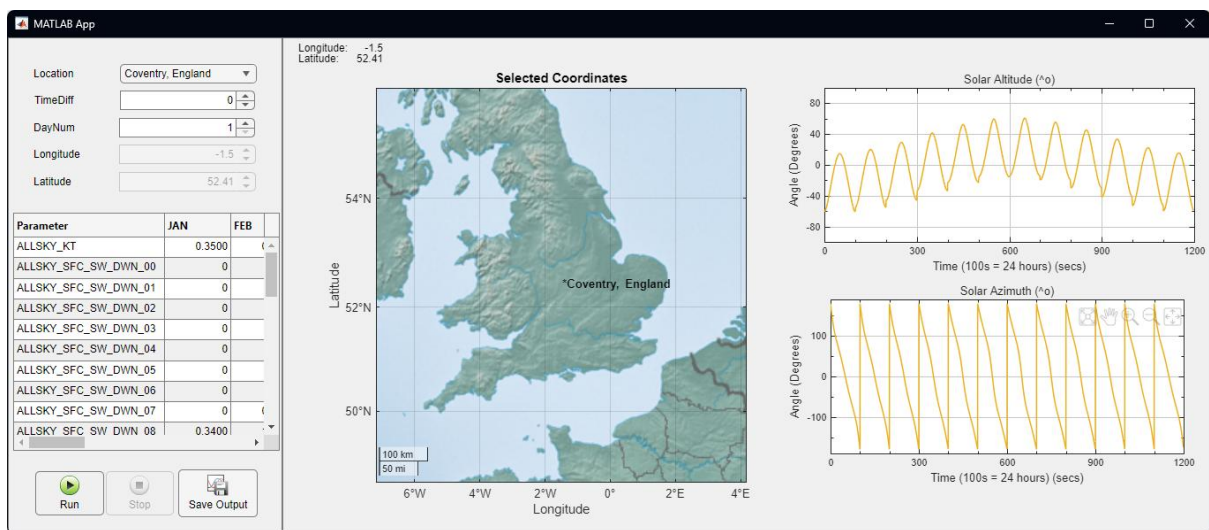


Figure 45: MATLAB application developed for style and ease of input to simulate various positions yearly solar path.

The developed application allows for the selection of any location in the excel lookup table, but is also adaptable to manual input for the simulation of any location based on the input of these latitudinal and longitudinal positions.

The variables are input into the Simulink model as follows:

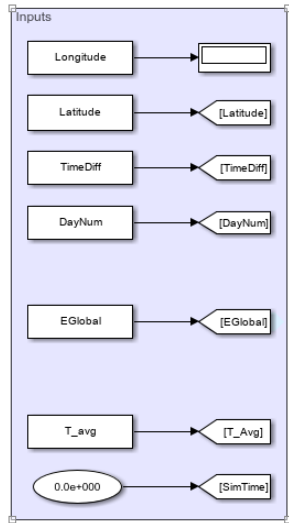


Figure 46: Simulink Model Inputs

These inputs are interpreted by the following sections of the same model,

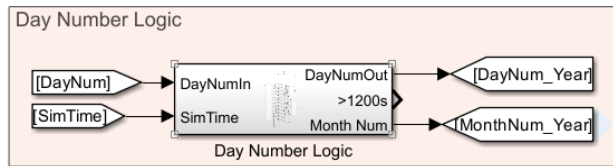


Figure 47: Day Number Logic - used to iterate the day number based on the chosen input. This is limited between 1-28, to simulate the 1-28 day of each month (i.e. if 3rd is selected, the 3rd of January is simulated, the 3rd of February is simulated and so on.)

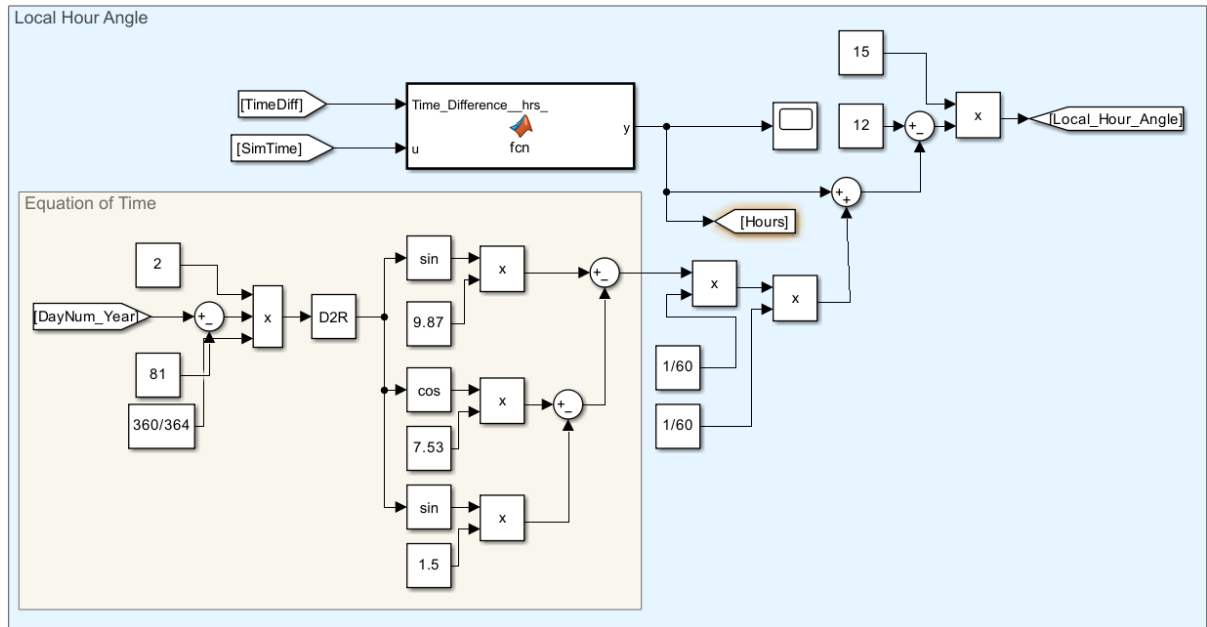


Figure 48: Calculation of the local hour angle based on the same inputs with a MATLAB function converting between simulation time and real observed time.

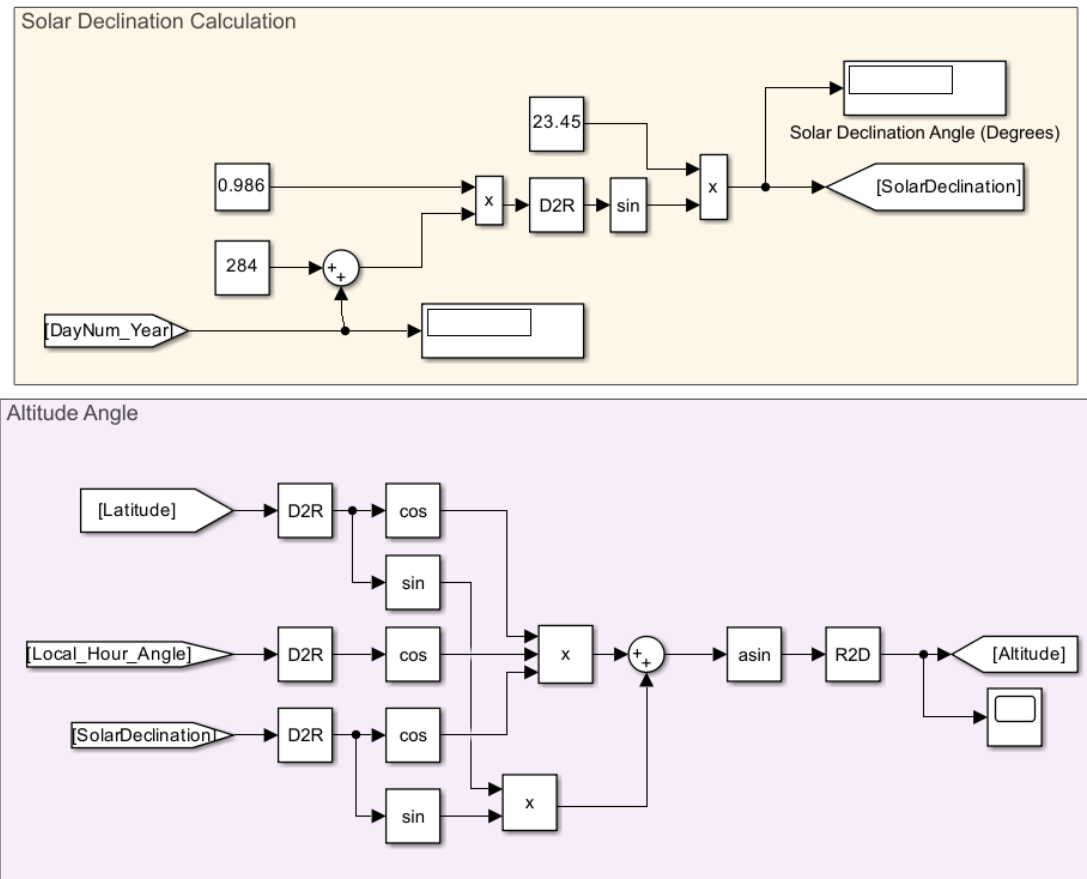


Figure 49: Solar declination based on the simulated date in the year, and altitude angle resultant of the previously described models.

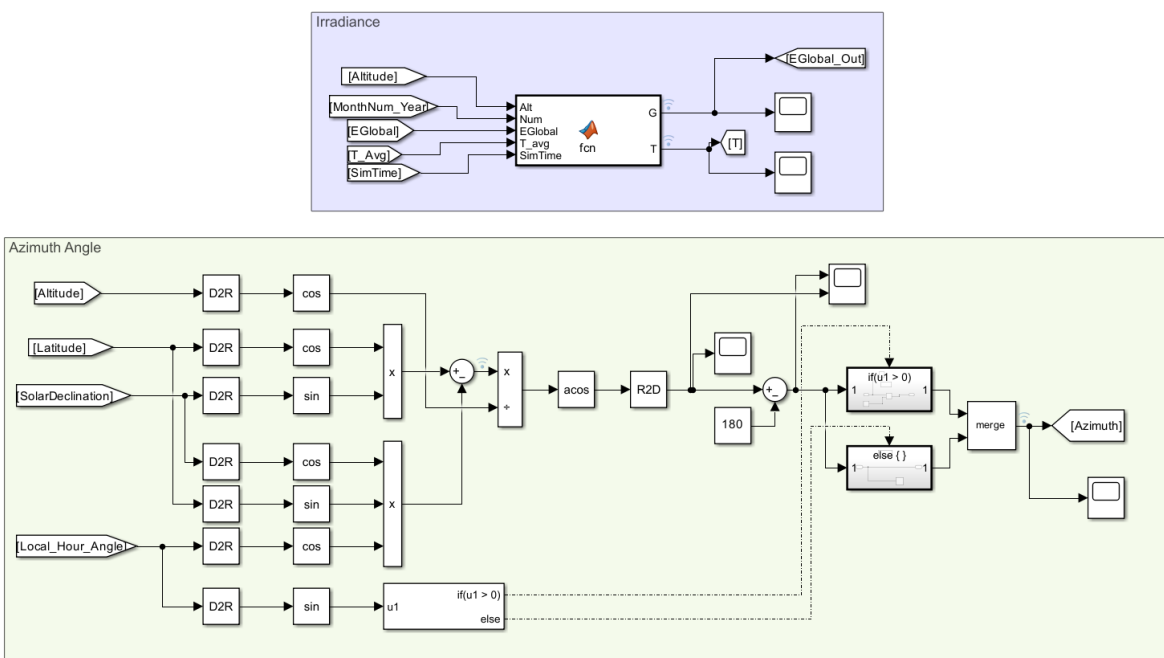


Figure 50: Solar irradiance, derived from the aforementioned excel document, converting the global irradiance array into a timeseries signal, and the average ambient temperature likewise.

And finally outputs the logged signals as follows:

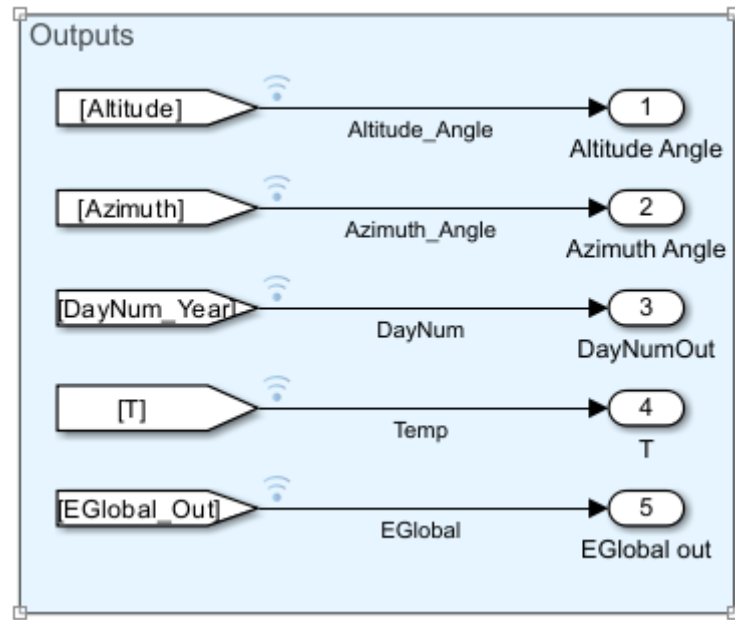


Figure 51: Output signals of the simulation.

To form a final Simulink inputs model as follows:

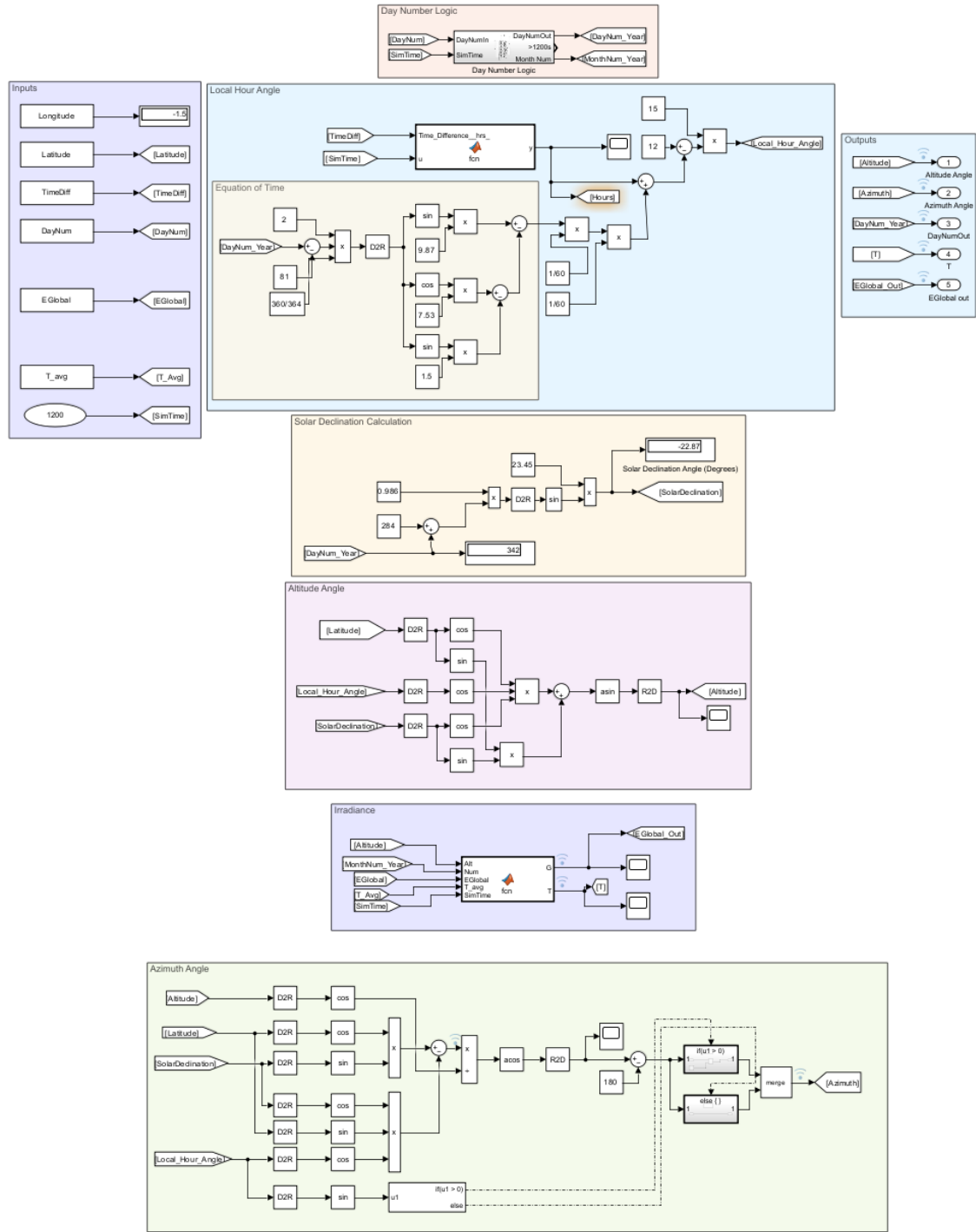


Figure 52: Entire derived Simulink model for solar position and irradiance signal construction.

These signals are fed into the final simulation model as a scenario structure, which can be immediately interpreted by a signal editor block to output the timeseries with respect to the simulation time.

8.4 – PV Model

8.4.1 – PV Model Simulink

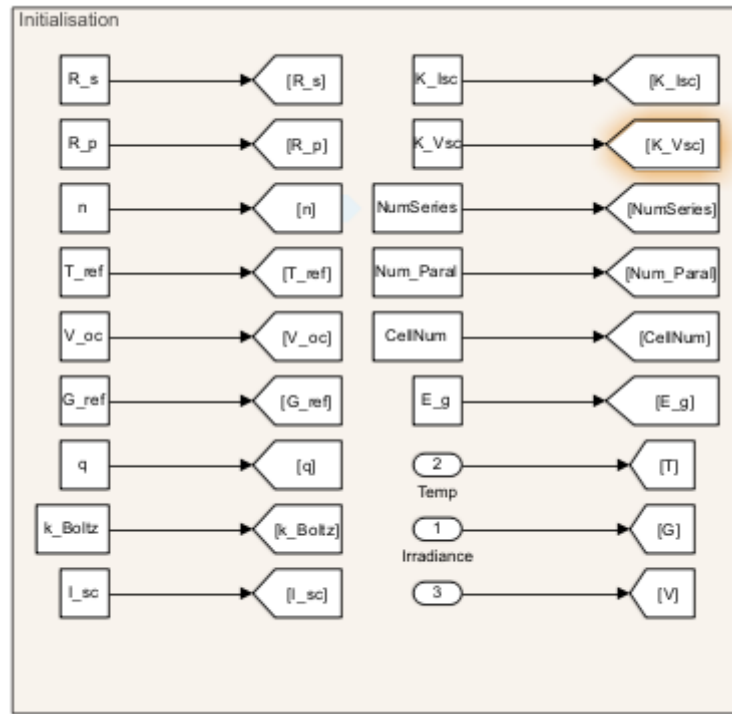


Figure 53: Intialisation of parameters, importing the variables as they were loaded in via MATLAB and sending their values to "GoTo" blocks.

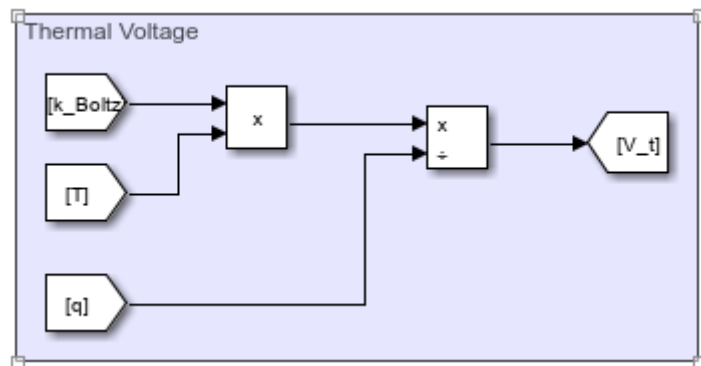


Figure 54: Thermal Voltage calculated as per Eq. 1 in 4.2.1 – Photovoltaic Cell Model.

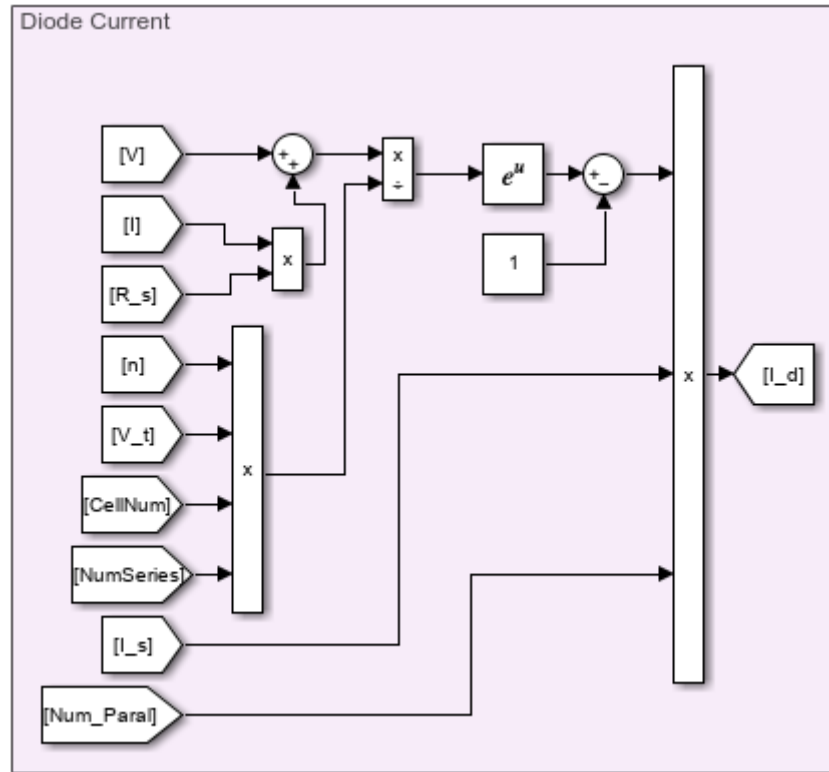


Figure 55: Diode current block diagram built in Simulink using Eq.2 in section 4.2.1 - Photovoltaic Cell Model

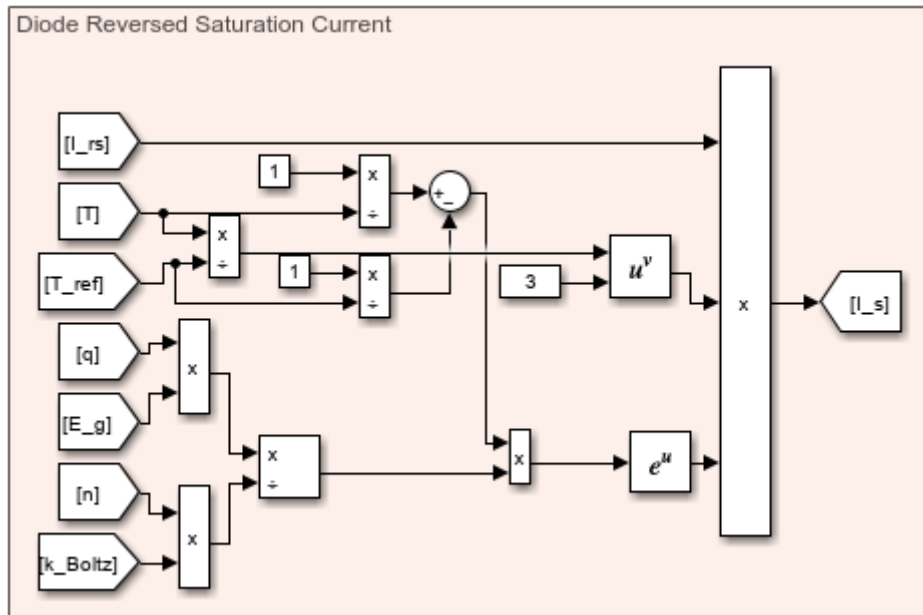


Figure 56: Diode reversed saturation current at STC block diagram built in Simulink using Eq.3 in section 4.2.1 - Photovoltaic Cell Model

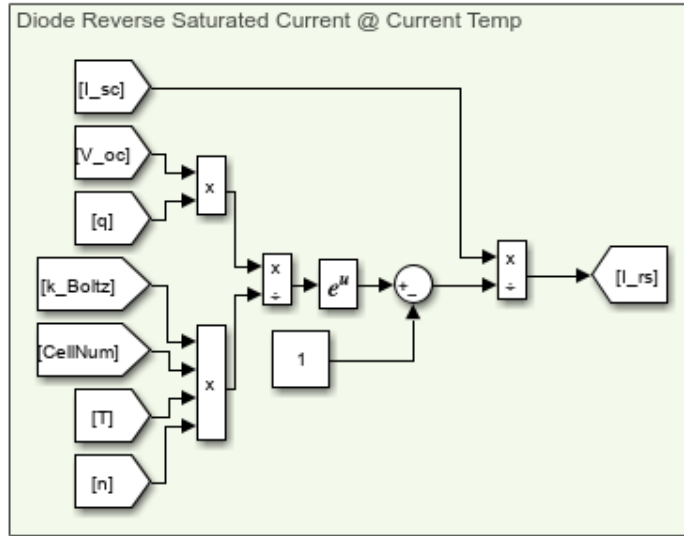


Figure 57: Diode reverse saturation current at observed temperature block diagram built in Simulink using Eq.4 in section 4.2.1 - Photovoltaic Cell Model

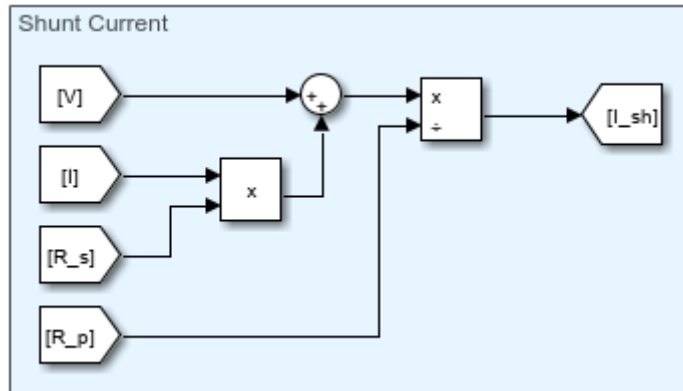


Figure 58: Shunt current block diagram built in Simulink using Eq.5 in section 4.2.1 - Photovoltaic Cell Model

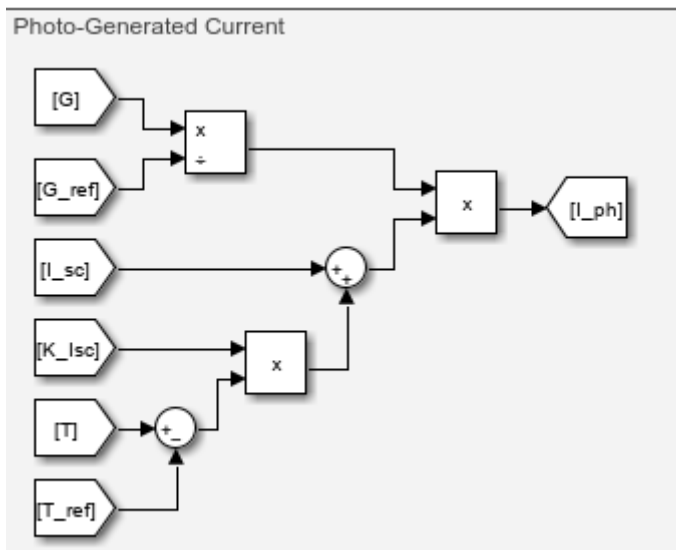


Figure 59: Photon generated current block diagram built in Simulink using Eq.6 in section 4.2.1 - Photovoltaic Cell Model

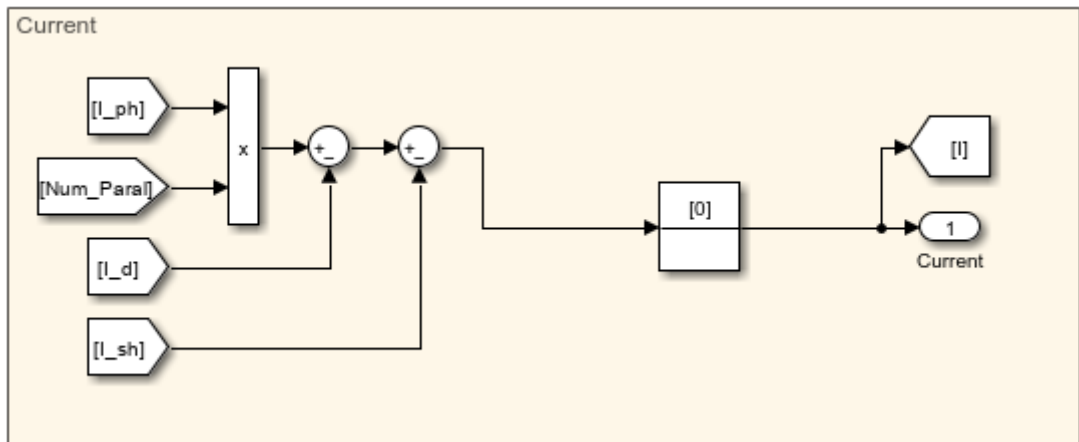


Figure 60: Total output current by the photovoltaic model.

8.4.1a – Full PV Simulink Model

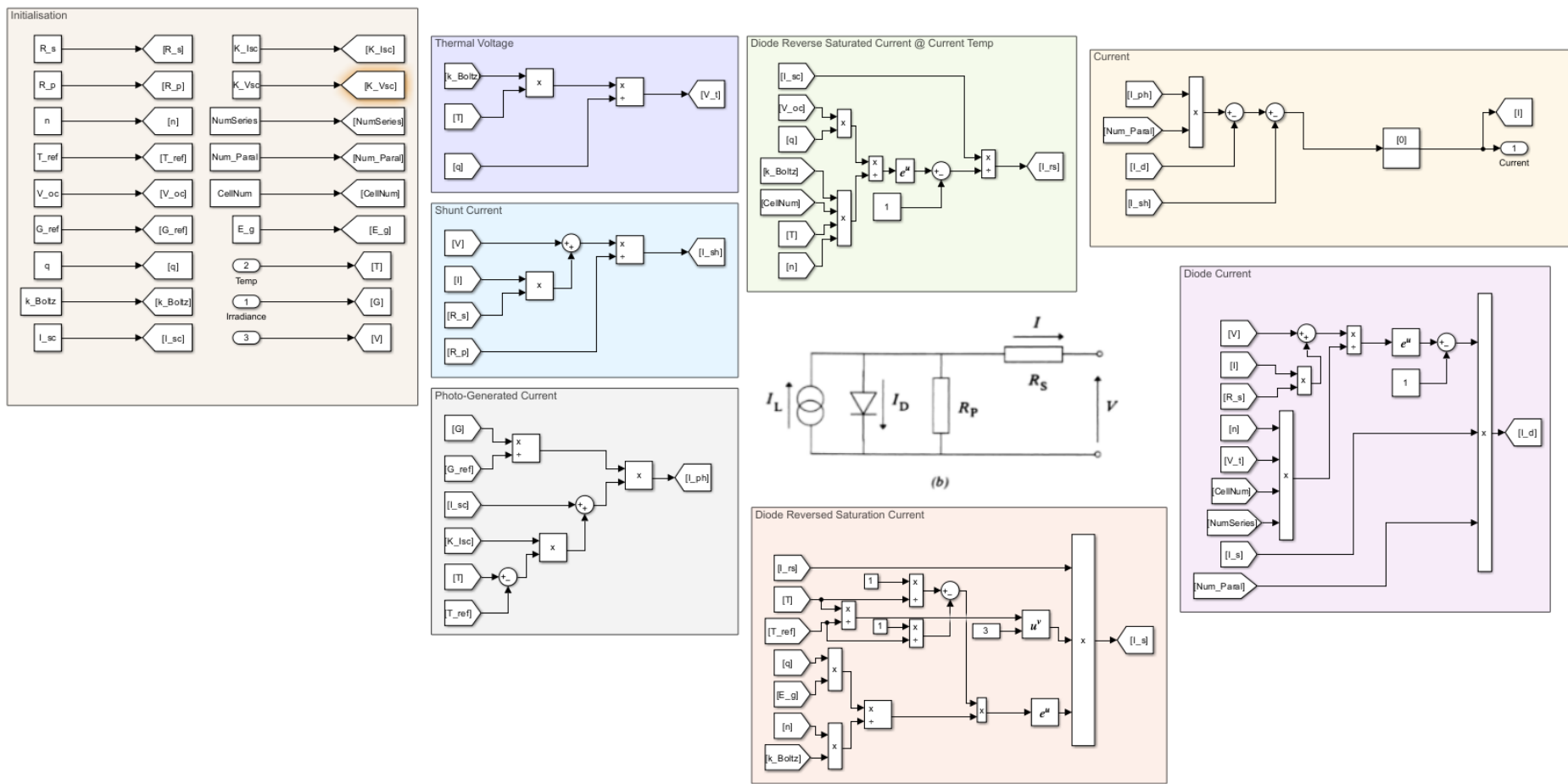
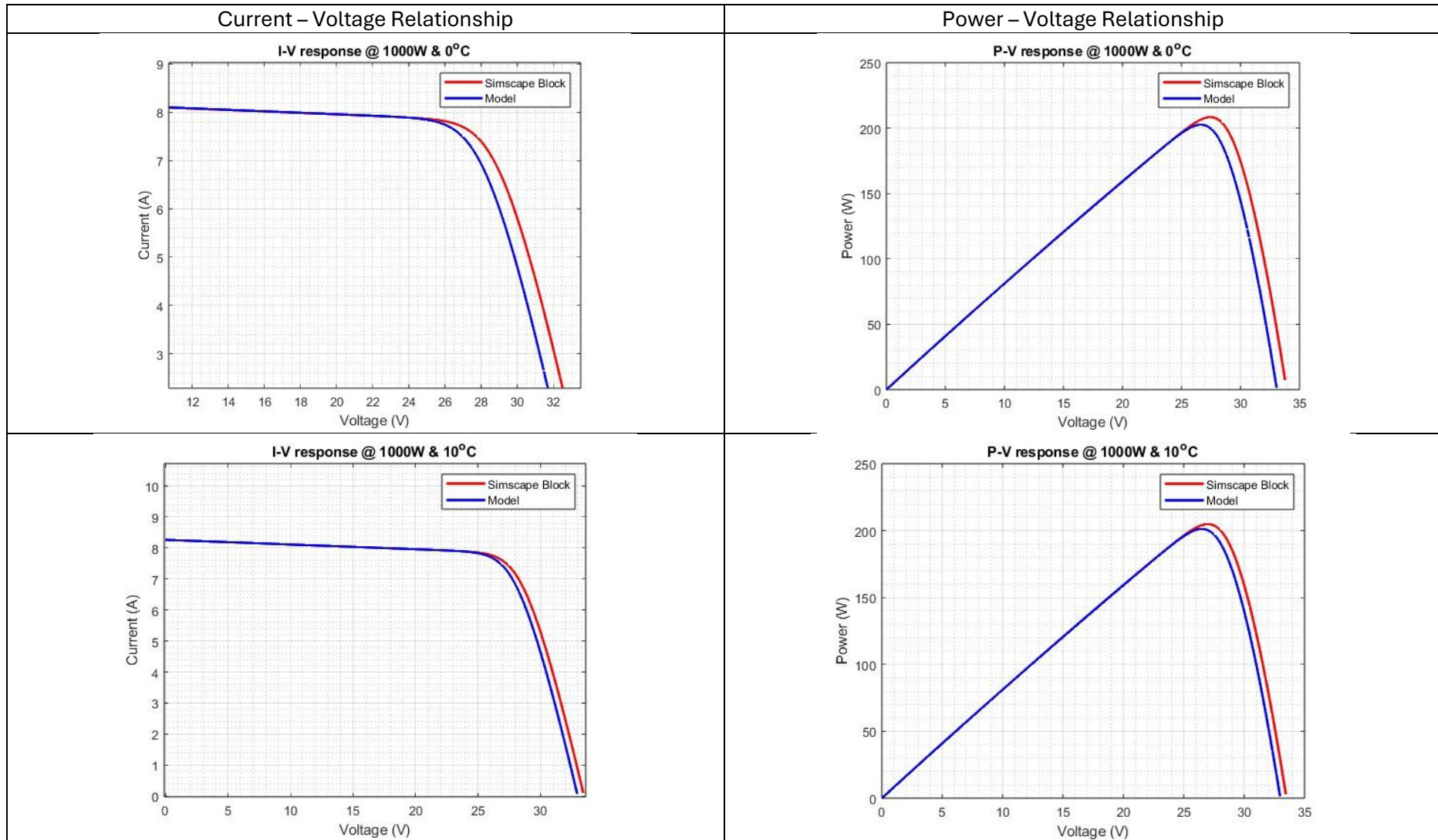
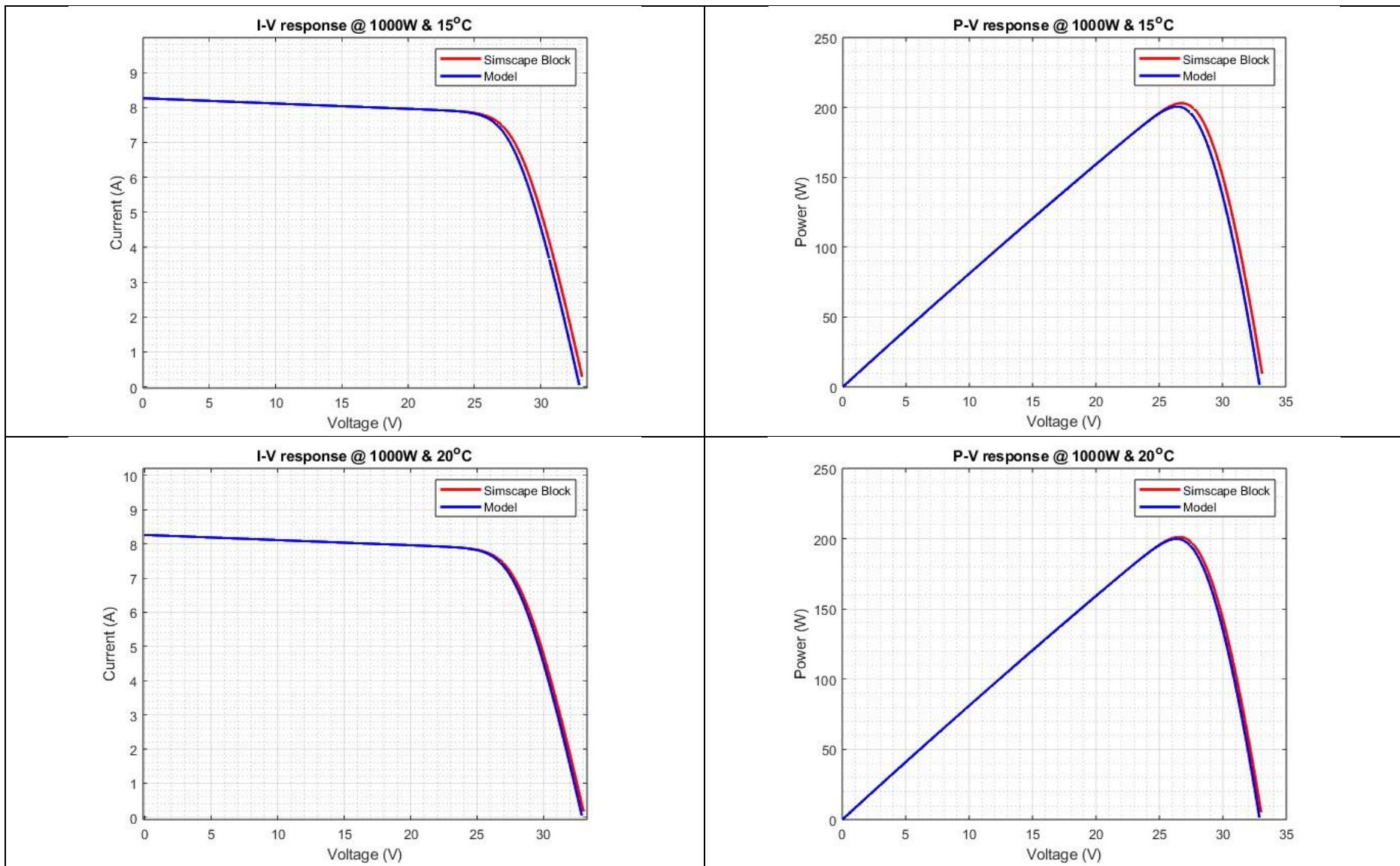


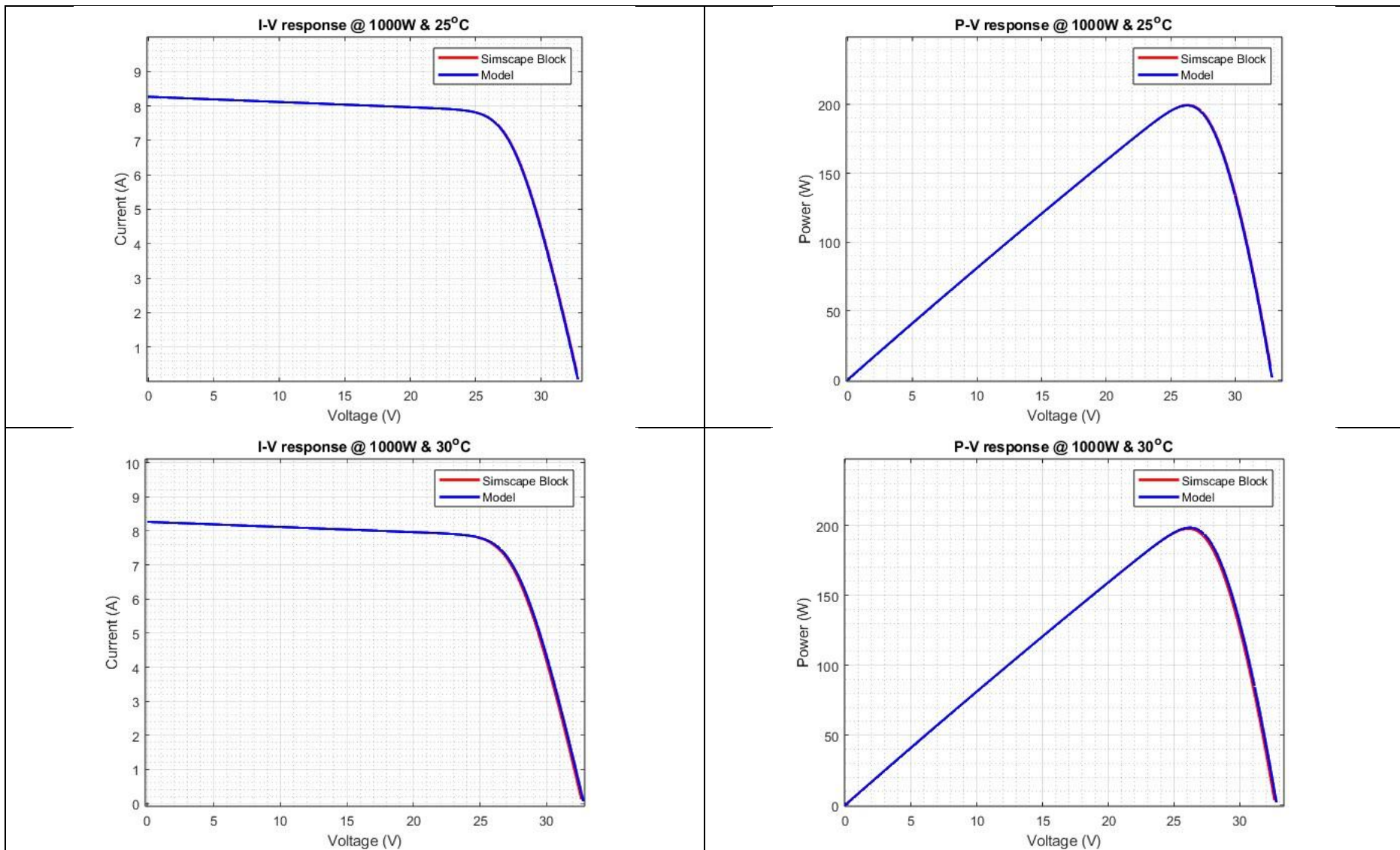
Figure 61: Complete Simulink model of the photovoltaic cell.

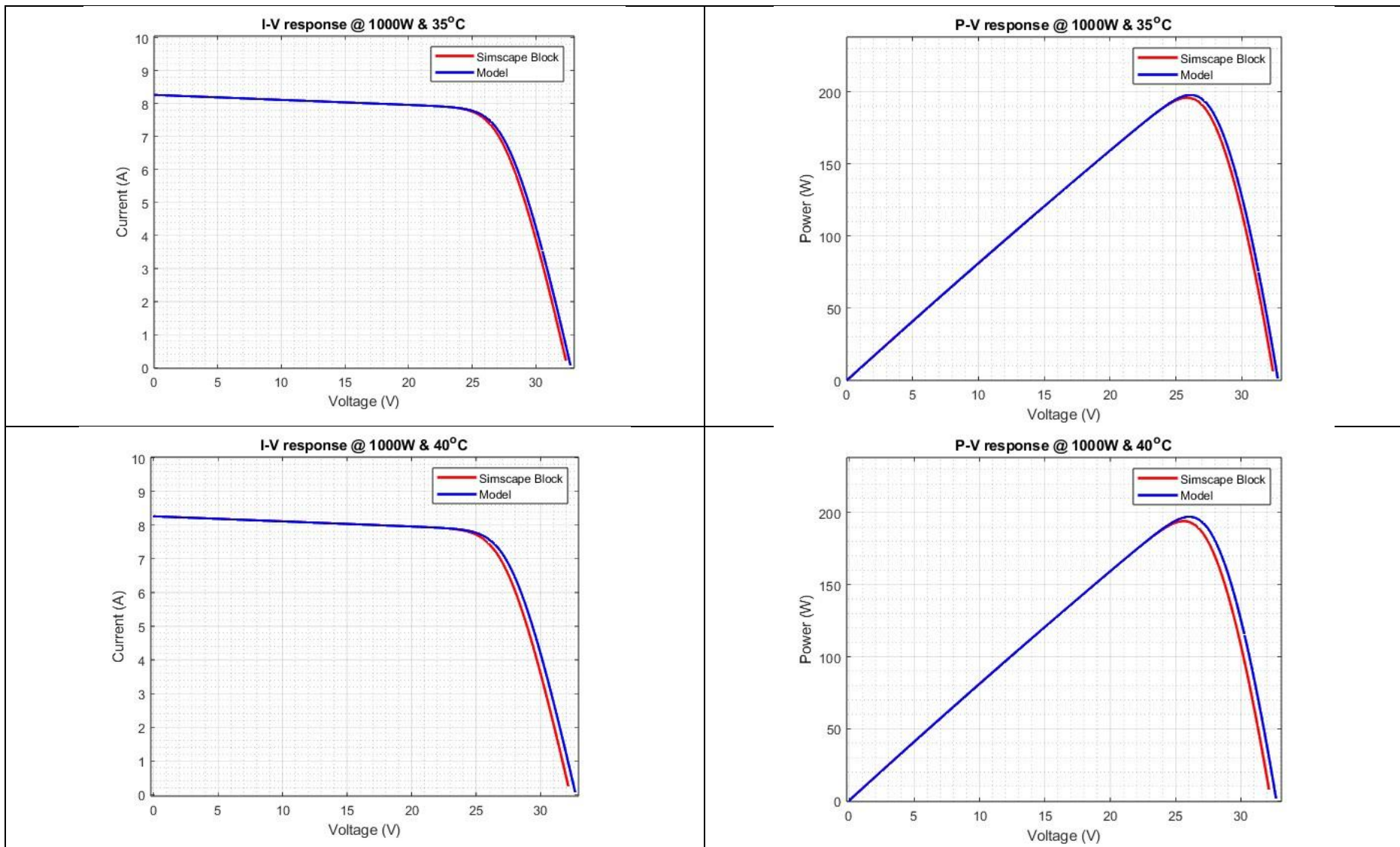
8.4.2 – Photovoltaic model validation

Table 17: Validation results for the photovoltaic model given a constant irradiance of 1000W and a varying temperature.









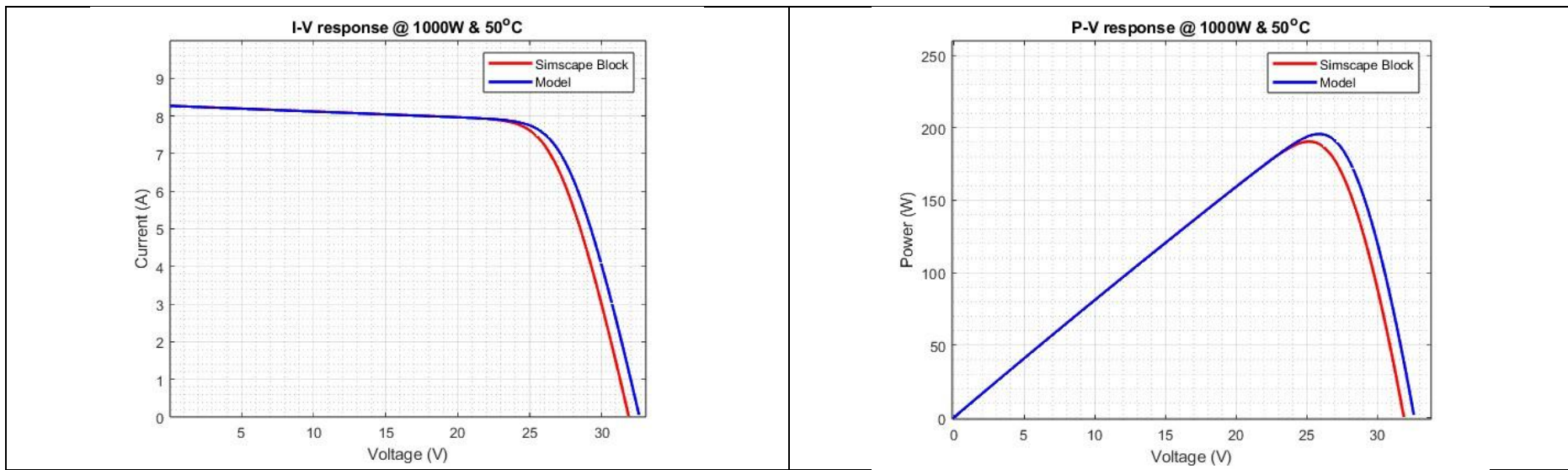
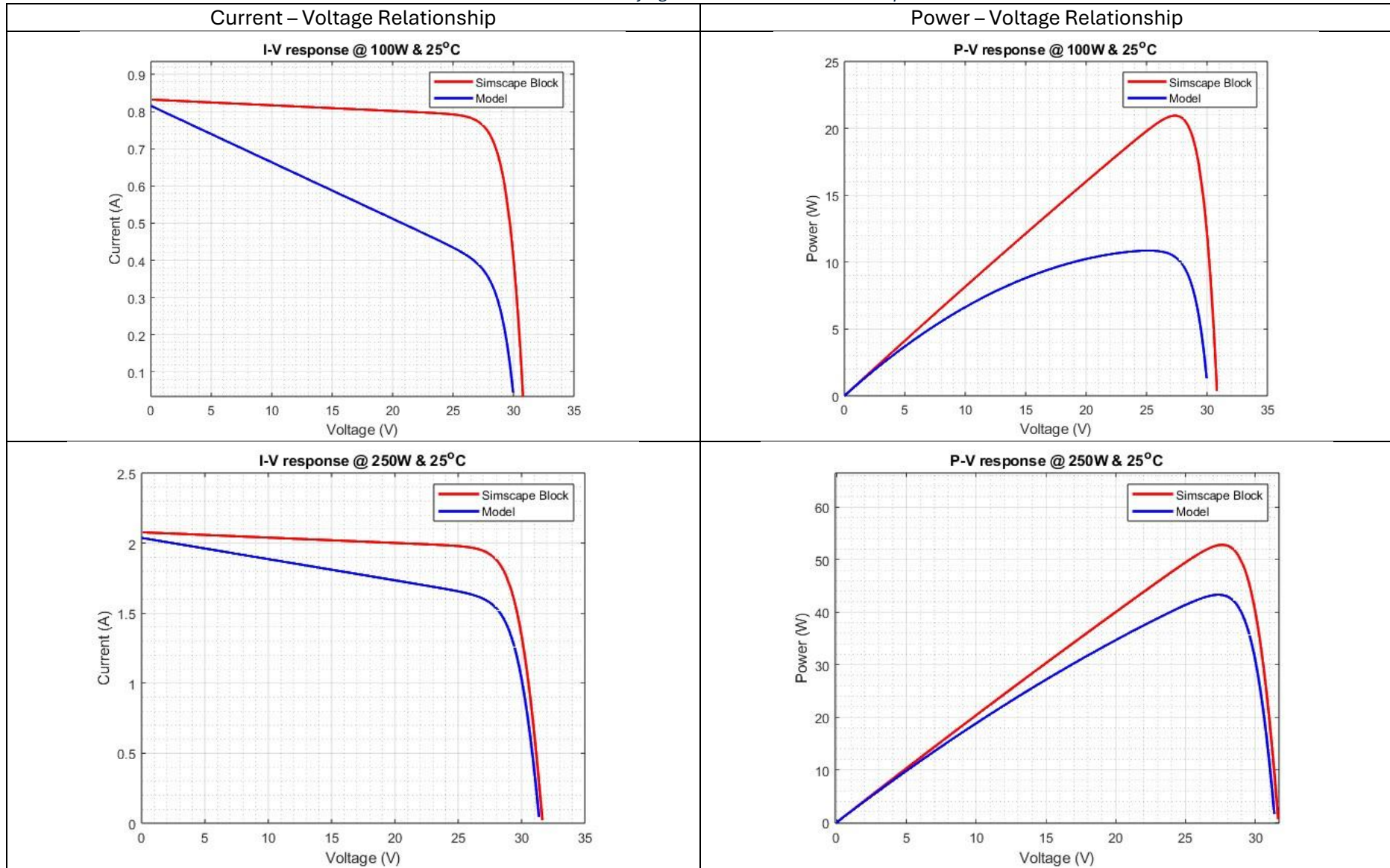
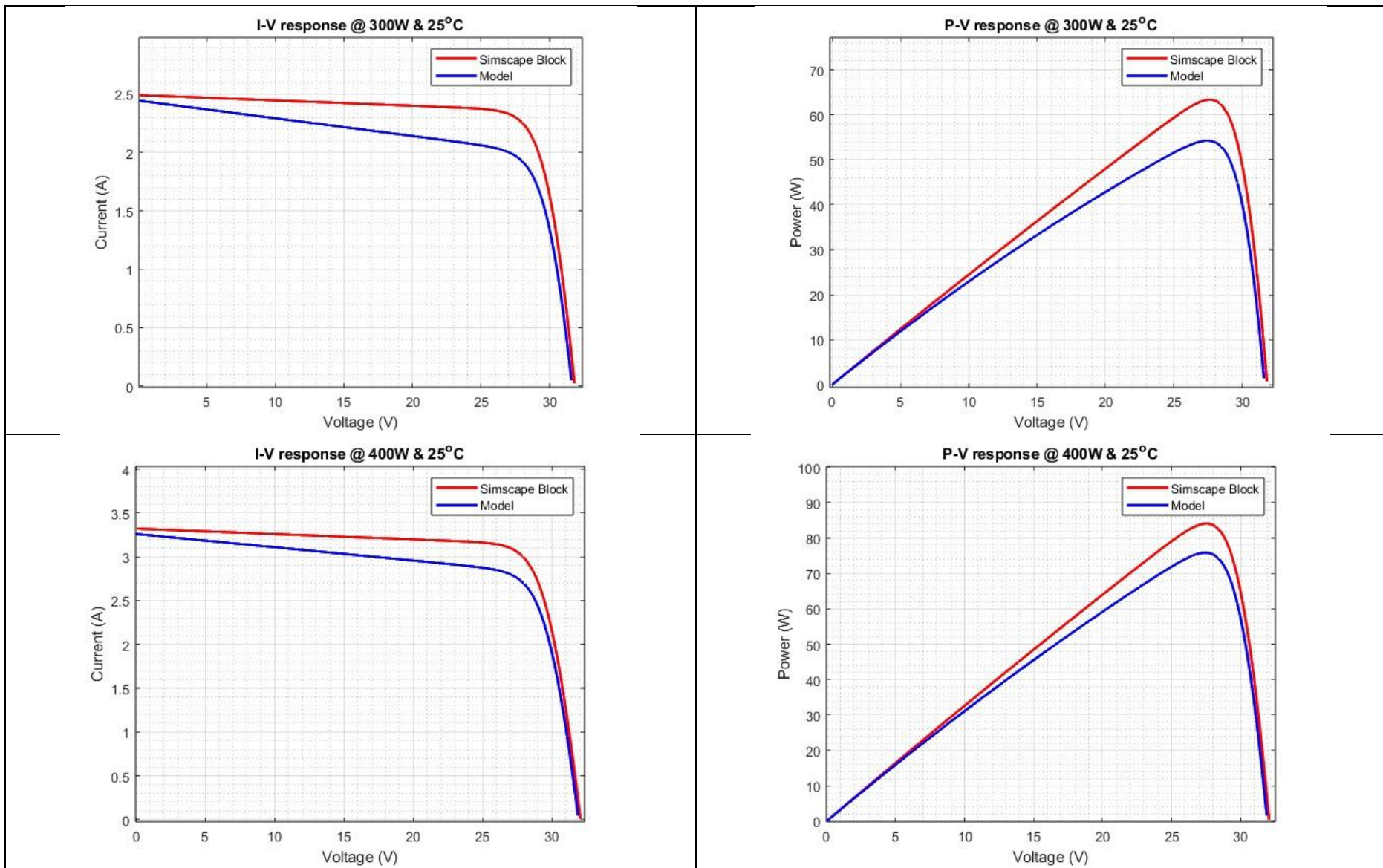
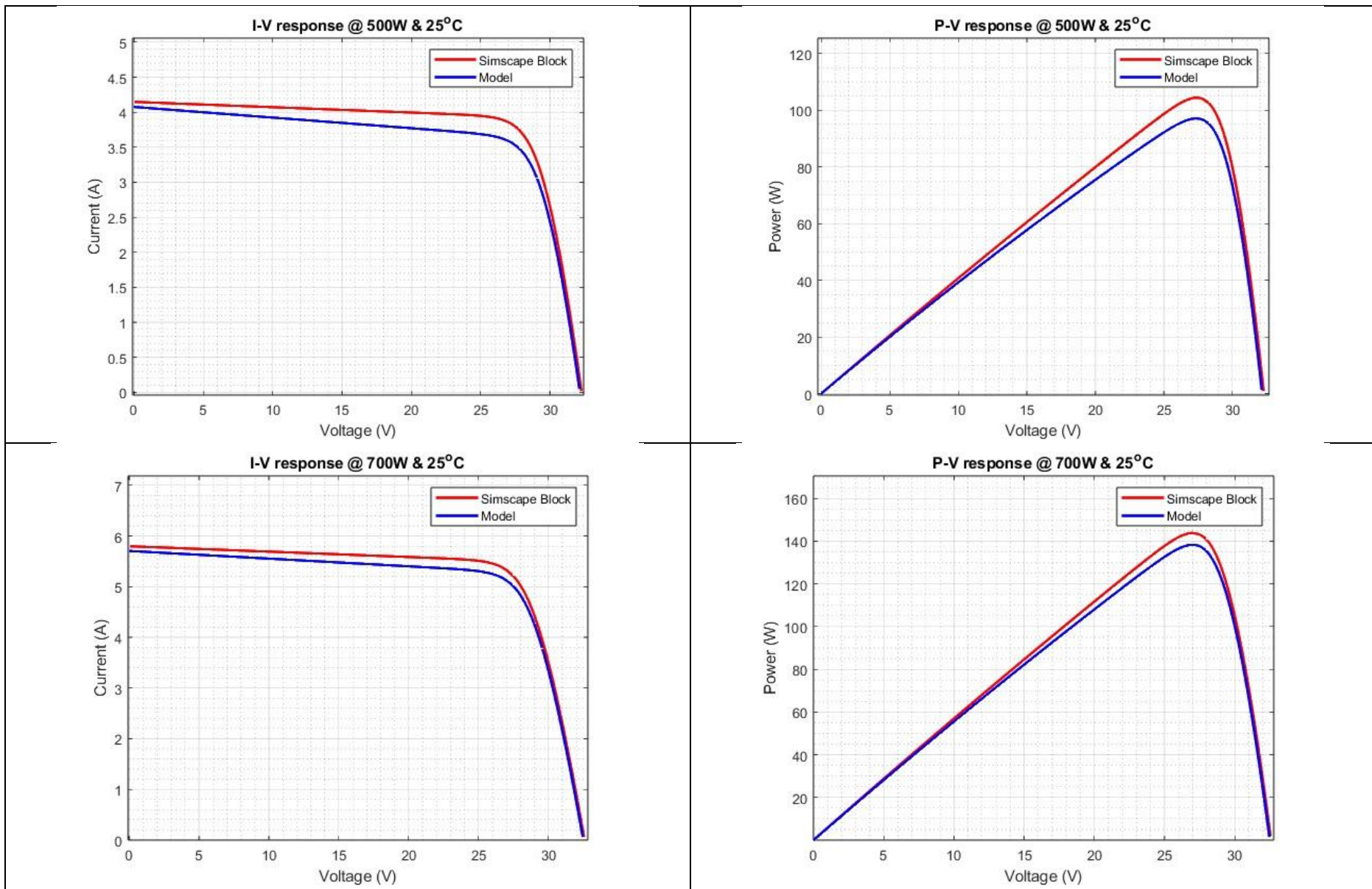
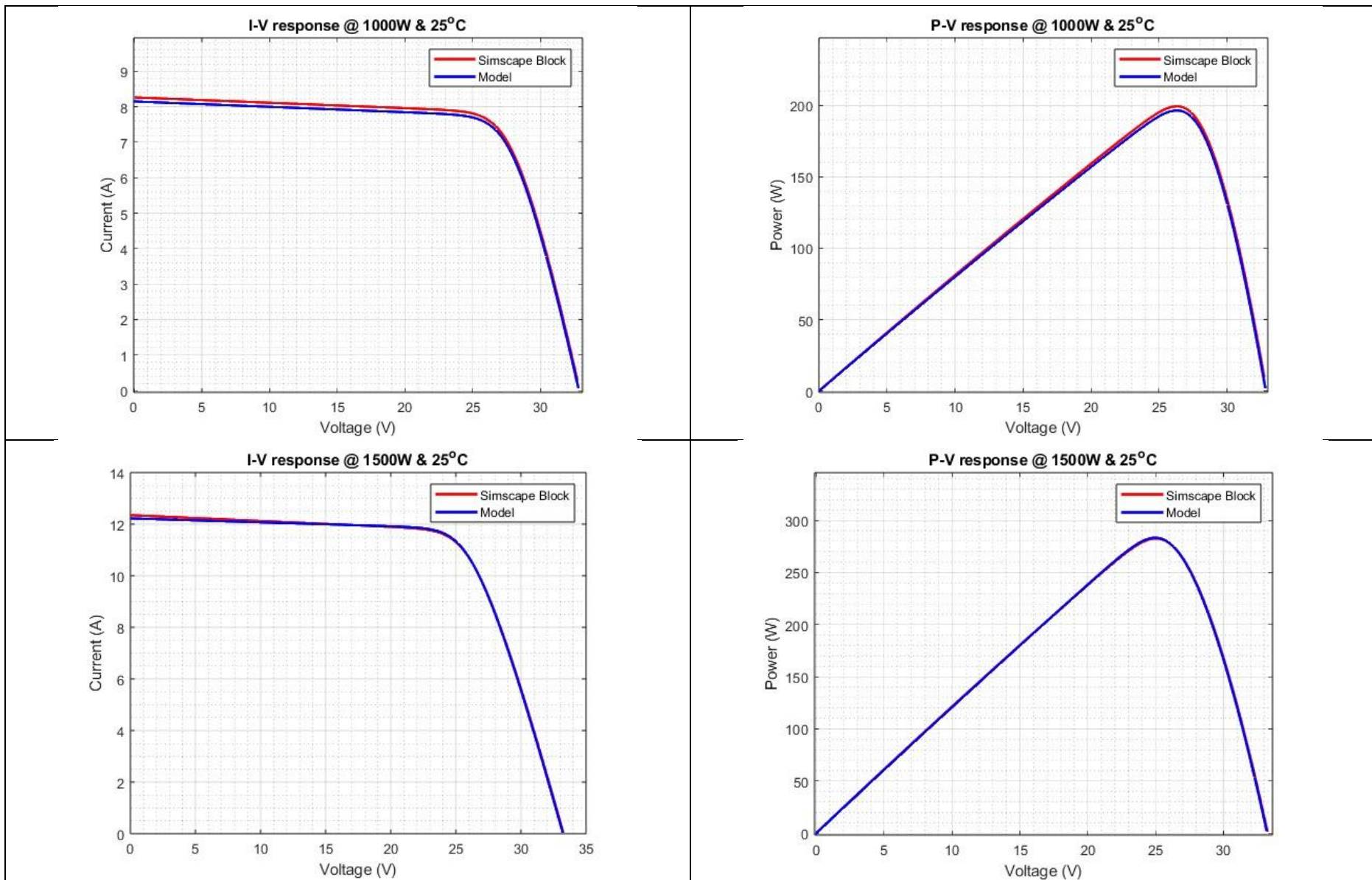


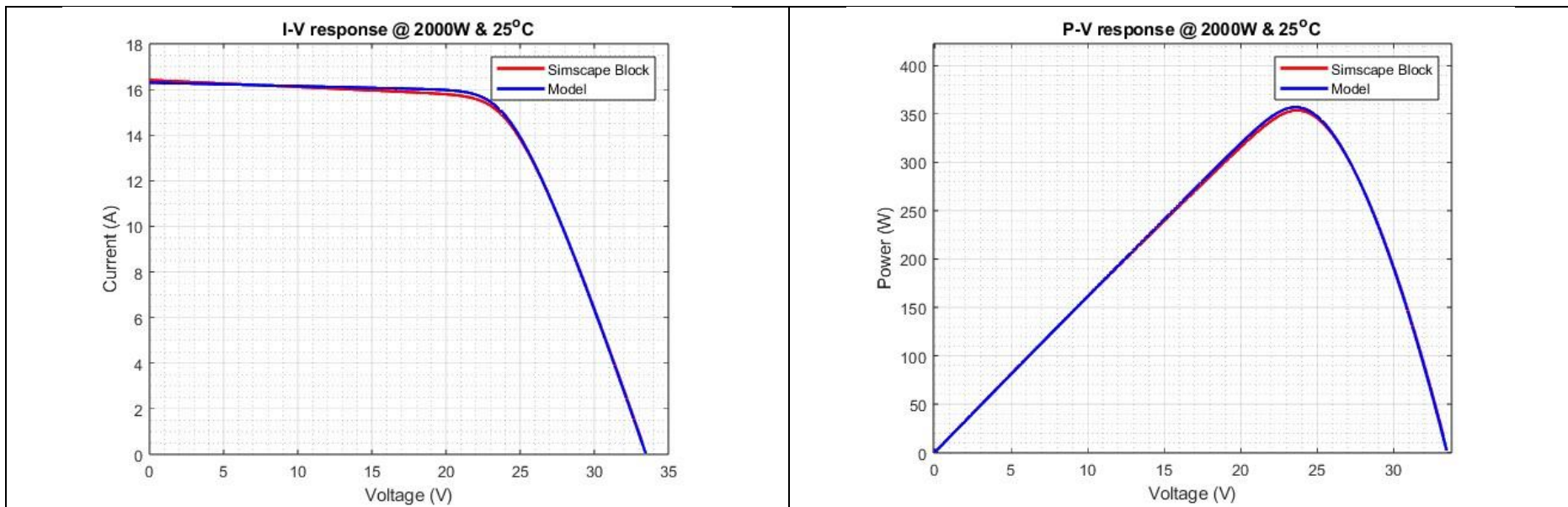
Table 18: Validation results for varying irradiance for a constant temperature of $T=25$

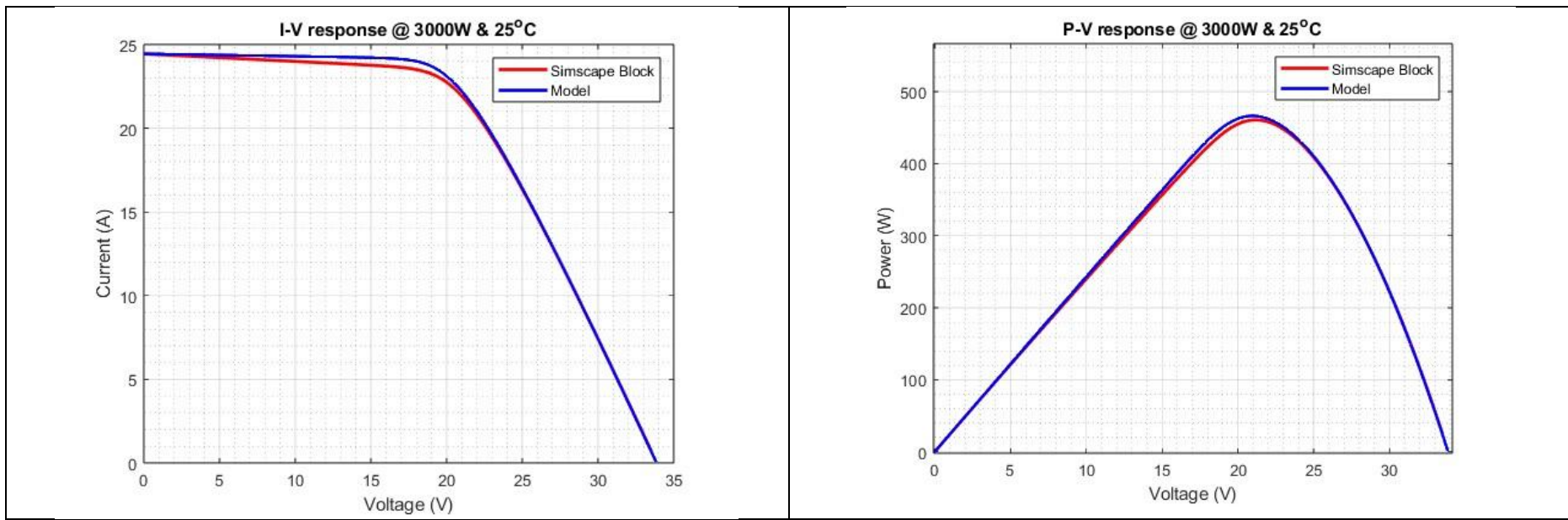












8.5 – Results

8.5.1 – Scenario 1

8.5.1a – Dual Axis

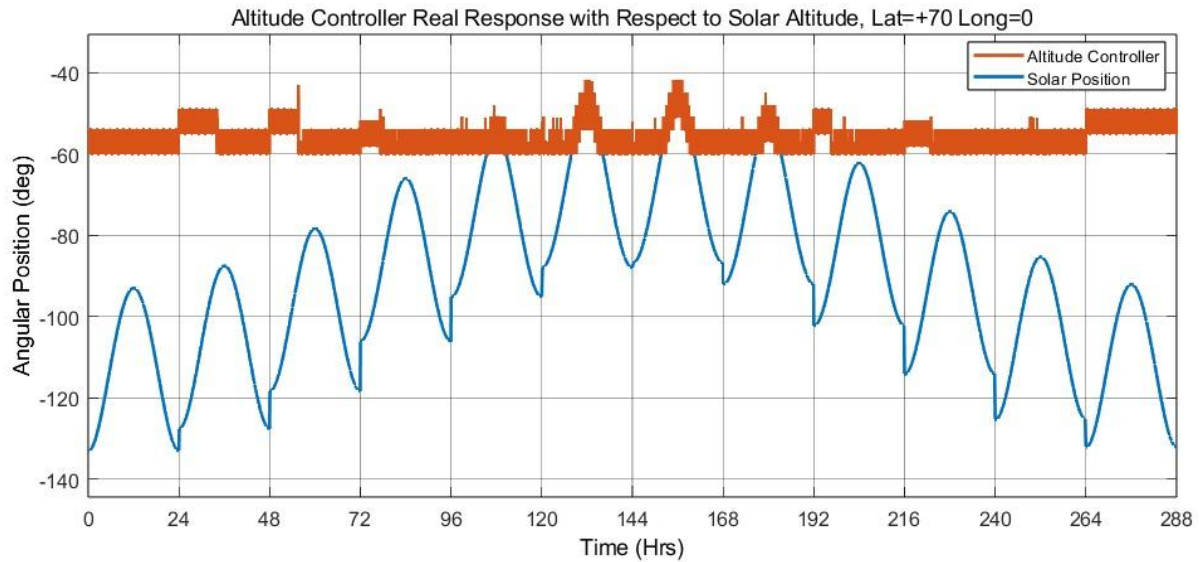


Figure 62:Altitude controller real response with respect to solar altitude for scenario 1

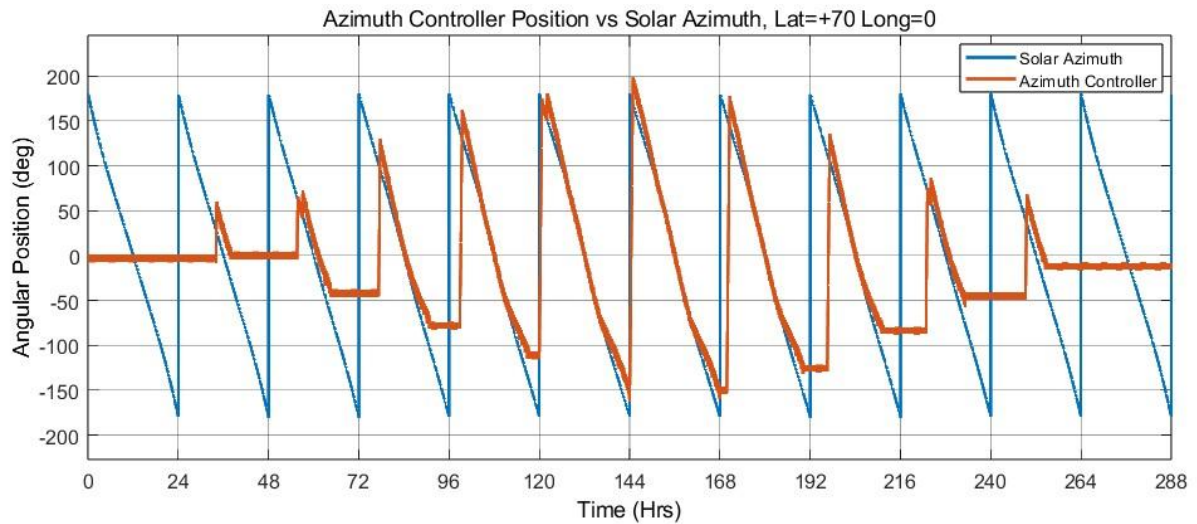


Figure 63:Azimuth controller real response with respect to solar altitude for scenario 1

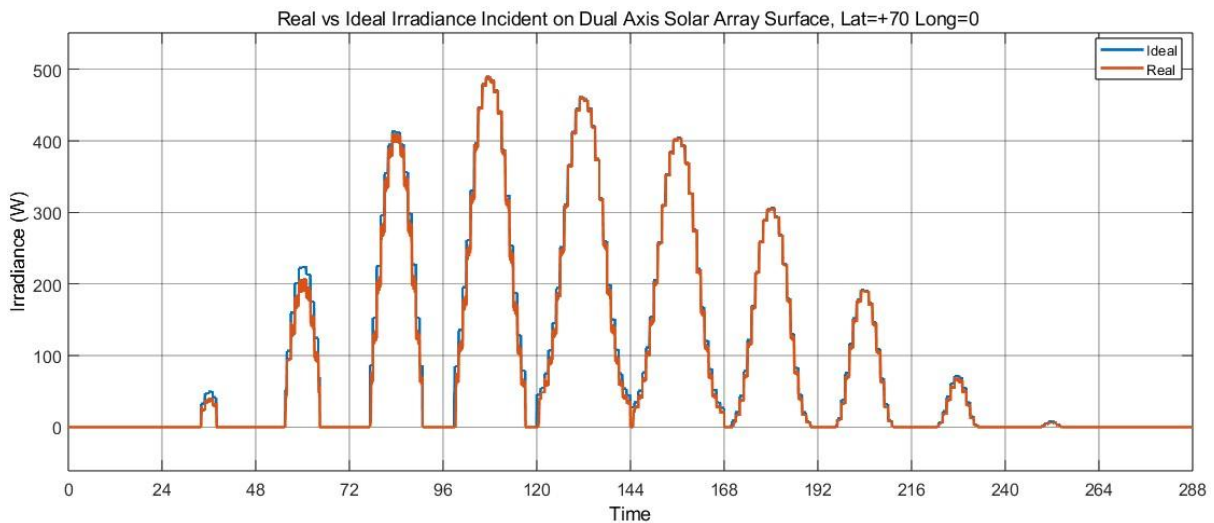


Figure 64: Real vs maximum incident irradiation on dual axis solar array surface for scenario 1

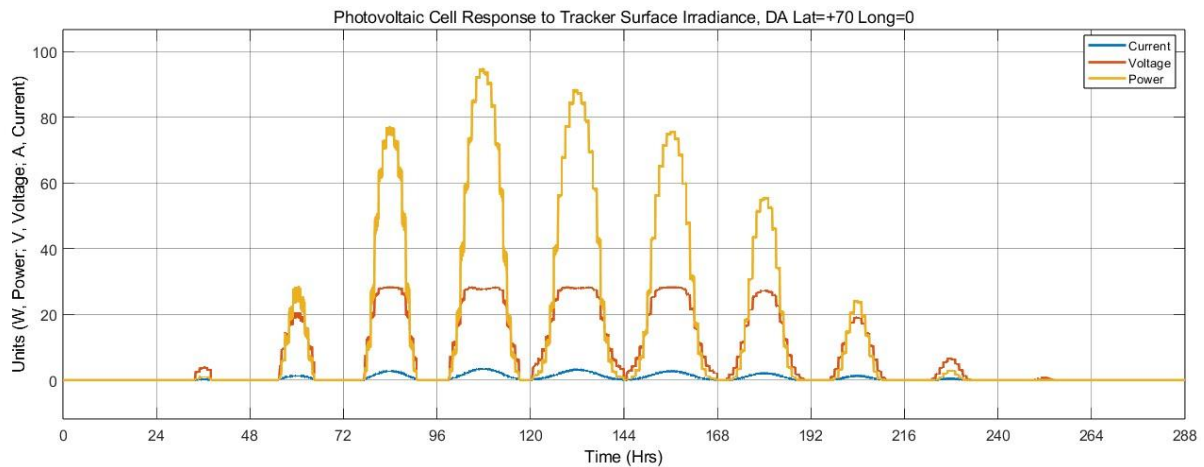


Figure 65: Photovoltaic model output for incident irradiation for dual axis tracking of scenario 1.

8.5.1b – Single Axis

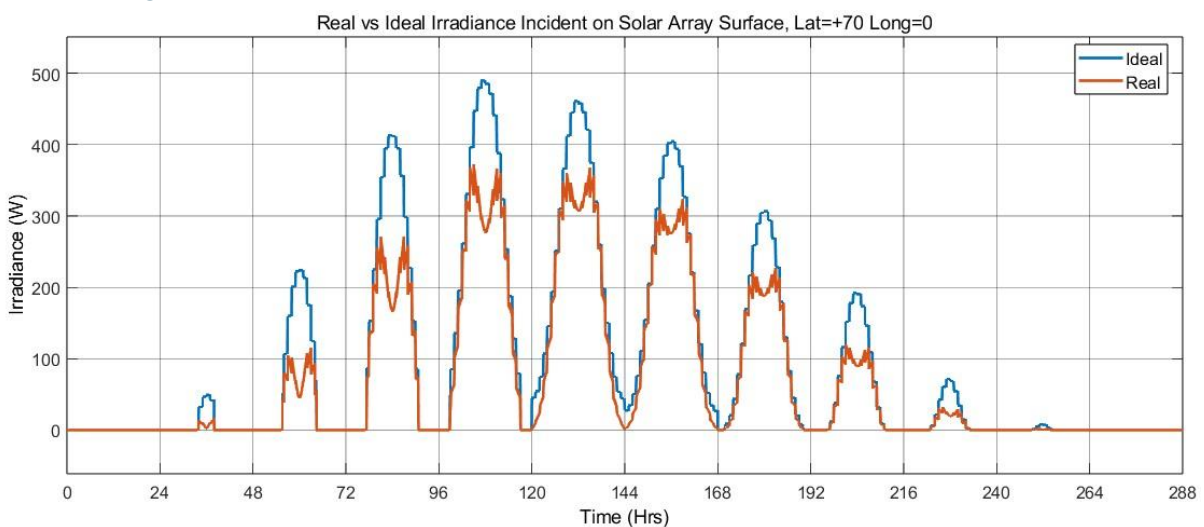


Figure 66: Single axis real vs maximum irradiance incident on the array surface, for scenario 1

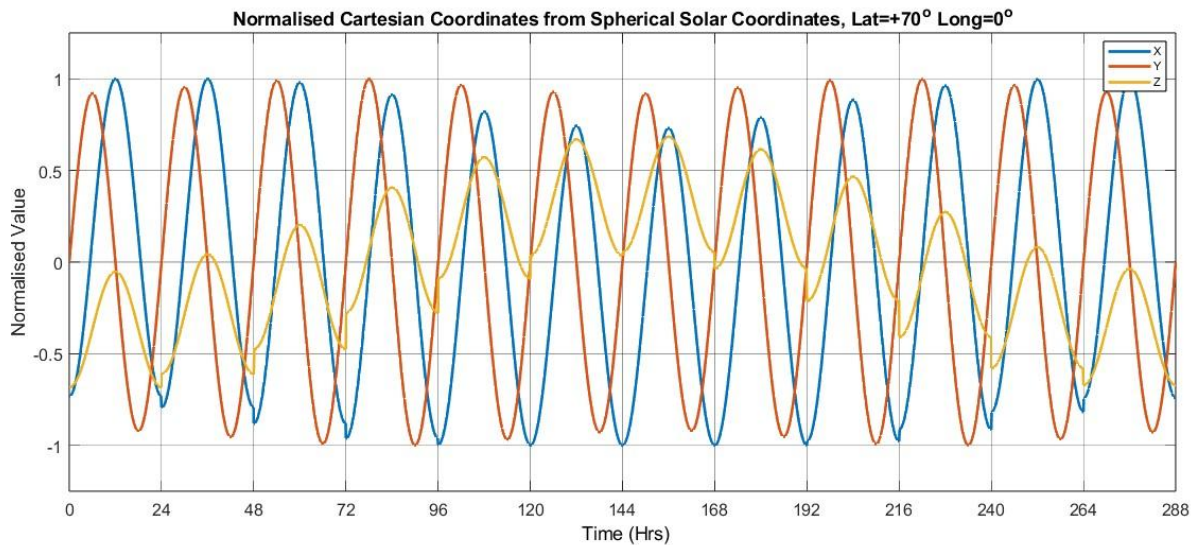


Figure 67: Normalised cartesian coordinates from spherical solar coordinates for scenario 1,

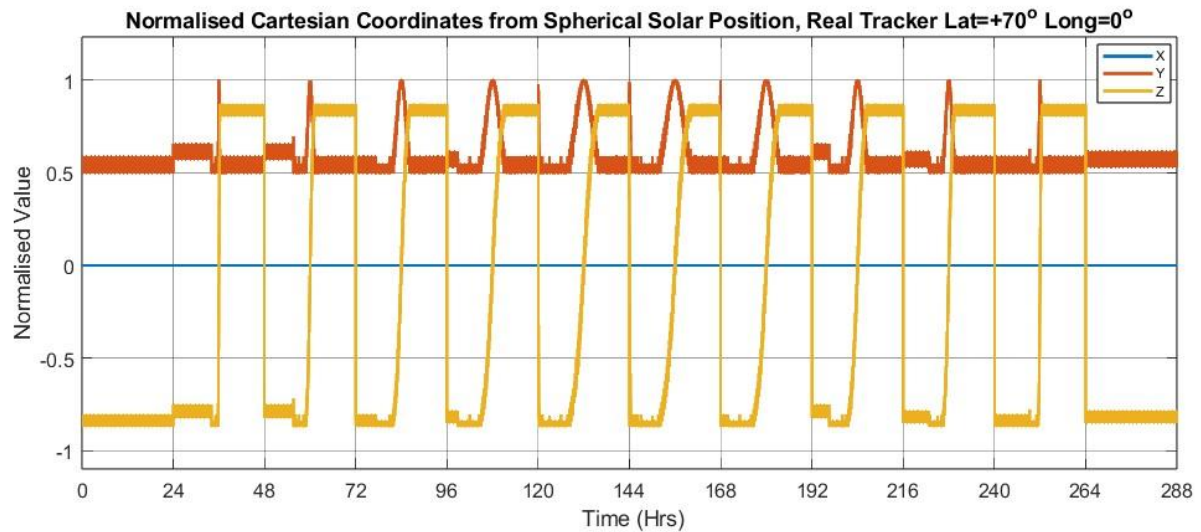


Figure 68: Single axis tracking surface normalised cartesian coordinates from normal of the array surface for scenario 1.

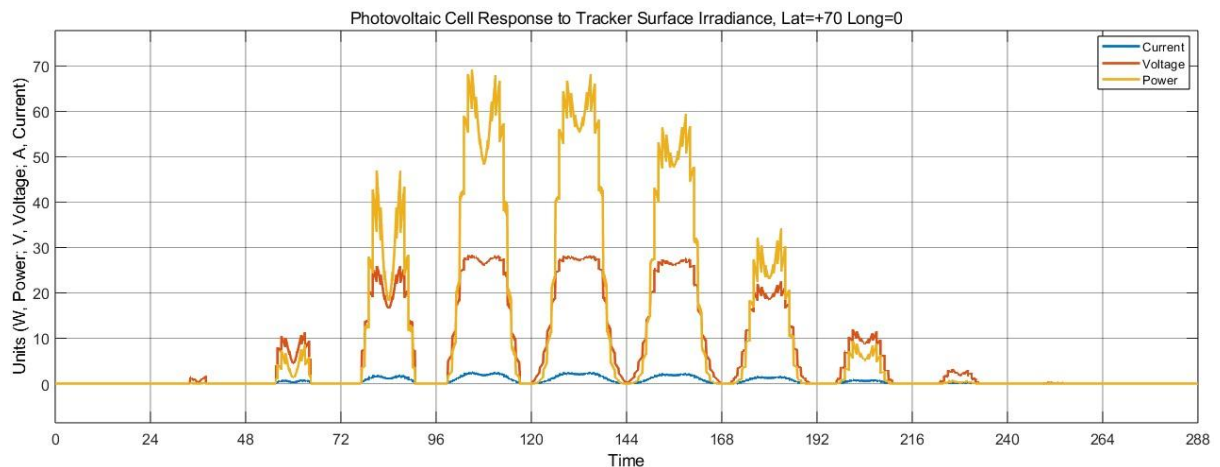


Figure 69: Power output by the photovoltaic module utilising the incident irradiation on the single axis tracking solar array surface for scenario 1

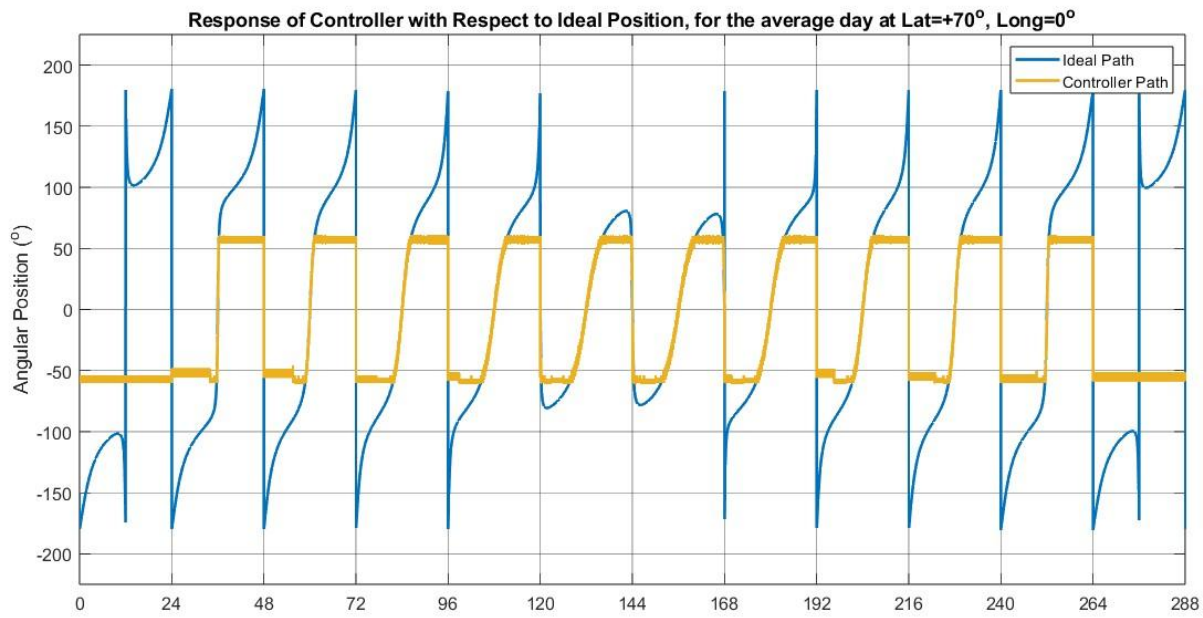


Figure 70: controller demand (Set point) with respect to the ideal path generated for the single axis tracking solar array in scenario 1.

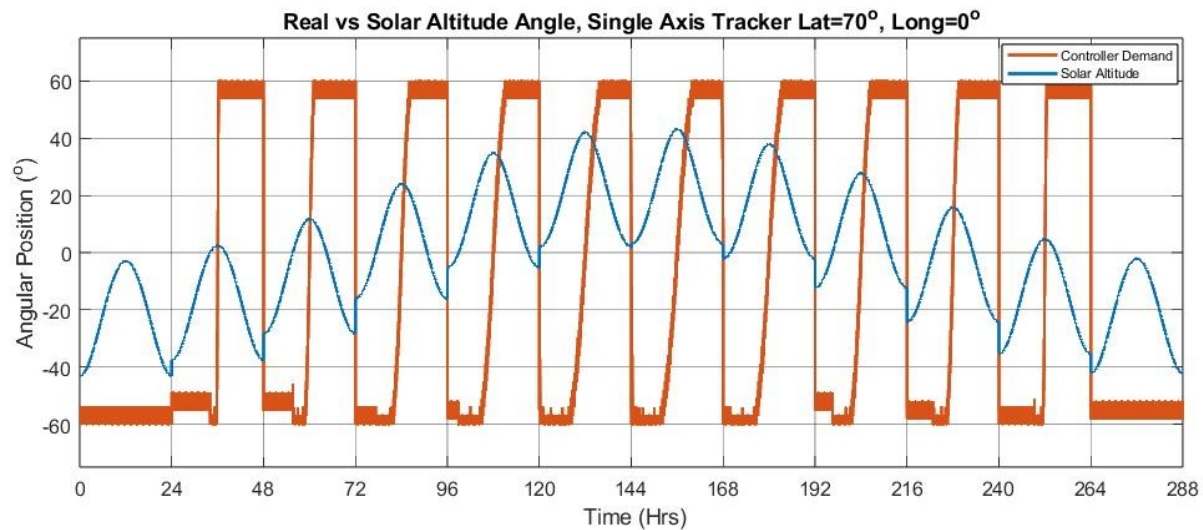


Figure 71:Real solar altitude angle vs the altitude setpoint demand by the controller, for scenario 1.

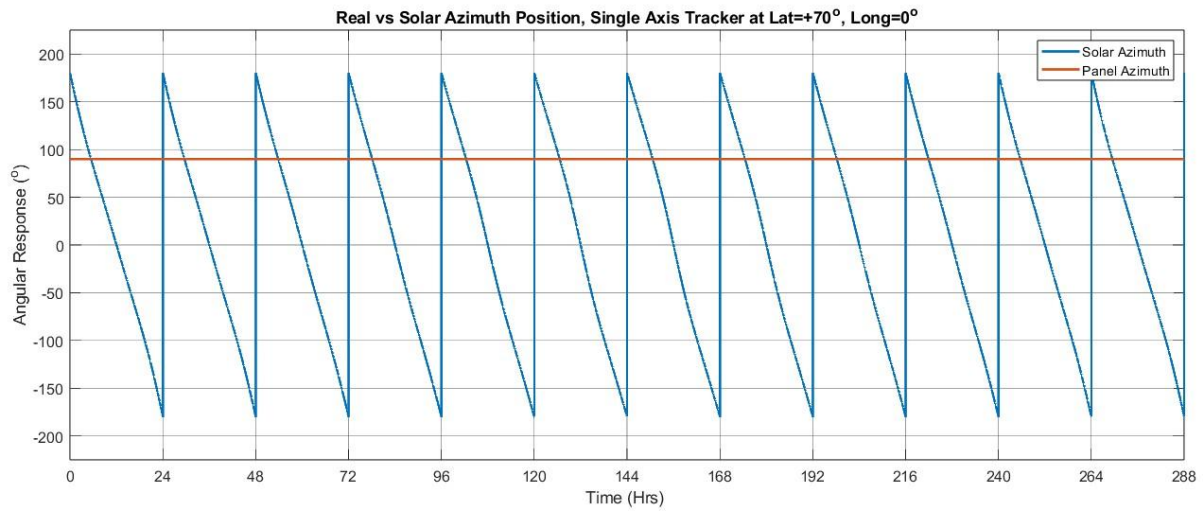


Figure 72: Real controller setpoint demand vs solar azimuth position for the single axis tracking of scenario 1.

8.5.2 – Scenario 2

8.5.2a – Dual Axis

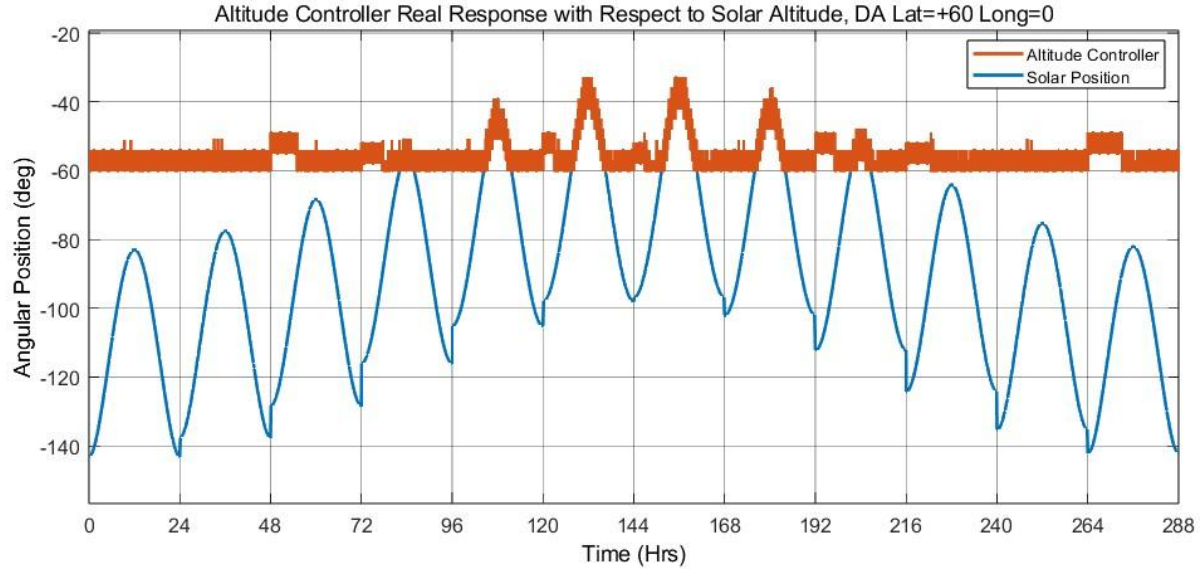


Figure 73: Altitude controller real response with respect to solar altitude for scenario 2

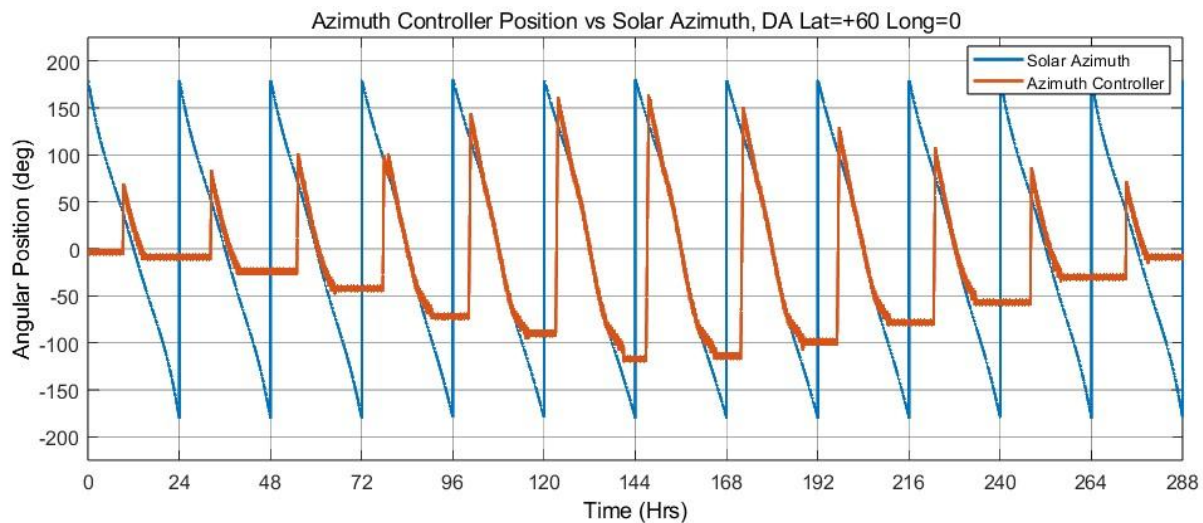


Figure 74: Azimuth controller real response with respect to solar altitude for scenario 2

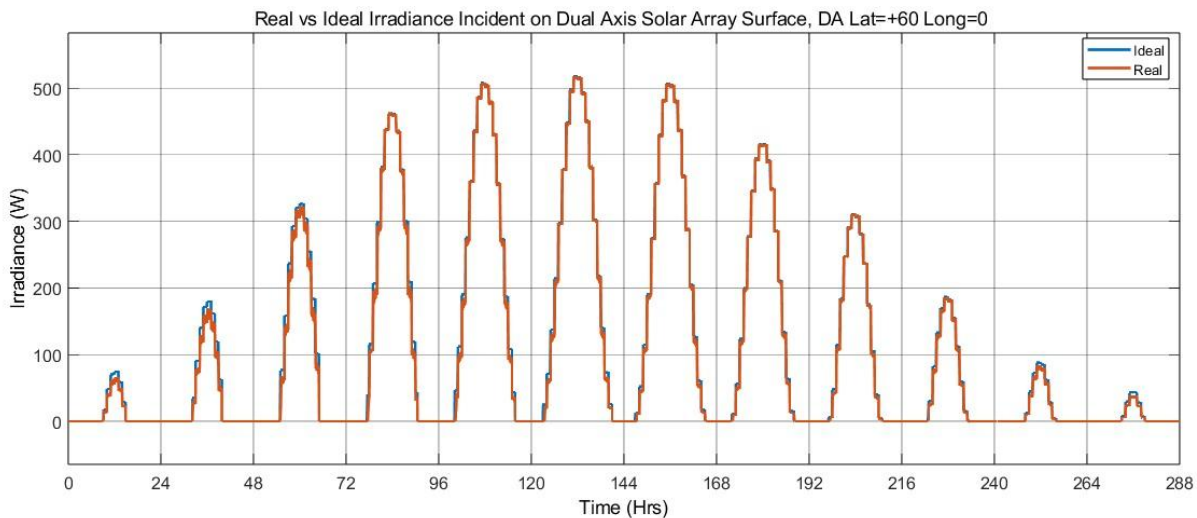


Figure 75: Real vs maximum incident irradiation on dual axis solar array surface for scenario 2

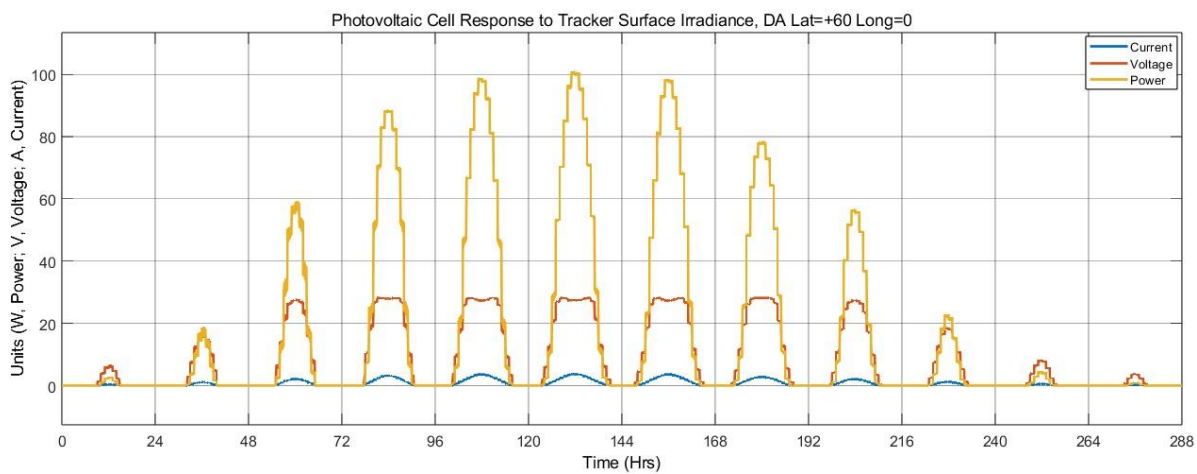


Figure 76: Photovoltaic model output for incident irradiation for dual axis tracking of scenario 2

8.5.2b – Single Axis

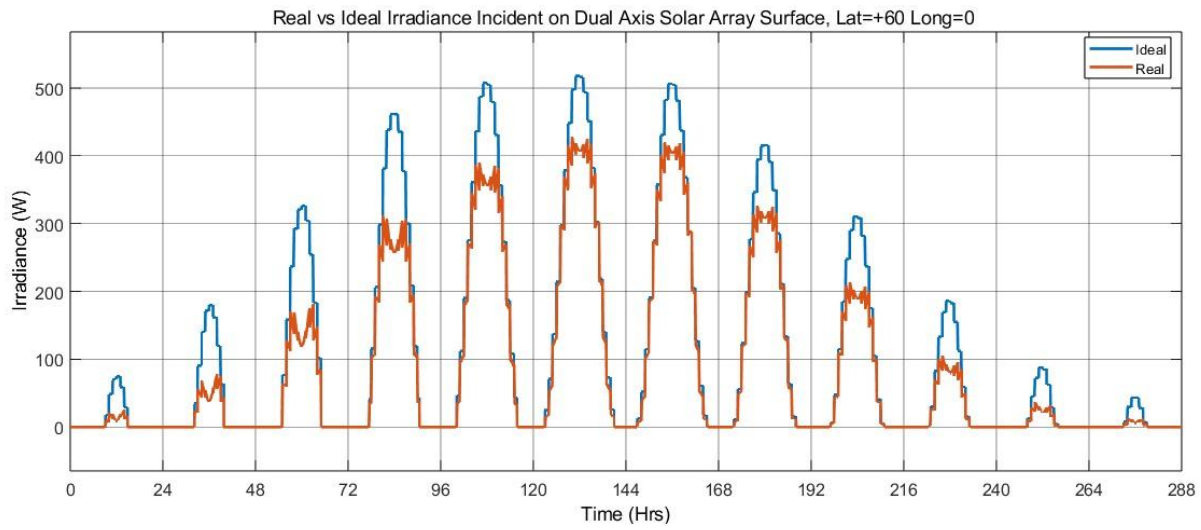


Figure 77:Single axis real vs maximum irradiance incident on the array surface, for scenario 2

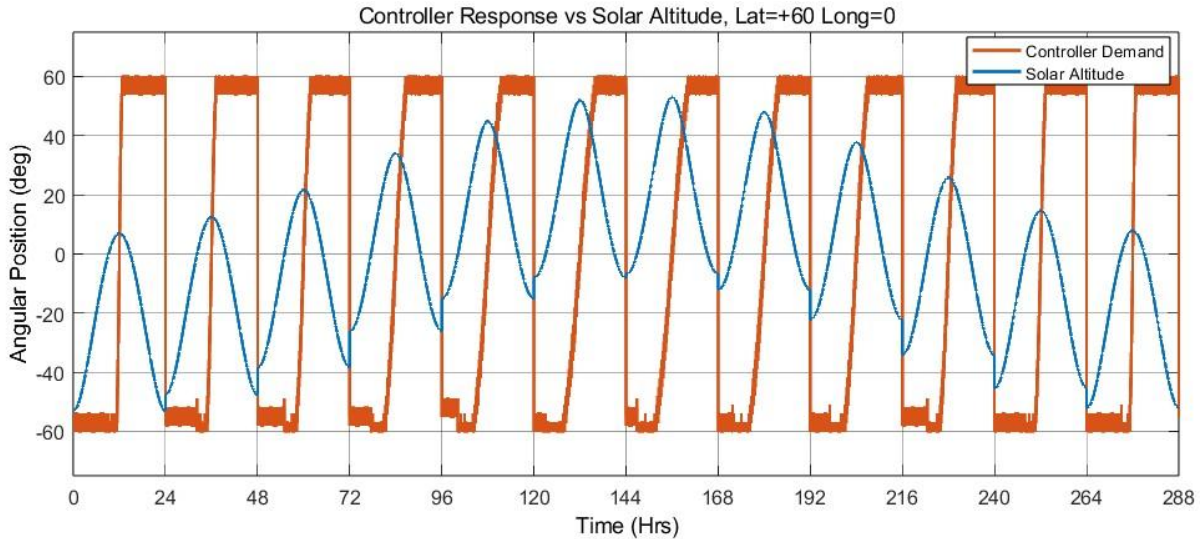


Figure 78:Real solar altitude angle vs the altitude setpoint demand by the controller, for scenario 2.

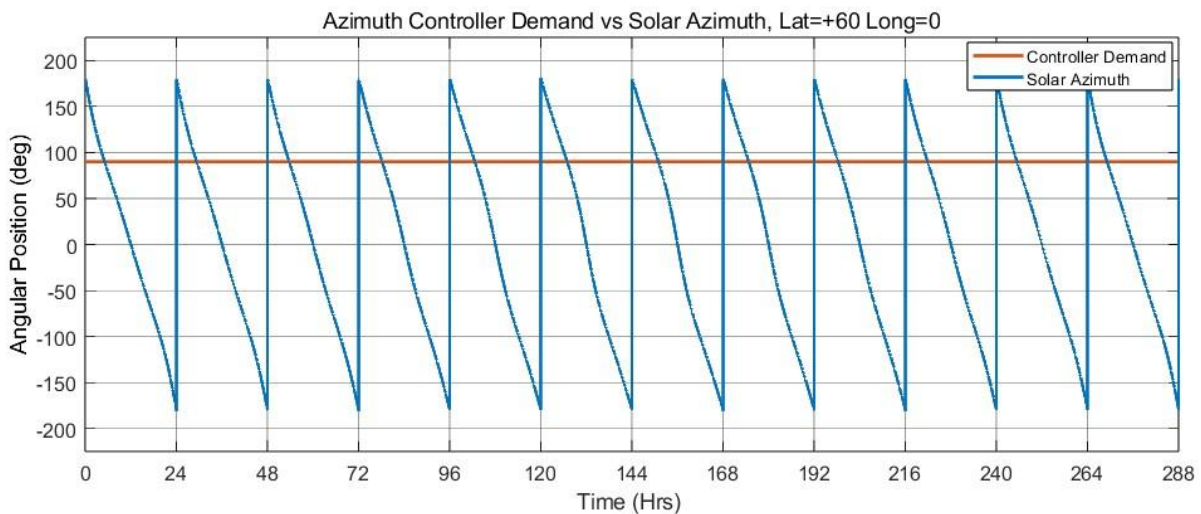


Figure 79:Real controller setpoint demand vs solar azimuth position for the single axis tracking of scenario 2

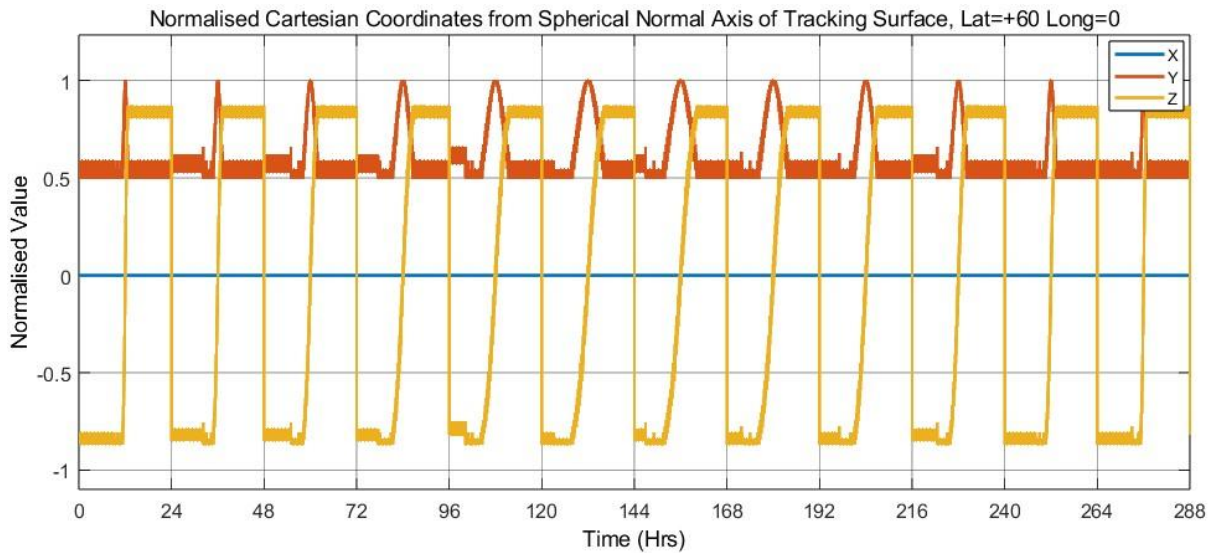


Figure 80: Single axis tracking surface normalised cartesian coordinates from normal of the array surface for scenario 2

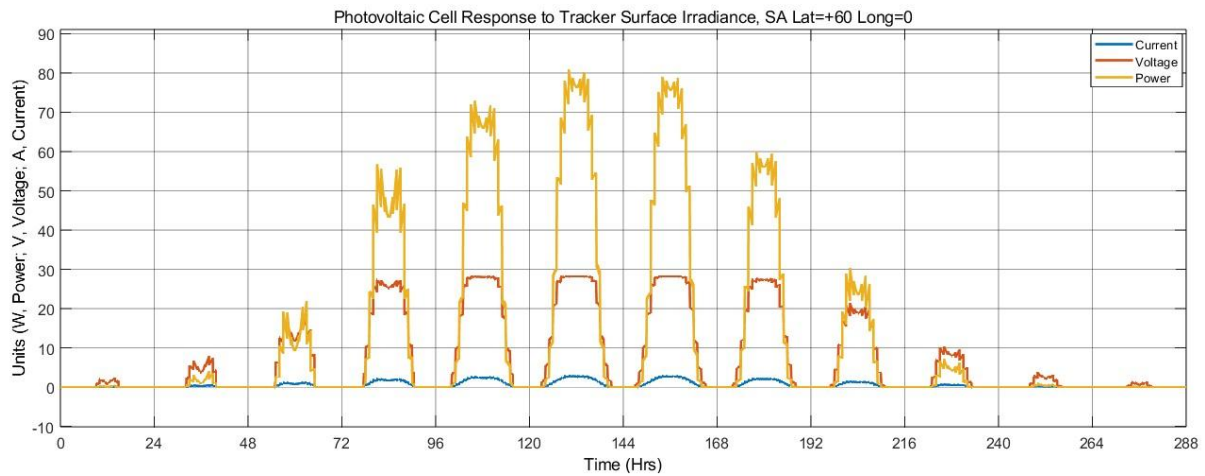


Figure 81: Power output by the photovoltaic module utilising the incident irradiation on the single axis tracking solar array surface for scenario 2

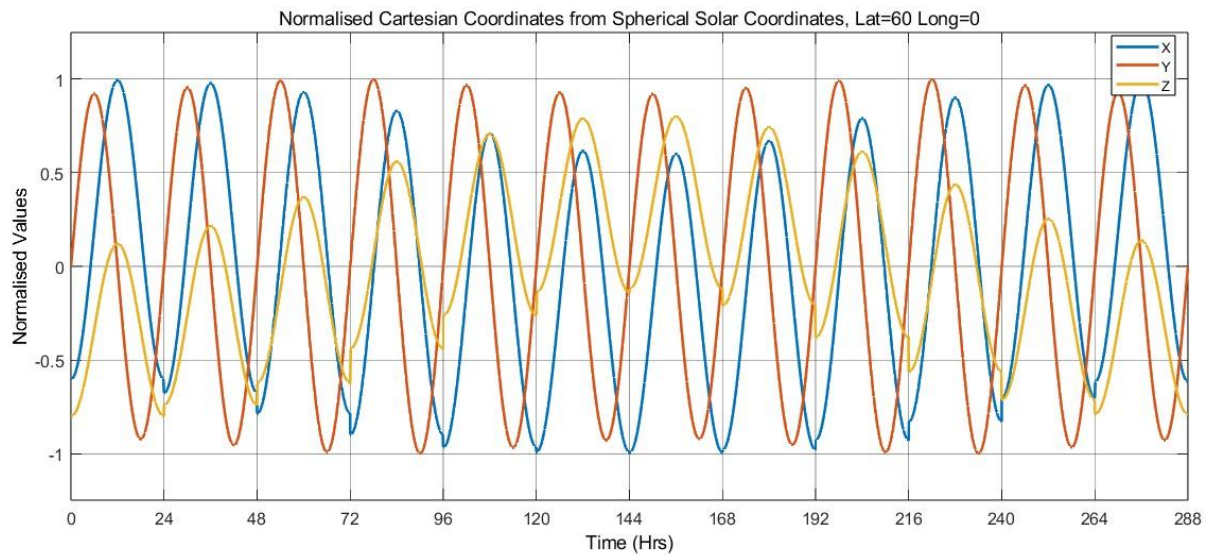


Figure 82: Normalised cartesian coordinates from spherical solar coordinates for scenario 2

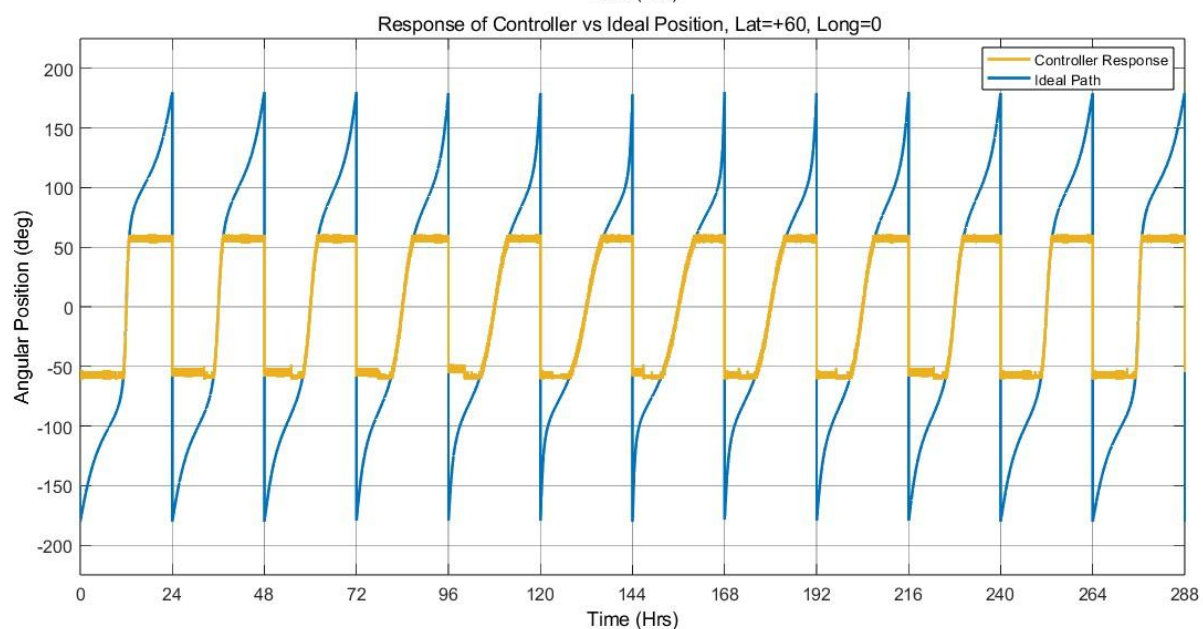
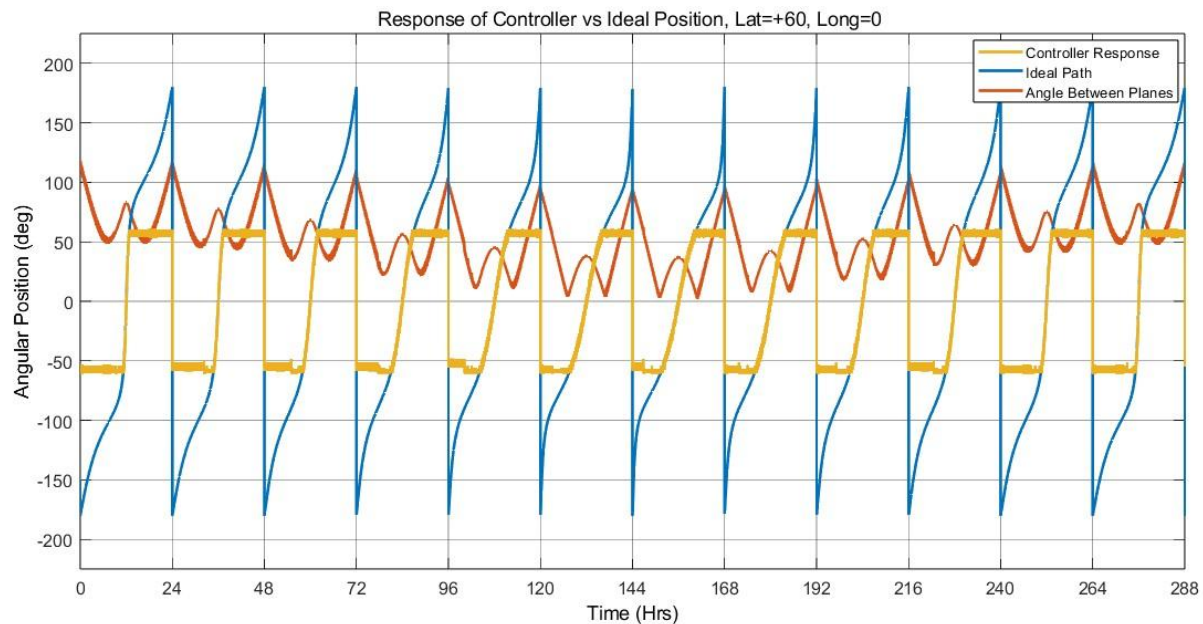


Figure 83: controller demand (Set point) with respect to the ideal path generated for the single axis tracking solar array in scenario 2

8.5.3 – Scenario 3

8.5.3a – Dual Axis

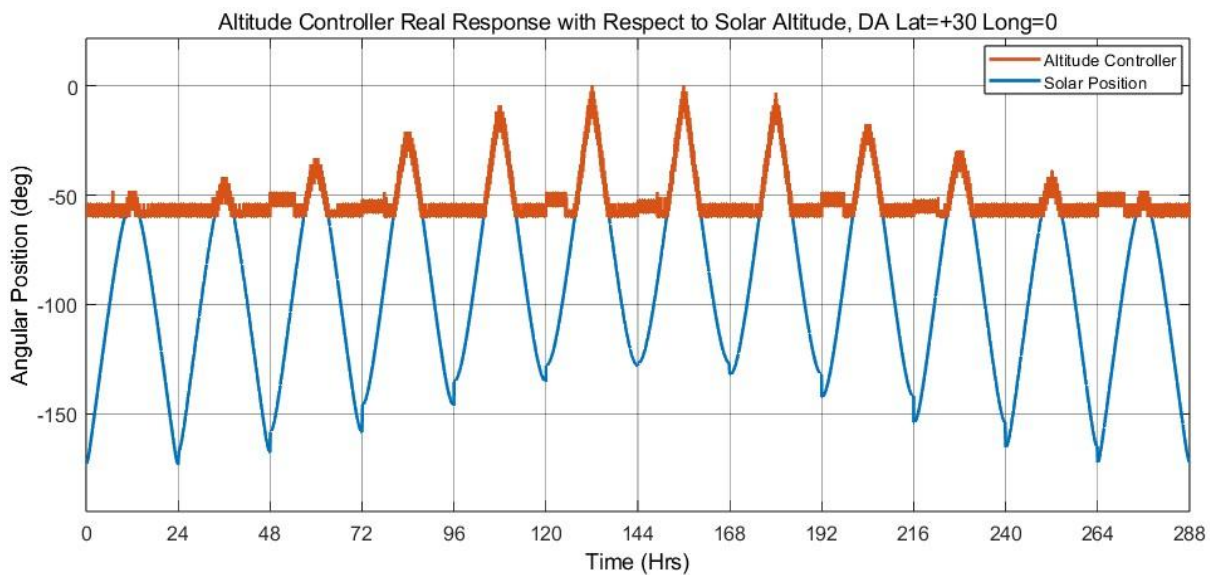


Figure 84: Altitude controller real response with respect to solar altitude for scenario 3

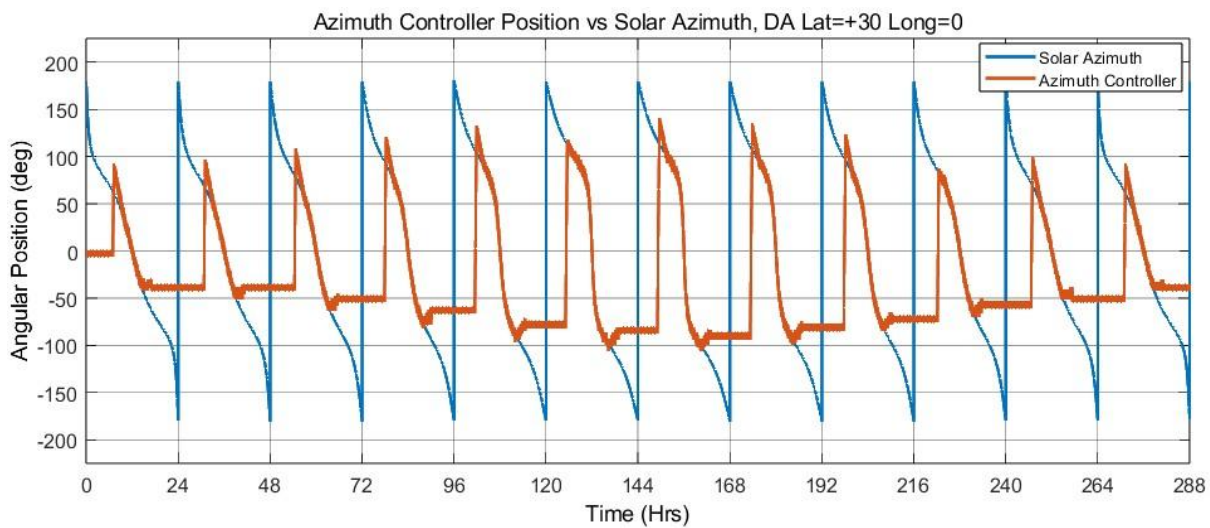


Figure 85: Azimuth controller real response with respect to solar altitude for scenario 3

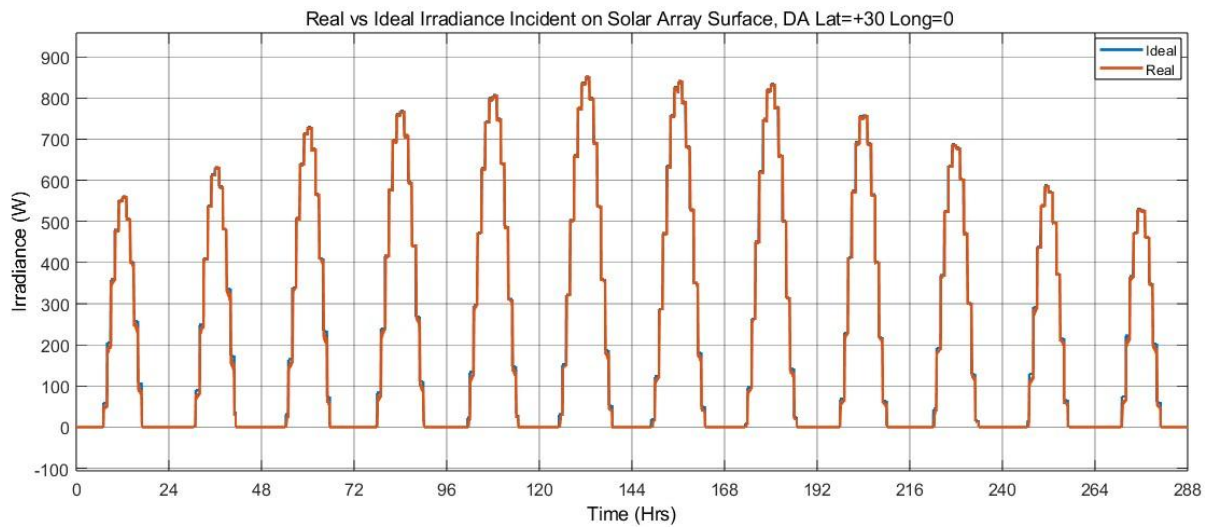


Figure 86: Real vs maximum incident irradiation on dual axis solar array surface for scenario 3

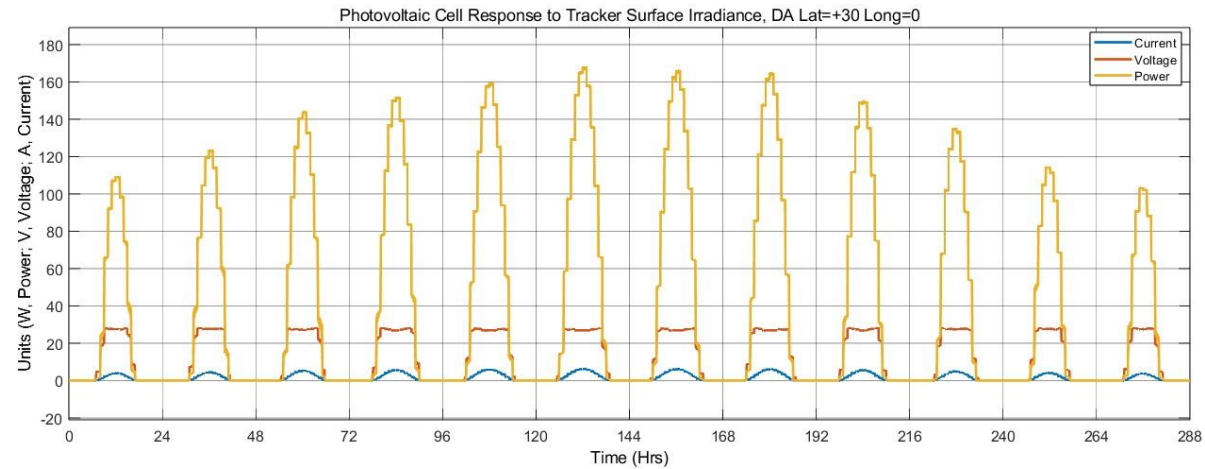


Figure 87: Photovoltaic model output for incident irradiation for dual axis tracking of scenario 3

8.5.3b – Single Axis

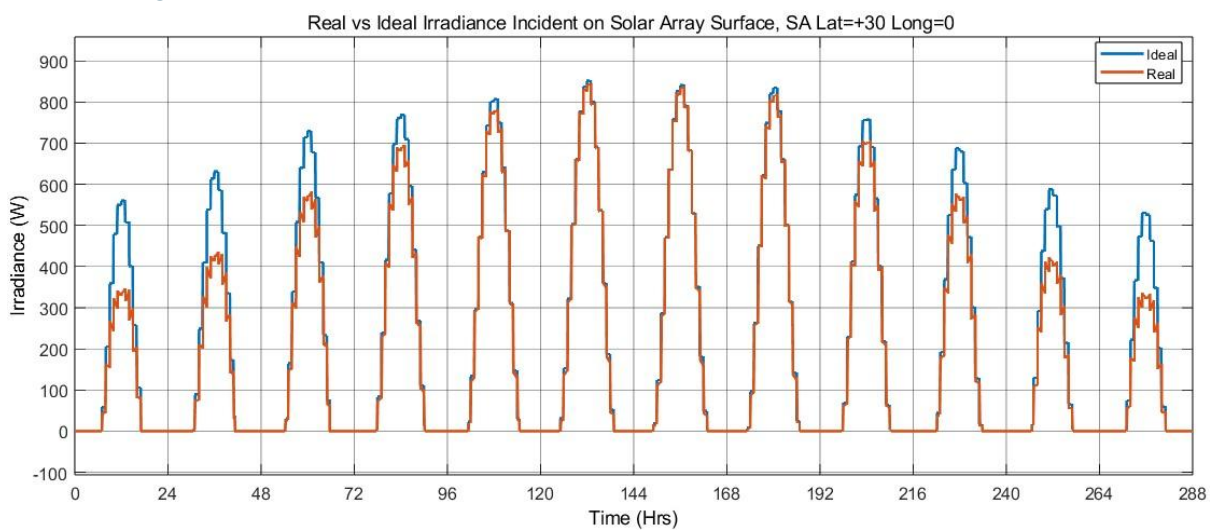


Figure 88: Single axis real vs maximum irradiance incident on the array surface, for scenario 3

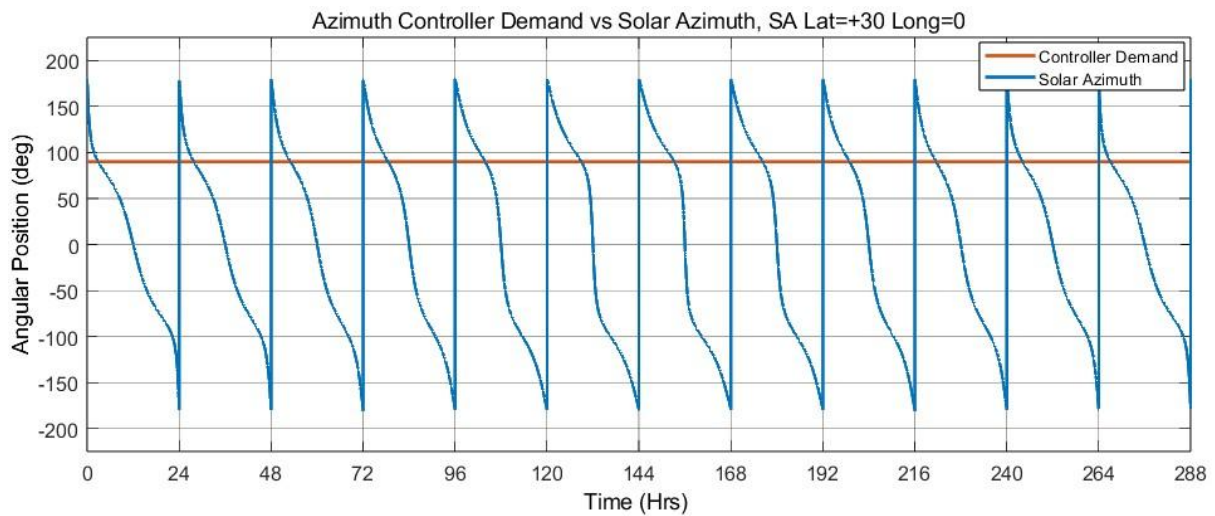


Figure 89: Real controller setpoint demand vs solar azimuth position for the single axis tracking of scenario 3

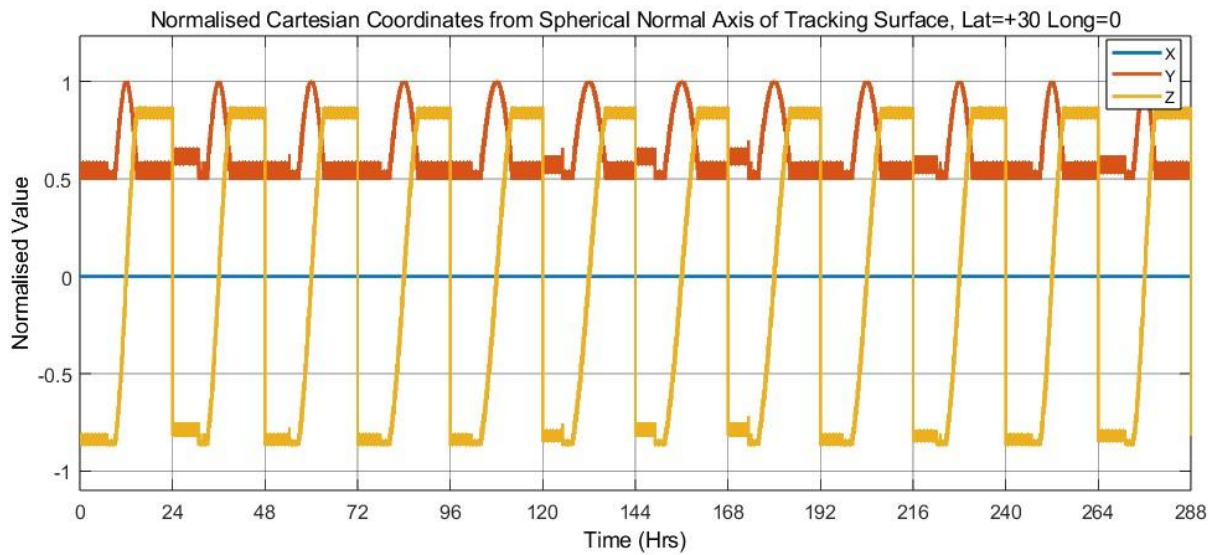


Figure 90: Single axis tracking surface normalised cartesian coordinates from normal of the array surface for scenario 3

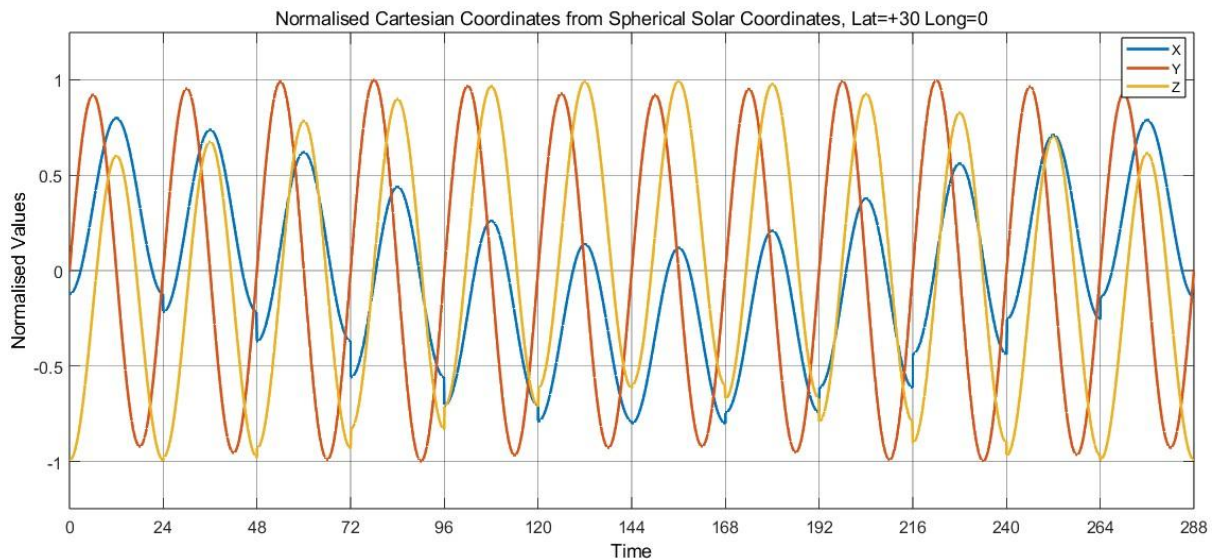


Figure 91: Normalised cartesian coordinates from spherical solar coordinates for scenario 3

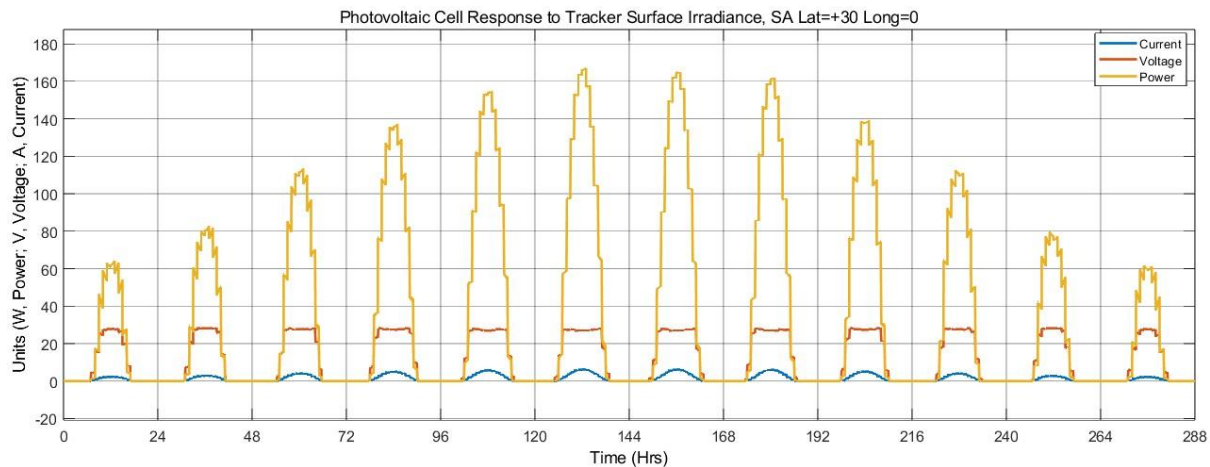


Figure 92: Power output by the photovoltaic module utilising the incident irradiation on the single axis tracking solar array surface for scenario 3

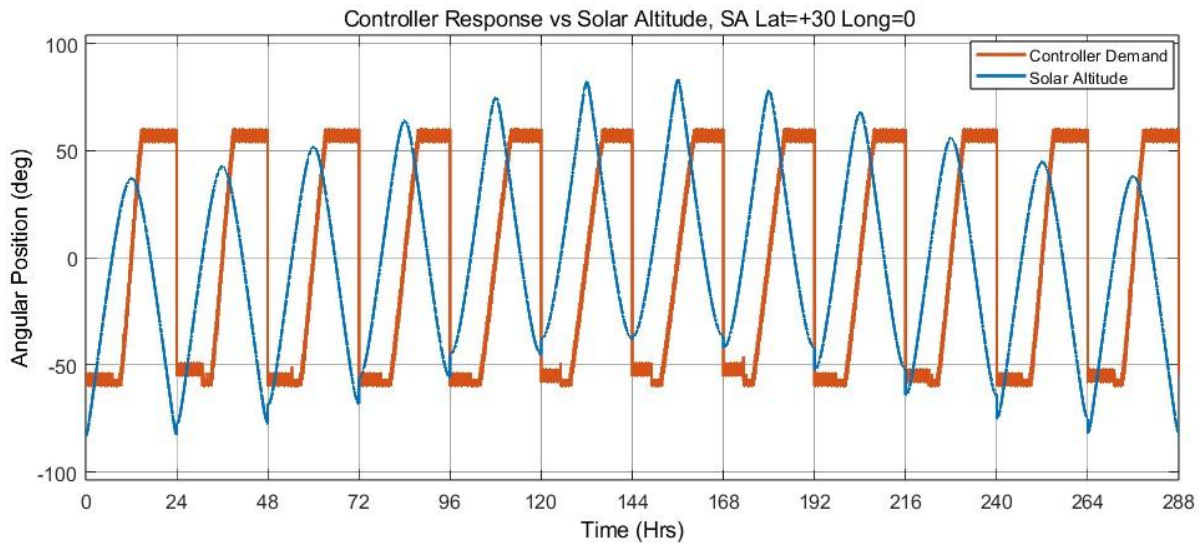
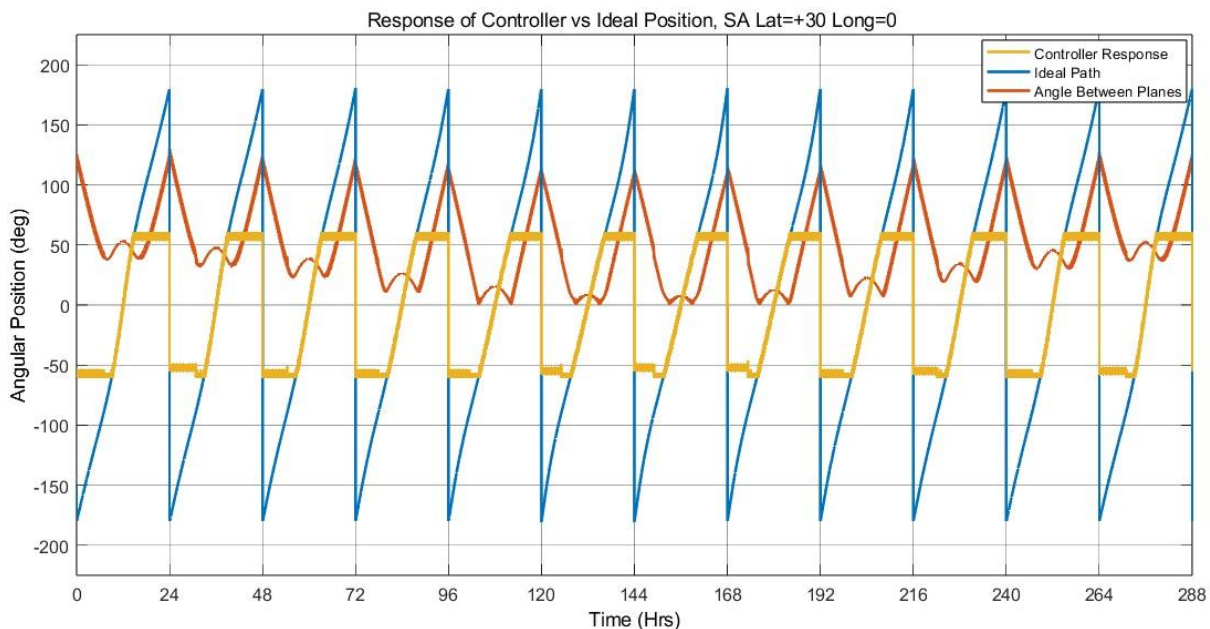


Figure 93: Real solar altitude angle vs the altitude setpoint demand by the controller, for scenario 3



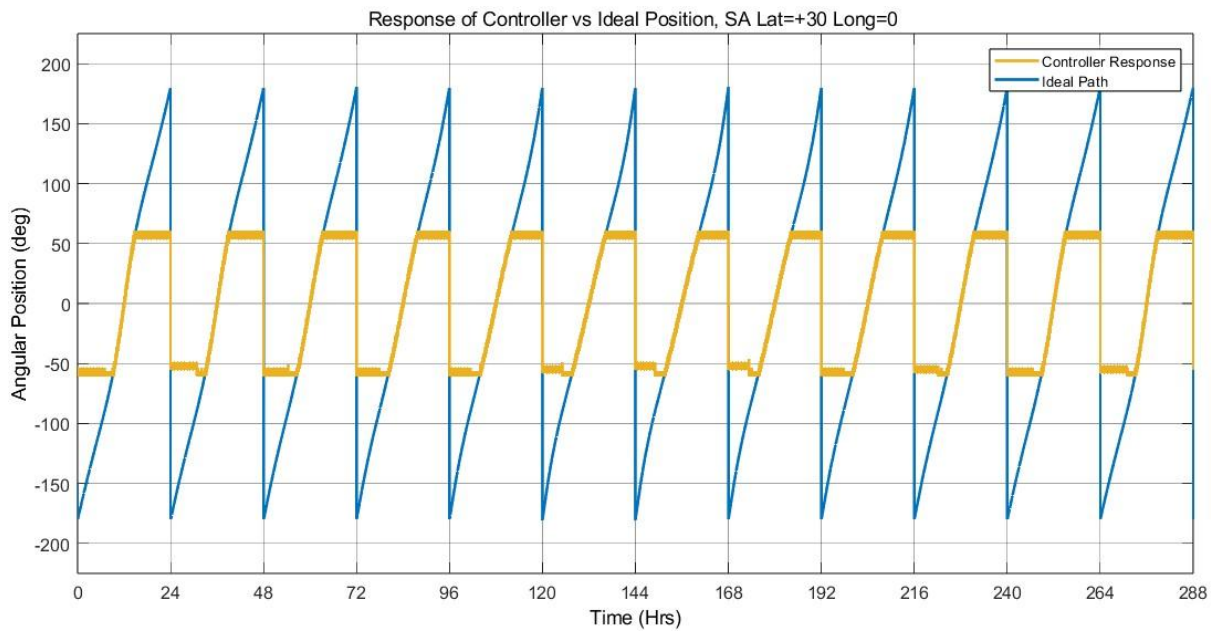


Figure 94: controller demand (Set point) with respect to the ideal path generated for the single axis tracking solar array in scenario 3

8.5.4 – Scenario 4

8.5.4a – Dual Axis

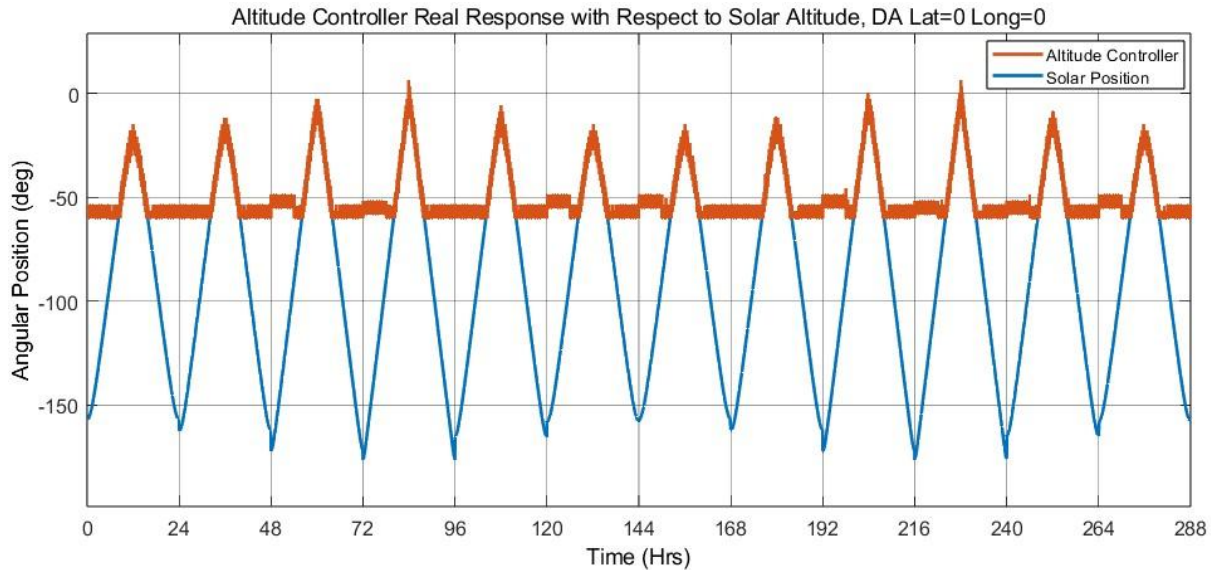


Figure 95: Altitude controller real response with respect to solar altitude for scenario 4

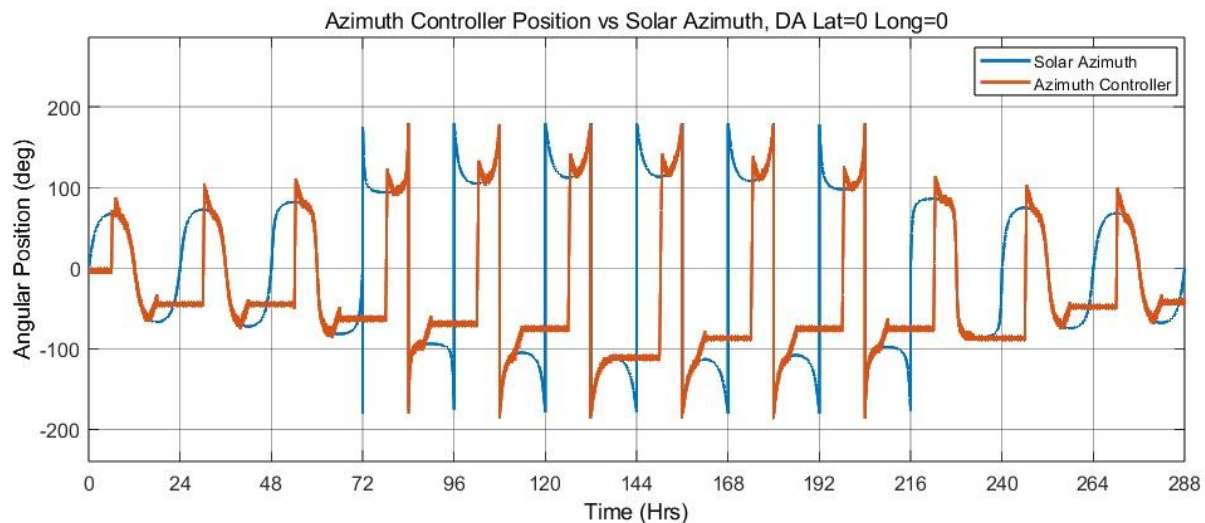


Figure 96: Azimuth controller real response with respect to solar altitude for scenario 4

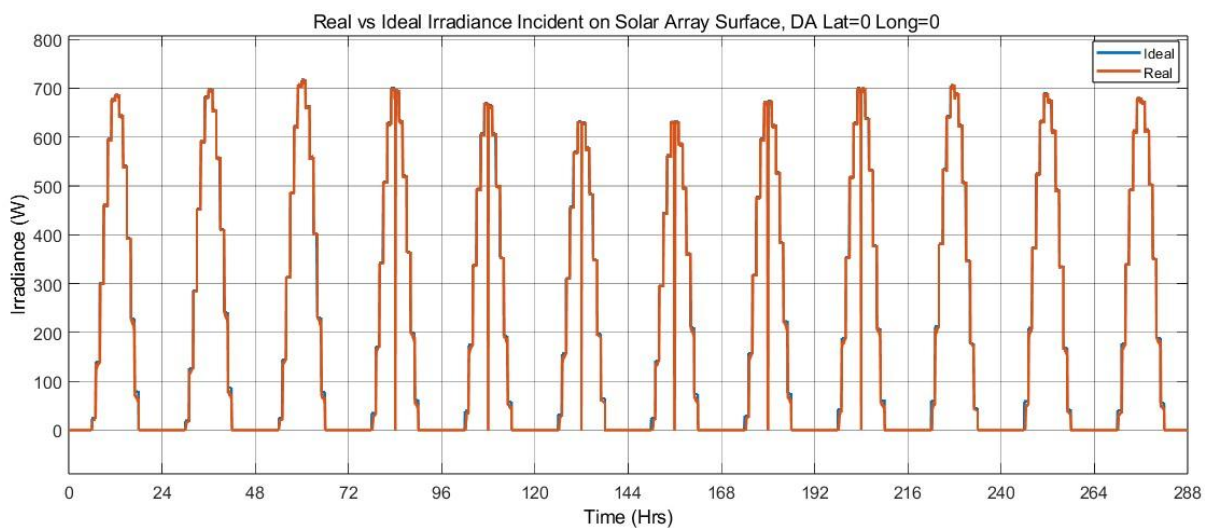


Figure 97: Real vs maximum incident irradiation on dual axis solar array surface for scenario 4

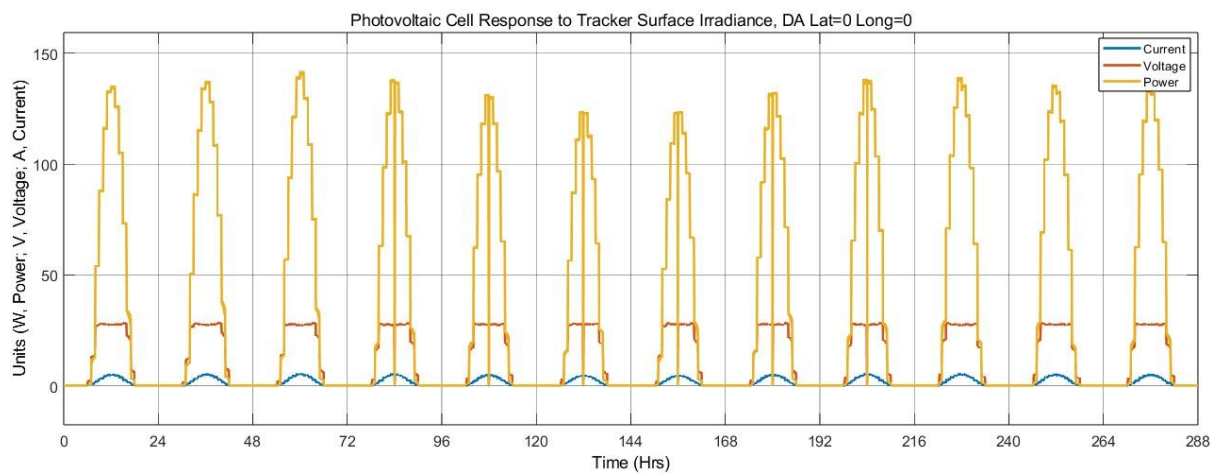


Figure 98: Photovoltaic model output for incident irradiation for dual axis tracking of scenario 4

8.5.4b – Single Axis

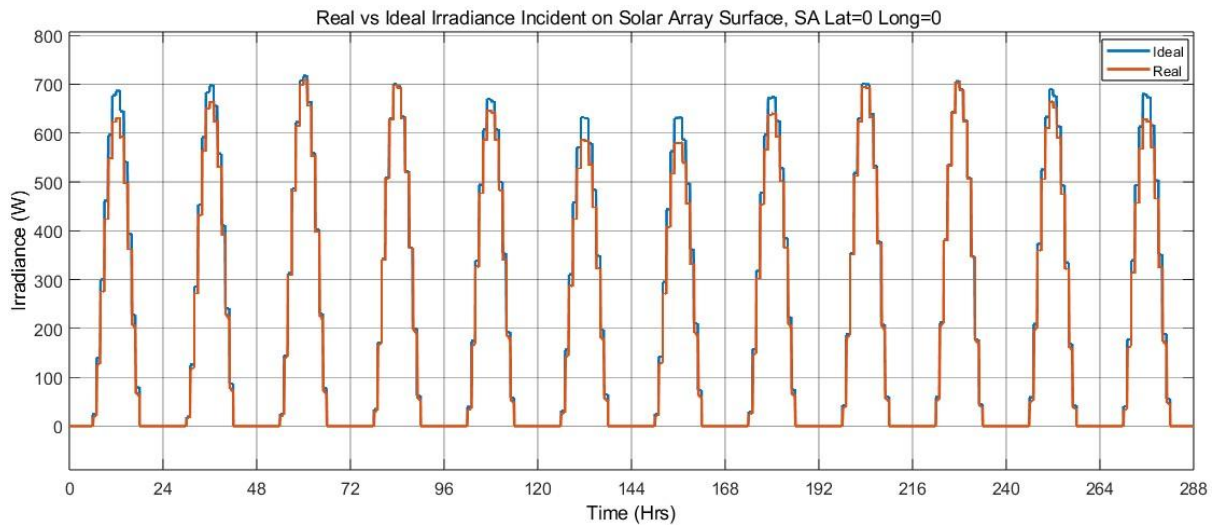


Figure 99: Single axis real vs maximum irradiance incident on the array surface, for scenario 4

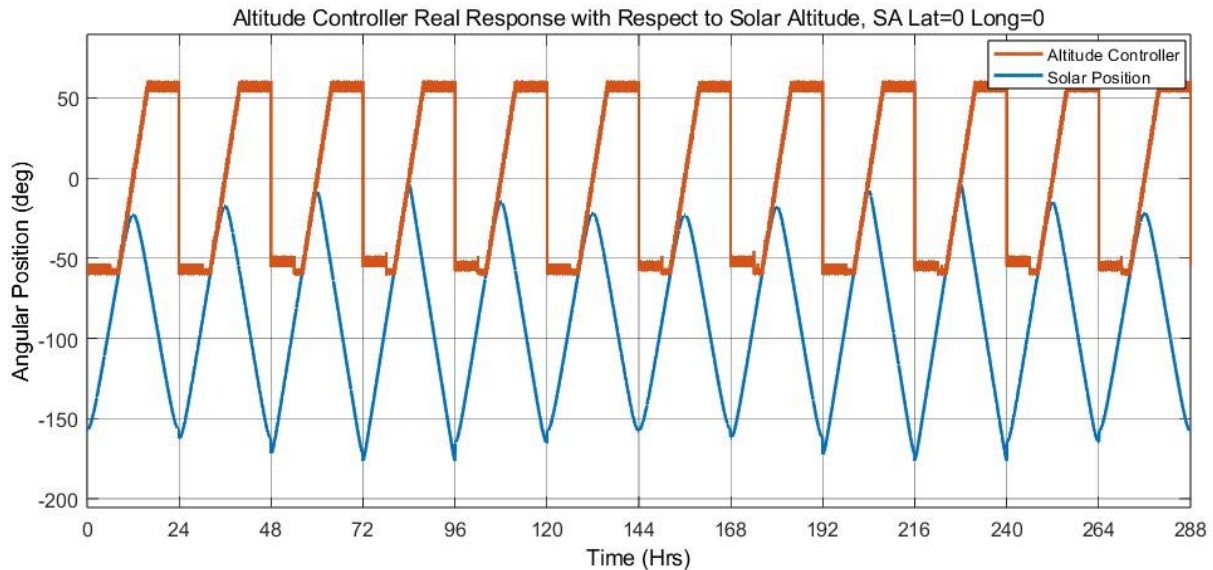


Figure 100: Real solar altitude angle vs the altitude setpoint demand by the controller, for scenario 4

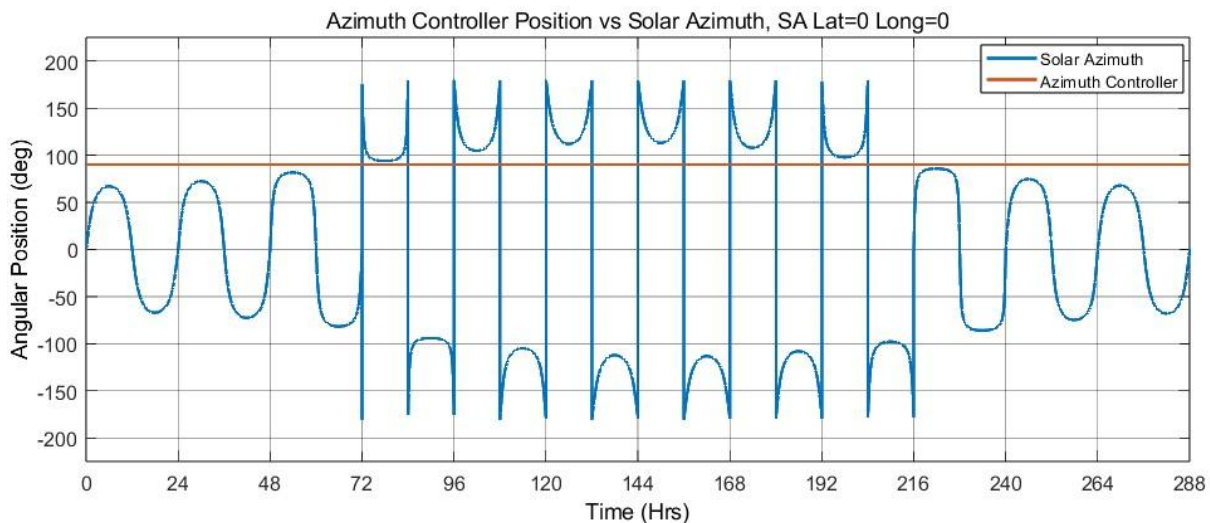


Figure 101: Real controller setpoint demand vs solar azimuth position for the single axis tracking of scenario 4

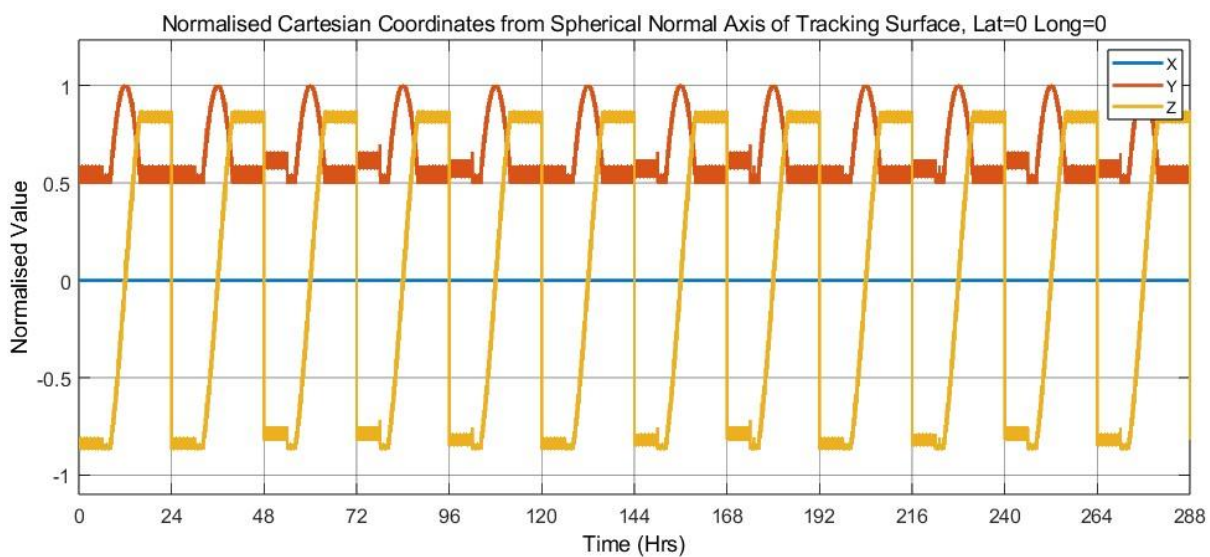


Figure 102: Single axis tracking surface normalised cartesian coordinates from normal of the array surface for scenario 4

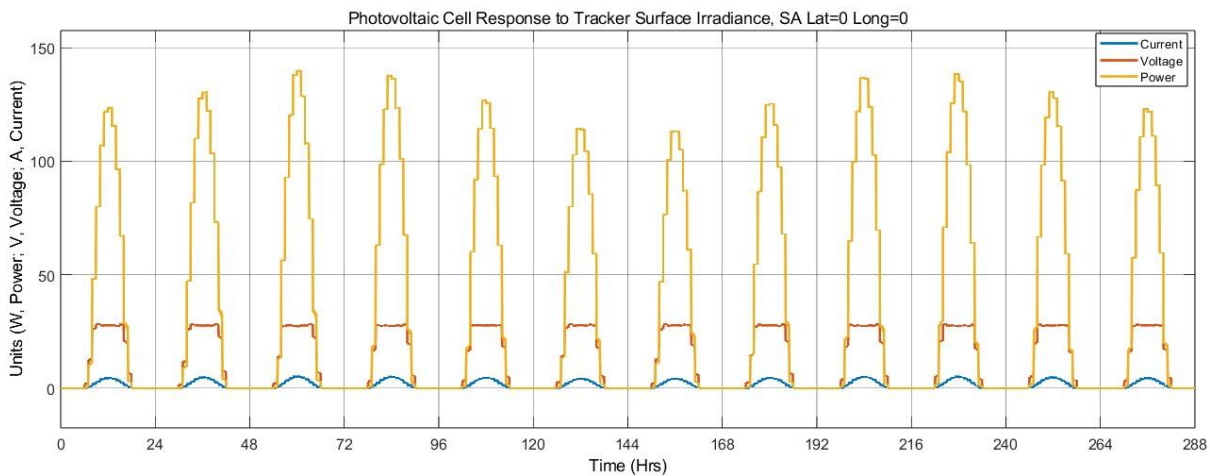


Figure 103: Power output by the photovoltaic module utilising the incident irradiation on the single axis tracking solar array surface for scenario 4

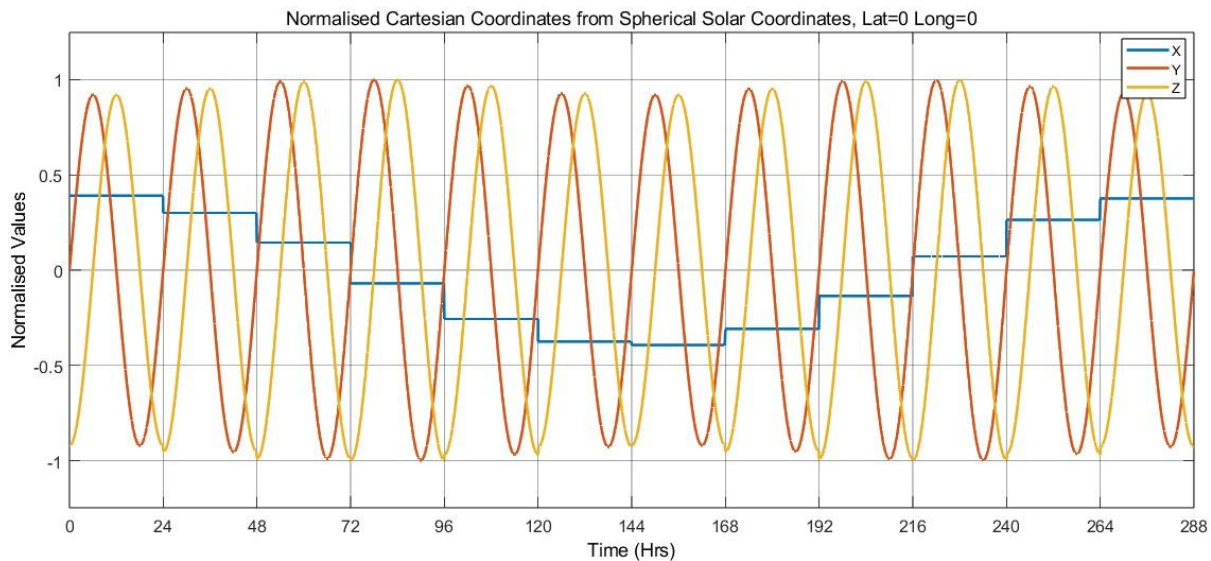
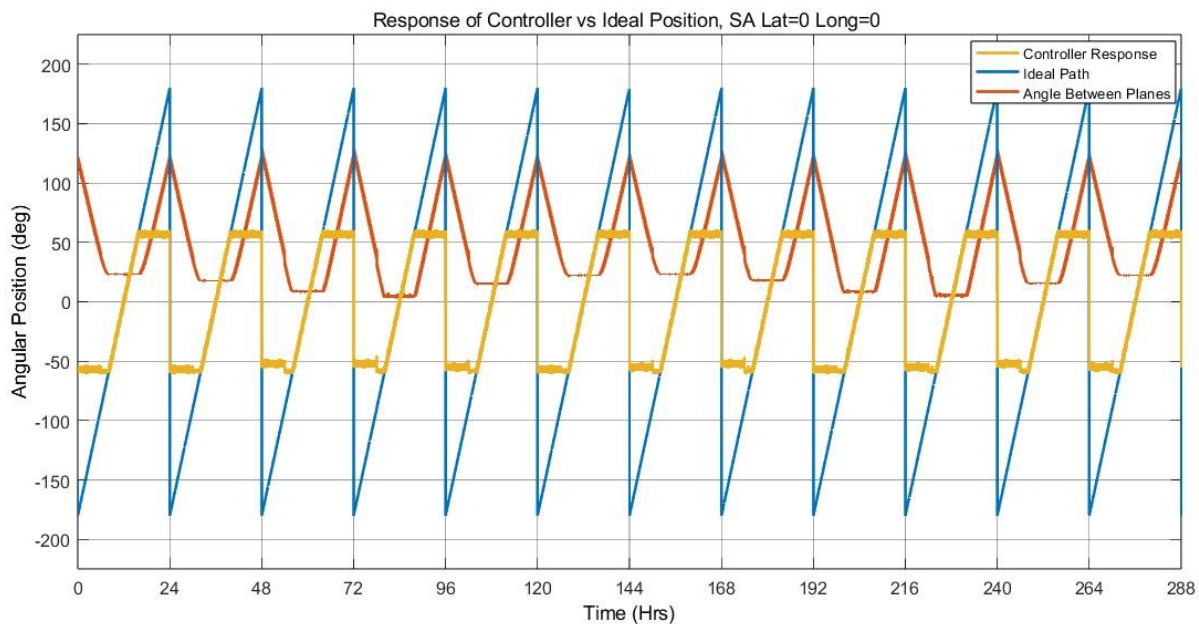


Figure 104: Normalised cartesian coordinates from spherical solar coordinates for scenario 4



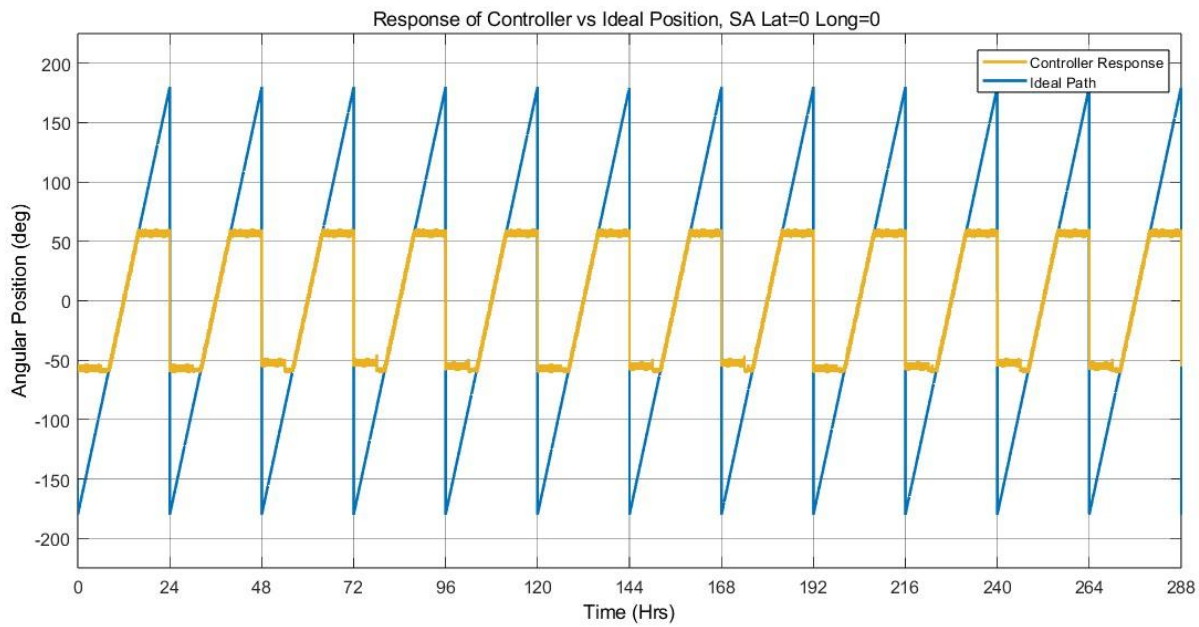


Figure 105: controller demand (Set point) with respect to the ideal path generated for the single axis tracking solar array in scenario 4

8.5.5 – Scenario 5

8.5.5a – Dual Axis

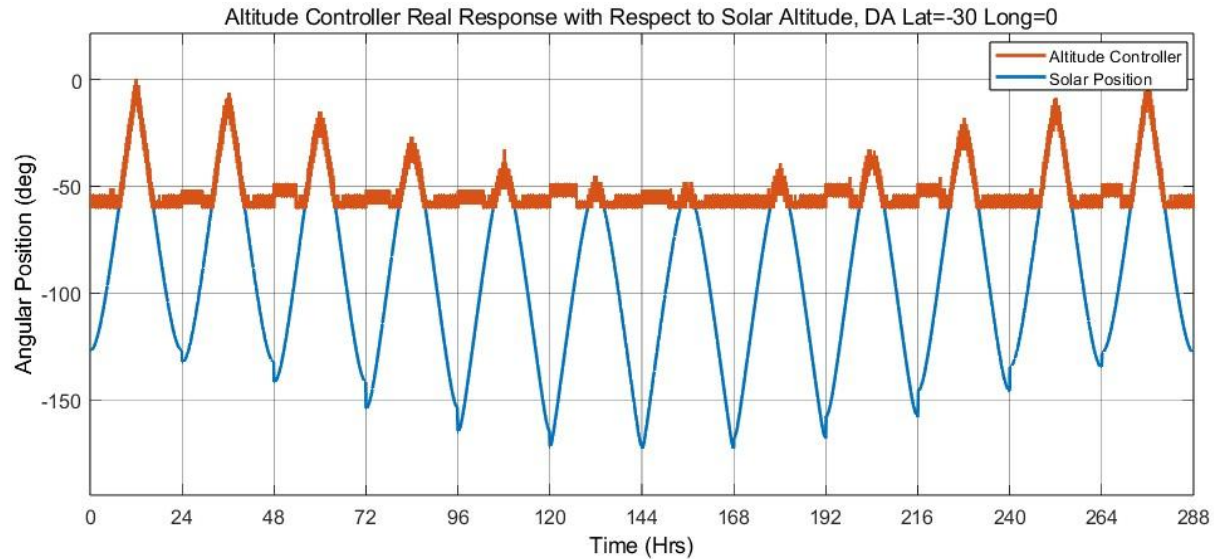


Figure 106: Altitude controller real response with respect to solar altitude for scenario 5

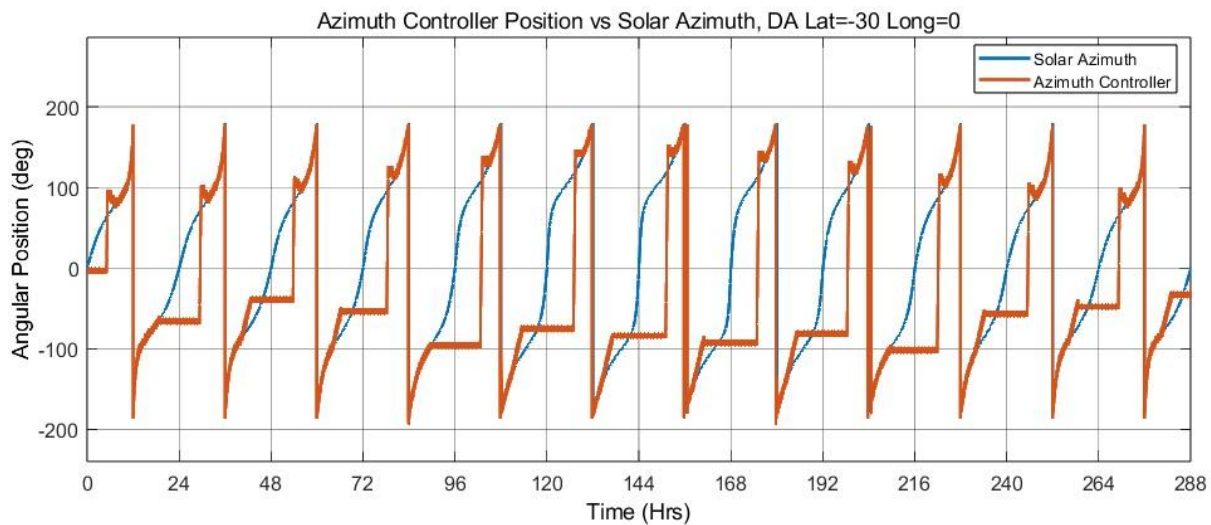


Figure 107: Azimuth controller real response with respect to solar altitude for scenario 5

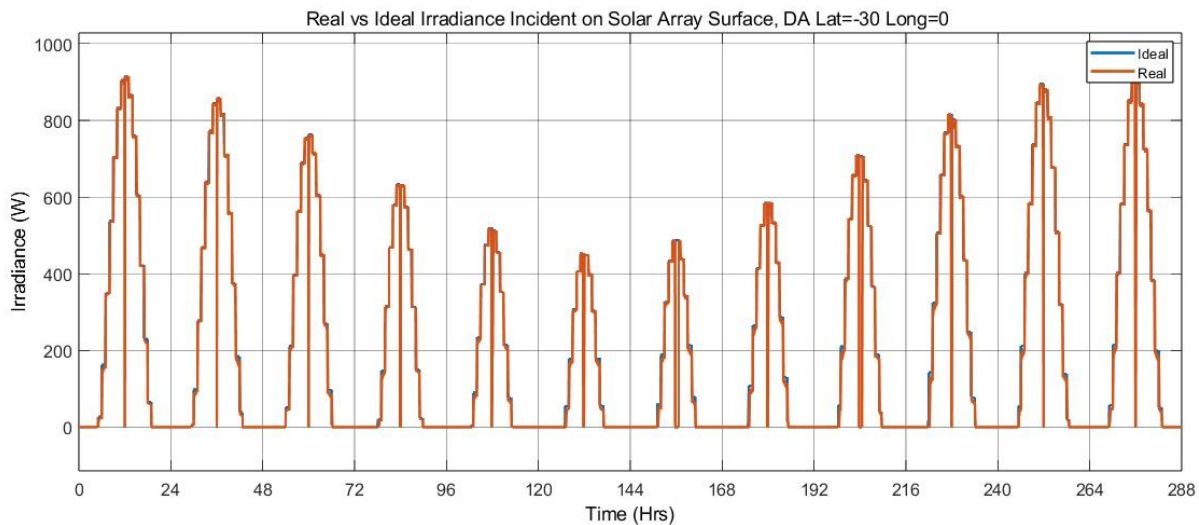


Figure 108: Real vs maximum incident irradiation on dual axis solar array surface for scenario 5

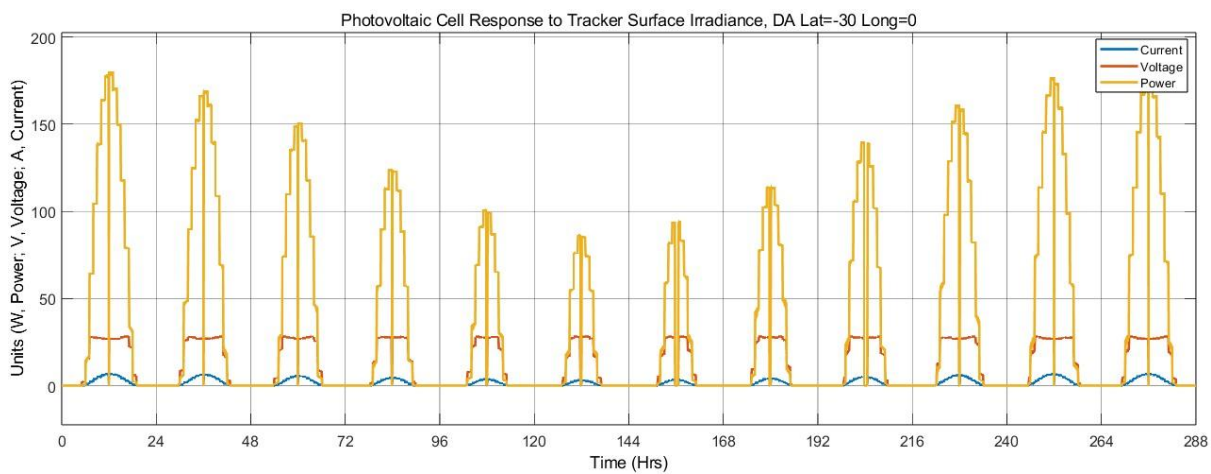


Figure 109: Photovoltaic model output for incident irradiation for dual axis tracking of scenario 5

9.5.5b – Single Axis

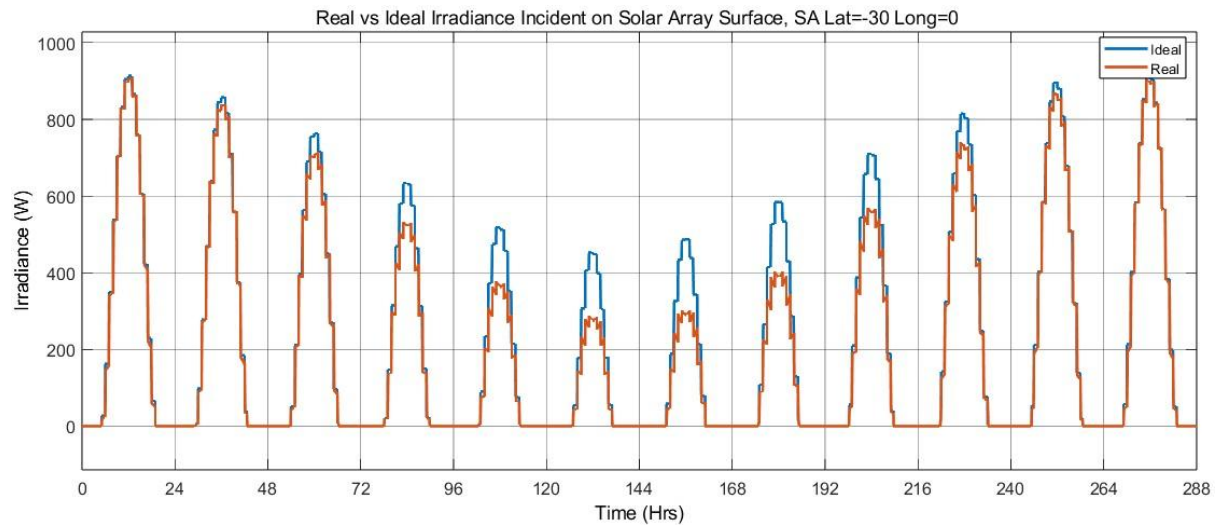


Figure 110:Single axis real vs maximum irradiance incident on the array surface, for scenario 5

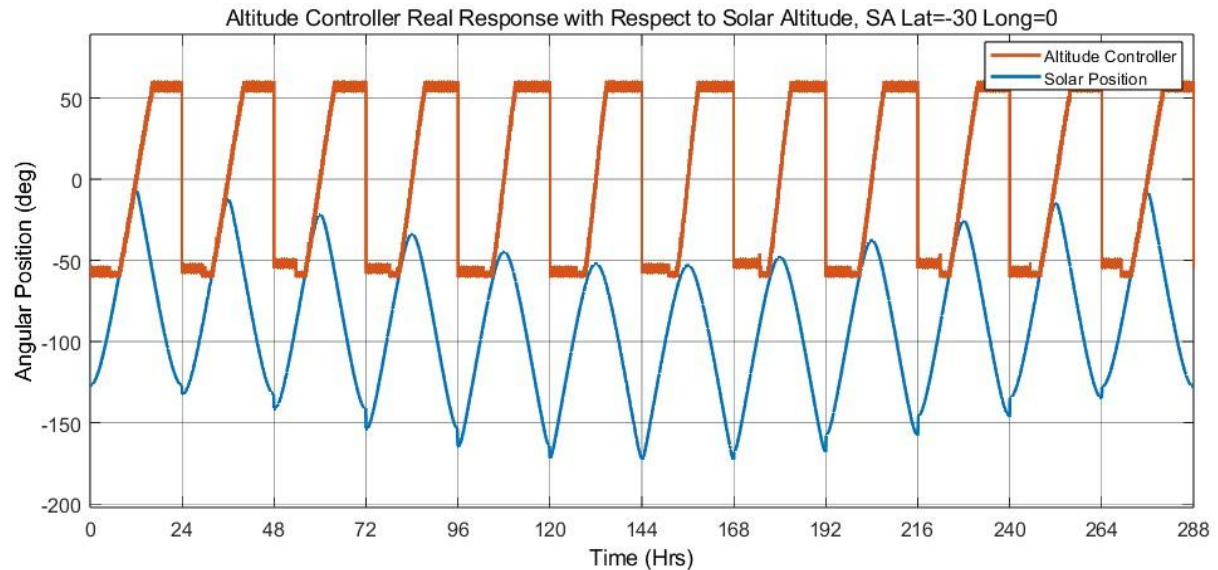


Figure 111:Real solar altitude angle vs the altitude setpoint demand by the controller, for scenario 5

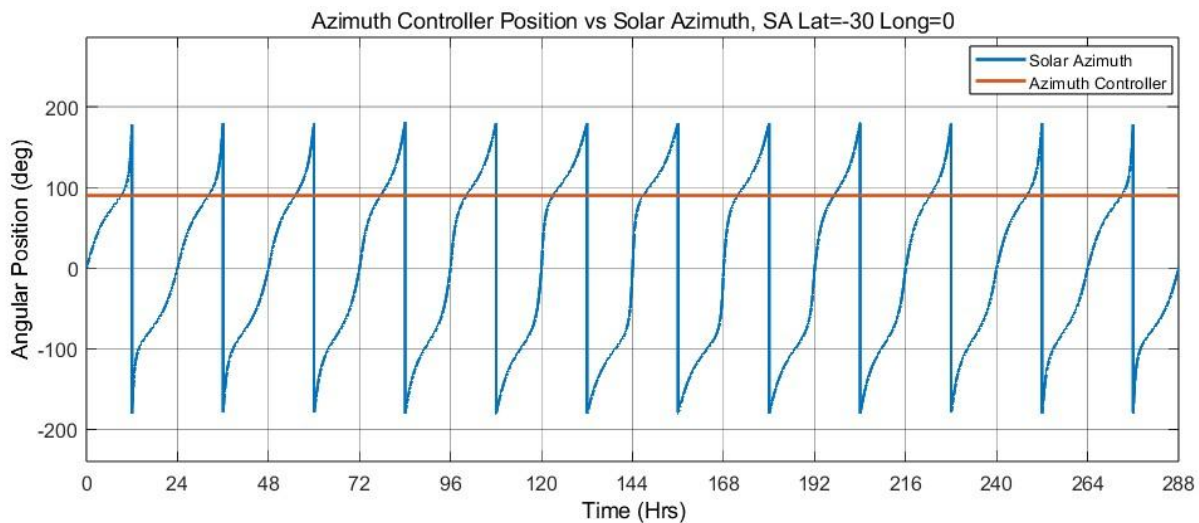


Figure 112: Real controller setpoint demand vs solar azimuth position for the single axis tracking of scenario 5

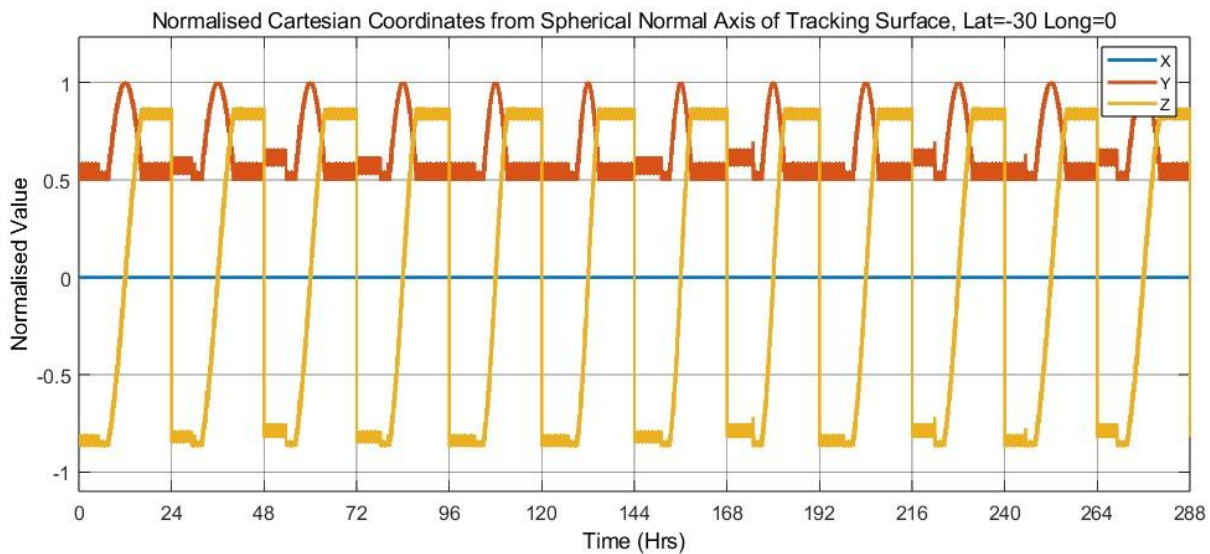


Figure 113: Single axis tracking surface normalised cartesian coordinates from normal of the array surface for scenario 5

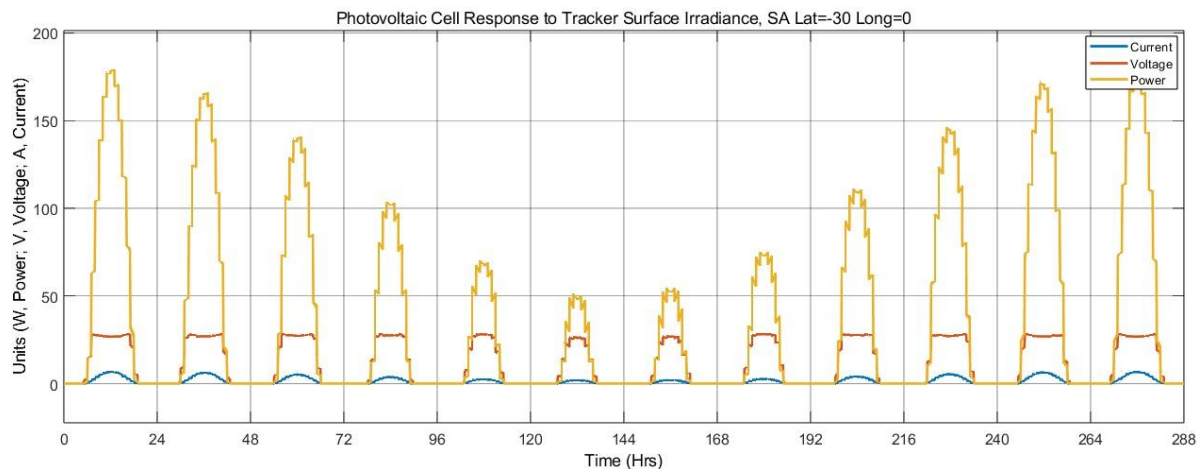


Figure 114: Power output by the photovoltaic module utilising the incident irradiation on the single axis tracking solar array surface for scenario 5

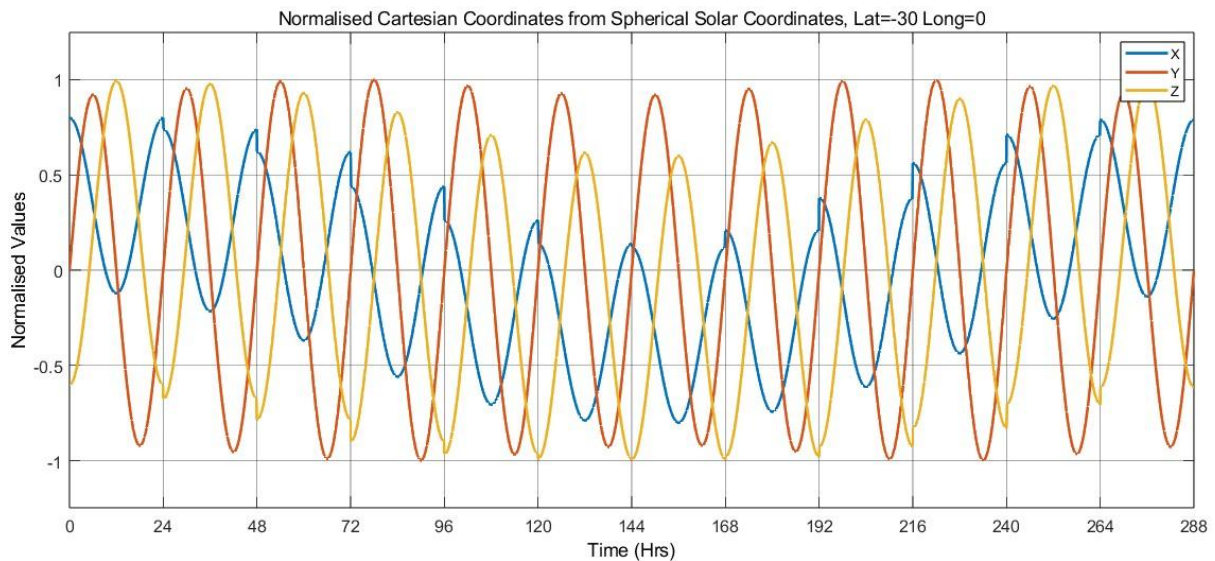
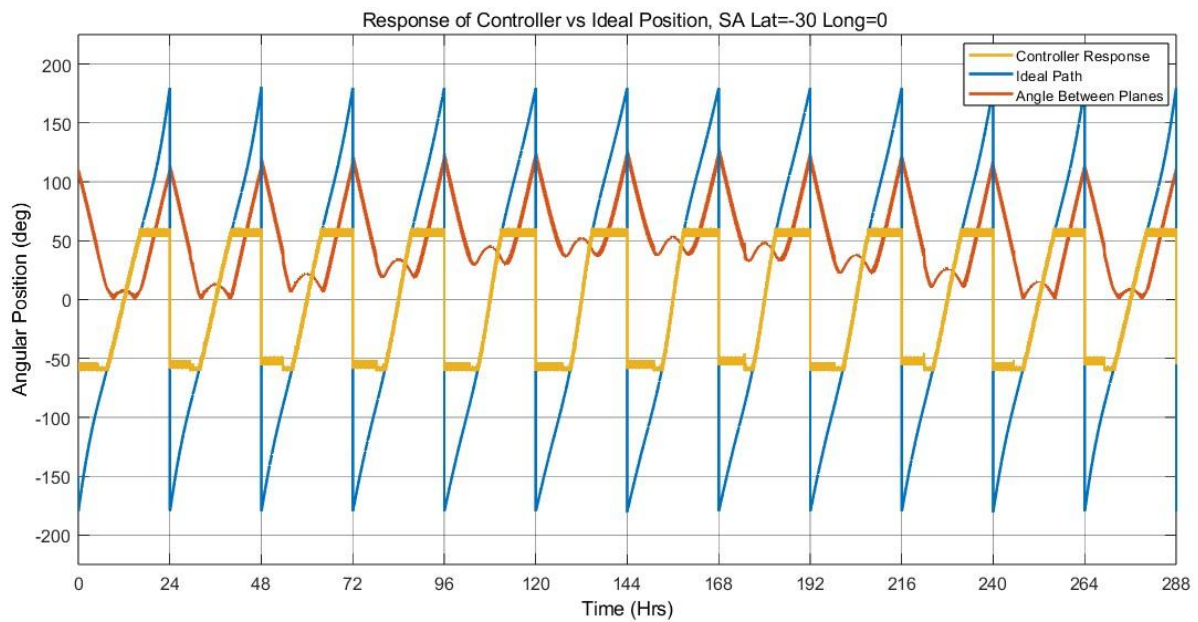


Figure 115: Normalised cartesian coordinates from spherical solar coordinates for scenario 5



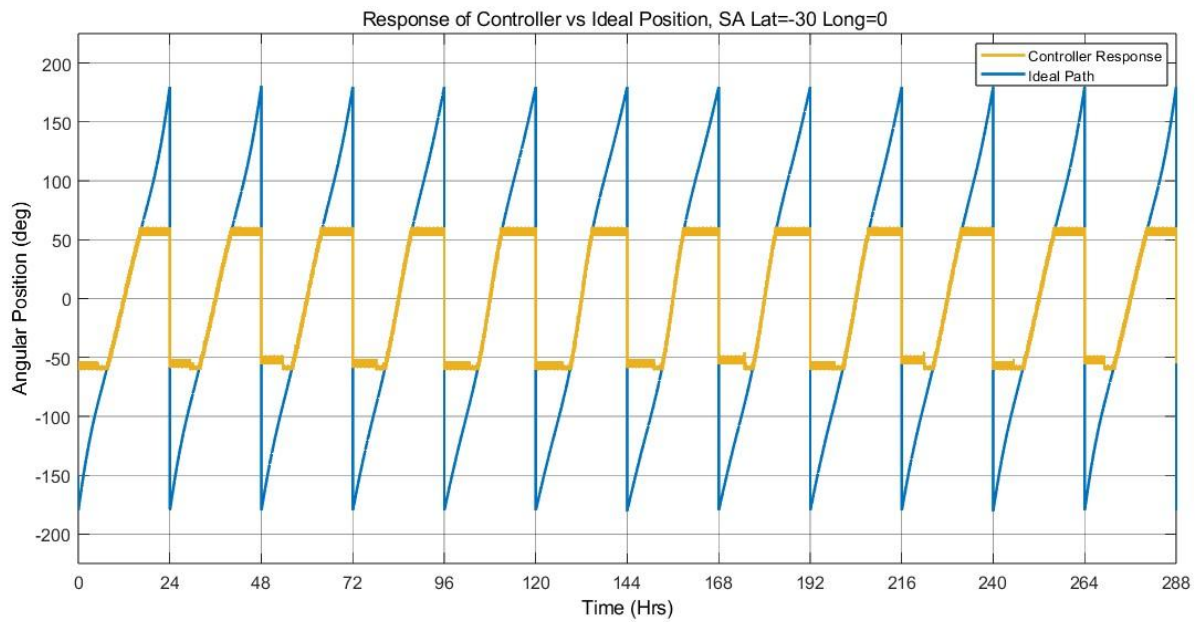


Figure 116: controller demand (Set point) with respect to the ideal path generated for the single axis tracking solar array in scenario 5

8.5.6 – Scenario 6

8.5.6a – Dual Axis

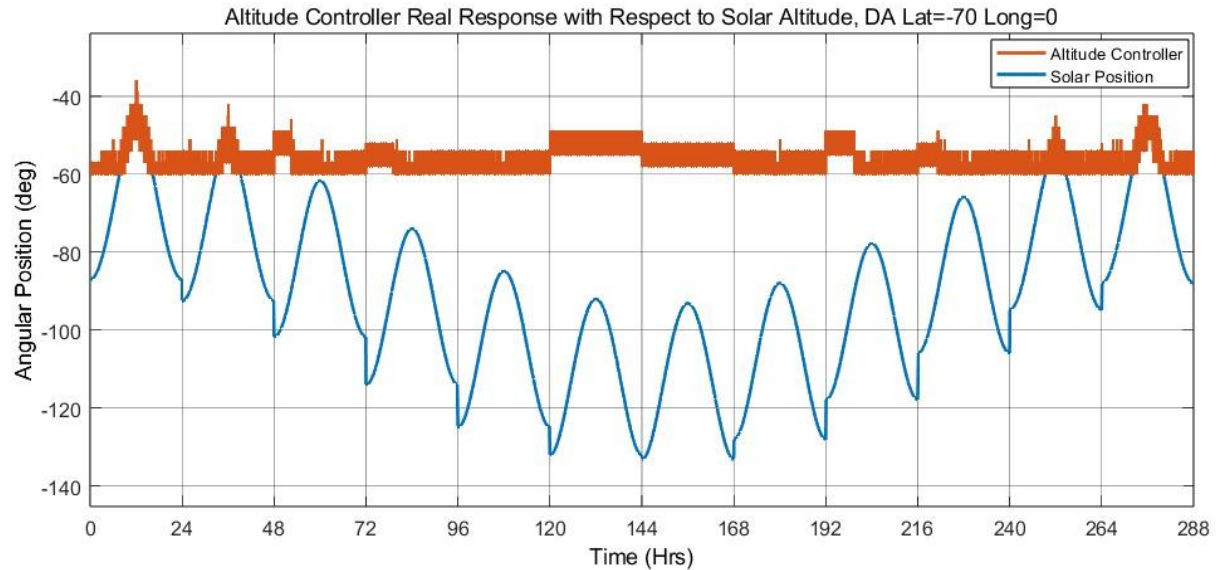


Figure 117: Altitude controller real response with respect to solar altitude for scenario 6

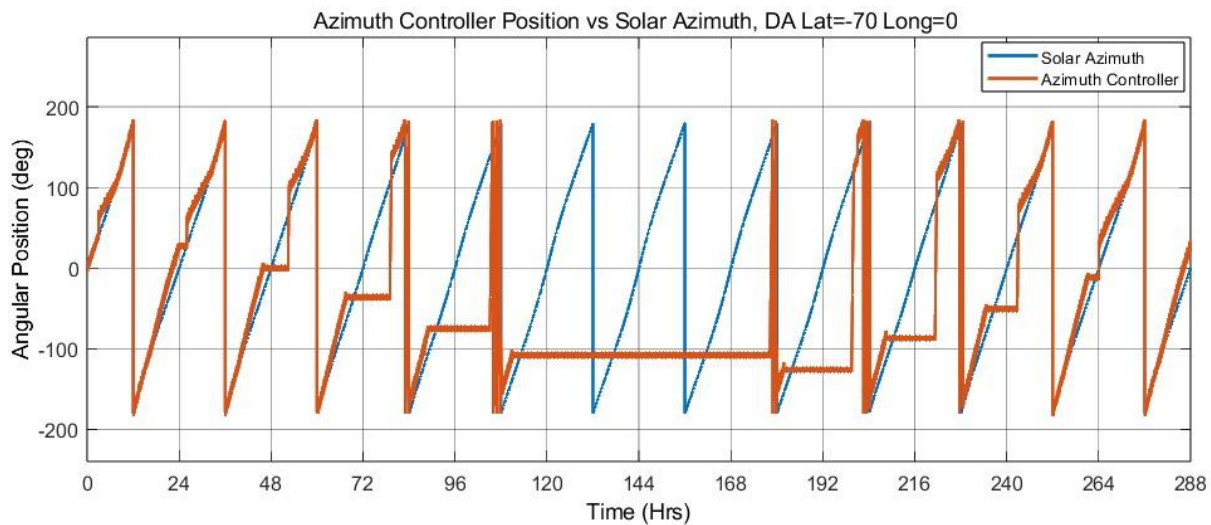


Figure 118: Azimuth controller real response with respect to solar altitude for scenario 6

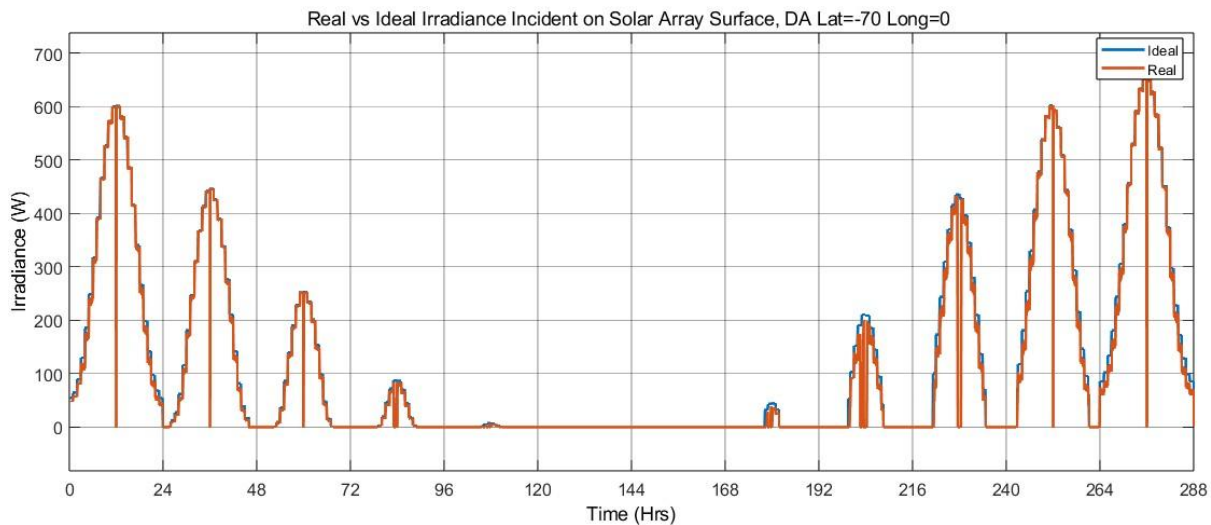


Figure 119: Real vs maximum incident irradiation on dual axis solar array surface for scenario 6

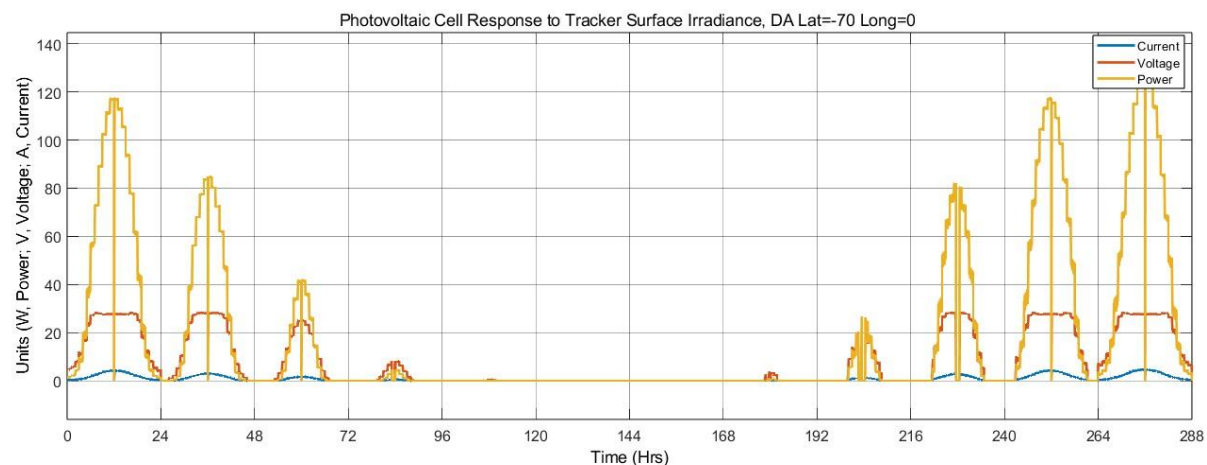


Figure 120: Photovoltaic model output for incident irradiation for dual axis tracking of scenario 6

8.5.6b – Single Axis

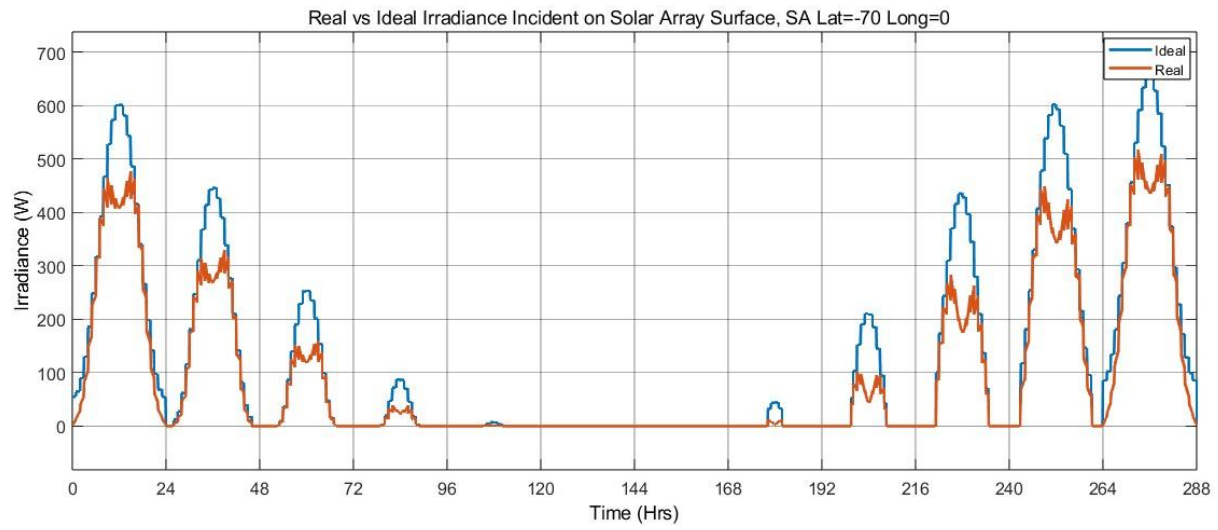


Figure 121: Single axis real vs maximum irradiance incident on the array surface, for scenario 6

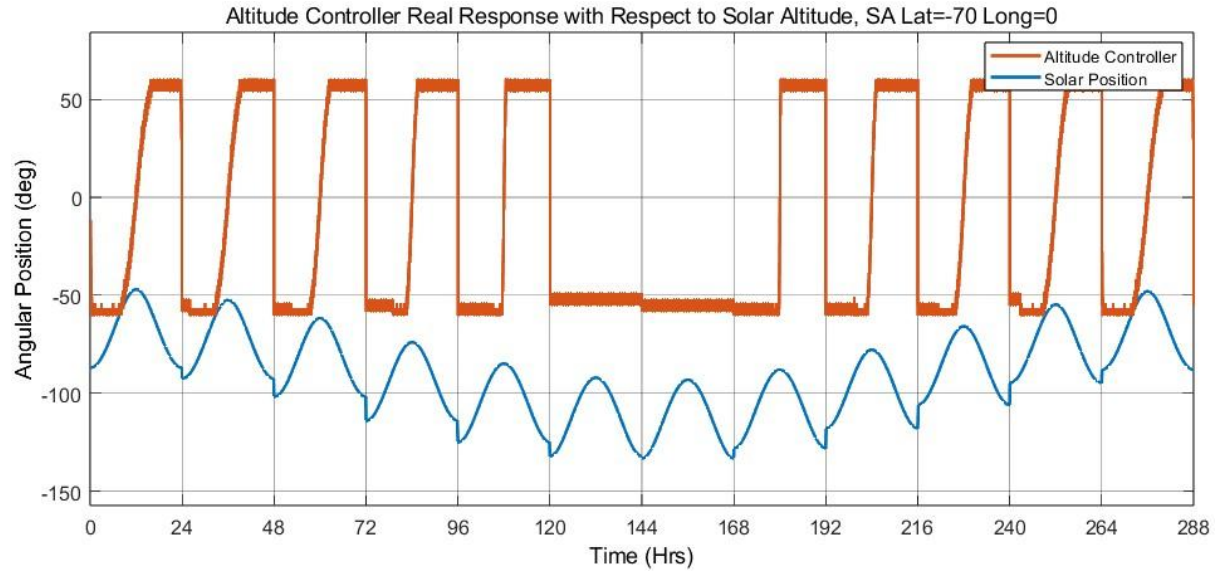


Figure 122: Real solar altitude angle vs the altitude setpoint demand by the controller, for scenario 6

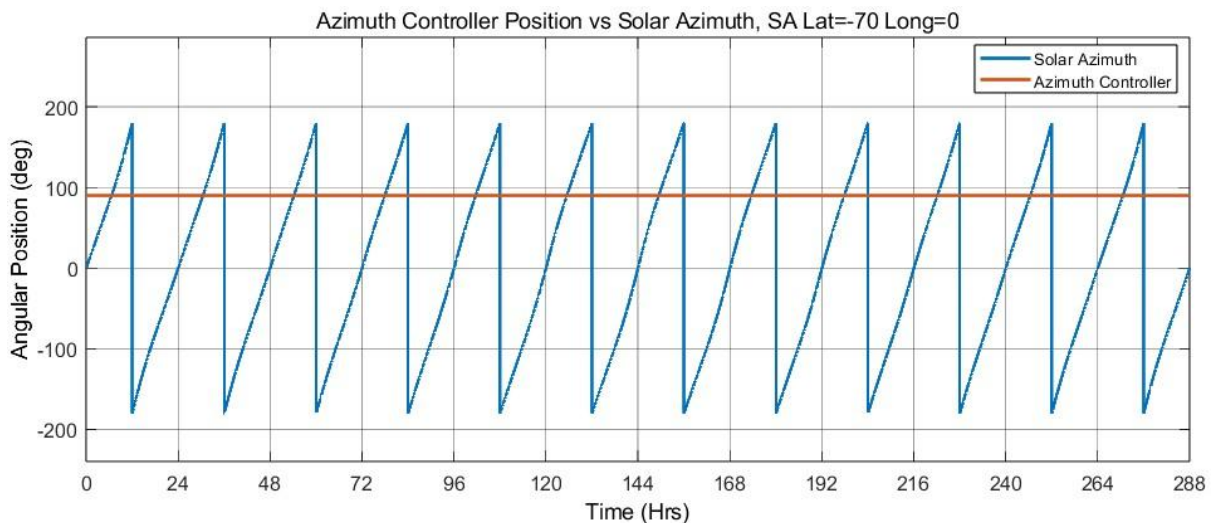


Figure 123: Real controller setpoint demand vs solar azimuth position for the single axis tracking of scenario 6

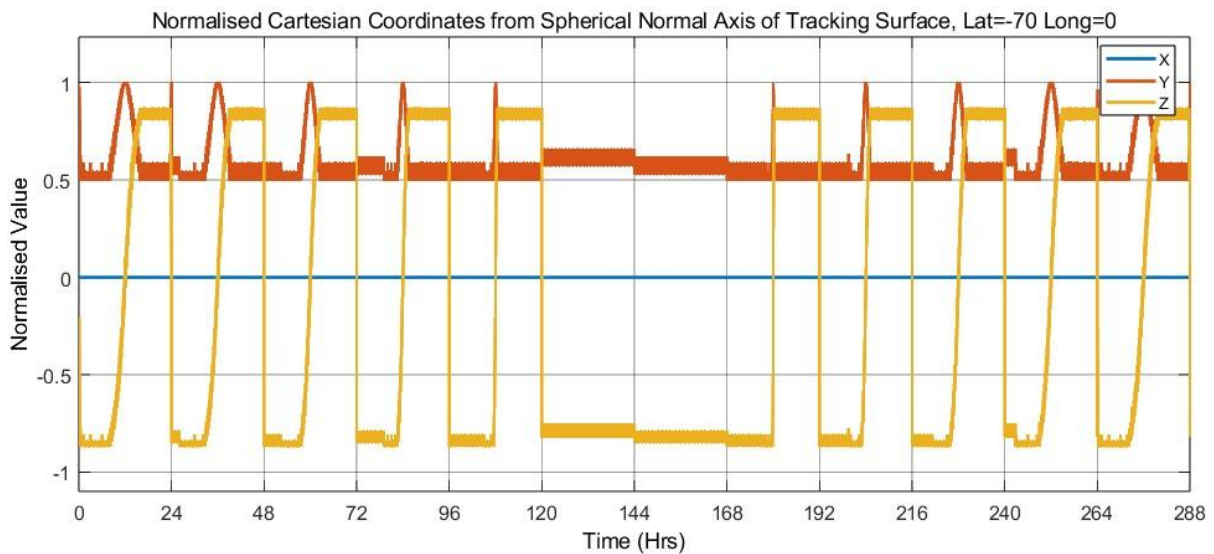


Figure 124: Single axis tracking surface normalised cartesian coordinates from normal of the array surface for scenario 6

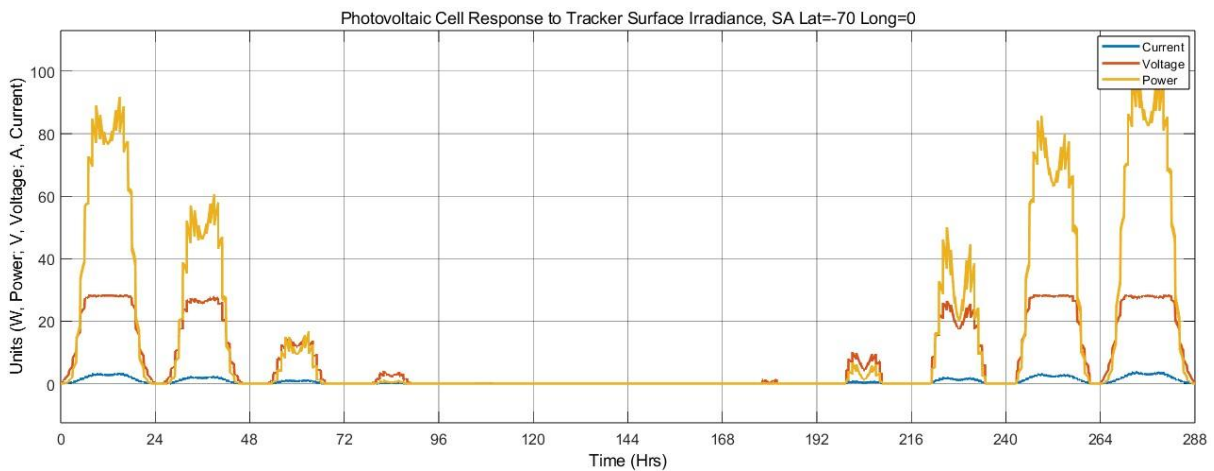


Figure 125: Power output by the photovoltaic module utilising the incident irradiation on the single axis tracking solar array surface for scenario 6

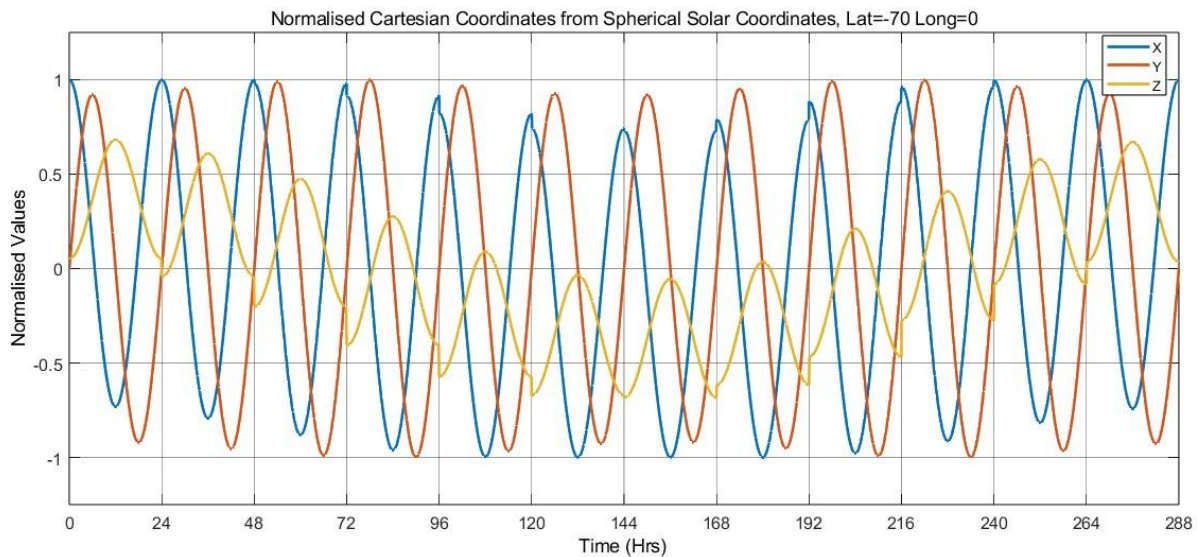
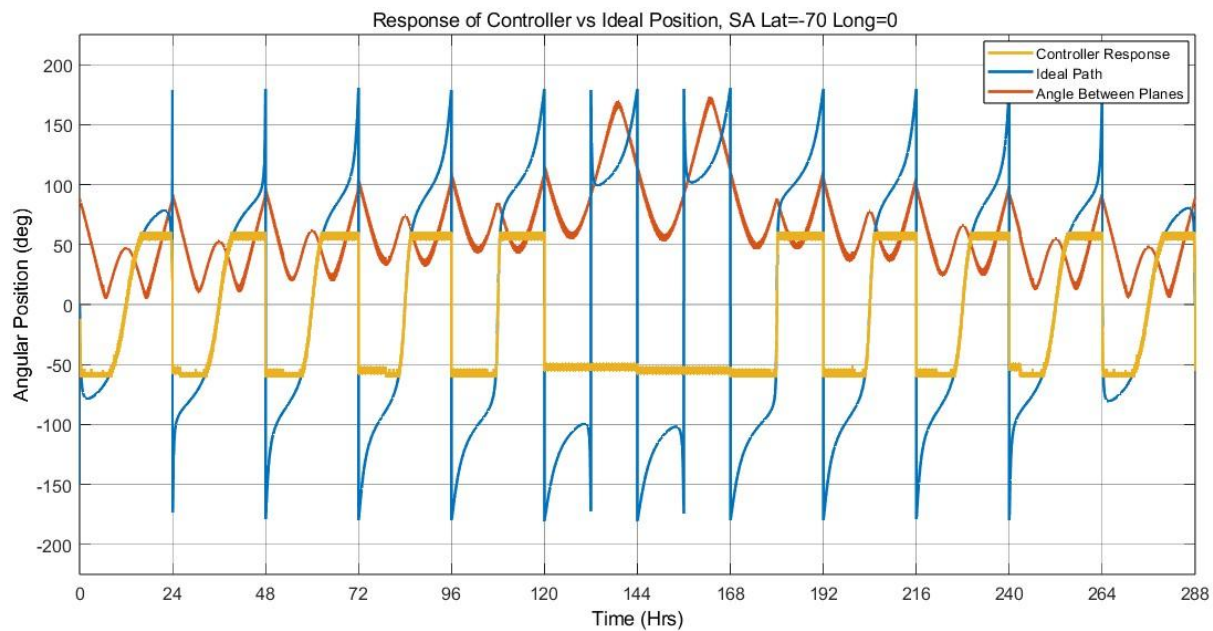


Figure 126: Normalised cartesian coordinates from spherical solar coordinates for scenario 6



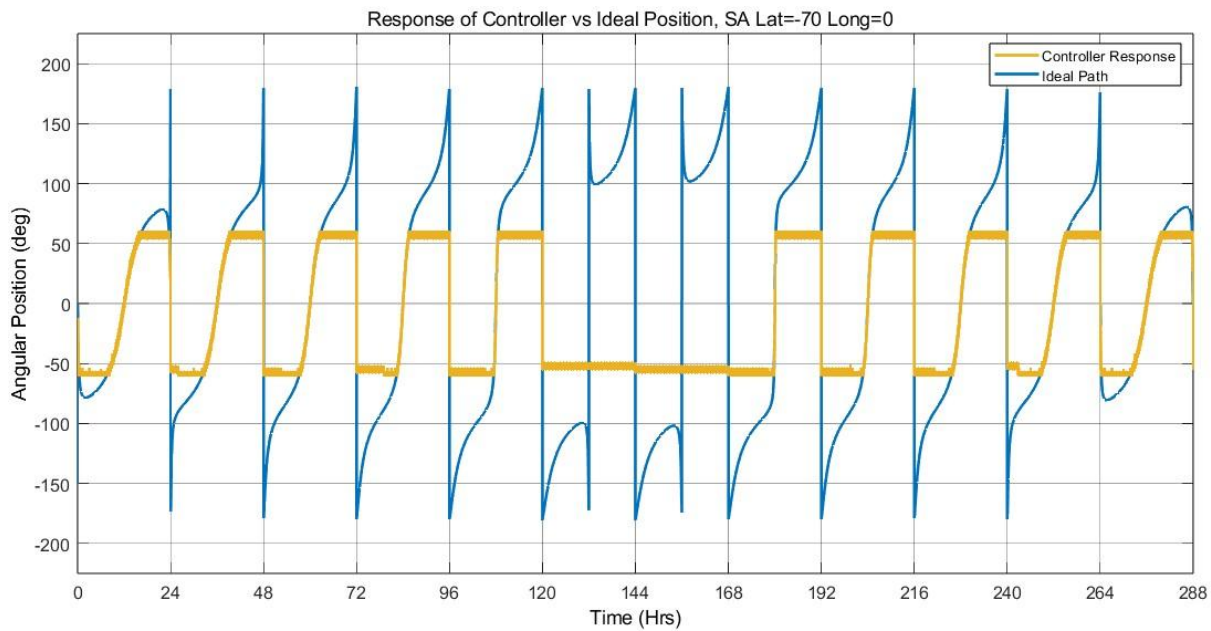


Figure 127: controller demand (Set point) with respect to the ideal path generated for the single axis tracking solar array in scenario 6

8.5.7 – MPPT Efficiency as % of Maximum Irradiance Incident on Module

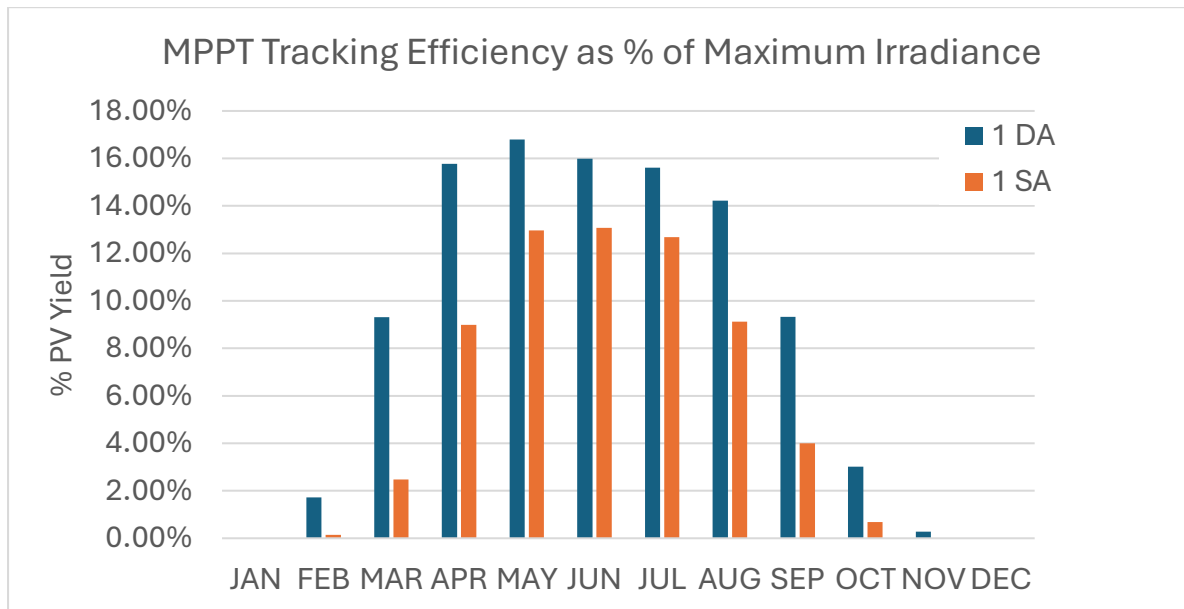


Figure 128: MPPT Tracking strategy efficiency as a percentage of maximum irradiation utilised as output power for scenario 1.

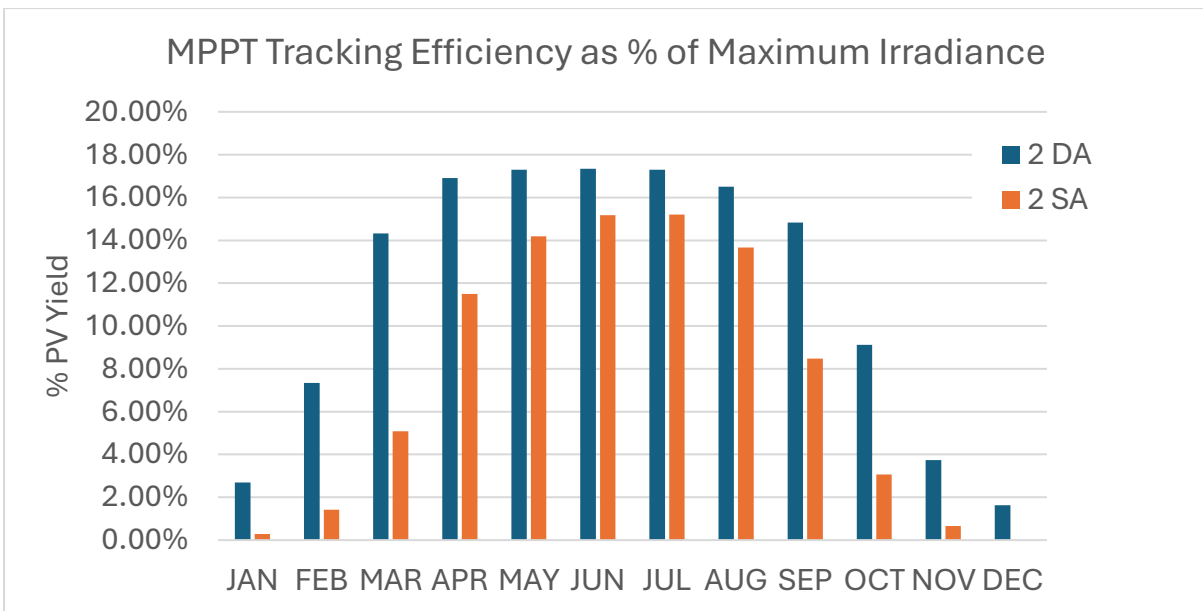


Figure 129: MPPT Tracking strategy efficiency as a percentage of maximum irradiation utilised as output power for scenario 2

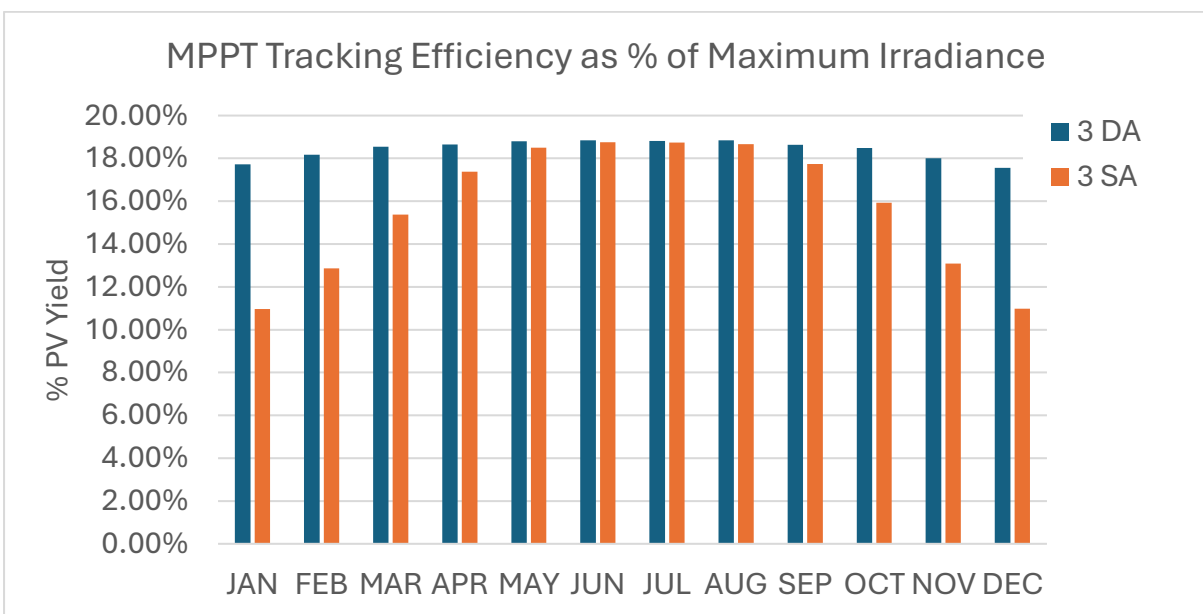


Figure 130: MPPT Tracking strategy efficiency as a percentage of maximum irradiation utilised as output power for scenario 3

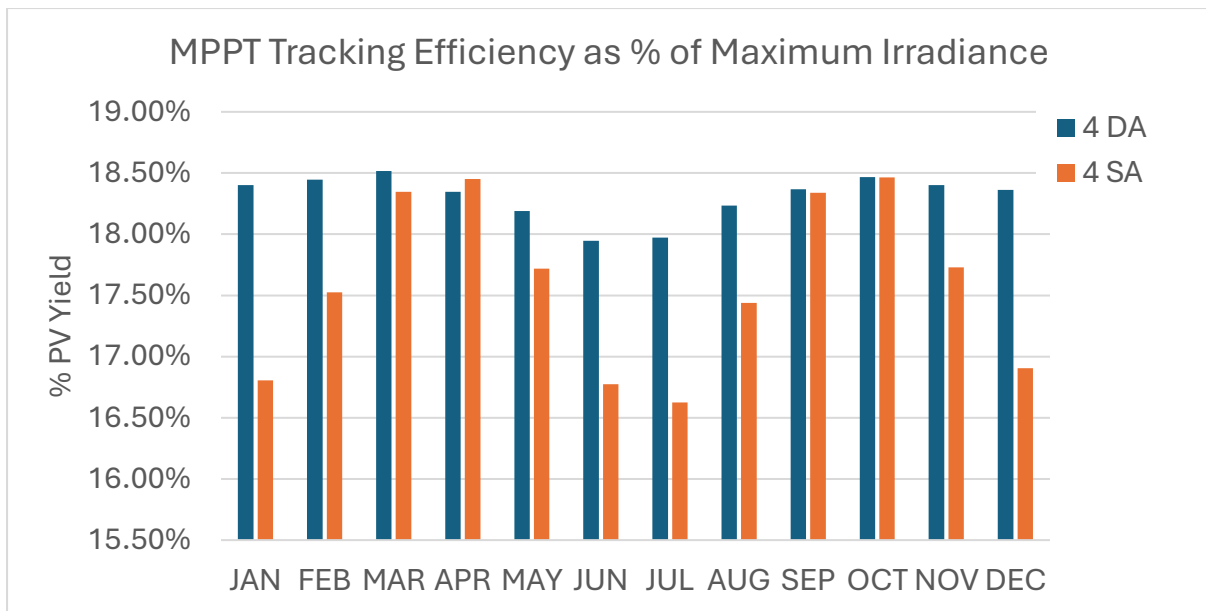


Figure 131: MPPT Tracking strategy efficiency as a percentage of maximum irradiation utilised as output power for scenario 4

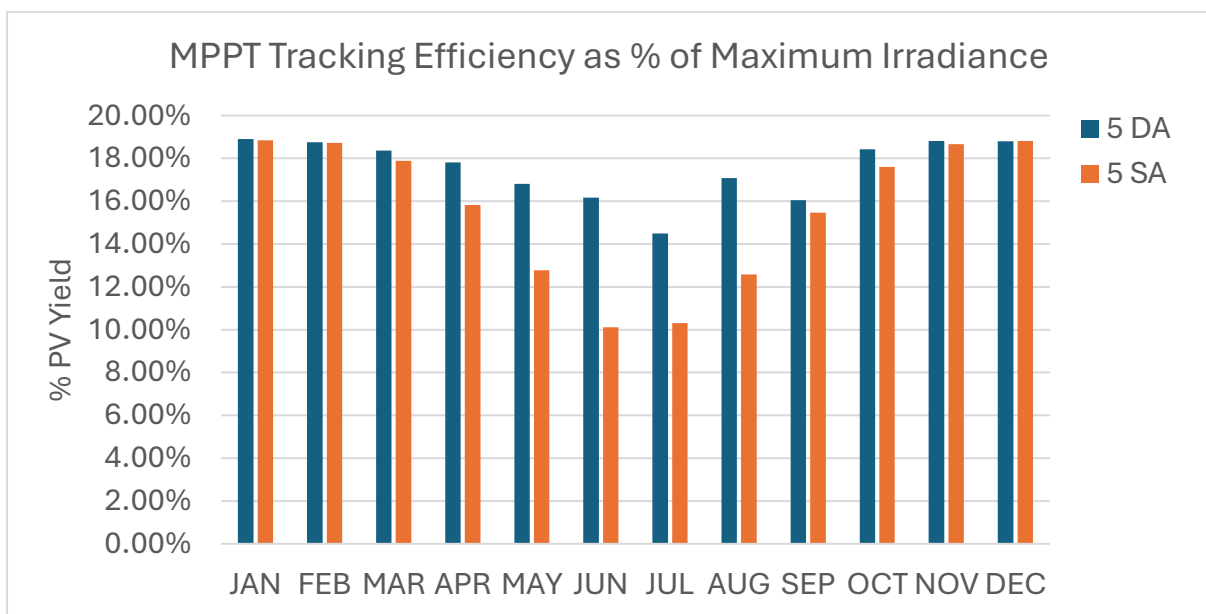


Figure 132: MPPT Tracking strategy efficiency as a percentage of maximum irradiation utilised as output power for scenario 5

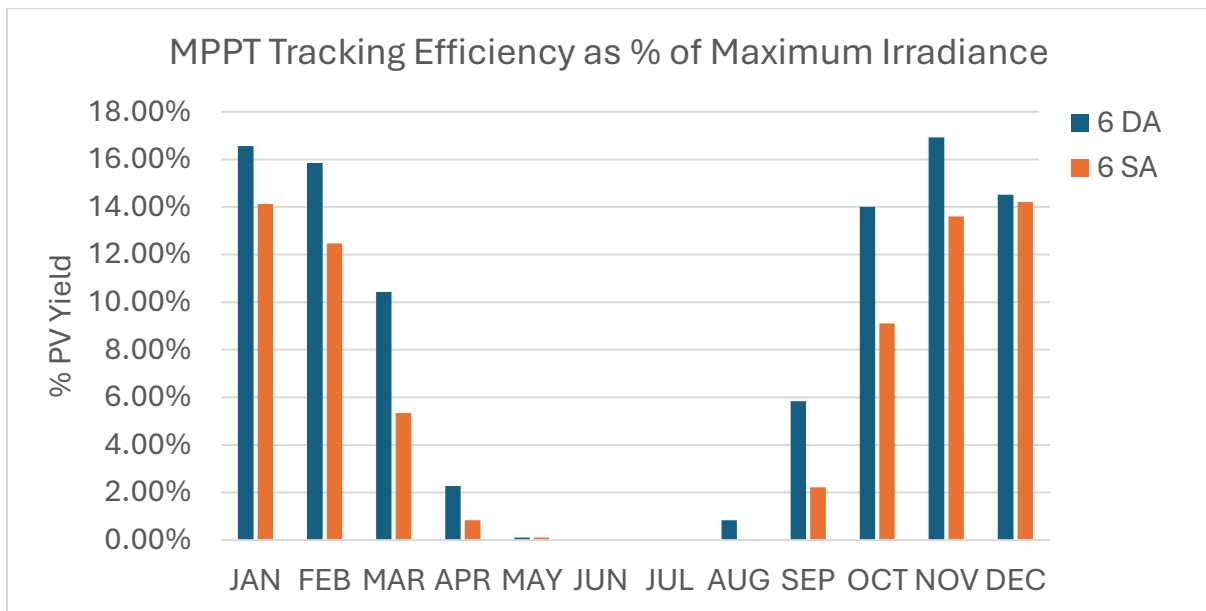


Figure 133: MPPT Tracking strategy efficiency as a percentage of maximum irradiation utilised as output power for scenario 6

8.5.8 – MPPT Efficiency as % of Maximum Power Generated by Module

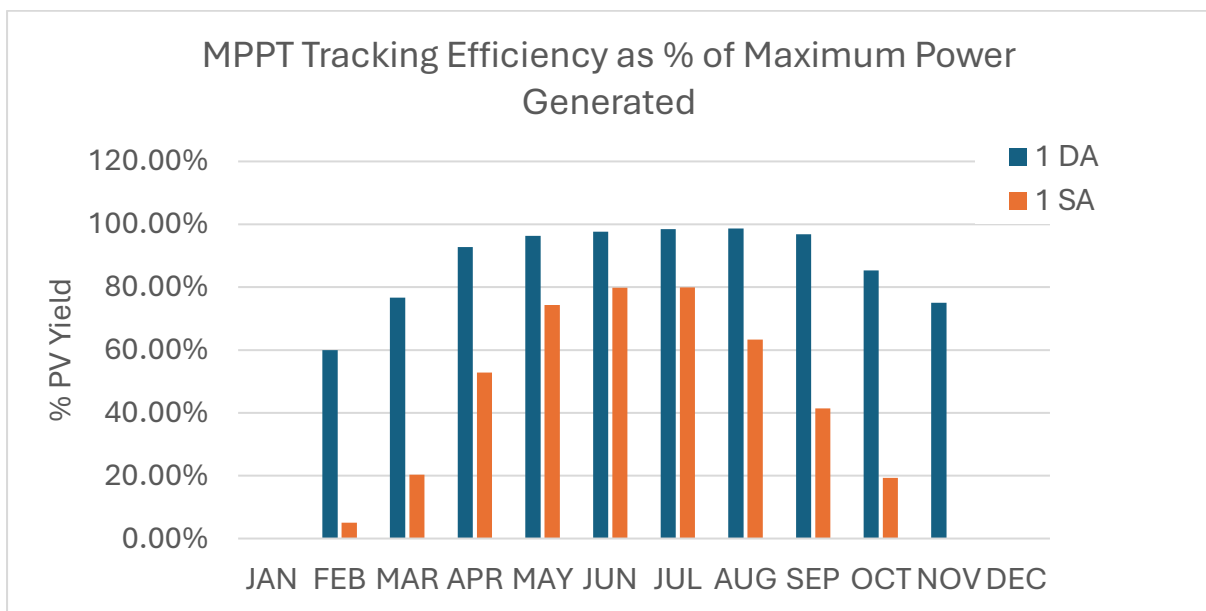


Figure 134: MPPT Tracking strategy efficiency as a percentage of maximum power potential to be generated (by direct incidence for all active solar hours) compared to the actual quantity generated for scenario 1.

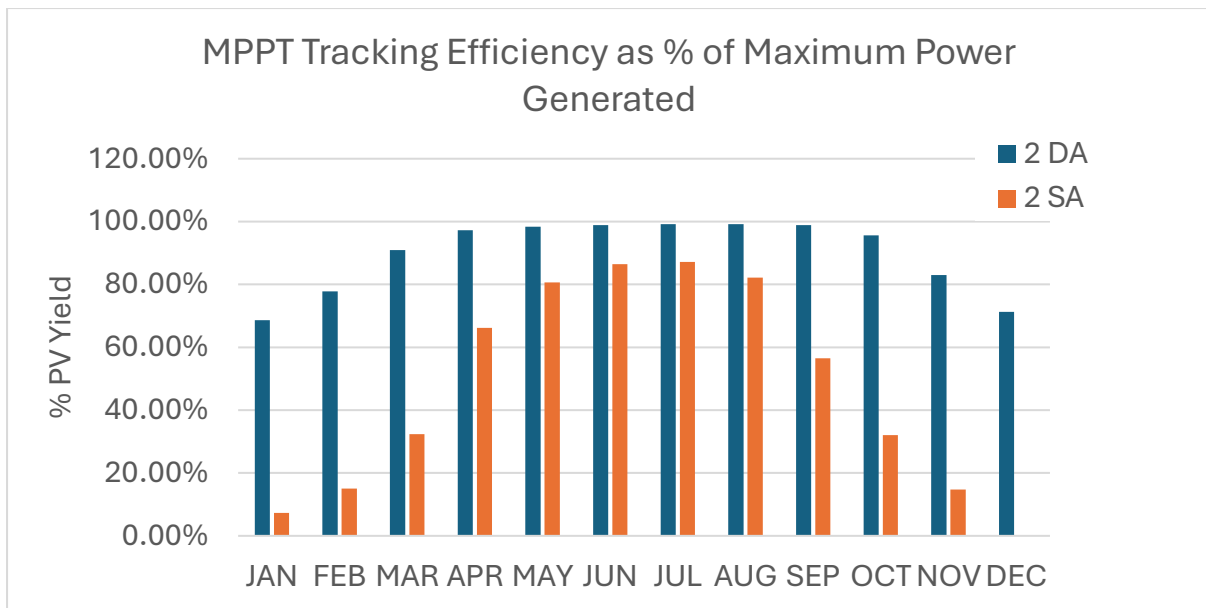


Figure 135: MPPT Tracking strategy efficiency as a percentage of maximum power potential to be generated (by direct incidence for all active solar hours) compared to the actual quantity generated for scenario 2.

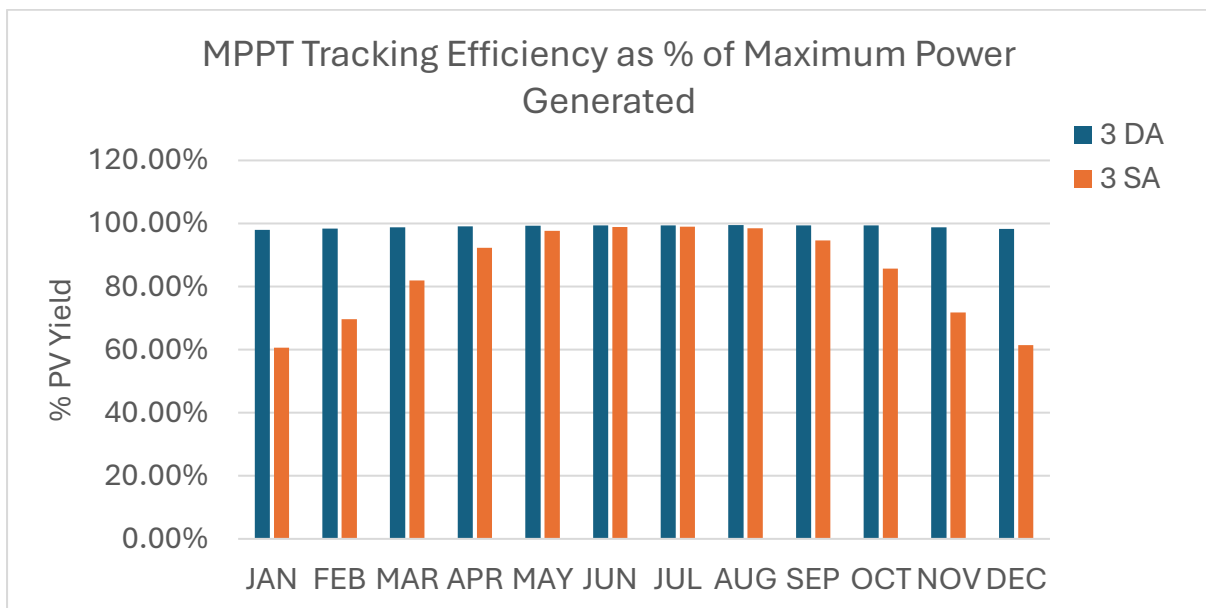


Figure 136: MPPT Tracking strategy efficiency as a percentage of maximum power potential to be generated (by direct incidence for all active solar hours) compared to the actual quantity generated for scenario 3

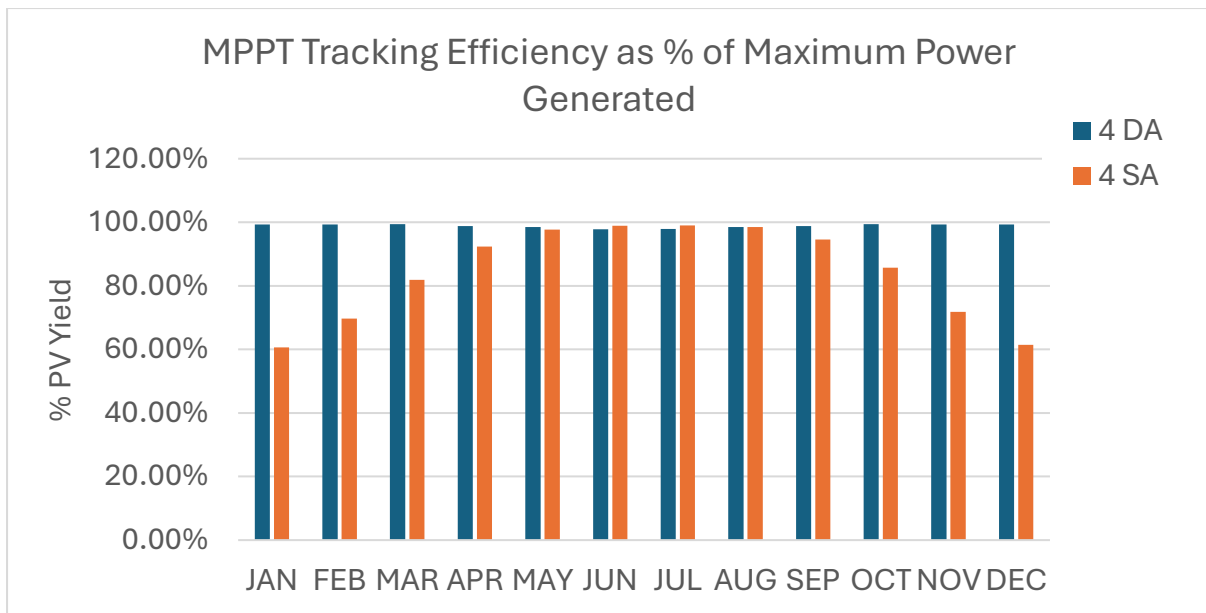


Figure 137: MPPT Tracking strategy efficiency as a percentage of maximum power potential to be generated (by direct incidence for all active solar hours) compared to the actual quantity generated for scenario 4

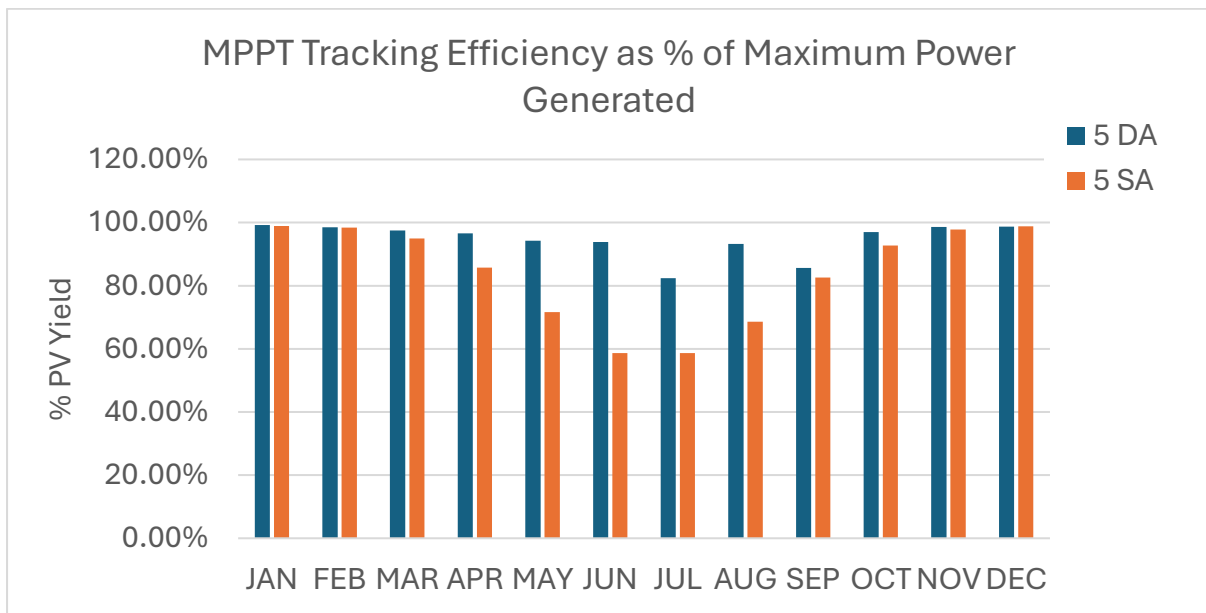


Figure 138: MPPT Tracking strategy efficiency as a percentage of maximum power potential to be generated (by direct incidence for all active solar hours) compared to the actual quantity generated for scenario 5

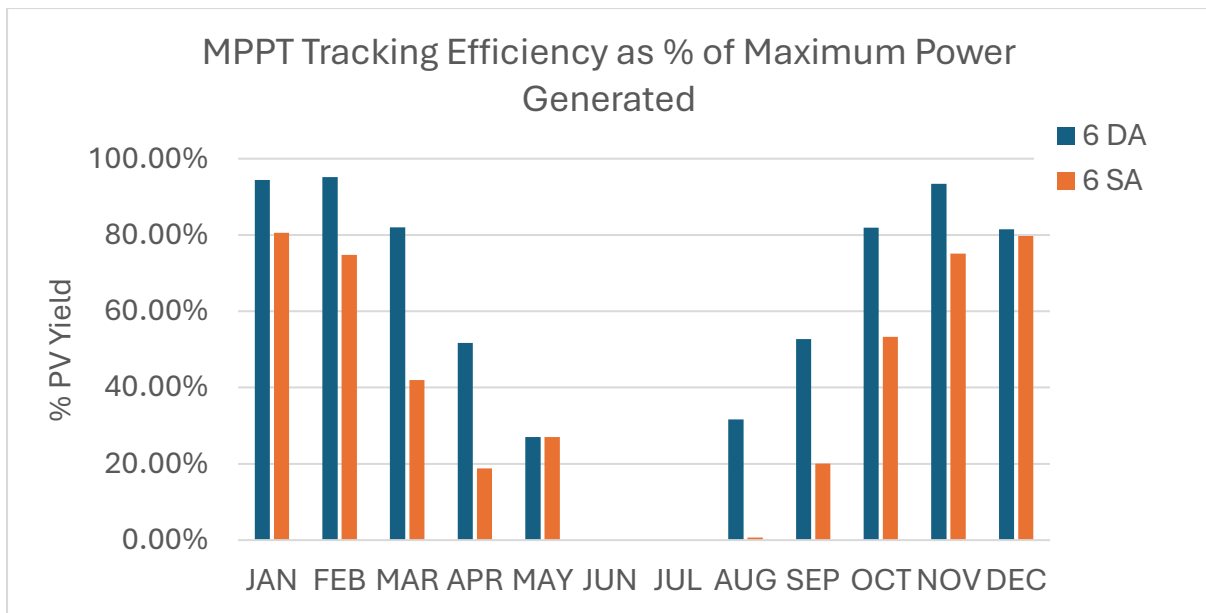


Figure 139: MPPT Tracking strategy efficiency as a percentage of maximum power potential to be generated (by direct incidence for all active solar hours) compared to the actual quantity generated for scenario 6

9.5.9 - % Difference Between Incident and Maximum Irradiation on Module

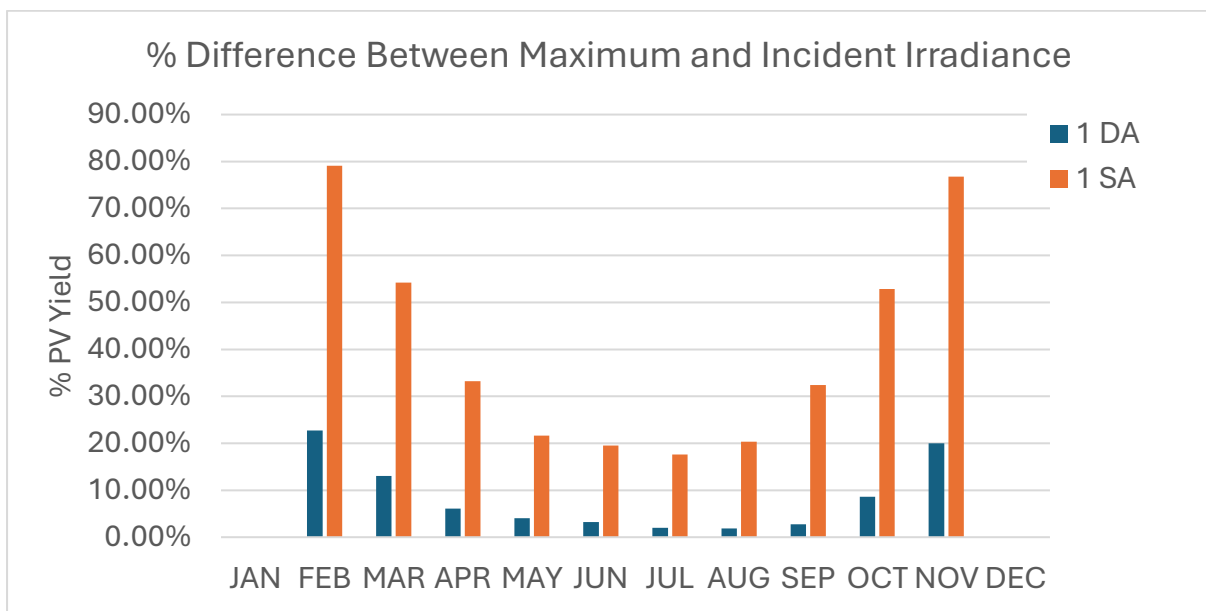


Figure 140: Percentage difference between total irradiation and the incident portion on the solar array, for scenario 1

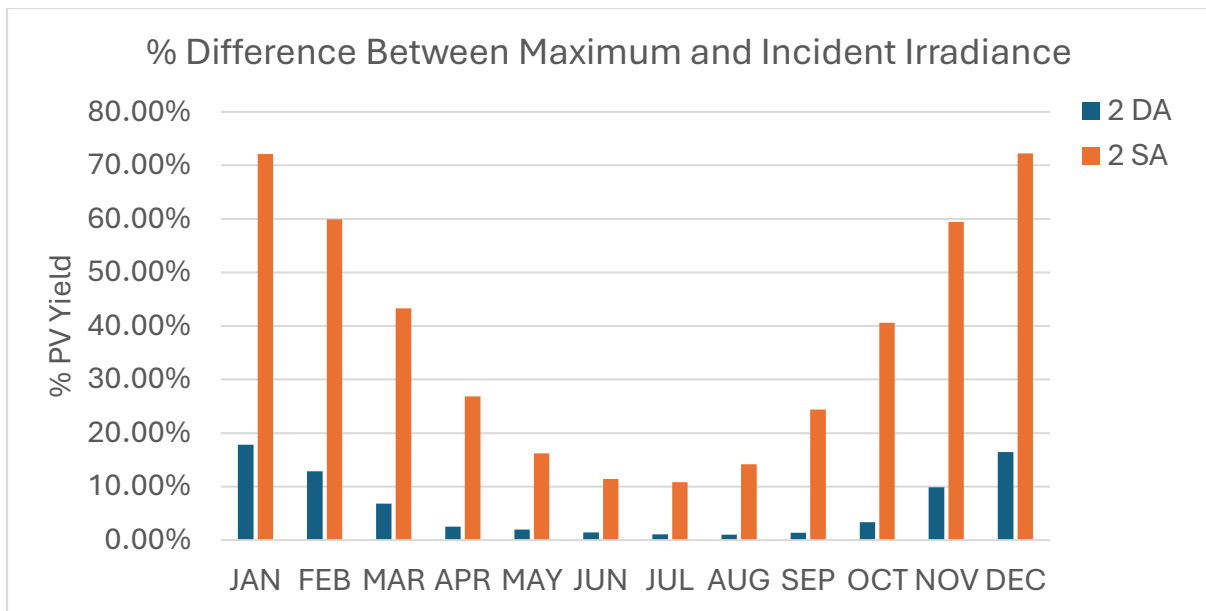


Figure 141: Percentage difference between total irradiation and the incident portion on the solar array, for scenario 2

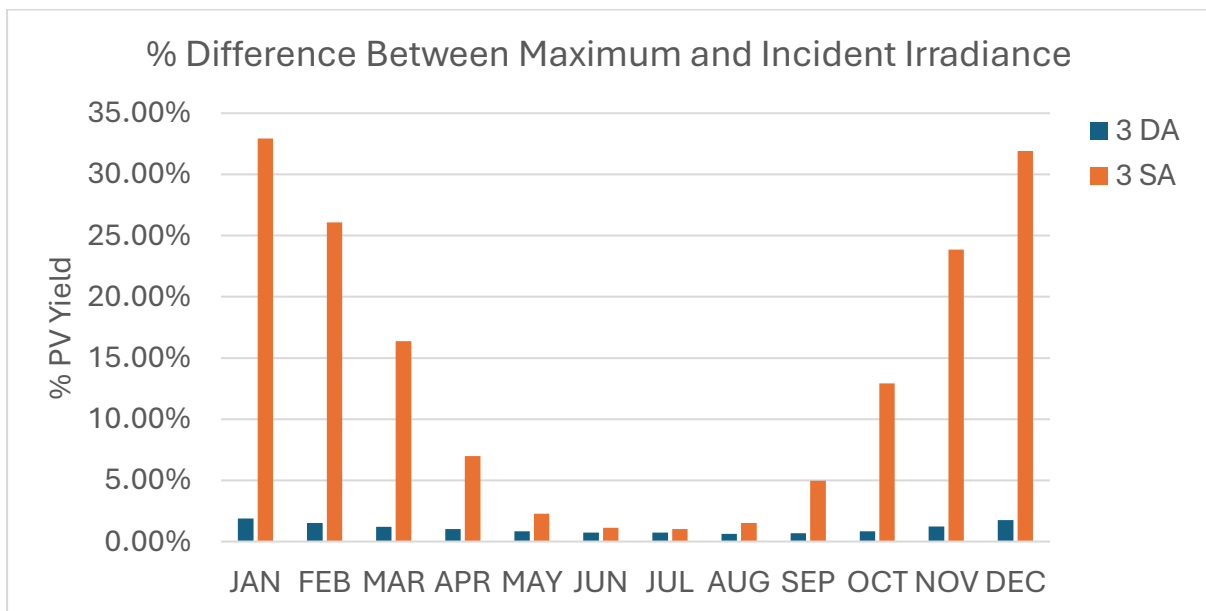


Figure 142: Percentage difference between total irradiation and the incident portion on the solar array, for scenario 3

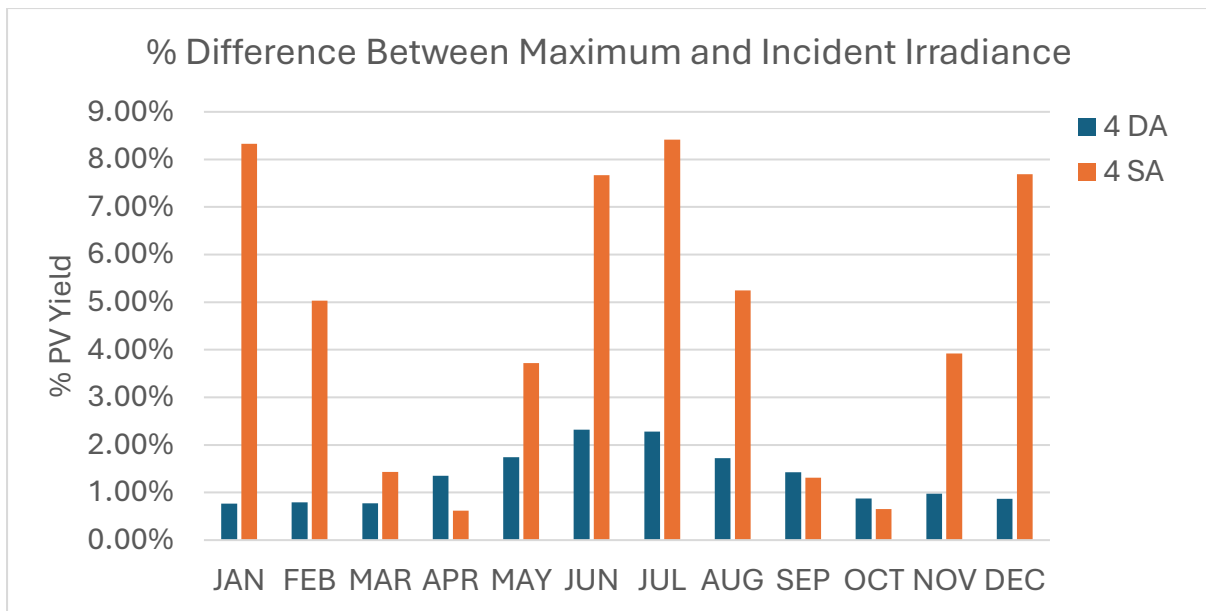


Figure 143: Percentage difference between total irradiation and the incident portion on the solar array, for scenario 4

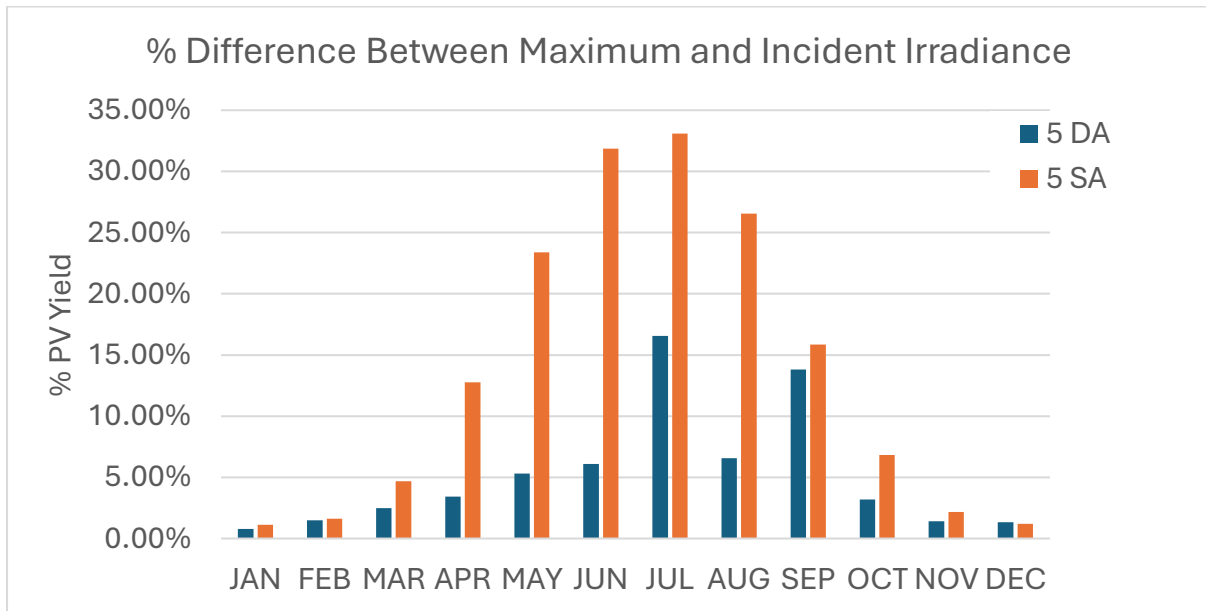


Figure 144: Percentage difference between total irradiation and the incident portion on the solar array, for scenario 5

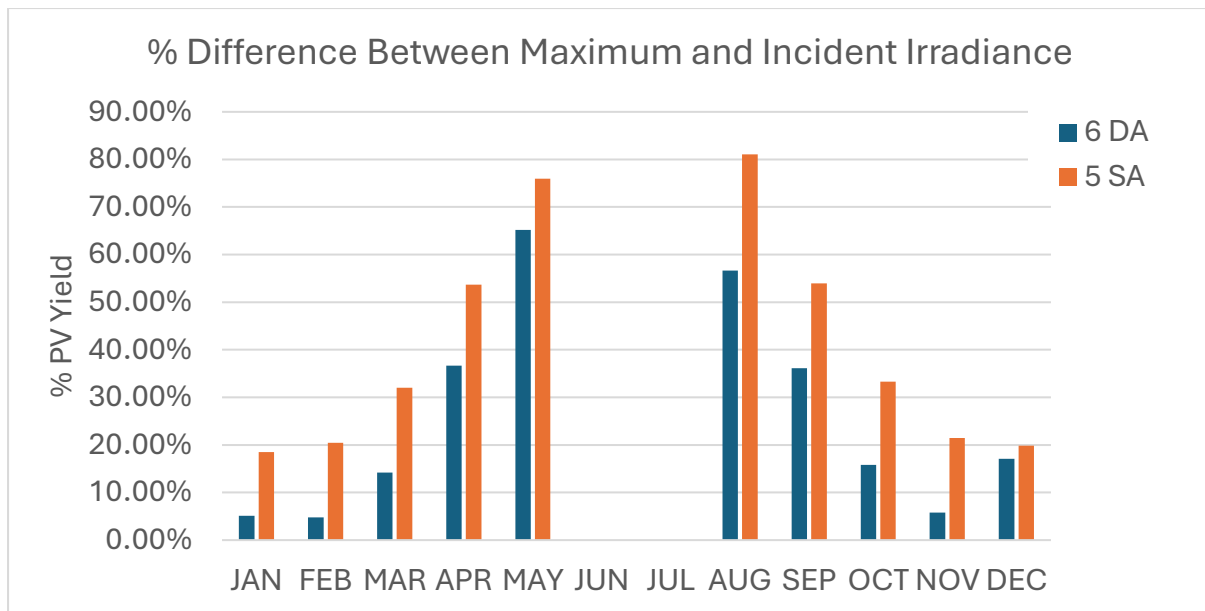


Figure 145: Percentage difference between total irradiation and the incident portion on the solar array, for scenario 6

8.5.10 – Efficiency of Tracking Strategies in all 6 Scenarios

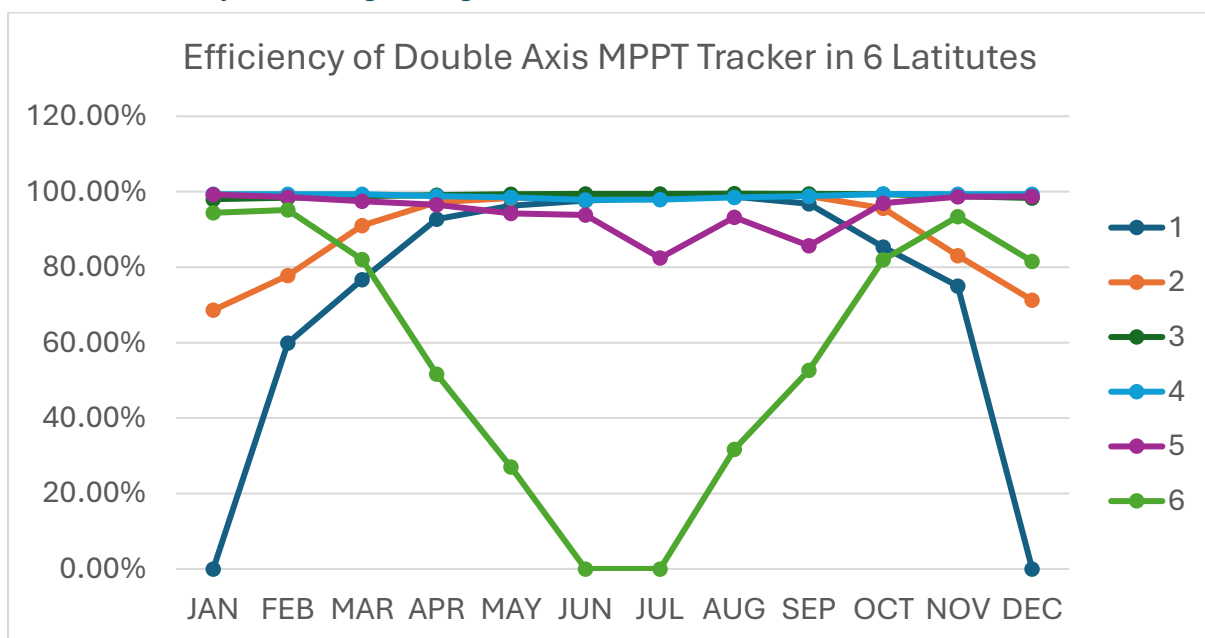


Figure 146: Efficiency of double axis tracking strategy for all 6 latitudes, based on the % of maximum power output utilised per month.

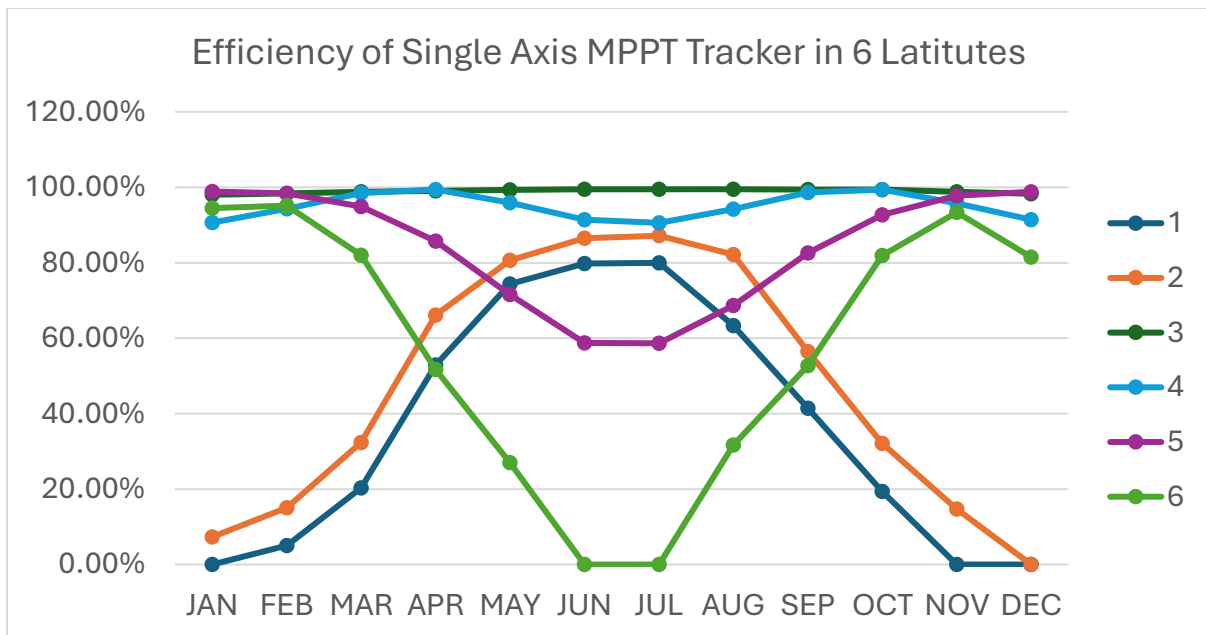


Figure 147: Efficiency of single axis tracking strategy for all 6 latitudes, based on the % of maximum power output utilised per month.

8.5.11 – Raw Data Extracted

8.5.11a – Double Axes

Table 19: Raw results data gathered by the simulation for double axis controller methods.

Scenario	Parameter	JAN	FEB	MAR	APR	MAY	JUN	JUL	AUG	SEP	OCT	NOV	DEC
1	Power Yield	0.0	12.1	573.8	2499.1	3913.3	3863.0	3135.6	1823.7	581.1	47.6	0.3	0.0
1	Maximum Power	0.0	20.3	748.5	2695.3	4063.9	3955.8	3185.7	1848.1	600.2	55.8	0.4	0.0
1	Irradiance on Array	0.0	543.8	5352.9	14883.0	22346.4	23365.9	19689.5	12588.4	6053.1	1445.0	84.0	0.0
1	Maximum Irradiance	0.0	703.7	6157.6	15848.9	23293.4	24153.1	20090.8	12826.6	6226.0	1581.0	105.0	0.0
1	%Yield Array	0.00%	1.72%	9.32%	15.77%	16.80%	15.99%	15.61%	14.22%	9.33%	3.01%	0.29%	0.00%
1	%MPPT Efficiency	0.00%	59.91%	76.66%	92.72%	96.29%	97.65%	98.43%	98.68%	96.82%	85.30%	75.00%	0.00%
1	%Max Irrad	0.00%	22.72%	13.07%	6.09%	4.07%	3.26%	2.00%	1.86%	2.78%	8.60%	20.00%	0.00%
2	Power Yield	32.8	287.5	1346.7	2708.9	3449.6	3751.3	3542.2	2537.0	1455.6	428.8	62.1	10.9
2	Maximum Power	47.7	369.6	1480.2	2785.5	3508.5	3793.1	3571.4	2556.9	1472.5	448.4	74.8	15.3
2	Irradiance on Array	1001.4	3416.4	8767.2	15618.2	19550.1	21314.9	20256.6	15218.2	9683.0	4546.0	1499.0	558.0
2	Maximum Irradiance	1218.1	3919.3	9407.9	16024.8	19939.2	21628.5	20479.1	15377.1	9820.0	4702.0	1663.0	668.0
2	%Yield Array	2.69%	7.34%	14.31%	16.90%	17.30%	17.34%	17.30%	16.50%	14.82%	9.12%	3.73%	1.63%
2	%MPPT Efficiency	68.60%	77.79%	90.98%	97.25%	98.32%	98.90%	99.18%	99.22%	98.85%	95.63%	83.02%	71.24%
2	%Max Irrad	17.79%	12.83%	6.81%	2.54%	1.95%	1.45%	1.09%	1.03%	1.40%	3.32%	9.86%	16.47%
3	Power Yield	2575.4	3118.3	3909.2	4410.8	4898.9	5304.5	5128.6	4914.6	4218.1	3576.3	2787.9	2391.1
3	Maximum Power	2627.5	3169.7	3957.2	4452.4	4933.2	5334.2	5157.2	4940.1	4243.6	3599.1	2820.6	2432.8
3	Irradiance on Array	14256.2	16905.6	20819.5	23409.6	25833.1	27947.0	27070.0	25909.0	22476.0	19192.0	15294.0	13378.0
3	Maximum Irradiance	14528.1	17167.6	21072.3	23651.0	26052.0	28154.0	27266.0	26072.0	22631.0	19355.0	15485.0	13615.0
3	%Yield Array	17.73%	18.16%	18.55%	18.65%	18.80%	18.84%	18.81%	18.85%	18.64%	18.48%	18.00%	17.56%

3	%MPPT Efficiency	98.01%	98.38%	98.79%	99.07%	99.30%	99.44%	99.45%	99.48%	99.40%	99.37%	98.84%	98.29%
3	%Max Irrad	1.87%	1.53%	1.20%	1.02%	0.84%	0.74%	0.72%	0.63%	0.68%	0.84%	1.23%	1.74%
4	Power Yield	3658.9	3697.0	3820.8	3719.1	3563.3	3338.6	3340.7	3615.1	3790.6	3794.3	3694.4	3621.3
4	Maximum Power	3684.9	3722.8	3844.8	3762.3	3617.7	3412.9	3412.0	3671.5	3836.6	3817.3	3719.3	3645.4
4	Irradiance on Array	19732.0	19882.2	20475.5	19998.8	19247.5	18172.0	18165.0	19486.0	20343.0	20367.0	19881.0	19552.0
4	Maximum Irradiance	19885.0	20041.9	20635.0	20272.5	19588.6	18604.0	18589.0	19827.0	20637.0	20546.0	20077.0	19723.0
4	%Yield Array	18.40%	18.45%	18.52%	18.35%	18.19%	17.95%	17.97%	18.23%	18.37%	18.47%	18.40%	18.36%
4	%MPPT Efficiency	99.29%	99.31%	99.38%	98.85%	98.50%	97.82%	97.91%	98.46%	98.80%	99.40%	99.33%	99.34%
4	%Max Irrad	0.77%	0.80%	0.77%	1.35%	1.74%	2.32%	2.28%	1.72%	1.42%	0.87%	0.98%	0.87%
5	Power Yield	5811.2	5185.4	4264.6	3202.6	2315.8	1875.7	1843.5	2756.6	3349.1	4699.5	5538.4	5810.1
5	Maximum Power	5855.8	5261.6	4374.8	3317.1	2457.6	1998.4	2236.9	2955.9	3908.9	4845.1	5615.6	5884.1
5	Irradiance on Array	30493.5	27245.3	22640.6	17363.6	13047.0	10900.0	10620.0	15076.0	17985.0	24700.0	29010.0	30495.0
5	Maximum Irradiance	30734.9	27653.8	23218.2	17979.8	13778.3	11606.0	12726.0	16135.0	20866.0	25511.0	29428.0	30906.0
5	%Yield Array	18.91%	18.75%	18.37%	17.81%	16.81%	16.16%	14.49%	17.08%	16.05%	18.42%	18.82%	18.80%
5	%MPPT Efficiency	99.24%	98.55%	97.48%	96.55%	94.23%	93.86%	82.41%	93.26%	85.68%	96.99%	98.63%	98.74%
5	%Max Irrad	0.79%	1.48%	2.49%	3.43%	5.31%	6.08%	16.55%	6.56%	13.81%	3.18%	1.42%	1.33%
6	Power Yield	5137.9	3002.8	848.3	42.8	0.1	0.0	0.0	4.9	326.0	2259.0	4760.7	5155.1
6	Maximum Power	5439.9	3156.0	1034.7	82.9	0.4	0.0	0.0	15.4	618.7	2756.5	5097.1	6326.9
6	Irradiance on Array	29447.5	18042.5	6980.2	1190.5	34.0	0.0	0.0	254.2	3565.4	13584.9	26504.2	29433.6
6	Maximum Irradiance	31028.8	18940.7	8134.5	1880.6	97.6	0.0	0.0	586.4	5583.0	16133.1	28135.3	35504.0
6	%Yield Array	16.56%	15.85%	10.43%	2.28%	0.10%	0.00%	0.00%	0.83%	5.84%	14.00%	16.92%	14.52%
6	%MPPT Efficiency	94.45%	95.15%	81.98%	51.68%	27.03%	0.00%	0.00%	31.66%	52.70%	81.95%	93.40%	81.48%
6	%Max Irrad	5.10%	4.74%	14.19%	36.70%	65.16%	0.00%	0.00%	56.65%	36.14%	15.79%	5.80%	17.10%

8.5.11b – Single Axis

Table 20: Raw results data gathered by the simulation for single axis controller methods.

Scenario	Parameter	JAN	FEB	MAR	APR	MAY	JUN	JUL	AUG	SEP	OCT	NOV	DEC
1	Power Yield	0.0	1.0	152.2	1424.7	3021.3	3157.3	2547.5	1170.2	248.7	10.8	0.0	0.0
1	Maximum Power	0.0	20.3	748.5	2695.3	4063.9	3955.8	3185.7	1848.1	600.2	55.8	0.4	0.0
1	Irradiance on Array	0.0	147.3	2820.0	10582.6	18257.0	19441.7	16552.8	10213.7	4210.2	745.8	24.4	0.0
1	Maximum Irradiance	0.0	703.7	6157.6	15848.9	23293.4	24153.1	20090.8	12826.6	6226.0	1581.0	105.0	0.0
1	%Yield Array	0.00%	0.15%	2.47%	8.99%	12.97%	13.07%	12.68%	9.12%	3.99%	0.68%	0.00%	0.00%
1	%MPPT Efficiency	0.00%	5.06%	20.33%	52.86%	74.34%	79.81%	79.97%	63.32%	41.44%	19.35%	0.00%	0.00%
1	%Max Irrad	0.00%	79.07%	54.20%	33.23%	21.62%	19.51%	17.61%	20.37%	32.38%	52.83%	76.76%	0.00%
2	Power Yield	3.5	55.6	478.7	1842.9	2828.0	3280.6	3112.8	2100.5	831.8	143.8	11.0	0.0
2	Maximum Power	47.7	369.6	1480.2	2785.5	3508.5	3793.1	3571.4	2556.9	1472.5	448.4	74.8	15.3
2	Irradiance on Array	339.4	1570.4	5333.6	11722.5	16707.4	19155.5	18268.2	13198.2	7424.8	2792.2	674.2	185.5
2	Maximum Irradiance	1218.1	3919.3	9407.9	16024.8	19939.2	21628.5	20479.1	15377.1	9820.0	4702.0	1663.0	668.0
2	%Yield Array	0.29%	1.42%	5.09%	11.50%	14.18%	15.17%	15.20%	13.66%	8.47%	3.06%	0.66%	0.00%
2	%MPPT Efficiency	7.33%	15.04%	32.34%	66.16%	80.61%	86.49%	87.16%	82.15%	56.49%	32.07%	14.71%	0.00%
2	%Max Irrad	72.14%	59.93%	43.31%	26.85%	16.21%	11.43%	10.80%	14.17%	24.39%	40.62%	59.46%	72.23%
3	Power Yield	1594.0	2209.6	3240.9	4111.3	4818.7	5277.8	5107.6	4866.6	4013.7	3083.4	2026.0	1495.2
3	Maximum Power	2627.5	3169.7	3957.2	4452.4	4933.2	5334.2	5157.2	4940.1	4243.6	3599.1	2820.6	2432.8
3	Irradiance on Array	9745.0	12689.6	17620.6	21997.9	25460.6	27835.3	26987.0	25680.0	21505.0	16855.0	11792.0	9270.0
3	Maximum Irradiance	14528.1	17167.6	21072.3	23651.0	26052.0	28154.0	27266.0	26072.0	22631.0	19355.0	15485.0	13615.0
3	%Yield Array	10.97%	12.87%	15.38%	17.38%	18.50%	18.75%	18.73%	18.67%	17.74%	15.93%	13.08%	10.98%
3	%MPPT Efficiency	60.66%	69.71%	81.90%	92.34%	97.68%	98.94%	99.04%	98.51%	94.58%	85.67%	71.83%	61.46%

3	%Max Irrad	32.92%	26.08%	16.38%	6.99%	2.27%	1.13%	1.02%	1.50%	4.98%	12.92%	23.85%	31.91%
4	Power Yield	3341.5	3512.2	3785.9	3740.5	3470.6	3120.8	3090.2	3457.7	3784.5	3793.7	3559.7	3333.9
4	Maximum Power	3684.9	3722.8	3844.8	3762.3	3617.7	3412.9	3412.0	3671.5	3836.6	3817.3	3719.3	3645.4
4	Irradiance on Array	18228.8	19033.2	20338.7	20147.3	18859.3	17177.7	17025.0	18786.0	20367.0	20412.0	19289.0	18206.0
4	Maximum Irradiance	19885.0	20041.9	20635.0	20272.5	19588.6	18604.0	18589.0	19827.0	20637.0	20546.0	20077.0	19723.0
4	%Yield Array	16.80%	17.52%	18.35%	18.45%	17.72%	16.77%	16.62%	17.44%	18.34%	18.46%	17.73%	16.90%
4	%MPPT Efficiency	90.68%	94.34%	98.47%	99.42%	95.93%	91.44%	90.57%	94.18%	98.64%	99.38%	95.71%	91.45%
4	%Max Irrad	8.33%	5.03%	1.44%	0.62%	3.72%	7.67%	8.41%	5.25%	1.31%	0.65%	3.92%	7.69%
5	Power Yield	5789.8	5176.8	4152.8	2843.7	1759.5	1173.2	1311.9	2028.7	3226.7	4491.3	5491.2	5812.8
5	Maximum Power	5855.8	5261.6	4374.8	3317.1	2457.6	1998.4	2236.9	2955.9	3908.9	4845.1	5615.6	5884.1
5	Irradiance on Array	30392.5	27208.8	22132.0	15683.0	10554.8	7907.0	8514.0	11849.0	17561.0	23767.0	28790.0	30537.0
5	Maximum Irradiance	30734.9	27653.8	23218.2	17979.8	13778.3	11606.0	12726.0	16135.0	20866.0	25511.0	29428.0	30906.0
5	%Yield Array	18.84%	18.72%	17.89%	15.82%	12.77%	10.11%	10.31%	12.57%	15.46%	17.61%	18.66%	18.81%
5	%MPPT Efficiency	98.87%	98.39%	94.93%	85.73%	71.59%	58.71%	58.65%	68.63%	82.55%	92.70%	97.78%	98.79%
5	%Max Irrad	1.11%	1.61%	4.68%	12.77%	23.40%	31.87%	33.10%	26.56%	15.84%	6.84%	2.17%	1.19%
6	Power Yield	4385.4	2361.2	434.3	15.6	0.1	0.0	0.0	0.1	124.3	1468.5	3827.1	5044.6
6	Maximum Power	5439.9	3156.0	1034.7	82.9	0.4	0.0	0.0	15.4	618.7	2756.5	5097.1	6326.9
6	Irradiance on Array	25283.1	15072.6	5528.2	870.8	23.5	0.0	0.0	110.9	2569.0	10756.2	22098.8	28460.9
6	Maximum Irradiance	31028.8	18940.7	8134.5	1880.6	97.6	0.0	0.0	586.4	5583.0	16133.1	28135.3	35504.0
6	%Yield Array	14.13%	12.47%	5.34%	0.83%	0.10%	0.00%	0.00%	0.02%	2.23%	9.10%	13.60%	14.21%
6	%MPPT Efficiency	80.62%	74.82%	41.97%	18.79%	27.03%	0.00%	0.00%	0.65%	20.08%	53.27%	75.08%	79.73%
6	%Max Irrad	18.52%	20.42%	32.04%	53.70%	75.92%	0.00%	0.00%	81.09%	53.99%	33.33%	21.46%	19.84%